Coherent manipulation of ultracold atoms on atom chips

Dissertation submitted to the Faculty of Physics
of the
Ludwig–Maximilians–Universität München

by

Philipp Treutlein

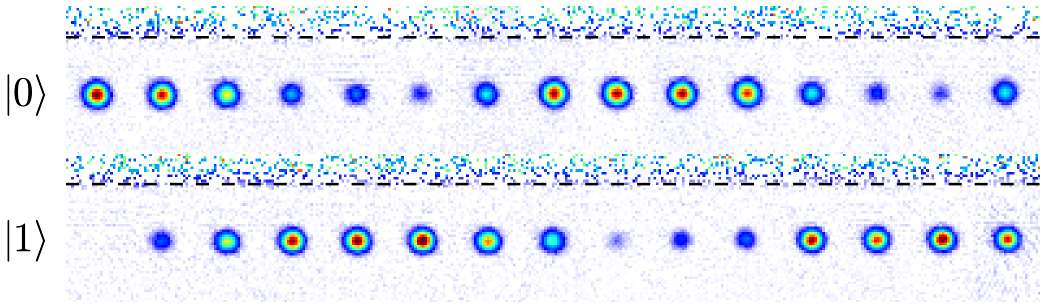

München, February 22, 2008

Referees: Prof. Dr. Theodor W. Hänsch
Prof. Dr. Jakob Reichel

Date of the oral examination: April 01, 2008

Meinen Eltern

Zusammenfassung

Diese Dissertation umfasst Experimente und theoretische Überlegungen zur kohärenten Manipulation von ultrakalten Atomen auf einem Atomchip. In Experimenten untersuchen wir den Einfluss der Chipoberfläche auf die Kohärenz von Superpositionen interner atomarer Zustände und realisieren eine Chip-basierte Atomuhr. Weiterhin werden detaillierte theoretische Vorschläge für ein Atomchip-Quantengatter sowie für die Kopplung von Bose-Einstein-Kondensaten an nanoelektromechanische Systeme gemacht.

Wir fangen Atome in einer magnetischen Mikrofalle auf einem Chip und präparieren sie in einer kohärenten Superposition zweier interner Zustände, deren magnetisches Moment nahezu identisch ist. Mit Hilfe von Ramsey-Interferometrie wird untersucht, welchen Einfluss die Wechselwirkungen mit der Chipoberfläche auf die Kohärenz der Zustände haben. In Abständen von $5 - 130$ μm von der Oberfläche beobachten wir Kohärenzzeiten und Lebensdauern der Atome von über 1 s. Die Atome in der Chipfalle weisen eine vergleichbare Kohärenzzeit auf wie Atome in makroskopischen Magnetfallen. Bei kleineren Abständen beobachten wir einen Verlust von Atomen aufgrund des anziehenden Casimir-Polder-Oberflächenpotentials.

Die guten Kohärenzeigenschaften ermöglichen es uns, eine Atomuhr auf dem Mikrochip zu realisieren. Eine Messung der relativen Frequenzstabilität ergibt 1.7×10^{-11} $(\tau[\mathrm{s}])^{-1/2}$. Wir zeigen einfache Verbesserungen auf, mit denen sich eine Stabilität von 10^{-13} $(\tau[\mathrm{s}])^{-1/2}$ erreichen lassen sollte. Eine solche Uhr könnte Anwendungen als portabler sekundärer Frequenzstandard sowie in der Satellitennavigation finden.

Das von uns untersuchte Zustandspaar kann für die Quanteninformationsverarbeitung verwendet werden. Dazu machen wir einen detaillierten theoretischen Vorschlag für ein Kollisions-Quantengatter auf einem Atomchip. Ein wesentlicher Bestandteil des Gatters sind zustandsselektive Potentiale, die durch Mikrowellen-Nahfelder erzeugt werden. Diese neuartigen Potentiale verbinden Eigenschaften von optischen Dipolpotentialen mit denen magnetischer Nahfeldfallen. Wir beschreiben das Design und die Fabrikation eines mehrlagigen Atomchips für Experimente mit Mikrowellen-Nahfeldern.

Über die quantenmechanische Manipulation von Atomen hinaus ermöglichen Atomchips neue Experimente im Grenzbereich von Quantenoptik und Festkörperphysik. Atomare Bose-Einstein-Kondensate könnten zum Beispiel an die Schwingungen eines mechanischen Nanoresonators gekoppelt werden. Wir analysieren dieses System theoretisch und zeigen, dass es ein mechanisches Analogon zur Resonator-Quantenelektrodynamik im Regime starker Kopplung darstellt.

Abstract

In this thesis, I report experiments and theoretical work on the coherent manipulation of ultracold atoms on an atom chip. We experimentally investigate the effect of the atom chip surface on internal-state coherence and demonstrate a chip-based atomic clock. Theoretical proposals are made for a robust atom chip quantum gate and for the coupling of a Bose-Einstein condensate to a nanoelectromechanical system.

In our experiments, we trap atoms in a magnetic microchip trap and prepare them in a coherent superposition of two internal states with nearly identical magnetic moments. By performing Ramsey interferometry we investigate the effect of atom-surface interactions on internal-state coherence. Trap and coherence lifetimes exceeding 1 s are observed with atoms at distances of $5 - 130$ μm from the chip surface. The coherence lifetime in the chip trap agrees well with the results of similar measurements in macroscopic magnetic traps. At distances below 5 μm, loss of atoms occurs due to the attractive Casimir-Polder surface potential.

We make use of the good coherence properties to demonstrate a chip-based atomic clock and measure its relative frequency stability to 1.7×10^{-11} $(\tau[\mathrm{s}])^{-1/2}$. Our measurements show that with straightforward improvements a relative stability in the 10^{-13} $(\tau[\mathrm{s}])^{-1/2}$ range is realistic. An atom chip clock may find applications as a portable secondary standard and in satellite navigation.

We propose to use our state pair for quantum information processing and describe a realistic implementation of a collisional quantum phase gate on an atom chip. In our proposal, a key role is played by state-selective microwave near-field potentials. These potentials are a useful new tool for atom chip experiments. They combine the versatility of optical dipole traps with the dissipationless character of static magnetic potentials and the adjustable geometry of a near-field trap. We describe the design and fabrication of a multi-layer atom chip for experiments with microwave near-fields.

The work reported here shows that atom chips are a versatile system for quantum engineering. Moreover, atom chips enable new and intriguing experiments at the boundary between quantum optics and condensed matter physics. As an example, we propose to couple a Bose-Einstein condensate to the mechanical oscillations of a nanoscale cantilever with a magnetic tip. This system realizes a mechanical analog of cavity quantum electrodynamics, with the possibility to reach the strong coupling regime.

Contents

Introduction

Quantum mechanics was developed as a theory to describe the behavior of microscopic objects, such as atoms in a gas. Since its inception in the early 20th century, the often counterintuitive predictions of this theory have been confirmed in numerous experiments on electrons [1], photons [2, 3], atoms [4], and many other microscopic particles, but also on mesoscopic systems such as large biomolecules [5, 6].

Truly macroscopic objects, on the other hand, behave classically. This is surprising, considering that these objects are composed of the same microscopic particles, which, if isolated, show quantum behavior. Indeed, quantum mechanics is required for a satisfactory explanation of many of the material parameters, such as electric conductivity, optical refractive index, or heat capacity. However, the dynamics of the macroscopic degrees of freedom, such as the position and the velocity of the center of mass, is governed by classical physics. The absence of quantum behavior in the dynamics of macroscopic objects is commonly explained by the process of decoherence [7], induced by the uncontrolled interaction of the object with its environment.

Quantum engineering aims at creating large quantum systems in which decoherence is suppressed. The goal is to build complex systems out of simple ones, while maintaining full quantum control over the constituents. Engineered quantum systems can be used to perform quantum computations [8, 9], improve measurement precision beyond what is possible by classical means [10, 11], or simulate other quantum systems where such a high degree of control is not available [12, 13]. Furthermore, large quantum systems may enable experimental tests of theories beyond standard quantum mechanics, which predict a fundamental upper limit on the “size” of quantum mechanical superposition states [14, 15]. Experiments in quantum engineering require an exceptional isolation of the system from its environment, and sophisticated technologies for quantum control [16, 17, 18, 19, 20].

Ultracold neutral atoms in magnetic microtraps on a chip are a new and exciting system for quantum engineering [21, 22, 23, 24]. Because of their electric neutrality, the atoms are very well decoupled from the environment.

With the achievement of Bose-Einstein condensation (BEC) in a gas of neutral atoms [25, 26], it has become possible to initialize a large number of atoms in a well defined quantum state. In 1999, the first experiment was reported in which atoms were trapped in magnetic fields generated by microfabricated wires on a substrate [27]. Soon thereafter, these "atom chips" were used to prepare BECs, with a much simpler experimental setup and in much shorter time than in traditional experiments [28, 29]. The versatility of this technique was further demonstrated in experiments where atoms were guided, transported, split and merged with the help of suitably designed microfabricated wire patterns (see [21, 22, 23, 24] and chapter 1 of this thesis for a review of atom chips). Inspired by the enormous success of microfabrication technology in miniaturizing and integrating electronics components in modern computers, this has sparked the vision of a "quantum laboratory on a chip", where a large number of ultracold atoms can be manipulated on the quantum level, with the help of tiny wires, magnets, and optical elements.

Coherent superpositions of quantum states, quantum interference, and entanglement are the main resources which distinguish such a quantum laboratory from its classical counterpart. The capability to manipulate these resources and to preserve the coherence of the created quantum states for a long time are thus essential prerequisites for applications of atom chips in quantum engineering.

Many of the proposed applications (see [22, 23, 24] and references therein) require that the atoms be trapped at very small distance from the chip surface, typically a few micrometers. This is because the distance of the trapped atoms to the wires and other structures on the chip sets the length scale on which the atoms can be manipulated. On a small scale, the dynamics are faster, which is important e.g. for quantum information processing. Furthermore, features smaller than the size of the atomic wave function are required for "wave function engineering", i.e. full quantum control of the atomic motion.

Trapping ultracold atoms a few micrometers away from a room-temperature chip surface raises interesting questions about decoherence. Consider that the mean thermal energy of a single degree of freedom of the surface is about nine orders of magnitude larger than the mean energy of a trapped atom. When the first atom chip experiments were carried out, it was largely unknown which role atom-surface interactions would play in such a situation. The question was raised whether surface effects would prevent coherent manipulation on atom chips. In [30, 31] it was predicted that magnetic noise caused by the thermal motion of the electrons in the chip conductors leads to significantly reduced trap lifetimes at small atom-surface distances. This effect was first observed in [32], for a recent review see [24]. These and other measurements reporting the fragmentation of BECs near the chip surface [33] raised doubt about the usefulness of atom chips for quantum engineering, in particular since none of the experiments up to then had actually demonstrated coherent manipulation of the atoms.

This thesis

In this thesis, I describe experiments in which atoms are manipulated coherently on an atom chip and report internal-state coherence lifetimes exceeding one second at a few micrometers distance from the chip surface. Based on these results, I present experimental and theoretical work towards three applications of atom chips: a chip-based *atomic clock*, a robust atom chip *quantum gate*, and a *hybrid quantum system* composed of ultracold atoms coupled to a solid-state nanosystem.

Coherence near the chip surface. — In order to investigate their coherence properties near the chip surface, we prepare atoms in a coherent superposition of two internal states $|0\rangle$ and $|1\rangle$ which are both magnetically trappable, and measure the coherence lifetime. Because the magnetic moments of the two states are nearly equal, the states experience nearly identical trapping potentials and the superpositions are very robust against magnetic-field induced decoherence. This allows us to obtain coherence lifetimes exceeding 1 s, measured at several distances in the range of $5 - 130$ μm from the microchip surface. Our measurements show that with the right choice of atomic states and a suitable design of the structures on the chip, surface-induced and other loss and decoherence effects can be suppressed to a level that is compatible with the requirements of the proposed atom chip applications.

Atomic clock on a chip. — We make use of the good coherence properties of our state pair to experimentally demonstrate the first application of an atom chip in precision metrology. In a proof-of-principle experiment, we realize a chip-based atomic clock and measure the relative stability of its transition frequency to 1.7×10^{-11} $(\tau[\mathrm{s}])^{-1/2}$. Our measurements show that with straightforward improvements, a portable atom chip clock with a relative stability in the 10^{-13} $(\tau[\mathrm{s}])^{-1/2}$ range is realistic. Such a clock would outperform today's best commercial atomic clocks by a factor of 10, while being much smaller than the atomic fountain primary standards.

Microwave near-fields for robust quantum gates on atom chips. — A detailed theoretical proposal is made for an atom chip quantum gate. The gate is based on entanglement of atoms via internal-state dependent elastic collisions, as suggested by Calarco *et al.* [34]. Our proposal describes a realistic scenario for the implementation of such a gate, using the same robust state pair $|0\rangle$ and $|1\rangle$ as in the coherence measurements. We find an overall infidelity compatible with requirements for fault-tolerant quantum computation.

A key role in our proposal is played by microwave near-fields, which are used to add the required internal-state dependence to the trapping potentials. I discuss the theory of microwave potentials and show experimentally how microwaves can be guided on atom chips. Besides applications in quantum information processing, microwave near-fields could be useful for experiments on chip-based atomic clocks, atom interferometry, the Josephson effect, and the entanglement of BECs.

Ultracold atoms coupled to solid-state nanosystems. — The fact that atoms can be manipulated coherently at micrometer distance from a surface has prompted us to investigate the coupling of atoms to nanostructured solid-state systems on the chip. As a realistic example of such a hybrid quantum system, we propose to couple a BEC to a nanomechanical cantilever resonator with a magnetic tip. We find that the BEC can be used as a sensitive quantum probe which allows one to detect the thermal motion of the resonator at room temperature. At lower resonator temperatures, the backaction of the atoms onto the resonator is significant and the coupled system realizes a mechanical analog of cavity quantum electrodynamics in the strong coupling regime. This could be used for interesting experiments at the boundary between quantum optics and solid state physics.

Chip fabrication and compact glass cell vacuum system. — The proposed experiments require chips with much smaller and more complex structures than those which were used in experiments up to now. The chips of our earlier experiments were fabricated at other research institutes and had only a single layer of wires. In this thesis, a new fabrication process is described which we have developed to fabricate atom chips with several layers of metallization, where the smallest structures are of the order of one micrometer. Our chips are integrated into a very compact glass cell vacuum chamber, a technique developed in [35]. This provides excellent access to the chip wires, which is important in particular for the microwave experiments. Although the chip and the glass cell are simply attached to each other by epoxy glue, we achieve ultra-high vacuum and are able to prepare BECs in the cell. The compact vacuum chamber makes experiments simpler and thus quantum phenomena more accessible, and will enable portable atom chip setups.

Organization of the chapters

- In chapter 1, I review basic concepts of atom chips, including wire structures for magnetic trapping and properties of Bose-Einstein condensates in chip traps. A detailed discussion of atom-surface interactions and other loss and decoherence mechanisms follows.

- In chapter 2, I describe in detail our new fabrication process for atom chips with multiple layers of metallization. The microwave atom chip and a chip for magnetic multi-well potentials are shown, which have been fabricated with this process.

- In chapter 3, the experimental setup is described. Special emphasis is on the compact glass cell vacuum chamber and on low noise absorption imaging of small numbers of atoms. The chapter concludes with a description of a typical experimental sequence for Bose-Einstein condensation on the chip.

- In chapter 4, our experiments on coherent internal-state manipulation of atoms in chip traps are described. The effects of atom-surface interactions on trap and coherence lifetimes are investigated experimentally. I report on the realization of a chip-based atomic clock and a measurement of its frequency stability.

- In chapter 5, microwave near-fields on atom chips are discussed. First, I develop the theory of microwave near-field potentials. Then, I show how microwave guiding structures can be designed and integrated on an atom chip. An experimental characterization of such structures follows.

- In chapter 6, a robust quantum gate on an atom chip is proposed and theoretically analyzed, which makes use of the microwave near-field potentials.

- In chapter 7, I theoretically investigate the coupling of ultracold atoms to a nanomechanical resonator on an atom chip.

- An outlook (chapter 8) on future experiments concludes this thesis.

Publications of thesis work

- *Coherence in Microchip Traps.*
  P. Treutlein, P. Hommelhoff, T. Steinmetz, T. W. Hänsch, and J. Reichel,
  Physical Review Letters **92**, 203005 (2004).

- *Coherent Atomic States in Microtraps.*
  P. Treutlein, P. Hommelhoff, T. W. Hänsch, and J. Reichel,
  in: "Laser Spectroscopy: Proceedings of the XVI International Conference (ICOLS 2003)", ed. by P. Hannaford, A. Sidorov, H. Bachor, K. Baldwin (World Scientific, Singapore, 2004) pp. 231-236.

- *Quantum information processing in optical lattices and magnetic microtraps.*
  P. Treutlein, T. Steinmetz, Y. Colombe, B. Lev, P. Hommelhoff, J. Reichel, M. Greiner, O. Mandel, A. Widera, T. Rom, I. Bloch, and T. W. Hänsch,
  Fortschritte der Physik/Progress of Physics **54**, 702 (2006).

  This article also appeared in: "Elements of Quantum Information", ed. by W. P. Schleich and H. Walther (Wiley-VCH, Weinheim, Germany, 2007), pp. 121-144.

- *Microwave potentials and optimal control for robust quantum gates on an atom chip.*
  P. Treutlein, T. W. Hänsch, J. Reichel, A. Negretti, M. A. Cirone, and T. Calarco,
  Physical Review A **74**, 022312 (2006).

- *Bose-Einstein Condensate Coupled to a Nanomechanical Resonator on an Atom Chip.*
  P. Treutlein, D. Hunger, S. Camerer, T. W. Hänsch, and J. Reichel,
  Physical Review Letters **99**, 140403 (2007).

Chapter 1

Atom chip theory

In this chapter I review fundamental concepts of atom chips which are of importance for the work in this thesis. Starting from the principles of magnetic trapping I discuss the basic wire trap configurations used in our experiments. Important properties of Bose-Einstein condensates in chip traps are briefly summarized. A substantial part of this chapter is devoted to processes which can limit the coherent manipulation of atoms in chip traps: First, collisional loss processes are discussed which are relevant at the high atomic number densities in the tight traps of our experiments. Second, a detailed overview over atom-surface interaction effects is given, including formulae for quantitative estimates of their magnitude. This serves as a theoretical background for the coherence measurements near the chip surface in chapter 4.

1.1 Atoms in chip traps

We use microfabricated current-carrying wires on a chip to create tightly confining magnetic traps for ultracold neutral atoms. Such an "atom chip", proposed by Weinstein and Libbrecht in 1995 [36], was first successfully realized in 1999 by Reichel, Hänsel, and Hänsch [27], following earlier experiments with discrete wires and permanent magnets [37, 38, 39]. The maximum magnetic field modulus, gradient, and curvature which can be generated by an arrangement of current-carrying wires scale as I/s, I/s^2, and I/s^3, respectively, where I is the current and s is the characteristic size of the wire arrangement. Microfabricated wires can therefore be used to generate much more tightly confining magnetic traps with less power dissipation than possible with macroscopic coils. The achievement of Bose-Einstein condensation (BEC) [28, 29] and Fermi degeneracy [40] on atom chips in single-chamber vacuum systems and with an overall experimental cycle as short as a few seconds [29, 40] beautifully illustrates how this benefits atomic physics experiments.

Even more important, atom chips provide a versatile technique for the coherent manipulation of ultracold atoms on the micrometer scale. Elaborate wire patterns can be fabricated by lithographic techniques as described in chapter 2. In the near-field of the wires, potentials with complex structure can be created, tailored to a specific purpose, with narrow features such as tunneling barriers. The potentials are not restricted to periodic arrangements and can be easily modulated with high spatial and temporal resolution by adjusting individual wire currents. First steps in this direction are the transporting, splitting, and merging of atomic ensembles with an "atomic conveyor belt" [41, 42].

To create potentials with small features of size l, it is in general[1] required that both s and the atom-wire distance d be small, $s, d \leq l$. However, as d decreases, atom-surface interactions come into play, which ultimately limit coherent manipulation in chip traps, as first pointed out in [30]. These interactions set a lower limit on d and thus on l. This, in turn, also sets a lower limit on the time scale $t \sim h/E \sim ml^2/h$ of fully controlled motional dynamics, where $E \sim h^2/ml^2$ is the kinetic energy of atoms of mass m localized on the scale l. Atom-surface interactions in chip traps have now been extensively studied and I summarize the relevant effects in this chapter. With proper choice of chip materials and fabrication techniques, atom trapping at d as small as a few hundred nanometers is possible, as has been experimentally demonstrated in [44]. Furthermore, quantum-mechanical coherence can indeed be preserved on atom chips. This was first shown for atomic internal degrees of freedom in the experiments reported in chapter 4 of this thesis, and subsequently for motional degrees of freedom in [45, 46].

In recent years, several review papers on atom chips appeared [21, 22, 23, 24], with special emphasis on wire-based magnetic traps. Wire traps are the workhorses of atom chip experiments, but several other trapping and manipulation techniques have been added to the stable. These include permanent magnet traps (for recent work, see e.g. [47, 48, 49, 50]), traps using combined magneto- and electrostatic fields [51], traps based on time-varying electric fields [52], superconducting wires [53, 54], and on-chip optics [45]. Combined radio-frequency and static magnetic fields have been used to create double well potentials on a chip [46, 43], closely related to our work on microwave potentials (see chapter 5). Recently, optical cavities were integrated with atoms chips [55, 56, 57, 58] and used as single-atom detectors,

---

[1] Resonant state dressing with microwave or radio-frequency fields allows one to beat this limit in specific geometries, see chapter 5 and [43].

paving the way for single atom manipulation.

Atom chips have been successfully used to explore new physics in experiments on cavity quantum electrodynamics with trapped BECs [56], low-dimensional quantum gases [59], number squeezing of BECs [60], the Casimir effect and other phenomena of atom-surface interactions [44], to name but some examples. As a first application, a miniaturized atomic clock has been investigated (see chapter 4). Experiments are underway to extend this list to quantum information processing (see chapter 6) and the study of atoms coupled to nanostructured condensed-matter systems (see chapter 7).

1.2 Magnetic trapping of neutral atoms

Magnetic trapping relies on the interaction of the magnetic moment $\boldsymbol{\mu}$ of a particle with an external magnetic field $\mathbf{B}$. In a classical description,[2] the particle experiences a potential energy

$$E = -\boldsymbol{\mu} \cdot \mathbf{B} = -\mu B \cos\theta. \tag{1.1}$$

The angle θ between the magnetic moment and the magnetic field is stabilized due to the rapid Larmor precession of $\boldsymbol{\mu}$ around the magnetic field direction. Quantum mechanically, the Zeeman energy levels of a neutral atom with total angular momentum $\mathbf{F}$ and corresponding magnetic moment $\boldsymbol{\mu} = -\mu_B g_F \mathbf{F}$ are

$$E_{F,m_F} = \mu_B g_F m_F B, \tag{1.2}$$

where μ_B is the Bohr magneton, g_F is the Landé g-factor of the angular momentum state F, and m_F is the magnetic quantum number associated with the projection of $\mathbf{F}$ onto the direction of $\mathbf{B}$. The classical term $\cos\theta$ is now replaced by the discrete values m_F/F; the classical picture of constant θ is equivalent to the atom remaining in a state with constant m_F.

If the atom is moving in an inhomogeneous magnetic field $\mathbf{B}(\mathbf{r})$, it still remains in a state with constant m_F if the precessing spin can adiabatically follow the local direction of the magnetic field.[3] Equation (1.2) then describes an effective magnetic potential energy for the state $|F, m_F\rangle$ which depends only on the magnitude $B(\mathbf{r}) = |\mathbf{B}(\mathbf{r})|$ of the field. Atoms can be trapped in a minimum of this potential energy. States with $g_F m_F > 0$ are attracted to a magnetic field minimum, such states are called "low-field seekers". States with $g_F m_F < 0$ are attracted to a magnetic field maximum, these states are

---

[2] This discussion follows [61].

[3] In this description m_F is defined with respect to a position dependent quantization axis which is taken along the local direction of the magnetic field.

called “high-field seekers”. Since Maxwell’s equations do not allow a local magnetic field maximum in a source-free region [62], only low-field seeking states can be trapped with static magnetic fields. Atoms with $g_F m_F = 0$ are not influenced by the magnetic field to lowest order.

Majorana spin flips

An atom is lost from the trap if it makes a transition from a low-field seeking state to a high-field seeking state or to a state with $m_F = 0$. Such a transition can be induced by the motion of the atom in the trap. Due to this motion, the atom experiences a changing magnetic field direction and magnitude in its moving frame. The trap is only stable if the precessing atomic spin can follow the changing magnetic field direction adiabatically. This requires that the rate of change of the magnetic field direction θ is small compared to the Larmor frequency ω_L:

$$\frac{d\theta}{dt} \ll \omega_L = \frac{\mu_B |g_F| B}{\hbar}. \tag{1.3}$$

If this condition of adiabaticity is fulfilled, m_F is a constant of the motion. An upper bound for $d\theta/dt$ in a harmonic magnetic trap is the trapping frequency. The condition in Eq. (1.3) is violated in regions of vanishing (or very small) magnetic field strength B. In these regions, transitions between m_F levels occur, taking the atom to untrapped states. This trap loss mechanism is known as Majorana spin flips.

1.2.1 Hyperfine structure

For an atom with hyperfine structure such as ^{87}Rb, Eq. (1.2) provides an approximate description of the magnetic potential energy for weak magnetic fields where E_{F,m_F} is small compared to the hyperfine splitting E_{hfs}. For many experiments with magnetic traps, this description is sufficiently accurate. Figure 1.1 shows the hyperfine energy levels of the ^{87}Rb electronic ground state in this limit.[4] The magnetically trappable states are indicated.

1.2.2 Breit-Rabi formula

The experiments with internal-state superpositions in chapter 4 of this thesis require a more accurate description of the hyperfine energy levels. Due to the high spectroscopic precision, deviations from Eq. (1.2) are resolved even though the applied magnetic fields of a few Gauss fall into the weak-field

---

[4] Properties of ^{87}Rb are listed in appendix A.1.

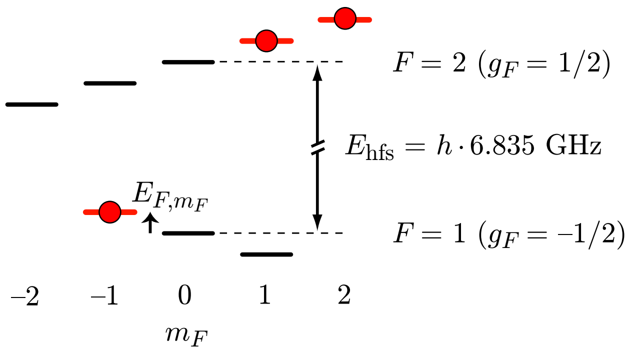

Figure 1.1: Hyperfine structure of ^{87}Rb in a weak magnetic field. Magnetic sublevels $|F, m_F\rangle$ are shifted due to the Zeeman effect by E_{F,m_F}. States marked with a circle are weak-field seekers which can be magnetically trapped.

regime. An accurate description of the $5^2\mathrm{S}_{1/2}$ ground state of ^{87}Rb in a static magnetic field is provided by the Hamiltonian

$$H = A_{\rm hfs}\mathbf{I}\cdot\mathbf{J} + \mu_B B\,(g_J J_z + g_I I_z)\,. \tag{1.4}$$

The first term describes the hyperfine interaction between the nuclear angular momentum **I** and the electron angular momentum **J**, while the other terms describe the couplings of **J** and **I** to the magnetic field (we have taken the z-axis along **B**). Although $|g_I/g_J| \sim 10^{-3}$, the coupling of **I** to the magnetic field is not negligible in this context. Since $I = 3/2$ and $J = 1/2$, the total atomic angular momentum $\mathbf{F} = \mathbf{J} + \mathbf{I}$ can take on the values $F = 2$ and $F = 1$. The energy levels are obtained by diagonalizing the Hamiltonian Eq. (1.4), which yields the Breit-Rabi formula [63, 64], valid for $J = 1/2$, arbitrary I, and arbitrary B:

$$E_{F,m_F} = -\frac{E_{\rm hfs}}{2(2I+1)} + \mu_B g_I m_F B \pm \frac{E_{\rm hfs}}{2}\left(1 + \frac{4m_F\xi}{2I+1} + \xi^2\right)^{1/2},$$
$$\text{where}\quad \xi = \frac{\mu_B(g_J - g_I)B}{E_{\rm hfs}}. \tag{1.5}$$

Here, $E_{\rm hfs} = A_{\rm hfs}(I + 1/2)$ is the hyperfine splitting, the + (−) sign is for the $F = I + 1/2$ ($F = I - 1/2$) manifold, and the energies E_{F,m_F} are now measured with respect to the "center of gravity" of the hyperfine levels. To avoid a sign ambiguity in Eq. (1.5), the formula

$$E_{F=2,m_F=\pm 2} = E_{\rm hfs}\frac{I}{2I+1} \pm (g_J + 2Ig_I)\frac{\mu_B B}{2} \tag{1.6}$$

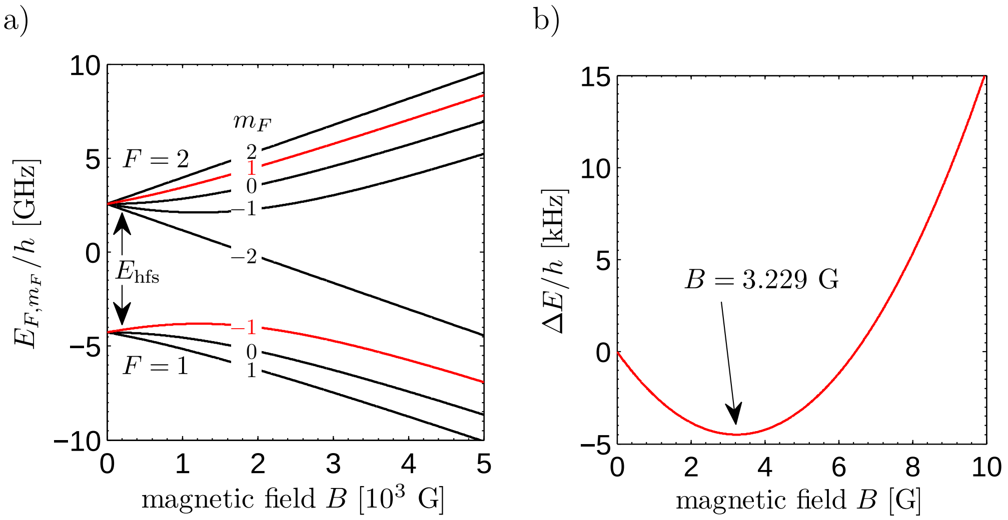

Figure 1.2: Hyperfine energy levels of the ^{87}Rb ground state as a function of magnetic field. (a) Energies of the states $|F, m_F\rangle$ calculated with the Breit-Rabi formula. (b) Energy difference $\Delta E = (E_{2,1} - E_{1,-1} - E_{\mathrm{hfs}})$ between the states $|2, +1\rangle$ and $|1, -1\rangle$, which are marked red in (a). Note the difference in axis scaling compared to (a). The "sweet spot" at $B = 3.229$ G is indicated.

can be used for the states $|F = 2, m_F = \pm 2\rangle$. Figure 1.2(a) shows E_{F,m_F} calculated with the Breit-Rabi formula. We use the convention that $|F, m_F\rangle$ refers to the eigenstates of the Hamiltonian Eq. (1.4), which depend on B. For small magnetic fields, the linear dependence of E_{F,m_F} on B described by Eq. (1.2) is recovered, and $|F, m_F\rangle$ can be approximated by the eigenstates at $B = 0$, see also appendix A.3.

Magnetic traps are in general not as well suited for experiments involving internal-state superpositions as for example optical dipole traps. Only weak-field seeking states can be trapped, and furthermore, the magnetically trappable states experience different potentials due to their different magnetic moments. A notable exception are the states $|1, -1\rangle$ and $|2, +1\rangle$ of ^{87}Rb, which are both magnetically trappable and have nearly equal magnetic moments. These "qubit" states experience nearly identical magnetic trapping potentials and superposition states are very robust against decoherence. In Fig. 1.2(b), the energy difference between the two states is shown as a function of magnetic field. At $B = 3.229$ G, the magnetic-field dependence of the energy difference vanishes to first order. In the experiments described in chapter 4, we prepare the atoms at this "sweet spot" to study internal-state superpositions in a magnetic chip trap.

1.3 Quadrupole and Ioffe-Pritchard traps

The magnetic traps used in our experiments can be divided into two categories [65, 23]: Quadrupole traps and Ioffe-Pritchard traps.

Quadrupole trap

In a quadrupole trap, the minimum is a zero crossing of the magnetic field. The field around the minimum is of the form

$$\mathbf{B} = B'_x x\,\mathbf{e}_x + B'_y y\,\mathbf{e}_y + B'_z z\,\mathbf{e}_z, \tag{1.7}$$

with the additional requirement on the field gradients $B'_x + B'_y + B'_z = 0$ to satisfy Maxwell's equations. Here we have chosen the cartesian coordinate vectors $\mathbf{e}_i$ along the main axes of the quadrupole. The trapping potential given by Eqs. (1.2) and (1.7) is proportional to $B(\mathbf{r}) = \sqrt{(B'_x x)^2 + (B'_y y)^2 + (B'_z z)^2}$ and thus provides linear confinement. In the special case of $B'_x = 0$, we obtain a two-dimensional quadrupole field in the yz-plane with $B'_y = -B'_z$. Atoms in a quadrupole trap suffer from Majorana spin flips since $B = 0$ in the trap center. Quadrupole traps are nevertheless useful for ensembles of relatively hot atoms which spend most of their time far away from the "hole" in the trap center where Majorana losses occur [61]. Furthermore, quadrupole fields are used for magneto-optical traps.

Ioffe-Pritchard trap

The Ioffe-Pritchard trap provides quadratic confinement and has a finite magnetic field in the trap center.[5] In the simplest, axially symmetric case, the trapping field is of the form

$$\mathbf{B} = B_0 \begin{pmatrix} 1 \\ 0 \\ 0 \end{pmatrix} + B' \begin{pmatrix} 0 \\ -y \\ z \end{pmatrix} + \frac{B''}{2} \begin{pmatrix} x^2 - (y^2 + z^2)/2 \\ -xy \\ -xz \end{pmatrix}. \tag{1.8}$$

It arises from the combination of a two-dimensional quadrupole field in the yz-plane with gradient B' and a "bottle-field" with constant term B_0 and curvature B'' along x [65]. The magnetic field modulus expanded to second order in the displacement from the trap center has the form

$$B(\mathbf{r}) \approx B_0 + \frac{B''}{2} x^2 + \frac{1}{2} \left(\frac{B'^2}{B_0} - \frac{B''}{2} \right) \left(y^2 + z^2 \right). \tag{1.9}$$

---

[5] A quadratic trap is the lowest-order trap that can have a non-vanishing field in the center. Indeed, adding a bias field to a three-dimensional linear (quadrupole) trap only shifts the location of the zero crossing, but does not remove it.

This leads to harmonic confinement of atoms of mass m and magnetic moment $\mu = \mu_B g_F m_F$ with trap frequencies

$$\omega_x = \sqrt{\frac{\mu}{m} B''} \quad \text{and} \quad \omega_\perp = \sqrt{\frac{\mu}{m}\left(\frac{B'^2}{B_0} - \frac{B''}{2}\right)} \tag{1.10}$$

in the axial (ω_x) and radial ($\omega_\perp$) direction, respectively. Equation (1.10) shows that the trap aspect ratio $\omega_x/\omega_\perp$ of an ideal Ioffe trap can be tuned from prolate (cigar-shaped) to isotropic and further to oblate (pancake-shaped), depending on the value of B'' compared to B'^2/B_0, as experimentally demonstrated e.g. in [66]. In general, a Ioffe-Pritchard trap need not be axially symmetric, and the field in the trap center may be tilted with respect to the principal axes of the harmonic potential. These deviations from Eq. (1.8) become important for wire traps outside the cigar-shaped regime, as shown in appendix B.

The Majorana loss rate in a Ioffe-Pritchard trap has been calculated for $F = 1$ in [67]. For $\omega_x \ll \omega_\perp$, it is

$$\gamma_M = 4\pi\omega_\perp \exp\left(-2\omega_L/\omega_\perp\right). \tag{1.11}$$

In experiments, we typically adjust the Larmor frequency in the trap center to $\omega_L \geq 7\,\omega_\perp$ to make Majorana losses negligible ($\gamma_M \leq 10^{-5}\,\omega_\perp$).

1.4 Basic wire trap configurations

Magnetic traps can be created on a chip using lithographically patterned current-carrying wires [21, 22, 23, 24] or permanent magnets [47, 48, 49, 50] as the magnetic field sources. A great variety of trap geometries is possible [65]. In the following, we concentrate on wire-based traps which we employ in our experiments.

1.4.1 Principle of wire traps

The principle of a simple wire trap is illustrated in Fig. 1.3(a). An infinitely thin, straight wire carrying a current I creates a radial magnetic field, whose magnitude, gradient, and curvature scale with the distance z to the wire as

$$B = \frac{\mu_0 I}{2\pi z}, \quad B' = -\frac{\mu_0 I}{2\pi z^2}, \quad \text{and} \quad B'' = \frac{\mu_0 I}{\pi z^3}, \tag{1.12}$$

respectively. If a homogeneous bias field B_b is added perpendicular to the wire, the fields cancel, forming a line of zero field at a distance

$$z_0 = \frac{\mu_0 I}{2\pi B_b}. \tag{1.13}$$

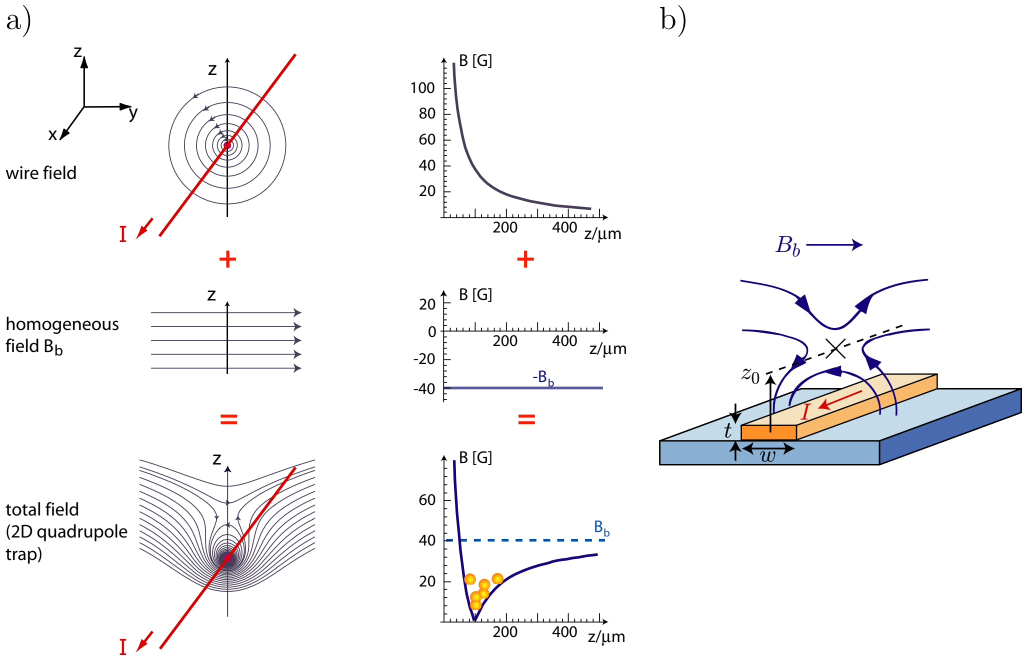

Figure 1.3: Simple wire trap providing two-dimensional confinement. (a) By combining the radial field of a straight wire with a homogeneous bias field, a two-dimensional quadrupole field forms in the plane perpendicular to the wire. Left column: magnetic field lines. Right column: field magnitude $B(z)$ at $y = 0$ for a wire current $I = 2$ A and a bias field $B_b = 40$ G. Figure adapted from [23]. (b) Waveguide for neutral atoms formed at a distance z_0 from a lithographically fabricated wire on a chip.

In the vicinity of this line, the magnetic field has the form of a two-dimensional quadrupole field with gradient $B' = -\mu_0 I/(2\pi z_0^2)$ in the plane perpendicular to the wire. From the scaling of B' it is evident that for a given current I the traps become tighter as z_0 is decreased.

In our experiments, we trap atoms with the help of planar wires on a chip substrate, as schematically shown in Fig. 1.3(b). The substrate provides mechanical stability and efficient heat transport from the wires. Lithographic techniques allow complex wire structures to be fabricated. The chip wires have rectangular cross-section, w is the width and t is the thickness of the wire. The field of an infinitely thin wire is a good approximation to the field of real wires as long as $z_0 \gg w, t$. For small z_0, the finite wire dimensions have to be taken into account, as described in section 1.6. Note that the homogeneous bias field can be generated by larger wires on the same chip.

The straight wire trap provides two-dimensional confinement and can

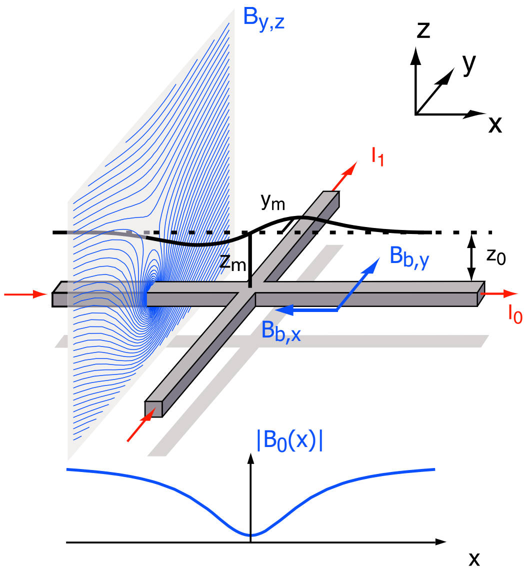

Figure 1.4: "Dimple" trap above the intersection of two straight wires. (a) A three-dimensional Ioffe-Pritchard trap is formed (see text), with the transverse quadrupole field $B_{y,z}$ and the field modulus on the trap axis $|B_0(x)|$ as shown. Figure adapted from [21].

thus be used to guide atoms on a chip. Traps providing three-dimensional confinement can easily be obtained by either bending the wire ends or adding additional crossing wires, as explained in the following.

1.4.2 Dimple trap above a conductor crossing

The "dimple" trap is a very versatile Ioffe-Pritchard trap which can be created above the intersection of two straight wires, see Fig. 1.4. It is based on a two-dimensional quadrupole field in the yz-plane, provided by the current I_0 and the bias field $B_{b,y}$ as explained in the previous section. The field zero forms in the transverse plane at $z = z_0 \equiv \mu_0 I_0 / 2\pi B_{b,y}$ and $y = 0$. By adding an additional homogeneous bias field $B_{b,x}$ along x, the field zero is removed and a two-dimensional Ioffe-Pritchard potential results, which provides harmonic confinement in the yz-plane, but no axial confinement along x. The role of the current I_1 in the crossing wire is to modulate the field on the trap axis to provide axial confinement as well.

For sufficiently small I_1 (for a quantitative criterion see appendix B), the field components $\tilde{B}_x(x,z)$ and $\tilde{B}_z(x,z)$ of the crossing wire are weak compared to the transverse quadrupole field. $\tilde{B}_z$ results in a shift $y_m(x)$ of the trap minimum, i.e. it tilts the trap axis in the xy-plane, see Fig. 1.4. The gradient of $\tilde{B}_x$ shifts the minimum to $z = z_m$. For small I_1, $y_m \approx 0$ and $z_m \approx z_0$ and the transverse confinement is nearly unchanged by the crossing wire. The axial confinement can then be obtained by evaluating the field modulus on the axis of the unperturbed trap, $B_0(x) \approx |B_{b,x} + \tilde{B}_x(x, z = z_0)|$. If $B_{b,x}$ and $\tilde{B}_x$ have opposite sign, a cigar-shaped Ioffe-Pritchard trap forms [65, 21]. Comparing with the ideal Ioffe trap of Eq. (1.8), one can roughly say that the field due to I_0 and $B_{b,y}$ provides the transverse quadrupole with gradient

$$B' = \mu_0 I_0 / 2\pi z_0^2, \tag{1.14}$$

the field due to I_1 and $B_{b,x}$ is responsible for

$$B_0 = |B_{b,x} + \mu_0 I_1 / 2\pi z_0|, \tag{1.15}$$

and the field of I_1 also provides the curvature

$$B'' = \left. \frac{\partial^2 \tilde{B}_x}{\partial x^2} \right|_{x=0, z=z_0} = \mu_0 I_1 / \pi z_0^3. \tag{1.16}$$

The trap frequencies are well approximated by

$$\omega_x = \sqrt{\frac{\mu}{m} B''} \quad \text{and} \quad \omega_\perp = \sqrt{\frac{\mu}{m} \frac{B'^2}{B_0}}. \tag{1.17}$$

However, these formulae are only valid for small I_1, where the trap is in the cigar-shaped regime, as in most experiments. The actual field configuration of the dimple trap is more complicated. This is discussed in appendix B, where we also investigate whether isotropic and pancake-shaped dimple traps can be formed.

1.4.3 Quadrupole U-trap and Ioffe-Pritchard Z-trap

Three-dimensional traps can also be created with a single wire by bending the wire ends at right angles to form a “U” or “Z”, as shown in Fig. 1.5. In both cases, the central part of the wire in combination with the bias field forms a two-dimensional quadrupole for transverse confinement, while the bent wire parts provide the axial confinement. The trapping potential is qualitatively different for the case of a “U” and a “Z”: In the case of a “U”, the field components $\tilde{B}_x$ generated by the two bent wires point in opposite directions and cancel at $x = 0$. The resulting potential is that of a three-dimensional quadrupole trap, with field zero at $x = 0$, $y > 0$, and $z \approx z_0$. The trap is shifted along y due to the field components $\tilde{B}_z$ of the bent wires. In the

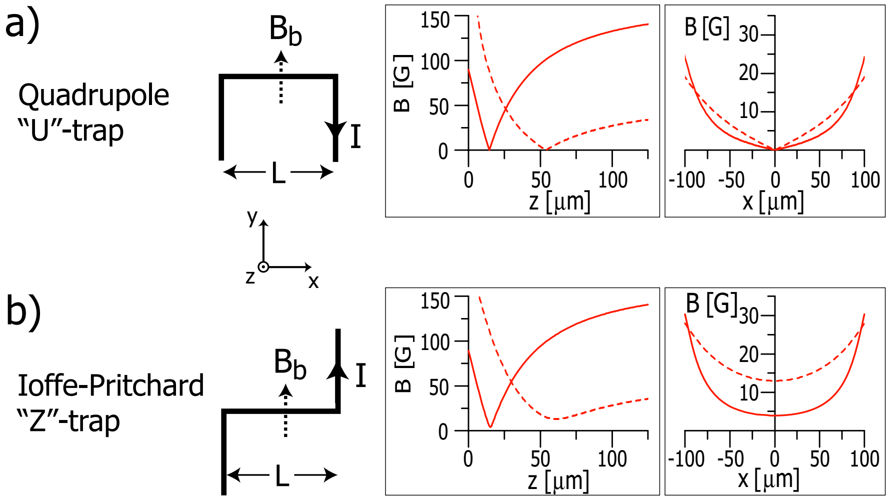

Figure 1.5: (a) Quadrupole "U"-trap and (b) Ioffe-Pritchard "Z"-trap. Both traps provide three-dimensional confinement. Left column: wire layout in the plane $z = 0$ and orientation of the bias field. Center column: Magnetic field modulus on a line along z through the trap center. Right column: Magnetic field modulus on a line along x through the trap center. The fields were calculated for $L = 250$ μm and $I = 2$ A, taking a finite wire width of 50 μm into account. The bias field along y is $B_b = 54$ G (dashed lines) and $B_b = 162$ G (solid lines). Figure adapted from [23].

case of a "Z", the components $\tilde{B}_x$ point in the same direction, adding up to a finite field along x in the trap center. The result is a three-dimensional Ioffe-Pritchard trap with trap center located at $x = 0$, $y = 0$, and $z \approx z_0$. The axial confinement is provided by the curvature $\partial^2 \tilde{B}_x / \partial x^2$. Since in this configuration $\tilde{B}_z$ vanishes at $x = 0$, the trap center is unshifted. However, the trap axis is tilted, as discussed above for the dimple trap.

1.4.4 Maximum trap frequency and field gradient

Due to the great flexibility in trap design, it is difficult to quote "typical" chip trap parameters. Even for a fixed wire geometry, parameters such as the frequency and aspect ratio of the trapping potential can be tuned over several orders of magnitude by adjusting currents and magnetic fields. Of particular interest are the maximum magnetic field gradient B' and trap frequency $\omega_\perp$ that can be created with a wire trap. For a cylindrical wire of diameter w, B' increases with decreasing trap-wire distance, reaching a value of $B' = \mu_0 j/2$ at the wire surface, where j in the current density in the wire. The maximum B' is thus limited by the maximum j the wire can support, which is independent of w for micrometer-sized wires where the total dissipated power is small [23]. For a typical value of $j_{\mathrm{max}} = 10^{11}$ A/m^2, corresponding to a current of 0.1 A and $w = 1$ μm, a gradient of $B' = 2 \times 10^6$ G/cm can be obtained at a distance of 0.5 μm from the wire surface. The trap frequency $\omega_\perp$ is given by Eq. (1.17), where B_0 has to be chosen such that Majorana spin flips are negligible. As shown in [23], this results in a maximum trap frequency $\omega_\perp/2\pi \sim 1$ MHz for the above parameters and ^{87}Rb. Note, however, that these values are only useful in traps for single atoms, since atomic ensembles suffer from collisional loss processes already at much lower trap frequencies, see section 1.8 below. For a discussion of the minimum trap-surface distance that can be achieved, see section 1.9. The maximum trap depth depends on the wire geometry used, for "U" and "Z"-traps an upper bound is given by the homogeneous bias field B_b, see Fig. 1.5 and [23].

1.5 Arrays of potential wells

The "dimple" trap is an important building block for more complex potentials [21]. Note that by reversing the direction of the current I_1 in the crossing wire, a guide with a potential barrier is formed instead of a trap. Multiple potential wells with adjustable barriers in between can thus be formed by multiple crossing wires carrying currents in alternating directions, as schematically shown in Fig. 1.6. The length scale of the potential modulation is given by the spacing between the wires, and for a modulation of significant amplitude the distance of the atoms to the chip surface has to be of the same order as the wire spacing. To avoid short cuts, the wires have to be arranged in two layers which are insulated from each other. In chapter 2, I show how such chips can be fabricated. This is an example where atom chips offer features which are complementary to those of optical lattices: while optical lattices are better suited for the creation of almost perfectly periodic potentials, atom chips have the advantage that the potential wells and the barriers can be individually addressed and tuned by the currents without the restriction to a periodic situation.

Although the design of complex potentials by combining wells and barriers generated by wire crossings seems straightforward, it is important to keep in mind that while the magnetic potential is only a function of the field modulus, the fields of different wires add up vectorially. Therefore, the potential generated by several wires is not simply the sum of the potentials generated by the individual wires. For complex wire layouts, numerical simulations are required to accurately determine the resulting magnetic fields and potentials.

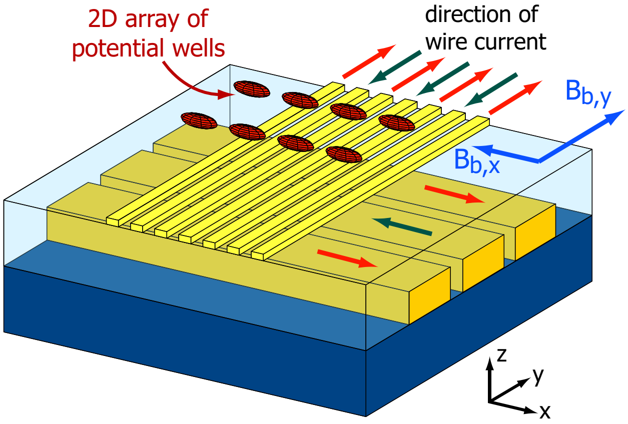

Figure 1.6: An array of wires can be used to create an array of dimple traps (shown schematically in red) which are separated by adjustable barriers. The wires carry currents whose direction is indicated by the arrows. Red (green) arrows correspond to currents forming a potential well (barrier).

1.6 Simulation of trapping potentials

To calculate and analyze the potentials generated by complex wire structures, I have written a collection of simulation routines based on the software packages MATLAB and COMSOL. For numerically intensive tasks, functions written in C are used (MATLAB MEX-files).

The magnetic fields generated by the wires are determined from the current density using the Biot-Savart law [68]. A wire can be described in several ways, depending on the level of idealization which is appropriate:

- An analytical solution exists for the magnetic field of a straight conductor of finite length and rectangular cross-section, carrying a constant current density, see appendix A.2. The solution simplifies for a conductor of zero thickness [65]. In many cases, complex wire layouts can be approximated by segments of such conductors.

- In cases where the approximation of constant current density inside the conductors is not valid, e.g. in the near-field of a conductor crossing or for conductors of complex shape, the current density is determined by solving the Laplace equation for the electrostatic potential inside the conductor [68], using the finite elements methods provided by COMSOL. The current density is subsequently extracted on a grid, the Biot-Savart calculation is done numerically with a custom C routine.

In most cases it is a good approximation to assume that all wires have zero thickness and lie in several planes parallel to the chip surface. Wires of finite thickness can often be approximated by several parallel planes of zero thickness. In addition to the field of current-carrying wires, the field of permanent magnets can also be included in the simulation.

From the magnetic field, the magnetic potential is calculated, using either the simple formula (1.2) or the Breit-Rabi formula (1.5). The simulations also include gravity and the atom-surface potential (see below). To analyze the potential, various functions have been written which find potential minima, trace minima along given directions (similar to the method described in [65]), find trap frequencies, or isopotential surfaces. The visualization is based on the plotting routines of MATLAB. Examples can be found in Figs. 5.11 and B.2. The simulation routines have been adapted to the calculation of microwave dressed-state potentials, as described in chapter 5.

1.7 Bose-Einstein condensation in chip traps

The achievement of Bose-Einstein condensation (BEC) in chip traps [28, 29] attracted great attention and triggered a rapid growth of the field of atom chips. The significance of achieving BEC goes beyond the interest in the phenomenon itself. The BEC phase transition provides a powerful technique to prepare a large number of atoms in a single quantum state. By cooling the gas sufficiently below the transition temperature, a — for most practical purposes — "pure" BEC can be created, in which all internal and motional degrees of freedom of the atoms are under experimental control at the quantum level. This provides a starting point for subsequent experiments which is as well defined as nature allows it. For some experiments it is simply the small spatial extension, which can be below 1 μm, or the high atomic densities which make BEC necessary. Several excellent reviews of BEC exist [69, 70, 61, 71].

The characteristic feature of BEC in a system of N bosonic particles is that at least one single-particle state[6] is "macroscopically occupied", i.e. its occupation number N_0 is of order N, while the occupation of the other states is of order unity.[7] Consider a noninteracting gas in three dimensions in thermal equilibrium at temperature T. A simple rule of thumb is that BEC occurs when the degeneracy condition $p \lesssim N$ is satisfied, where p is the number of thermally accessible single-particle states [69]. In a harmonic trap, $p \propto (k_B T/\hbar\omega_{\mathrm{ho}})^3$, where $\omega_{\mathrm{ho}} = (\omega_x \omega_y \omega_z)^{1/3}$ is the geometric mean of

---

[6] A single-particle state is not necessarily an eigenstate of the single-particle Hamiltonian.

[7] This definition is independent of assumptions about interactions or thermal equilibrium [69].

the trap frequencies. We thus find for the transition temperature T_c

$$k_B T_c = 0.94\,\hbar\omega_{\mathrm{ho}} N^{1/3}, \tag{1.18}$$

where the numerical prefactor is obtained in the limit $N \gg 1$ by a rigorous calculation [70]. For $T < T_c$, the number of particles in the condensate is

$$N_0(T) = N\left[1 - (T/T_c)^3\right]. \tag{1.19}$$

At $T = 0$ (i.e. for most practical purposes $T \ll T_c$), the gas is fully condensed, $N_0 = N$, and all particles occupy identical single-particle wave functions $\phi(\mathbf{r})$. In the noninteracting case, the many-body wave function is thus simply the product of these single-particle wave functions

$$\Psi_N(\mathbf{r}_1, \mathbf{r}_2, \ldots, \mathbf{r}_N) = \prod_{i=1}^{N} \phi(\mathbf{r}_i), \tag{1.20}$$

and $\phi(\mathbf{r})$ is the single-particle ground state of the confining potential. The BEC order parameter is defined as $\Psi(\mathbf{r}) \equiv \sqrt{N}\phi(\mathbf{r})$, the atomic density is $n(\mathbf{r}) = |\Psi(\mathbf{r})|^2$, and $\int |\Psi(\mathbf{r})|^2 dr^3 = N$.

A realistic description must include atom-atom interactions. In a cold dilute gas of ^{87}Rb, these are dominated by elastic binary collisions. At microkelvin temperatures, the interaction is well approximated by considering only s-wave scattering, since the thermal deBroglie wavelength is much larger than the effective range of the van der Waals-type interatomic potential. In this regime the interatomic potential can be replaced by an effective contact interaction

$$V(\mathbf{r}_i - \mathbf{r}_j) = \frac{4\pi\hbar^2 a_s}{m} \cdot \delta(\mathbf{r}_i - \mathbf{r}_j) = g \cdot \delta(\mathbf{r}_i - \mathbf{r}_j), \tag{1.21}$$

where a_s is the s-wave scattering length, m is the mass of the atoms, and we have defined the coupling constant $g = 4\pi\hbar^2 a_s/m$. For ^{87}Rb, the interactions are repulsive with $a_s \approx 5$ nm, see appendix A.1 for accurate values depending on $|F, m_F\rangle$.

Under typical experimental conditions, the gas is dilute in the sense that the interparticle spacing is much larger than a_s, which can be expressed by the gas parameter $\langle n\rangle a_s^3 \ll 1$, where $\langle n\rangle$ is the mean density. The condensate depletion due to interactions, which is of order $(\langle n\rangle a_s^3)^{1/2}$, is small, typically $< 10^{-2}$. Such a weakly interacting gas is well described by a Hartree-Fock or mean-field ansatz for the many-particle state, which for $T = 0$ is of the same form as in the noninteracting case, Eq. (1.20). However, the interactions modify the single-particle state $\phi(\mathbf{r})$ into which the atoms condense, such that $\phi(\mathbf{r})$ is no longer an eigenstate of the single-particle Hamiltonian.[8] It can be determined self-consistently by minimizing the expectation value of the energy of the N-particle system, which, using Eqs. (1.20) and (1.21), takes the form

$$\langle H\rangle_N = N\int dr^3\left[\frac{\hbar^2}{2m}|\nabla\phi(\mathbf{r})|^2 + V_{\text{ext}}(\mathbf{r})|\phi(\mathbf{r})|^2 + \frac{gN}{2}|\phi(\mathbf{r})|^4\right], \tag{1.22}$$

where $V_{ext}(\mathbf{r})$ is the external potential and we have assumed $N \gg 1$. Minimization of Eq. (1.22) subject to the constraint $\int|\phi(\mathbf{r})|^2 dr^3 = 1$ leads to the well-known time-independent Gross-Pitaevskii equation [69]

$$-\frac{\hbar^2}{2m}\nabla^2\phi(\mathbf{r}) + V_{ext}(\mathbf{r})\phi(\mathbf{r}) + gN|\phi(\mathbf{r})|^2\phi(\mathbf{r}) = \mu_c\phi(\mathbf{r}), \tag{1.23}$$

which determines $\phi(\mathbf{r})$ and the chemical potential of the condensate μ_c. In many experimental situations the kinetic energy term in Eq. (1.23) is much smaller than the other terms, except very close to the edge of the condensate. In this case the description can be further simplified by dropping the kinetic term. This is the Thomas-Fermi (TF) approximation, which yields simple analytical expressions for many condensate properties [70], e.g.

$$n(\mathbf{r}) = N|\phi(\mathbf{r})|^2 = \begin{cases}\left[\mu_c - V_{\text{ext}}(\mathbf{r})\right]/g & \text{where } \mu_c > V_{\text{ext}}(\mathbf{r}),\\ 0 & \text{elsewhere,}\end{cases} \tag{1.24}$$

$$\mu_c = \frac{\hbar\omega_{\text{ho}}}{2}\left(\frac{15Na_s}{a_{\text{ho}}}\right)^{2/5}, \tag{1.25}$$

$$R_i = \sqrt{2\mu_c/m\omega_i^2}, \quad i = x, y, z. \tag{1.26}$$

Here, $a_{\text{ho}} = \sqrt{\hbar/m\omega_{\text{ho}}}$ is the mean oscillator length. The condensate density $n(\mathbf{r})$ has the form of an inverted parabola, R_i are the TF radii of the BEC. The mean density is

$$\langle n\rangle = (4/7)\mu_c/g, \tag{1.27}$$

and the mean square density is

$$\langle n^2\rangle = (8/21)\mu_c^2/g^2. \tag{1.28}$$

The TF regime implies[9] $Na_s/a_{\text{ho}} \gg 1$, and thus $\mu_c \gg \hbar\omega_{\text{ho}}$ and $R_i \gg \sqrt{\hbar/m\omega_i}$. It is interesting to compare the different energy and length scales

---

[8] Interactions also modify the thermodynamics of the gas, repulsive interactions shift T_c to lower temperatures [70]. Furthermore, the interactions introduce particle correlations on a length scale $\sim a_s$, which are neglected in mean-field theory [69].

[9] In very anisotropic traps, the TF approximation may be invalid along the tightly confining directions even if $Na_s/a_{\text{ho}} \gg 1$. For an interpolation of the TF expressions to the regime $Na_s/a_{\text{ho}} < 1$, see [72]. Note furthermore that the condition for the TF regime is different from the dilute gas condition.

of a BEC [61]. Table 1.1 shows typical values for condensates with small N in tight traps, as in our experiments. The scales are more similar than in conventional BEC experiments with large N in weak traps.

energy scales		length scales	
$\hbar^2/ma_s^2$	$= h \cdot 4$ MHz	a_s	$=$ 5 nm
$k_B T_c$	$= h \cdot 17$ kHz	$\langle n \rangle^{-1/3}$	$=$ 110 nm
μ_c	$= h \cdot 9.3$ kHz	$\xi = (8\pi \langle n \rangle a_s)^{-1/2}$	$=$ 100 nm
$\hbar\omega_{\text{ho}}$	$= h \cdot 1.9$ kHz	a_{ho}	$=$ 250 nm
		$R_{x,y,z}$	$= (3.7, 0.37, 0.37)$ μm

Table 1.1: Energy and length scales for a typical ^{87}Rb BEC in our experiments with $N = 10^3$ and $\omega_{x,y,z}/2\pi = (0.4, 4, 4)$ kHz. ξ is the healing length, which is relevant for superfluid effects [70].

The dynamics of the condensate wave function, for $T = 0$ and neglecting dissipation, are determined in mean-field theory by the time-dependent version of the Gross-Pitaevskii equation [69]

$$i\hbar \frac{\partial}{\partial t} \phi(\mathbf{r}, t) = -\frac{\hbar^2}{2m} \nabla^2 \phi(\mathbf{r}, t) + V_{ext}(\mathbf{r}) \phi(\mathbf{r}, t) + gN |\phi(\mathbf{r}, t)|^2 \phi(\mathbf{r}, t). \quad (1.29)$$

The description of a BEC discussed here shows remarkable accuracy in many situations although it neglects all interaction-induced particle correlations and assumes $N \gg 1$. Finite-size effects in atomic BECs are observable, but remain small down to $N \sim 10^2$ [73]. On the other hand, it has now become possible to prepare atoms in strongly correlated many-particle states where a mean-field description is no longer adequate. The first experiment of this kind was the observation of the Mott insulator transition in an optical lattice [74]. Atom chips are well suited to explore effects beyond mean-field physics, in particular in situations where tunable non-periodic traps, extreme trap aspect ratios, or high ω_{ho} is required. First experiments on atom number squeezing are reported in [60], future experiments may involve e.g. Tonks-Girardeau gases in very anisotropic traps [75], Schrödinger cat states in double well potentials [76], or collisional blockade mechanisms in tight, state-selective traps [77].

1.8 Collisional trap loss

We now turn to a first class of effects which limit the coherent manipulation of the atoms. At high density n, inelastic collisions between the trapped atoms occur, which change the atoms' internal state [71]. This causes trap loss if the collision partners are left in untrapped states.[10] While collisional losses are not peculiar to atom chips, they are relevant because the tight confinement provided by chip traps translates into high n, even for small total atom number N. For atoms in a single internal state, collisional trap loss is described by the rate equation

$$\begin{aligned} \frac{dN}{dt} &= -\gamma_{\mathrm{bg}} \int n(\mathbf{r})\, d^3r - K \int n^2(\mathbf{r})\, d^3r - L \int n^3(\mathbf{r})\, d^3r, \\ \Leftrightarrow \frac{1}{N}\frac{dN}{dt} &= -\gamma_{\mathrm{bg}} - K\langle n \rangle - L\langle n^2 \rangle. \end{aligned} \tag{1.30}$$

Effects of higher order in n are usually negligible. The background loss rate γ_{bg} is due to collisions with atoms from the residual gas in the vacuum chamber. It is proportional to the density of the residual gas, but independent of n. The second term in Eq. (1.30) describes inelastic two-body collisions between the trapped atoms. The corresponding trap loss rate is

$$\gamma_{2\mathrm{b}} = K\langle n \rangle \overset{\mathrm{TF}}{\propto} \omega_{\mathrm{ho}}^{6/5} N^{2/5}, \tag{1.31}$$

where the scaling with ω_{ho} and N is for a BEC in the Thomas-Fermi regime. The third term in Eq. (1.30) describes loss due to three-body recombination, with a loss rate

$$\gamma_{3\mathrm{b}} = L\langle n^2 \rangle \overset{\mathrm{TF}}{\propto} \omega_{\mathrm{ho}}^{12/5} N^{4/5}. \tag{1.32}$$

The constants K and L depend on the spin state of the atoms. Which process is dominant thus depends both on n and on $|F, m_F\rangle$.

The loss rates for thermal bosonic atoms are higher than for a BEC at the same density. This is because the atom-bunching which is observed for thermal bosons is absent in a BEC, analogous to photons in a thermal source and a laser. The rate of two-body (three-body) collisions is proportional to the second-order (third-order) correlation function; it is thus higher for thermal atoms by a factor of 2! (3!) [78]. In the following, all rate constants are quoted for a BEC.

Inelastic two-body collisions

Inelastic two-body collisions occur by two different mechanisms, the strong spin-exchange interaction and the much weaker spin-dipole interaction [71,

---

[10] In addition, the collisions can lead to heating, because energy is released in the inelastic process. This heating can be suppressed by applying an RF "shield", so that hot atoms are quickly removed from the trap [78].

79]. In state $|2,1\rangle$ of ^{87}Rb, spin-exchange processes such as $|2,1\rangle + |2,1\rangle \rightarrow |2,0\rangle + |2,2\rangle$ can occur, which conserve total m_F. A rate constant of $K_{|2,1\rangle} = 1.194(19) \times 10^{-13}\ \mathrm{cm}^3\,\mathrm{s}^{-1}$ was recently measured [80], significantly lower than the upper bound quoted in [81].

In states $|1,-1\rangle$ and $|2,2\rangle$, spin-exchange collisions are forbidden by angular momentum selection rules and conservation of energy [71, 79, 82]. Inelastic two-body collisions can occur only by the much weaker spin-dipole mechanism. At typical experimental parameters we therefore have $\gamma_{2\mathrm{b}} \ll \gamma_{\mathrm{bg}} + \gamma_{3\mathrm{b}}$ for these states.

Three-body recombination

Three-body recombination is dominant for $|1,-1\rangle$ and $|2,2\rangle$ at high n. In a three-body collision, two atoms form a molecule. The released binding energy is converted into kinetic energy of the molecule and the third atom, which is needed to satisfy energy and momentum conservation. The kinetic energy is typically larger than the trap depth, so that all three atoms are lost. The rate constant is $L_{|1,-1\rangle} = 5.8(1.9) \times 10^{-30}\ \mathrm{cm}^6\,\mathrm{s}^{-1}$ for state $|1,-1\rangle$ [78] and $L_{|2,2\rangle} = 1.8(0.5) \times 10^{-29}\ \mathrm{cm}^6\,\mathrm{s}^{-1}$ for state $|2,2\rangle$ [83].

Superpositions of internal states

If atoms are trapped in superpositions of different internal states $|F, m_F\rangle$, additional loss terms arise due to collisions between the different states. Due to the near-coincidence of the singlet and triplet scattering lengths of ^{87}Rb, spin-exchange rates are relatively small compared to other alkalis and any combination of spin states is thus relatively long-lived [79, 81]. For a superposition of $|0\rangle \equiv |1,-1\rangle$ and $|1\rangle \equiv |2,1\rangle$, collisional loss is described by

$$\begin{aligned} \frac{1}{N_0}\frac{dN_0}{dt} &= -\gamma_{\mathrm{bg}} - L_0\langle n_0^2\rangle - K_{01}\langle n_1\rangle \quad \text{and} \\ \frac{1}{N_1}\frac{dN_1}{dt} &= -\gamma_{\mathrm{bg}} - K_{01}\langle n_0\rangle - K_1\langle n_1\rangle, \end{aligned} \tag{1.33}$$

where N_i and n_i are the expectation values of number and density of atoms in state $|i\rangle$, respectively. We have included only the dominant processes, and assumed that the density distributions $n_0(\mathbf{r})$ and $n_1(\mathbf{r})$ overlap completely. For a BEC, the rate constants are $L_0 = L_{|1,-1\rangle}$ and $K_1 = K_{|2,1\rangle}$ as given above, and $K_{01} = 0.780(19) \times 10^{-13}\ \mathrm{cm}^3\,\mathrm{s}^{-1}$ [80].

In chapter 4 we will use Eqs. (1.33) to describe loss of atoms from a thermal ensemble in a superposition of $|0\rangle$ and $|1\rangle$. For thermal ensembles, the rate constants have to be multiplied with the appropriate statistical factors, as explained above. In terms of the BEC rate constants, we get for the thermal gas $L_0^{\mathrm{th}} = 6L_0$ and $K_1^{\mathrm{th}} = 2K_1$. If all atoms in the thermal ensemble are in the same coherent superposition of internal states, they are indistinguishable. Therefore we have $K_{01}^{\mathrm{th}} = 2K_{01}$, in contrast to an incoherent mixture, where $K_{01}^{\mathrm{th}} = K_{01}$ [84].

1.9 Atom-surface interactions

On atom chips, atom-surface interactions give rise to additional mechanisms of loss, decoherence, and heating. The atoms are trapped at nanokelvin temperatures, at a distance d of only a few micrometers from the room-temperature chip surface (Fig. 1.7). This is an intriguing situation, considering that the mean thermal energy of a single degree of freedom of the surface is about nine orders of magnitude larger than the mean energy of a trapped atom. It immediately raises the question how small d can be made before the atoms "feel" the presence of the surface. Besides being of fundamental interest, atom-surface interactions are potentially deleterious to the envisaged applications of atom chips, which require full coherent control in close proximity to the surface.

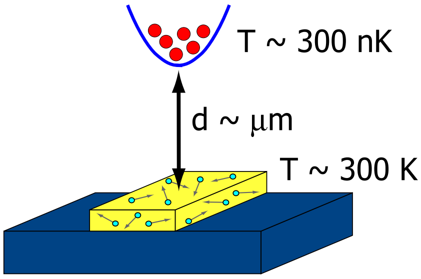

Figure 1.7: Ultracold atoms in chip traps interact with the room-temperature chip surface.

After the first successful chip trap experiments, a series of theoretical and experimental investigations of this new regime of surface physics was carried out, see [24, 85, 86] for a review. In chapter 4 of this thesis, I describe our investigation of atom-surface effects, including the first experiments with quantum-mechanical superposition states close to the chip surface [87]. In the following, the effects which are relevant for our experiments are discussed.

Neutral atoms interact with thermal and quantum-mechanical fluctuations of the electromagnetic field, which are substantially modified by the presence of the surface:

- Fluctuating magnetic fields interact with the atomic spin, leading to trap loss, decoherence, and heating. This effect is dominant near conductors, but negligible near dielectrics. All relevant trap and spin flip frequencies are < 10 GHz. At these frequencies, the atoms are in the near-field of the surface, and quantum fluctuations are negligible compared to thermal fluctuations.

- Fluctuating electric fields interact with electric dipole transitions of the atom at optical frequencies, giving rise to an attractive surface potential. This effect is present near dielectrics and conductors. At these frequencies, quantum fluctuations dominate.

In addition to these fundamental coupling mechanisms, technical effects like wire roughness and adsorbates on the chip surface can distort the trapping potential, which is a limitation for certain types of atom chip applications, e.g. waveguiding experiments.

1.9.1 Thermal magnetic near-field noise

In a conductor of conductivity σ at temperature T, thermal agitation of the electrons leads to current noise. This effect is known as Johnson-Nyquist noise in electronics. The conductor may be a chip wire used for trapping, but thermal currents exist in any conductor, independent of whether an external current is applied or not. The currents are the source of a fluctuating magnetic field, which is many orders of magnitude stronger than the field due to black body radiation in the near field of the conductor [31]. At the relevant frequencies $\omega/2\pi < 10$ GHz corresponding to wavelengths > 3 cm, the trap is in this near-field regime. If the magnetic trap is operated with very stable current sources, technical magnetic field noise can be made negligible. This leaves thermal magnetic near-field noise as the dominant effect limiting chip trap performance near conductors, as predicted in [30, 31] and subsequently observed in [32, 88, 44].

Spectral density

At distance d from a conducting, non-magnetic layer of thickness t, see Fig. 1.8(a), the spectral density of the magnetic field fluctuations is [89, 31]

$$S_{B\alpha\beta}(\omega) = \frac{\mu_0^2 \sigma k_B T}{16\pi d} \cdot s_{\alpha\beta} \cdot g(d,t,\delta), \quad (\alpha,\beta = x,y,z), \tag{1.34}$$

where $s_{\alpha\beta} = \mathrm{diag}(\frac{1}{2}, 1, \frac{1}{2})$ is a tensor which is diagonal in the coordinate system of Fig. 1.8(a). The distinguished axis is normal to the surface. The

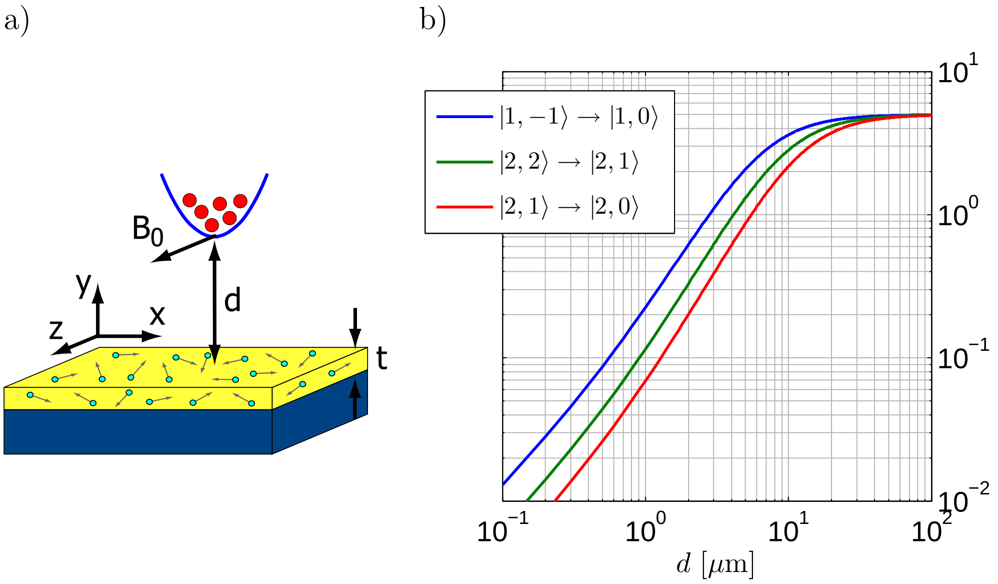

Figure 1.8: Trap loss due to spin flips caused by thermal magnetic near field noise. (a) Atoms near a conducting layer on top of a dielectric substrate. In addition to the geometry, the skin depth δ is an important length scale of the problem (see text). (b) Trap lifetime as a function of d for the indicated transitions, $t = 1\ \mu$m, $\delta \gg \max(d,t)$, and $\tau_{\text{bg}} = 5$ s.

dimensionless function $g(d,t,\delta)$ depends on the geometry and the skin depth $\delta = \sqrt{2/\sigma\mu_0\omega}$, which carries the frequency dependence of $S_B(\omega)$. The spectral density is related to the mean square fluctuations of the magnetic field components

$$\langle B_\alpha^2(t)\rangle = \frac{1}{\pi}\int_0^\infty S_{B\alpha\alpha}(\omega)\,d\omega. \tag{1.35}$$

It is difficult to obtain exact expressions for g, even for simple geometries. In various limiting cases, analytical expressions or empirical interpolation formulae exist [89, 44]:

$$g = \begin{cases} 1 & \text{for } d \ll \delta \ll t, \\ 3\delta^3/2d^3 & \text{for } \delta \ll \min(d,t), \\ \dfrac{t/d}{1+[4dt/(\pi^2\delta^2)]^2} & \text{for } t \ll \min(\delta,d), \\ t/(t+d) & \text{for } \delta \gg \max(d,t), \\ \dfrac{t}{t+d}\cdot\dfrac{w}{w+2d} & \text{for } \delta \gg \max(d,t) \text{ and finite } w, \end{cases} \tag{1.36}$$

where the last formula is for a wire of thickness t and width w (for a more accurate treatment of this case, see [90]). Note that if δ is the largest length scale, it drops out of the problem and S_B is a white noise spectrum at the relevant frequencies. For gold conductors and $\omega/2\pi \sim 1$ MHz (a typical Larmor frequency), one obtains $\delta \sim 75\ \mu$m, and we are well inside this regime for distances where surface effects matter. In this regime, the last two formulae in Eq. (1.36) give the following general scaling: for a metallic half space, g is a constant, for a thin layer, $g \propto t/d$, and for a thin and narrow wire, $g \propto tw/d^2$. To reduce magnetic field noise, it is thus desirable to make the on-chip conductors as thin and narrow as possible.[11] On chips with multiple metal layers where $t \ll \delta$ for each layer, we roughly estimate S_B by adding the spectral densities due to the individual layers.

Although it is a thermal effect, magnetic near-field noise near pure metal wires cannot be reduced by simply cooling the chip. Due to the temperature dependence of $\sigma(T)$, $S_B \propto \sigma(T)\,T$ actually increases if T is decreased [90]. If special alloys are used for the wires, a decrease of S_B by cooling is possible [90]. The use of superconducting wires would decrease S_B as well, although there is a theoretical controversy on how big this effect is [91, 92].

Trap loss due to spin flips

The fluctuating magnetic near-field couples to the magnetic moment $\boldsymbol{\mu}$ of the atoms in the trap. Components perpendicular to $\boldsymbol{\mu}$ drive spin flips, which result in decoherence and loss from the magnetic trap since only low-field seeking states are trapped. The transition rate γ_s between states $|i\rangle$ and $|f\rangle$ at frequency ω_{fi} is given by Fermi's golden rule

$$\gamma_s = \frac{1}{\hbar^2} \sum_{\alpha,\beta=x,y,z} \langle i|\mu_\alpha|f\rangle\langle f|\mu_\beta|i\rangle\, S_{B\alpha\beta}(\omega_{fi}). \tag{1.37}$$

Let us consider the spin-flip transition between adjacent magnetic sublevels $|i\rangle = |F=1, m_F=-1\rangle$ and $|f\rangle = |F=1, m_F=0\rangle$ at the Larmor frequency $\omega_{fi} = \omega_L$. In most magnetic chip traps, the static field in the trap center $\mathbf{B}_0$ is parallel to the surface, and we have chosen this direction as the z-axis in Fig. 1.8(a). In this case the evaluation of the matrix elements yields $|\langle 1,0|\mu_x|1,-1\rangle| = |\langle 1,0|\mu_y|1,-1\rangle| = \mu_B/\sqrt{8}$ and $\langle 1,0|\mu_z|1,-1\rangle = 0$, using $\mu_\alpha = -\mu_B g_F F_\alpha$ and Eq. (A.7). For $\delta \gg \max(d,t)$ we obtain a lifetime due

---

[11] Interestingly, for $d \gg \delta \gg \sqrt{dt}$, the scaling is $S_B \propto \delta^4/td^4$, and a smaller t actually increases S_B [89].

to spin flips of

$$\tau_s = \frac{1}{\gamma_s} = \frac{256\pi\hbar^2}{3\mu_0^2\mu_B^2\sigma k_B T} \cdot \frac{d(t+d)}{t} \quad \text{for state } |1,-1\rangle. \tag{1.38}$$

The overall trap lifetime is $\tau = (\tau_s^{-1} + \tau_{\mathrm{bg}}^{-1})^{-1}$, where we take into account a background lifetime τ_{bg} at large d where surface effects are negligible. In Fig. 1.8(b), we plot τ for different states in comparison. Atoms in $|2,2\rangle$ are lost in a cascade process $|2,2\rangle \rightarrow |2,1\rangle \rightarrow |2,0\rangle$ [44], however the first spin flip already destroys coherent dynamics.

The spectral density $S_B(\omega)$ decreases at high frequencies due to the skin effect. At $\omega/2\pi = 6.8$ GHz, $\delta = 0.9$ μm, which has to be compared with the geometrical dimensions d and t, see Eq. (1.36). For typical chip geometries, the loss rate for hyperfine-changing transitions at GHz frequencies is thus smaller than that for transitions between adjacent Zeeman sublevels at MHz frequencies.

In addition to spin flips, magnetic near-field noise causes dephasing, heating and motional decoherence. As discussed in the following paragraphs, the rates of these processes are all comparable to or smaller than γ_s.

Dephasing of spin superposition states

The component of the fluctuating magnetic field parallel to $\boldsymbol{\mu}$ leads to decoherence of spin superposition states $\alpha|0\rangle + \beta|1\rangle$, without changing the populations ("pure dephasing"). The dephasing rate is given by [31]

$$\gamma_\phi = \frac{\Delta\mu_\parallel^2}{2\hbar^2} S_{B\parallel}(\omega = 0), \tag{1.39}$$

where $\Delta\mu_\parallel = \langle 1|\mu_\parallel|1\rangle - \langle 0|\mu_\parallel|0\rangle$ is the differential magnetic moment of the states $|1\rangle$ and $|0\rangle$, $\parallel$ denotes the direction of the static trapping field, and $S_{B\parallel}$ is the component of S_B parallel to it. In Fig. 1.8(a), $\mu_\parallel = \mu_z$ and $S_{B\parallel} = S_{Bzz}$. In Eq. (1.39) we have made use of the fact that $S_B(\omega)$ is flat for small ω so that we can replace its low-frequency average by its value at $\omega = 0$ [31].

For most states $|0\rangle$ and $|1\rangle$, $\Delta\mu_\parallel \sim \mu_B$, so that γ_ϕ is comparable in magnitude to the spin flip rate γ_s. For a state pair with nearly equal magnetic moments, as we use it in the experiments of chapter 4, $\Delta\mu_\parallel \ll \mu_B$ and therefore γ_ϕ is negligible compared to γ_s.

Heating and decoherence of the center-of-mass motion

We now discuss how thermal magnetic near-field noise perturbs the center-of-mass motion of the atoms in the trap.

Spatially inhomogeneous fluctuations lead to heating and motional decoherence. Consider a transition between motional states $\psi_i(\mathbf{x})$ and $\psi_f(\mathbf{x})$ in the trap, assuming that the atom's internal state does not change. Fermi's golden rule yields a transition rate [31]

$$\gamma_h = \frac{\mu_\parallel^2}{\hbar^2} \int \mathrm{d}^3x\, \mathrm{d}^3x'\, M_{fi}^*(\mathbf{x}) M_{fi}(\mathbf{x}') S_{B\parallel}(\mathbf{x}, \mathbf{x}', \omega_{fi}), \tag{1.40}$$

where $M_{fi}(\mathbf{x}) = \psi_f^*(\mathbf{x})\psi_i(\mathbf{x})$ is the wave function overlap, $S_B(\mathbf{x}, \mathbf{x}', \omega)$ is the magnetic field correlation spectrum, and the transition frequency ω_{fi} is of order of the trap frequency ω_t. For small deviations $|\mathbf{x} - \mathbf{r}|$, $|\mathbf{x}' - \mathbf{r}| \ll l_c$ from the trap center $\mathbf{r}$, the field correlation spectrum is related to the noise spectrum by [31]

$$S_{B\parallel}(\mathbf{x}, \mathbf{x}', \omega) \approx S_{B\parallel}(\omega) \left[1 - \frac{(\mathbf{x} - \mathbf{x}')^2}{l_c^2} \right], \tag{1.41}$$

where $S_{B\parallel}(\omega)$ is evaluated at $\mathbf{r}$, and l_c is the coherence length of the field fluctuations. It can be shown [31] that $l_c \approx d$. In order to estimate the heating rate, we now consider the transition $\psi_0 \to \psi_1$ between the ground and first excited state along one dimension of a harmonic trap. The trap is tightly confining such that the size of ψ_0 is $a \ll l_c$. In this limit one obtains

$$\gamma_h \approx \frac{\mu_\parallel^2}{\hbar^2} S_{B\parallel}(\omega_t) \frac{a^2}{l_c^2} \approx \gamma_s \frac{a^2}{d^2}, \tag{1.42}$$

where we have related γ_h to the spin flip rate γ_s, making use of the fact that $\mu_\parallel \sim \mu_B$ and $S_{B\parallel}(\omega)$ is flat in the relevant frequency range. Motional decoherence occurs at a rate similar to γ_h [31]. For $a \ll d$, heating and motional decoherence due to near-field noise are thus negligible compared to spin flips. A similar reasoning applies to atoms split in a double-well potential, with a given by the separation of the wells [93]. For $a \gg d$, on the other hand, one obtains $\gamma_h \approx \gamma_s$.

Spatially homogeneous fluctuations can also lead to heating and decoherence, since they add to the trapping fields and thus lead to a fluctuating trap position and curvature. The rate for the transition $\psi_0 \to \psi_1$ is related to the spectral density of position fluctuations $S_r(\omega)$ by [94]

$$\gamma_h = \frac{m\omega_t^3}{2\hbar} S_r(\omega_t), \tag{1.43}$$

where S_r is normalized so that the equivalent of Eq. (1.35) holds. For transverse position fluctuations in a cigar-shaped Ioffe trap with gradient B', we can relate $S_r(\omega)$ to the transverse component $S_{B\perp}(\omega)$ of the magnetic field noise spectral density, $S_r(\omega) = S_{B\perp}(\omega)/B'^2$. Using $\omega_t = \omega_\perp$, Eq. (1.10), and $\omega_L = \mu_B |g_F| B/\hbar$, we obtain

$$\gamma_h \approx \frac{\mu_B^2}{\hbar^2} S_{B\perp}(\omega_\perp) \frac{\omega_\perp}{\omega_L} \approx \gamma_s \frac{\omega_\perp}{\omega_L}. \tag{1.44}$$

Since $\omega_\perp \ll \omega_L$ to avoid Majorana spin flips, we again find $\gamma_h \ll \gamma_s$. A similar reasoning also applies to fluctuations of the trap curvature.

Summary

In summary, one finds that all loss, heating, and decoherence rates due to thermal magnetic near-field noise are of the order of the spin-flip rate γ_s or smaller. In the following chapters, we will thus use γ_s as a measure for the importance of surface effects above metal layers.

Finally, we note that the effect of technical magnetic field noise can be analyzed along the same lines by simply identifying $S_B(\omega)$ with the corresponding technical noise spectral density. Noise from technical current fluctuations in a wire, for example, has $S_B = (\mu_0 \Delta I)^2/(4\pi d^2 \Delta\omega)$, where we have assumed that the spectrum is flat, ΔI is the RMS amplitude of the current fluctuations, and $\Delta\omega/2\pi$ the bandwidth of the current source.

1.9.2 Casimir-Polder and van der Waals-London surface potential

An atom in its ground state close to a metallic or dielectric surface feels an attractive potential $V_s(z)$ that arises due to the interaction of the fluctuating electric dipole of the atom with the fluctuating electromagnetic field, which depends on distance z from the surface [95, 85, 96]. Approaching the surface from large z, the atom experiences several regimes of this interaction, see Fig. 1.9 [96]. For $z \gg \lambda_T$, where $\lambda_T = \hbar c/k_B T$ is the thermal photon wavelength ($\lambda_T = 7.6$ μm for $T = 300$ K), thermal fluctuations of the field are dominant. In thermal equilibrium, the potential scales like $-T/z^3$ (Lifshitz or thermal regime). At smaller distances, $\lambda_T \gg z \gg \lambda_{\text{opt}}/2\pi$, quantum

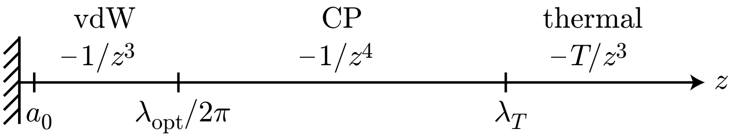

Figure 1.9: Scaling of $V_s(z)$ with distance z from the surface.

fluctuations dominate, and the potential scales like $-1/z^4$ (Casimir-Polder regime). Retardation effects are important, since z is larger than the (reduced) wavelength $\lambda_{\mathrm{opt}}/2\pi$ of the strongest electric dipole transition of the atom. For the Rb ground state, $\lambda_{\mathrm{opt}}/2\pi \approx 120$ nm for the D_2 and D_1 lines. At yet smaller distances, $\lambda_{\mathrm{opt}}/2\pi \gg z \gg a_0$, retardation is negligible and the potential scales like $-1/z^3$ (van der Waals-London regime). For completeness we note that for $z \sim a_0$, where a_0 is the Bohr radius, aspects of chemical physics come into play, governing phenomena like the adsorption of the atom on the surface. In most ultracold atom experiments, the strength of the surface potential is negligible in the Lifshitz regime (but see [97]). Of importance are the Casimir-Polder and van der Waals-London regimes; experimental studies with ultracold atoms are reported in [44, 98, 99]. In the experiments of chapter 4, we observe loss of atoms due to the Casimir-Polder potential.

The following formula for the surface potential of the atomic *ground state* interpolates between the Casimir-Polder and van der Waals-London regimes [100, 99]:

$$V_s(z) = -\frac{C_4}{z^3(z + 3\lambda_{\mathrm{opt}}/2\pi^2)} \quad \text{with} \quad C_4 = \frac{3\hbar c \alpha_0}{32\pi^2 \varepsilon_0} \cdot \frac{\varepsilon_r - 1}{\varepsilon_r + 1} \phi(\varepsilon_r). \tag{1.45}$$

It is valid for a planar dielectric substrate at $T = 0$, but also yields a good approximation for thermal equilibrium situations at room temperature. The substrate is assumed to fill the half space $z \leq 0$. α_0 is the static polarizability of the atomic ground state, and $n = \sqrt{\varepsilon_r}$ is the refractive index of the substrate material at wavelength λ_{opt}. The function $\phi(\varepsilon_r)$ is nearly constant and equals 0.81 for $n = 3.7$ (Silicon) [101]. The potential in front of a good conductor can be obtained by letting $\varepsilon_r \to \infty$, in which case $\phi \to 1$.

Figure 1.10(a) shows the combined potential $V_t(z) + V_s(z)$ seen by an atom close to a Si surface, where $V_t(z) = \frac{1}{2} m \omega_t^2 (z - d)^2$ is the trapping potential. In the limit of large d, the surface potential can be approximated to have zero range, and the trap depth is given by $V_t(0) = \frac{1}{2} m \omega_t^2 d^2$. The effect of the finite range of $V_s(z)$ is to decrease the trap depth to $V_b(d, \omega_t)$, as can be seen in the figure, and the trap vanishes already at $d > 0$. We now determine the minimum trap-surface distance d_m required to trap atoms of energy $E = \zeta \hbar \omega_t$, where ζ is a constant. From the condition $V_b(d_m, \omega_t) = \zeta \hbar \omega_t$, we numerically determine d_m as a function of ω_t, using Eq. (1.45) for the surface potential. Figure 1.10(b) shows the result for several values of ζ. For $V_b < \hbar \omega_t / 2$, the trap no longer supports a bound state. The curves yield a lower limit on d_m, since effects such as tunneling or evaporation of atoms from the potential have been neglected. To suppress these effects, only a moderate increase of d is required, since V_b increases stronger than quadratically with d.

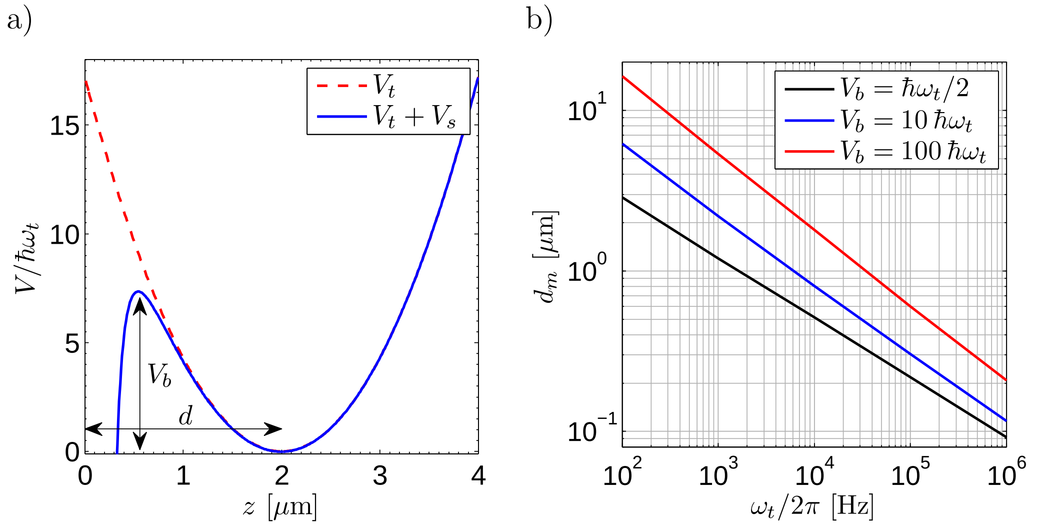

Figure 1.10: Decrease in trap depth due to the surface potential V_s. (a) Trapping potential with and without V_s, shown for a Si surface at $z = 0$ and a harmonic trap V_t of frequency $\omega_t/2\pi = 1$ kHz with minimum at $d = 2$ μm. The trap depth is decreased to $V_b(d, \omega_t)$. (b) Trap-surface distance d_m at which $V_b(d_m, \omega_t) = \zeta\hbar\omega_t$, shown for several values of ζ. (see text).

From Fig. 1.10(b) we conclude that it is possible to manipulate atoms at a distance of a few hundred nanometers from the chip surface with ω_t in the range of several kHz to hundreds of kHz. As discussed in section 1.4.4, such trap frequencies are indeed realistic. An even closer approach to the surface seems possible if the surface potential is modified. This can be achieved by structuring the surface [102] or by using substrate materials whose dielectric function has a resonance at the relevant wavelength [95]. Furthermore, quantum reflection could allow confinement of atoms with an attractive surface potential, although in the experiment [102] the observed trap lifetimes were smaller than the trap oscillation period.

The identification of the physical mechanisms giving rise to the Casimir-Polder and van der Waals-London interactions and their relation to the Casimir effect between macroscopic bodies is a fascinating subject with a long history [103, 104]. An "atomic physicist's interpretation" of the Casimir-Polder potential can be given in terms of the AC Stark effect caused by the interaction of the atomic dipole with the vacuum fluctuations of the electromagnetic field, treating the surface as a macroscopic object [95, 105]. In free space, this AC Stark effect is the main contribution to the Lamb shift. The presence of the surface modifies the boundary conditions and thus the mode spectrum of the electromagnetic field. The resulting change in the AC Stark effect leads to the Casimir-Polder potential. The distance-dependence arises because at distance z, only those modes whose wavelengths are greater than z have mode functions which are substantially modified by the surface. While the Casimir-Polder potential is thus a direct manifestation of the *vacuum fluctuations* of the electromagnetic field, the surface potential in the van der Waals regime cannot be interpreted in this way [95, 105]. Instead it is due to *self-reaction*, i.e. the interaction of the atomic dipole with its own field reflected by the surface. The common statement that the Casimir-Polder potential is a "retarded van der Waals potential" thus seems somewhat misleading in the light of the different interpretations [105].

1.9.3 Corrugated potentials

Technical imperfections such as wire roughness and contamination of the surface with adsorbates can distort the trapping potentials on an atom chip.

Adsorbates

When working with ultracold atoms on a chip, it is difficult to avoid that some of the atoms become stuck to the surface. Depending on the surface material, the electrons in the adatom and the surface will be redistributed such that each adatom develops a small electric dipole moment $\boldsymbol{\mu}_e$, oriented normal to the surface. The combined electric field $\mathbf{E}(\mathbf{r})$ of the adatoms interacts with the ultracold atoms trapped near the surface. An attractive potential

$$V_a(\mathbf{r}) = -\frac{\alpha_0}{2}|\mathbf{E}(\mathbf{r})|^2 \tag{1.46}$$

is created via the quadratic Stark effect, where α_0 is the atomic polarizability. In [106, 107], this effect was observed for ^{87}Rb adsorbates on Si, Ti, Y, Lu, Hf, and glass surfaces. The potential V_a is stronger above materials such as Si and Ti, whose work functions are comparable to or greater than the ionization energy of ^{87}Rb, resulting in strong polarization of the adatoms. An electric dipole moment of $\mu_e \approx 1 \times 10^{-29}$ C m per adatom was extracted from the data for Si. On glass, μ_e was found to be about one order of magnitude weaker.

The potential V_a strongly depends on the spatial distribution of adatoms on the surface [107]. To estimate the order of magnitude of the effect, we show V_a in Fig. 1.11 for several BECs deposited at the same location on a Si surface.

We assume a homogeneous distribution of N_a adatoms within a region of length L and width W, with L and W corresponding to the extension of a BEC. This is likely to overestimate the effect because a realistic distribution is smeared out [107]. Figure 1.11 shows that V_a can be stronger than the Casimir-Polder surface potential (1.45), resulting in tighter limits on the minimum atom-surface distance. In addition, an inhomogeneous distribution of adatoms can lead to corrugations of the potentials created on the chip. The effect of adatoms can be mitigated by careful experimental control to reduce N_a, and by passivating the chip surface with a thin layer of SiO_2 so that μ_e is smaller.

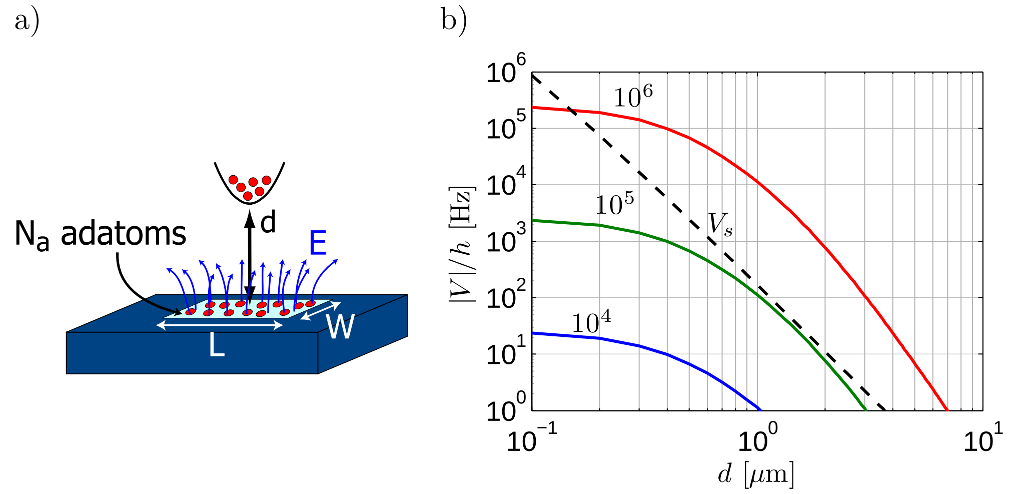

Figure 1.11: Electrostatic potential created by adsorbates on the chip surface. (a) Ultracold ^{87}Rb atoms trapped above N_a ^{87}Rb adatoms homogeneously distributed over a region of length L and width W on the chip surface. (b) Potential V_a due to the adatoms for different values of N_a as indicated in the figure (solid lines), with $L = 3$ μm and $W = 1$ μm, corresponding to the extension of a small BEC. For $N_a = 10^6$, the local surface coverage with ^{87}Rb is about 10% of a monolayer. The Casimir-Polder surface potential V_s is shown for comparison (dashed line).

Wire roughness

The wires on an atom chip show a certain degree of roughness, which arises from technical imperfections of the fabrication process, see Fig. 2.6 in chapter 2. This leads to deviations of the current flow from a straight path, resulting in corrugations of the magnetic potentials created by the wires. Under special circumstances, namely for very elongated and cold atomic clouds close to the surface, these corrugations have been observed to cause a break up of the atomic cloud into several fragments [24].

At distance d from the wire, only wire roughness on a length scale $s \geq d$ leads to potential corrugations with significant amplitude [24]. Features with $s \ll d$ average out at the position of the atoms. If the atomic ensemble is tightly trapped in all three dimensions, such that its size $R \ll d$, the corrugations manifest only as a constant offset of the trap bottom, which is easily compensated for by adjusting the wire current. If, on the other hand, $R \gg d$, as in waveguiding experiments, the atoms will see the corrugated potential and break up into fragments of size $\geq d$. This shows that wire roughness is a serious issue for waveguiding experiments on an atom chip. On the other hand, it is of minor importance for the experiments and proposals discussed in this thesis, where the atoms are tightly trapped in all three dimensions. Corrugations of the trapping potential can be reduced by using fabrication techniques which produce very smooth wires, such as those discussed in chapter 2. In addition, the corrugations can be suppressed by modulating the wire current, as demonstrated in [108].

Chapter 2

Multilayer atom chip fabrication

The microfabrication process which we have developed for our atom chips is described in this chapter. Using this process, we have fabricated atom chips carrying gold wires with lateral structure sizes down to 1 μm. The wires are arranged in two layers of metallization which are electrically insulated from each other by a micrometer-thin layer of polyimide. These new structures are significantly smaller and more complex than those employed in our earlier atom chip experiments [23]. Our new chips enable, among other things, the generation of tunable tunneling barriers for BECs, two-dimensional arrays of potential wells, and state-selective microwave potentials for quantum information processing.

After summarizing the fabrication goals and challenges, I discuss the main fabrication techniques used, the difficulties encountered, and their resolution. Furthermore, I show measurements of the maximum current density the chip wires can support. In appendix C, a detailed description of the fabrication recipe can be found. The multi-layer process developed here has been used to fabricate the chips for two new experiments which are currently underway. The first chip can be used to study Bose-Einstein condensates in small magnetic multi-well potentials. The second chip carries microwave guiding structures for the manipulation of atoms with microwave near-fields (see chapter 5). Both chips are shown at the end of this chapter.

We thank Prof. Kotthaus from the Center for NanoScience (CeNS) at LMU Munich for generously allowing us to fabricate our chips in the cleanroom facilities of his group.

2.1 Fabrication goals and challenges

Many of the proposed applications of atom chips in both fundamental science and technology require chips with smaller and more complex structures than those that were used in the experiments until now. Tunneling of atoms, for example, which is at the heart of certain schemes to generate Schrödinger cat states [76], can only be observed at very narrow potential barriers. Quantum information processing, as another example, will eventually require large arrays of individually addressable microtraps on a single chip [109]. Such potentials can be generated on atom chips with multiple layers of micrometer-sized wires, as shown schematically in Fig. 2.1. A two-layer chip allows for greater flexibility in trap design by avoiding wire crossings which would arise in a single layer. This is essential for the chip shown, where two perpendicular sets of wires are used to trap a BEC in a small array of magnetic potential wells, separated by tunable tunneling barriers (cf. section 1.5). Similar two-layer chip layouts are required for the experiments with microwave near-fields proposed in chapters 5 and 6 of this thesis. While fabrication techniques for complex microstructures are available [110], they have to be adapted to the peculiar requirements of ultracold atom experiments.

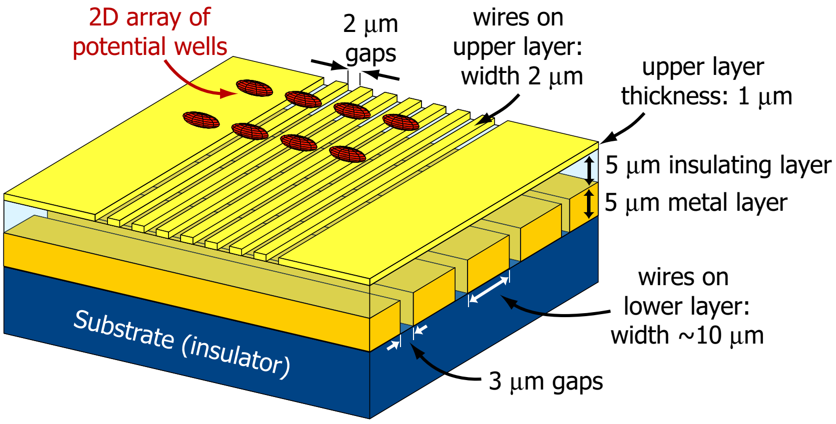

Figure 2.1: Atom chip with two layers of micrometer-sized wires, separated by a thin insulating layer. Only the chip center is shown where the smallest structures are located.

In our group, the first atom chip experiments were carried out with chips fabricated at other institutes [27, 111, 112]. Several research groups have developed custom fabrication processes for wire-based atom chips [113, 114, 111, 115, 116, 44, 117, 118, 119]. In these processes, optical or electron beam lithography is used to define the wire patterns, and metal is deposited by thermal evaporation, sputtering, or electroplating. Most chips have only a single layer of metallization, with wire widths in the range of $1-100\ \mu$m. A few impressive multi-layer chips were fabricated, albeit with structure sizes $\geq 100\ \mu$m. Multi-layer atom chips with micrometer-sized structures of high aspect ratio, as in Fig. 2.1, do not seem to be available. We therefore decided to develop the necessary fabrication process.

Fabrication challenges

The following challenges arise in fabricating the atom chip in Fig. 2.1:

- The lateral size of the wires in the top layer is near the resolution limit of standard laboratory equipment for optical lithography. The relatively high aspect ratio of the wires (thickness comparable to lateral size) is needed to support the DC and microwave currents for magnetic trapping, but poses additional difficulties in the fabrication process.

- The upper metal layer has to serve as a high quality mirror for the laser beams of the magneto-optical trap (see chapter 3), with small gaps between wires and few defects over a large surface area of several cm^2.

- The insulating layer has to fill the gaps between wires on the lower layer and planarize the chip for processing of the upper layer. At the same time, the experiments require the insulating layer to be a few micrometers thin and provide good heat conductivity.

- The wires on the lower gold layer have to be $\geq 5\ \mu$m thick in order to support currents of several amperes for trapping the relatively large atomic clouds in the initial stages of the experiment. At the same time, there are structures of $3\ \mu$m lateral size in this layer. Such high aspect ratio structures are difficult to fabricate.

- An insulating substrate with a large heat conductivity is needed to dissipate the heat generated in the conductors.

- All chip components have to be compatible with ultra-high vacuum conditions (10^{-10} mbar).

- The chip has to withstand temperatures up to 350 °C during fabrication and up to 150 °C when it is fully assembled (e.g. during gluing of glass cell and vacuum bake out).

- The chip wires have to be contacted without obstructing optical access for the trapping and imaging laser beams.

- Some experiments with elongated BECs require extremely smooth wire edges and surfaces to avoid corrugations of the trapping potential which have been observed to lead to fragmentation of the BEC.

The challenges peculiar to a two-layer fabrication process could be circumvented by fabricating two single-layer chips which are then glued on top of each other. In this case, however, the distance between the two metallization layers would be at least several tens of micrometers, since thinner substrates can hardly be processed without breaking. This has the drawback that the maximum confinement provided by wires on the lower layer is significantly reduced, and that the characteristic feature size of the potentials generated by the lower layer is much larger than that of the upper layer.

2.2 Fabrication process

The fabrication process we have developed meets all the requirements mentioned above. It can be broken down into the following steps:

- Substrate preparation.

- Fabrication of the lower wire layer by optical lithography and electroplating.

- Application of the insulating layer.

- Fabrication of the upper wire layer by optical lithography and lift-off metallization.

- Chip dicing, mounting, and bonding.

Both metal layers on our chip are made of gold because of its high conductivity of $\sigma = 4.5 \times 10^7\ \Omega^{-1}\,\mathrm{m}^{-1}$ at room temperature, its chemical inertness, and its high reflectivity of 98% for light at 780 nm. The insulating layer is made of spin-on polyimide.

A thorough introduction to the fundamentals of microfabrication can be found in [110]. For a good tutorial introduction to atom chip fabrication, see [111]. A very useful paper listing etch rates for a large number of etchants and materials is [120]. A detailed fabrication recipe for our process, with all relevant parameters, a list of chemicals, clean-room equipment, and microfabrication company web pages, can be found in appendix C.

2.2.1 Substrate

The substrate of the atom chip has to support the wires, provide electrical insulation between them, and dissipate the heat generated in the wires. Therefore, a substrate with high thermal conductivity and a smooth, insulating surface is needed. For chips with microwave or radio-frequency guiding structures, the dielectric constant and loss tangent are similarly important selection criteria. In addition, mechanical strength, low outgassing, and compatibility with the chemicals used for processing are required. In our experiments, we use silicon as substrate material for the experiment chip and aluminum nitride for the base chip.

Our two-layer chips are fabricated on single crystal Si wafers in (100) orientation. A common substrate thickness is 525 μm, the thermal conductivity is ≈ 150 W/(m K) at room temperature. The wafers are polished on one side and have very small surface roughness, sufficient even for the smallest wires. We cleave the wafers with a diamond scorer. Neither the resistivity of Si nor the 2 nm native oxide layer on the substrate are sufficiently insulating the wires if we aim for a control over the DC currents on the 10^{-5} level. We therefore grow a 20 nm layer of SiO_2 on the wafer by thermal oxidation at 1100 °C. This layer provides a DC resistance of > 40 MΩ between the wires. Since SiO_2 has a thermal conductivity of only 1.5 W/(m K), the insulating layer should not be made thicker than necessary [115].

AlN is a non-toxic polycrystalline ceramic [121] with an excellent heat conductivity of 180 W/(m K) at room temperature, a factor of five higher than that of Al_2O_3 (see [23] for a comparison with other materials). Compared with Si, AlN is less brittle. It can be laser machined and easily cleaved with a diamond scorer. A polished AlN surface (specified surface roughness Ra < 40 nm) has a significant residual roughness, with isolated defects of micrometer size. This is a problem if structures < 10 μm are desired. We use AlN for the base chips in our experiments, which have only a single layer of gold with structure size > 10 μm. We found that electroplated gold on AlN substrates is not compatible with the polyimide baking step in our two-layer fabrication process (see section 2.2.3 below). We therefore use AlN only for single layer chips which do not have to be heated to temperatures above 200 °C.

Both AlN and Si are common substrate materials for microwave circuits. AlN has a dielectric constant of $\varepsilon_r = 8.7$ and a loss tangent of $\tan\delta = 1 \times 10^{-3}$ at 10 GHz. If only DC currents are used in the experiment, Si of any doping level can be employed as substrate material. For microwave applications, however, it is very important to choose high-resistivity Si to avoid strong dielectric losses. High-resistivity Si is grown by the floatingzone method; our wafers have a resistivity of $\rho > 10^4\ \Omega\,\mathrm{cm}$, $\varepsilon_r = 11.9$, and $\tan\delta \approx 10^{-3}$ at 10 GHz. Although the nominal loss tangents are comparable, we found microwave loss to be somewhat higher on Si than on AlN. A possible explanation is the charge layer forming at the Si-SiO$_2$ interface [122].

The substrates have to be thoroughly cleaned before processing starts. This is a multi-step process detailed in appendix C. We furthermore bevel the edges of the Si substrate so that edge beads formed during spin coating with photoresist or polyimide do not give rise to a gap between the chip surface and the photomask during lithography (cf. Fig. 2.2).

2.2.2 Optical lithography

In optical lithography, light is used to transfer a pattern on a mask to a light-sensitive resist layer on a chip. In contact lithography, the mask is in direct contact with the resist during exposure. After developing, the resulting resist pattern is used as a stencil for etching or depositing material.

We use a commercial Cr mask for contact lithography for both wire layers on our chip. The mask itself is fabricated by laser lithography with a laser spot size of 0.8 μm, the manufacturer (Delta Mask) specifies a minimum line width of 1.5 μm. Masks with smaller structures can be written by electron beam lithography.

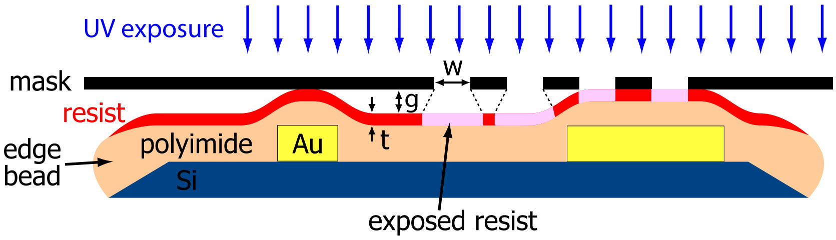

Figure 2.2: Optical lithography with a contact mask. A gap between the mask and the substrate decreases the spatial resolution due to diffraction of light.

The resolution of contact lithography is limited by the near-field diffraction of light at the structures in the mask and thus decreases if there is a gap between the mask and the substrate. Consider photoresist of thickness t exposed with light of wavelength λ through a mask with a pattern of equal lines and spaces of periodicity $2w$, see Fig. 2.2. The theoretical resolution, i.e. the minimum linewidth resolved, is given by Fresnel diffraction theory:

$$w_{\min} = (3/2)\sqrt{\lambda(g + t/2)},$$

where g is the gap between resist and mask [110, 123]. To obtain high resolution, g has to be as small as possible, meaning that any edge beads and defects of the photoresist and the underlying structures have to be avoided. Furthermore, the substrate has to be pressed flush against the mask, this may require supporting the chip below its center with a small rubber ring.

For lithography of the lower gold layer, the thickness of the resist is $t = 6.5\ \mu$m. The mercury lamp in the mask aligner provides light at several spectral lines near $\lambda = 400$ nm. For $g = 0$, we obtain a theoretical resolution of $w_{\text{min}} = 1.7\ \mu$m for this layer.

On our two-layer chips, the wires of the lower gold layer lead to an uneven topography, which is smoothed out but not completely planarized by the polyimide. This limits the resolution which can be achieved in the lithography of the upper layer. As shown in Fig. 2.2, a gap of $g = 5\ \mu$m forms where no wires are present in the lower layer. For $\lambda = 400$ nm and $t = 1.6\ \mu$m, we obtain a resolution of $w_{\text{min}} = 2.3\ \mu$m in this region, compared with $w_{\text{min}} = 0.8\ \mu$m where $g = 0$. Due to the high contrast of the photoresist, fine-tuning of the lithography parameters allows one to beat this limit, but feature sizes significantly smaller than w_{min} cannot be obtained. A further limitation of the attainable resolution arises due to the partially transparent polyimide layer, which leads to diffuse reflections of UV light from the gold surface underneath [124].

Even though our structure size is close to the resolution limit, we have decided to use optical lithography because it is a parallel process which allows large chips to be structured in seconds. Smaller structures can be fabricated by electron beam lithography, which has a resolution of $10 - 100$ nm depending on resist thickness, but is much slower and more difficult to implement.

2.2.3 Lower gold layer: electroplating

We use an electroplating technique to fabricate the lower gold layer [125, 126]. In electroplating, the chip serves as the cathode of an electrolytic cell. Resist structures on the chip form a mold for the electroplated gold. Under an applied voltage, gold ions from the plating solution deposit on the areas not covered by resist. The amount of deposited material per unit time is controlled by the current flow. Electroplating is more time and material efficient than metal deposition through thermal evaporation or sputtering. It is therefore better suited for the fabrication of wires with a thickness $> 1\ \mu$m. Furthermore, large aspect ratio structures are easier to fabricate than with lift-off or etching techniques.

The process flow is illustrated in Fig. 2.3. First, we deposit a 2 nm Ti adhesion layer and a 50 nm Au seed layer on the substrate by thermal

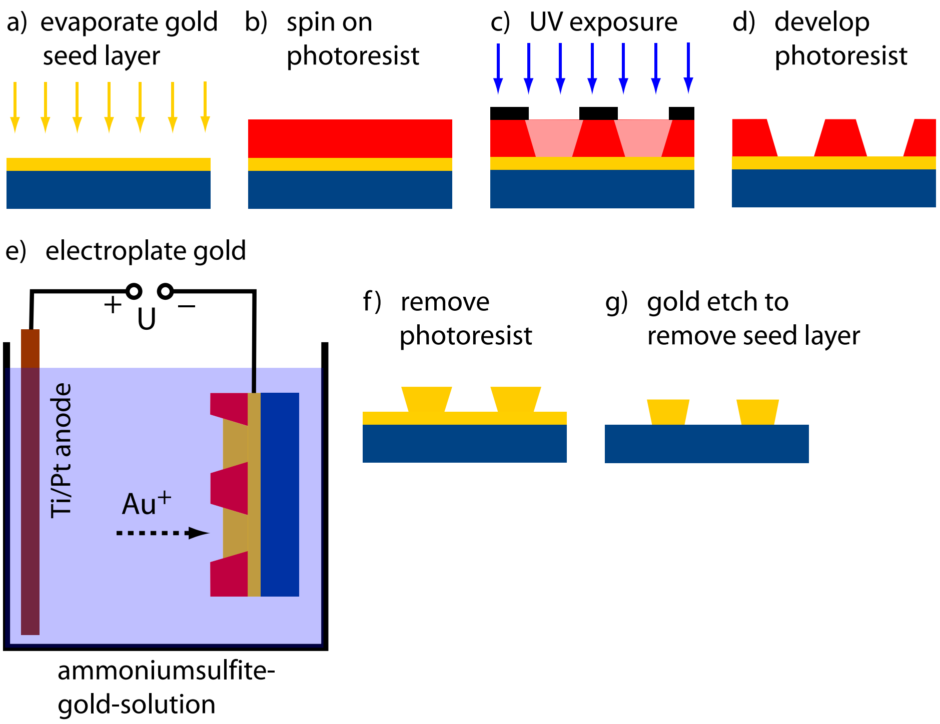

Figure 2.3: Electroplating. The process steps are explained in the text.

evaporation (a). This layer serves as the cathode. We spin coat the chip with a 6.5 μm thick layer of photoresist (b) and subsequently pattern it by optical lithography (c+d). The resist structures serve as a mold for the electroplated gold and should be slightly taller than the desired thickness of the wires. We use the positive tone resist ma-P 1240 from micro resist technology, which, according to the specifications, is characterized by high pattern stability in acidic and alkaline plating baths from $\mathrm{pH} = 1 - 13.5$. We routinely pattern 2 μm wide and 6 μm tall structures with this resist.

For the following electroplating step (e), we use the simple homemade setup shown in Fig. 2.4. The chip and the anode are connected to a power supply and submerged in 1 liter of a sulfite-based gold solution from Metakem which is kept at a temperature of $57 \pm 1\,^\circ\mathrm{C}$ in a water bath. The plating solution is based on ammoniumsulfite-gold(I) ($[(NH_4)_3Au(SO_3)_2]$), has $\mathrm{pH} = 7.5$ and contains 15 g of gold. It is commonly used for dentistry and jewelery and yields very smooth gold deposits of 99.99% purity. The anode is a platinized titanium mesh, also from Metakem. To start depositing gold, a voltage is gradually applied between the gold seed layer and the anode, until the desired plating current flows. While electroplating, the solution is stirred and the chip is constantly agitated with a motor to avoid local depletion of

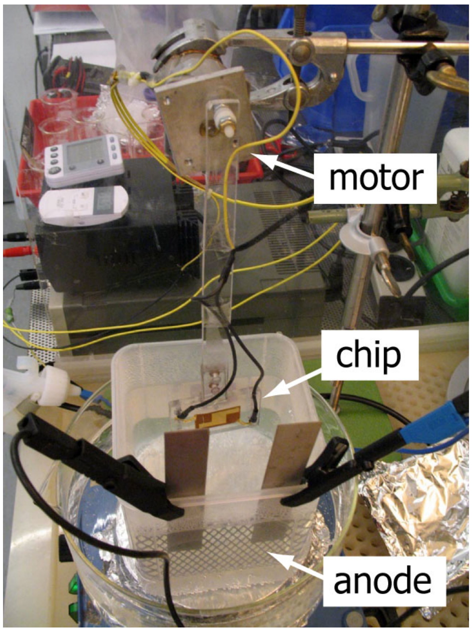

Figure 2.4: Electroplating equipment.

the solution and thus ensure a more homogeneous gold layer. The thickness h of the gold layer deposited after a time t can be determined by Faraday's law:

$$h = \alpha \frac{ItM}{nFS\varrho} = 1.1 \times 10^{-10}\,\frac{\mathrm{m}^3}{\mathrm{A\,s}} \times \frac{It}{S}, \tag{2.1}$$

where I is the plating current, M the molar mass and ϱ the mass density of gold, F is Faraday's constant, $n = 1$ is the charge of the gold ions, and $\alpha \approx 1$ the current efficiency for gold plating. The surface area S of the deposited gold film is given by the surface area of the wire layout plus the contact pads and connectors. The Metakem solution is specified for a current density $j = I/S = 1-15\ \mathrm{mA/cm^2}$. In the parallel plate configuration we use, the current density is approximately constant over the exposed gold areas of the chip. Since the contribution of the contact pads and connectors to S is not precisely known, Eq. (2.1) is used as a rough guideline. The actual deposition rate for a given layout is determined experimentally, and h varies by about 10% from chip to chip, probably because of varying contact pad size.

After the wires are electroplated to the desired thickness, the current is turned off. The chip is removed from the bath and thoroughly rinsed with water. The resist is stripped with acetone (f), residues in small gaps are removed with piranha etch. In the final step (g), the Au seed layer and the

Ti adhesion layer are removed by a wet etch with aqua regia. This isolates the electroplated wires from each other. The gold etch also attacks the wires, increasing surface roughness. It is therefore desirable to work with a seed layer as thin as possible.

Figure 2.5 shows electroplated gold structures on Si chips fabricated with our process. Fig. 2.5(c) shows a fully functional parallel wire structure corresponding to the lower gold layer of the chip design in Fig. 2.1.

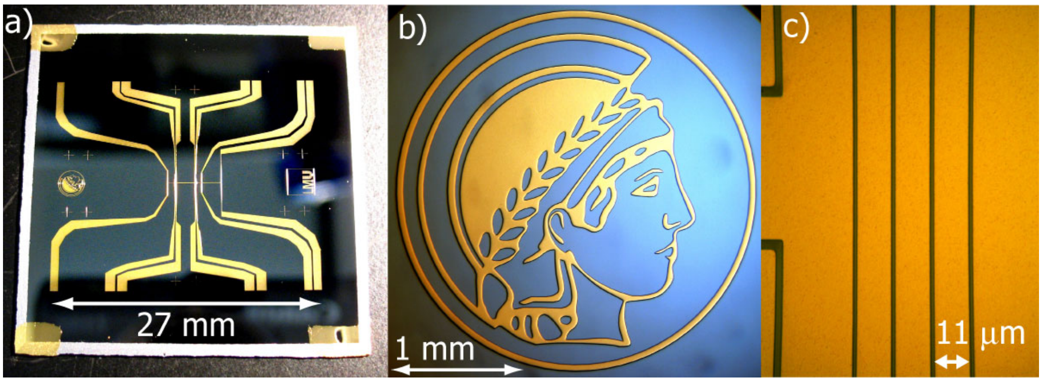

Figure 2.5: Electroplated gold structures (5 μm thick) on a Si chip. (a) Entire chip with contact pads. (b) Minerva, Roman goddess and logo of the Max Planck Society. (c) Microscope image of parallel gold wires fabricated according to the design in Fig. 2.1. The gaps are 3 μm wide.

Wire roughness

Wire roughness leads to deviations of the current flow from a straight path along the wire. This causes corrugations in the magnetic trapping potential, which are responsible for the fragmentation of Bose-Einstein condensates observed in very elongated traps at distances below several tens of micrometers from the atom chip wires (see section 1.9.3). In [117], the roughness of electroplated wires was analyzed and identified as the cause of fragmentation. The roughness was significantly larger than that of wires fabricated by thermal evaporation.

In Fig. 2.6, we show SEM micrographs of electroplated wires on our chip in comparison with the wires of [117]. The roughness of our wires is about one order of magnitude smaller than that of [117]. The RMS surface roughness of a 7 μm thick wire on Si fabricated with our method is 15 nm, measured with an AFM in a 20 μm × 20 μm window. In [117], a roughness of 200 nm RMS was measured.[1]

---

[1] In [117], the edge roughness of the wire was measured. From the SEM picture we

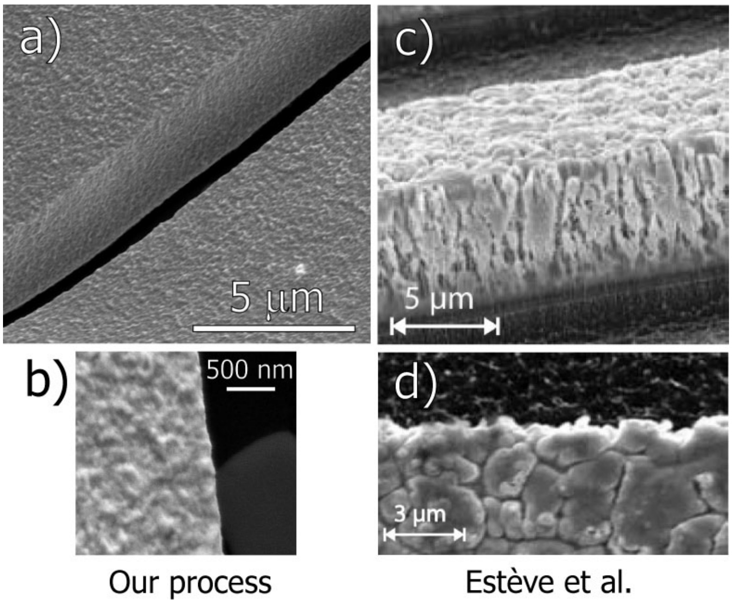

Figure 2.6: SEM images of electroplated gold wires fabricated by different methods. (a)+(b): Wires of 5 μm thickness on our chip. The grain size of the electroplated gold is of the order of 200 nm. (c)+(d): The wire analyzed in [117] (thickness 4.5 μm). Grains of micrometer-size are visible.

The smoother surface of our wires (and that of [116], where an even lower roughness is reported) is very likely due to the gold plating solution used. Different solutions (and also the same solution at different process parameters) deposit gold of very different grain size [126]. We have compared the Metakem solution to a cyanide-based solution (Auruna 5000 from Umicore). Wires fabricated with the cyanide-based solution showed roughness on a micrometer-scale, comparable to [117]. Wires electroplated with a potassiumsulfite-gold solution from Metakem had somewhat larger roughness than with the ammoniumsulfite-gold solution.

The roughness of our electroplated structures is still a factor of 2–3 larger than that of evaporated gold of similar thickness. Roughness increases with the thickness of the gold deposit and also depends on the substrate. On Si, the electroplated gold layers have a specular surface. On AlN, the defects of the substrate are visible in the gold surface.

---

conclude that the edge roughness is comparable to the surface roughness.

Caveats

Electroplating requires careful control of many process parameters. The complex chemistry of the plating bath is easily disturbed by contaminants. Incompatibilities with other processing chemicals have been observed. In the following, we list a number of potential problems which we have identified during optimization of the process.

- We found an incompatibility of AlN substrates with our electroplating process in combination with subsequent thermal processing. As shown in Fig. 2.7(a), defects in electroplated gold on AlN form if the chip is heated to temperatures $> 200\,^{\circ}\mathrm{C}$. On other substrate materials, this problem does not occur (Fig. 2.7(b)). We also observe directly that the AlN surface is attacked by the plating solution (Fig. 2.7(c+d)), even if no gold is deposited on this substrate. Due to this problem, AlN substrates are not compatible with the polyimide baking step in our two-layer fabrication process. However, electroplated gold on AlN can be used for single layer chips which are not heated to such high temperatures. The problem may be solved using a different plating solution. However, the alternatives we have tried all produced gold layers of larger roughness than the sulfite-based solution (see above). To solve the problem, we therefore decided to use Si as substrate material. Si has the additional advantage over AlN that it has much lower surface roughness.

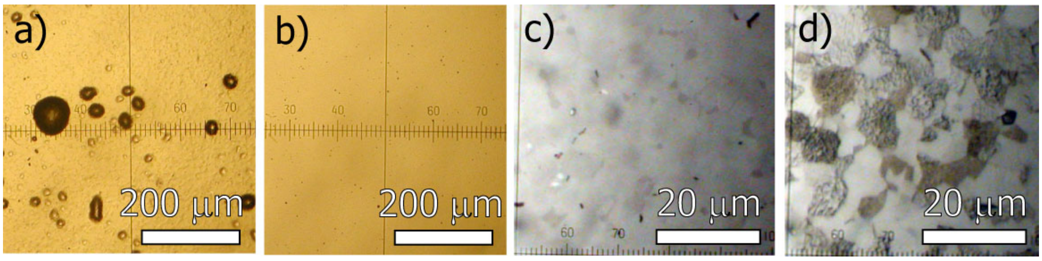

Figure 2.7: Incompatibility of electroplated gold on AlN with thermal processing. (a) Defects ("bubbles") in electroplated gold on AlN after heating to 350 °C. (b) No defects form in electroplated gold on a glass substrate, which was processed identically to (a). (c) Surface of AlN substrate before processing. (d) Same AlN substrate as in (c) after it has been submerged for 50 min in the plating solution.

- Initially we had problems with the adhesion of gold to the substrate, even after rigorous substrate cleaning. The electroplated gold and the seed layer could be easily peeled off. The problem may have been related to contamination of the Ti adhesion layer due to gettering of residual gas in the evaporation chamber. We now always pre-heat the Ti for a few minutes before deposition and avoid delay between the Ti and Au deposition. Now we obtain very good adhesion, which means that the adhesion of the gold to the substrate is stronger than the cohesion of the gold layer itself.

- Adhesion of the electroplated Au to the Au seed layer can be impaired by residual photoresist. By removing the residues in an oxygen plasma cleaner prior to electroplating, this problem can be avoided. We furthermore try to avoid any delay between this cleaning step and the electroplating.

- After the plating solution has been used for a number of chips, but long before the gold in the solution is exhausted, the gold starts to grow inhomogeneously and adhesion becomes worse. Depending on the flow direction of the solution during plating, a "shadow" behind the resist structures is visible in the gold layer, in particular at the edge of the chip. If the flow direction is reversed, the shadow forms on the other side. This problem is probably related to a change in bath chemistry, e.g. due to resist bleeding, although we have not tracked down the cause. It can be mitigated by reducing the flow speed of the plating solution, allowing for the fabrication of a few more chips. The problem can be reliably "solved" by purchasing a new bottle of plating solution.

- The plating solution is specified for temperatures of $55 - 65\,^{\circ}\mathrm{C}$, but we have observed rounding of the resist structures at temperatures $\geq 60\,^{\circ}\mathrm{C}$. This is a further indication that the solution attacks the photoresist.

- The bath has to be filtered after use. Particulate contaminations lead to defects on the chip.

- Uncontrolled voltage changes of the power supply (e.g. during turn on) have to be avoided while the chip is submerged in the plating solution. Reverse polarity, applied even for a short time, can prevent the growth of gold on the chip.

- Fresh aqua regia has to be used for etching the seed layer to avoid brownish deposits on the gold.

2.2.4 Insulating and planarizing polyimide layer

The purpose of the polyimide layer is to planarize the chip surface and electrically insulate the gold layers from each other. Polyimide has a thermal conductivity which is about three orders of magnitude smaller than that of gold or silicon. Therefore, the polyimide layer has to be as thin as possible to allow for large current densities in the wires of the upper gold layer.

As illustrated in Fig. 2.8, a layer of polyimide does not globally planarize a chip surface with an uneven topography. It rather acts as a "low-pass filter" which locally smoothes out the topography. Only features with a lateral extension smaller than the planarization length, which is $\approx 20\ \mu$m for our polyimide, can be fully flattened out [127].

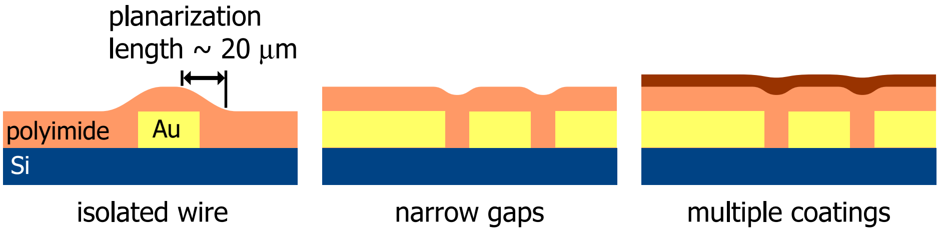

Figure 2.8: Planarization and insulation with polyimide. Narrow gaps are easier to planarize than broader, isolated features. Multiple coatings improve planarization.

We use the spin-on polyimide PI 2562 from HD Microsystems, which is specifically designed for planarization applications. The chip is spin-coated with the polyamic ester. Air bubbles in the coating have to be avoided by careful dispensing or manually removed before spinning. Curing of the polyimide is carried out at 200 °C in air and then at 350 °C in a nitrogen atmosphere.

The degree of planarization is higher for several thin coatings compared with a single thick coating of equal total thickness. We typically deposit three layers of 2.0 μm thickness, fully curing each layer before applying the next. For the first layer, an adhesion promoter is used (HD MicroSystems VM651). In Fig 2.9 we show AFM measurements of the polyimide surface topography above wires in the lower gold layer. Thin gaps (5 μm wide) between 5 μm thick wires are planarized to a step height of 300 nm, which is sufficient for our purpose.

Fully cured polyimide is resistant to solvents, most acids, and diluted piranha etch, but can be dry etched in an oxygen plasma [120]. If necessary, planarization can be improved by back-etching the polyimide [127]. The

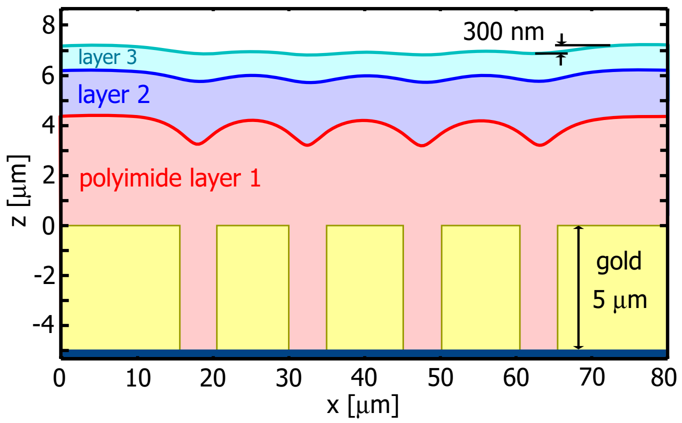

Figure 2.9: Planarization with polyimide. Surface topography of three polyimide layers above small gaps in the lower gold layer, measured with an AFM. Note the different scaling of the two axes. On this chip, the polyimide layers were 4.3, 1.9, and 1.0 μm thick.

polyimide layer protects the gold underneath and can be easily cleaned by wiping it off with acetone.

Polyimide has $\varepsilon_r = 4.2$ and $\tan\delta = 0.016$ at 10 GHz. Although dielectric losses are larger than for our substrate materials, we have successfully used thin layers of polyimide on our microwave chips.

As discussed in section 2.2.3, we found an incompatibility between electroplated gold wires on AlN substrates and the polyimide high temperature cure. On Si substrates, no such effect is observed. Still, the surface roughness of the lower gold layer increases slightly due to the high temperature.

2.2.5 Upper gold layer: lift-off metallization

We fabricate the upper gold layer with a lift-off metallization technique. In this technique, patterned resist acts as a mask for evaporated gold. After removal of the resist ("lift-off"), only the desired gold structures remain on the chip. Gold layers deposited by evaporation have smaller surface roughness than electroplated wires. This is important for the use of the upper gold layer as a mirror for the magneto-optical trap.

The lift-off sequence is illustrated in Fig. 2.10. We spin-coat the polyimide layer on our chip with a 1.6 μm thick layer of photoresist. We use the image reversal resist AZ 5214 E from Clariant, which allows one to create resist sidewalls with a negative slope ("undercut") for lift-off metallization. The resist is exposed for a few seconds with UV light through a mask which bears a negative image of the wires to be fabricated (a). Due to the small exposure

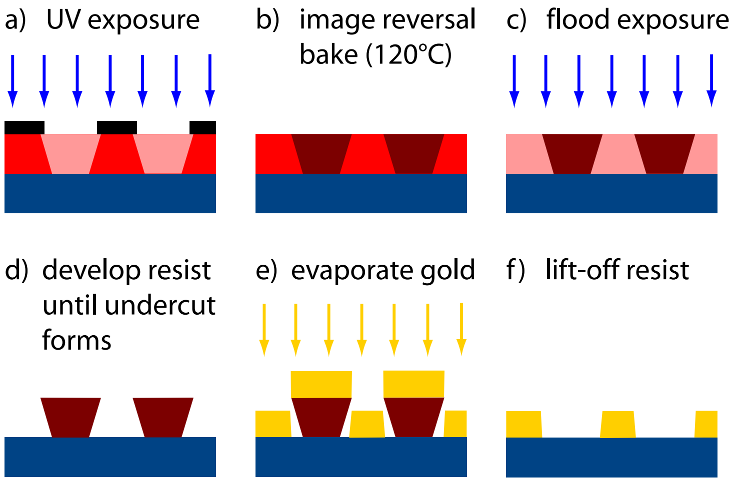

Figure 2.10: Lift-off sequence with an image reversal resist. Gold is deposited by e-beam evaporation. The process steps are explained in the text.

dose, the resist is not fully exposed down to the substrate. The exposed area is wider on the top than on the bottom of the resist layer, which will lead to a negative slope of the resist sidewalls after image reversal. The short exposure dose also helps to reduce loss of contrast due to diffuse reflections from the polyimide layer and the gold structures below it.

The image reversal bake on a hot plate at $120 \pm 1\,°\mathrm{C}$ cross-links the resist in the exposed areas and thus renders it insoluble in the developer and insensitive to further exposure (b). Subsequently, the chip is flooded with UV light (c), which now renders the previously unexposed areas soluble. These areas are removed during development (d). The development time is carefully adjusted so that the resist structures develop an undercut. Residues of photoresist are removed by a short oxygen plasma cleaning step. Subsequent baking of the resist structures on a hot plate was found to improve resist stability in the next step.

A 1 μm thick layer of gold is deposited on top of a 3 nm thick Ti adhesion layer by e-beam evaporation in a UHV evaporation chamber (e). The resist acts as a mask for the gold, the undercut prevents gold in the resist trenches from sticking to gold on top of the resist. The gold deposition rate should not exceed 1 Å/s and the undercut should not be too large to avoid collapse of the smallest resist structures during deposition. Lift-off is performed in a bath of hot acetone (f). This removes the resist and the gold on top of it and leaves behind the desired structures. If necessary, lift-off can be forced by agitation, with pliers, or by mild ultrasound.

For successful lift-off, the resist layer should be somewhat thicker than the thickness of the deposited gold layer. The resist undercut can be adjusted by changing exposure time, image-reversal temperature, and development time. In practice, once a suitable set of parameters has been found, we only adjust the development time for each series of chips. This adjustment is necessary, probably because of aging of the chemicals. A strong undercut can be seen in an optical microscope as a bright outline of the resist edges. However, for very small periodic structures, mechanical and thermal stability of the resist requires that development be stopped before the bright outline is visible. While developing the process, we checked the undercut with an electron microscope, see Fig. 2.11. However, we found that the electron beam bakes the resist to the polyimide layer, making lift-off difficult. We therefore use the electron microscope to check the undercut only on test chips.

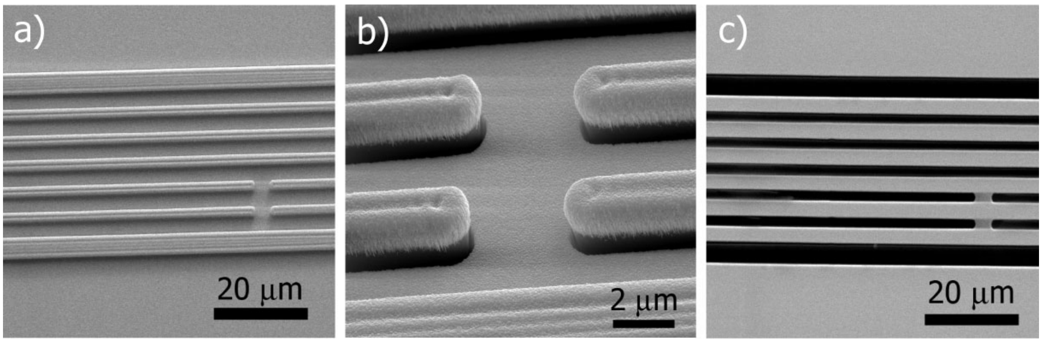

Figure 2.11: SEM images of the upper gold layer before and after lift-off. (a) Resist structure with deposited gold on top. (b) Close-up of (a), the undercut of the resist sidewalls is visible. (c) Gold structure remaining after lift-off.

Figure 2.12 shows wires on the upper gold layer. The smallest periodic wire arrays which we have fabricated consist of 2 μm wide and 1 μm thick wires separated by 2 μm gaps. The surface roughness is 3 nm RMS, measured with an AFM in a 2 μm × 2 μm window. As can be seen in Fig. 2.12(c), the smoothing of the surface topography provided by the polyimide layer enables the fabrication of micrometer-sized wires on top of larger gold structures.

After fabrication of the upper gold layer, it could be advantageous to passivate the chip surface by depositing a few nanometers of SiO_2. A thin SiO_2 layer could reduce the electric fields from Rb adsorbates on the surface, as discussed in section 1.9.3, without compromising the reflectivity of the gold mirror.

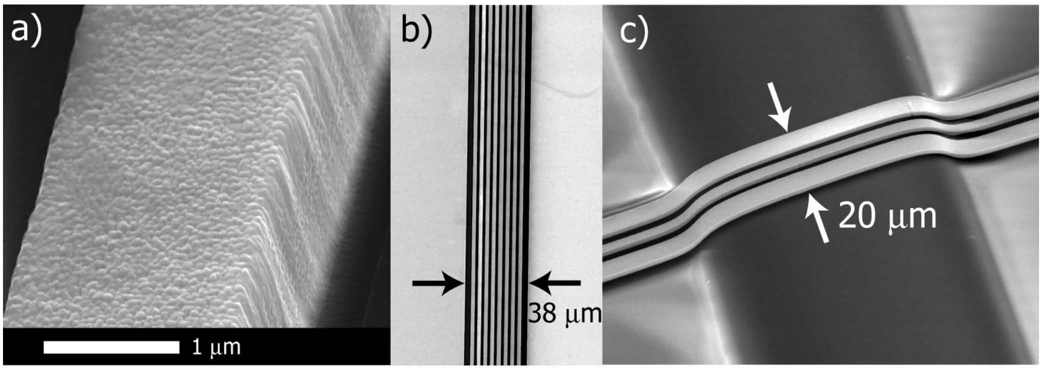

Figure 2.12: Wires on the upper gold layer of a two-layer chip. (a) Gold wire (1 μm thick and 1.7 μm wide) fabricated with the lift-off technique. The grain size of the evaporated gold is of the order of 100 nm. (b) Parallel wires fabricated according to the design in Fig. 2.1. Each wire is similar to the one shown in (a). (c) Small wires (800 nm thickness) on the upper gold layer cross a large wire on the lower gold layer. A single polyimide layer of only 4 μm thickness already provides sufficient smoothing of the underlying gold structure, which is 7 μm thick.

2.2.6 Chip dicing and bonding to the base chip

After the wire structures have been fabricated, the chip is cut to size with a diamond blade. This "experiment chip" is subsequently glued onto a "base chip", which serves as a carrier, heat sink, and electrical vacuum feed through (see section 3.1). Figure 2.15 shows an example of the complete atom chip package, fully bonded and connected.

The base chip consists of a single layer of electroplated wires on a 800 μm thick AlN substrate. AlN is preferred over Si because of its larger heat conductivity and better mechanical stability. The base chip wires are fabricated similarly to the wires on the lower gold layer of the experiment chip. The wires, which are designed to carry up to 10 A current, are electroplated to a thickness of 12 μm. The smallest structures on the base chip are $\approx$ 90 μm wide. We therefore use a simple lithography mask printed on an overhead transparency for this chip.

The base chip substrate has arrays of holes on each side, which are laser-cut by the company A.L.L. Lasertechnik before we fabricate the wires. The holes allow us to solder wires on the front side of the chip to pins of a connector fed through from the back side, using a 70In/30Pb reflow solder paste from Indium Corporation. A connector on the back side has the advantage that it does not inhibit optical access to the chip.

The experiment chip is glued onto the base chip using the UHV-compatible thermally conductive epoxy glue H77S from Epo-Tek, which is outgassed prior to application (see also section 3.1). The amount of glue used is important. Care is taken that the gap between the chips is completely filled with epoxy to avoid virtual leaks in the vacuum system. The glue layer should be as thin as possible for good thermal conductivity. Excess glue is wiped off prior to curing on a hot plate at 150 °C. The wires on the experiment chip are wire bonded to the base chip, using up to 15 gold bond wires per chip wire. To contact the wires on the lower gold layer of the experiment chip, the polyimide is scratched off above the contact pads.

2.3 Atom chips fabricated with this process

The development of the whole fabrication process took more than half a year of work. Now it takes about two days to fabricate a chip with a single gold layer and about one week to fabricate a two-layer chip. This enables us to try out new chip designs quickly, which proved to be extremely valuable in the development of chips with microwave guiding structures. With the process described above, we have fabricated the atom chips for two new experiments which are currently being pursued.

2.3.1 Chip for magnetic multi-well potentials

The first chip can be used to create a small array of magnetic potential wells for Bose-Einstein condensates. The potential wells, which can be individually addressed, are separated by tunable tunneling barriers. Experiments are currently underway in Jakob Reichel's group in Paris. Figure 2.13 shows pictures of this chip.

2.3.2 Microwave atom chip

The second chip can be used to study atoms in microwave near-field potentials, as described in chapter 5. Experiments with this chip are currently being pursued in our group in Munich. Figure 2.14 shows pictures of the experiment chip, Fig. 2.15 shows the chip as it is mounted on the base chip.

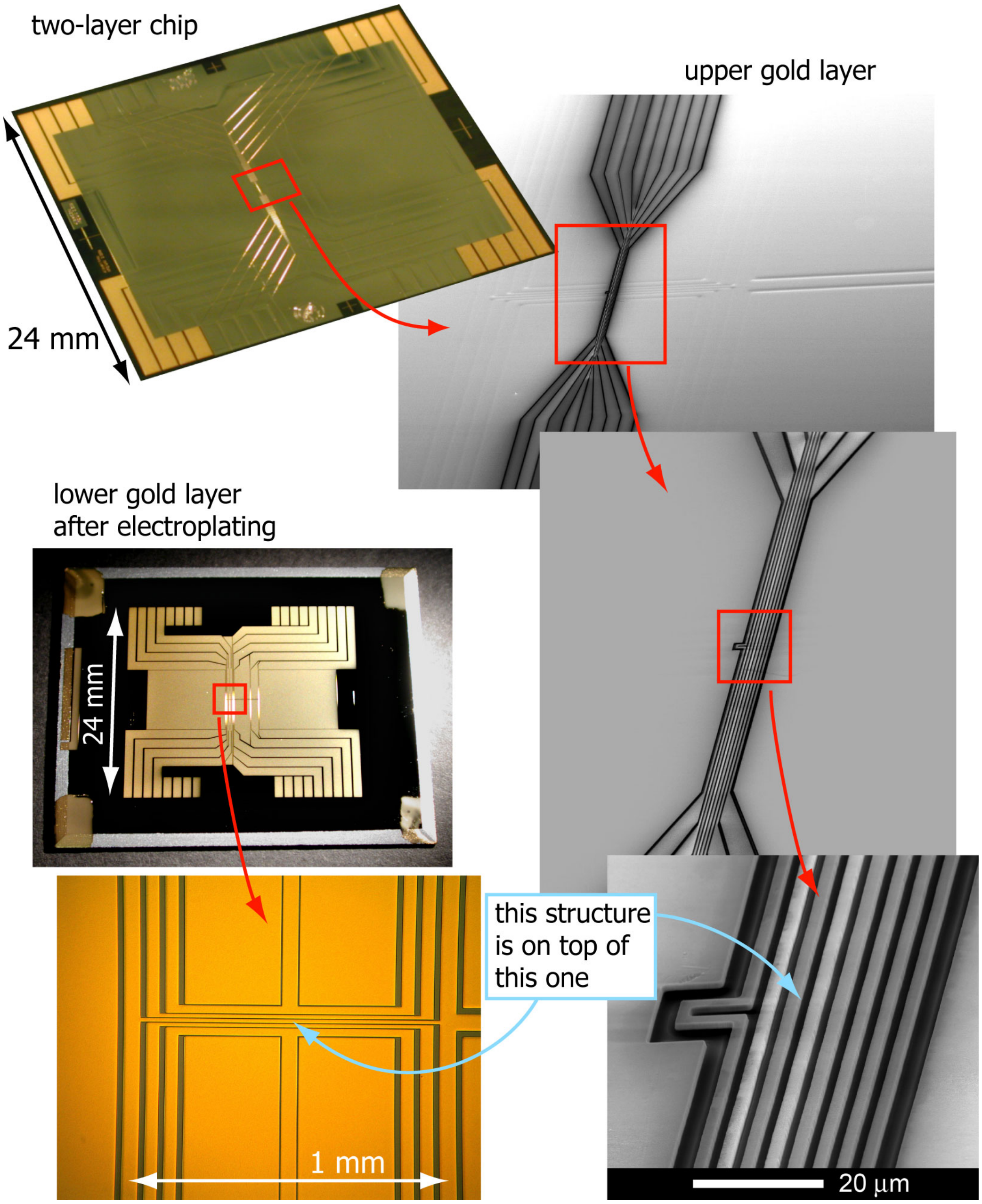

Figure 2.13: Atom chip for experiments with Bose-Einstein condensates in magnetic multi-well potentials.

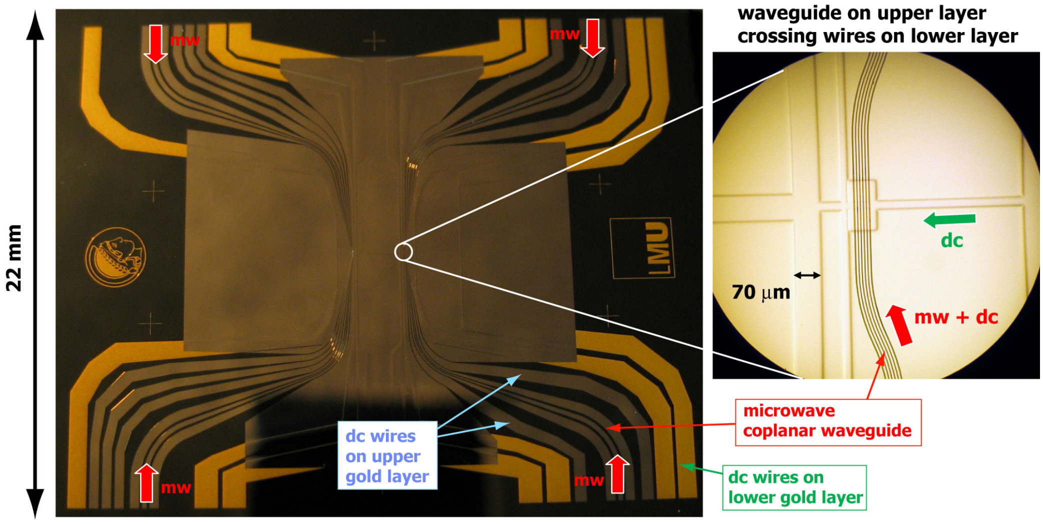

Figure 2.14: Atom chip for experiments with Bose-Einstein condensates in microwave near-fields.

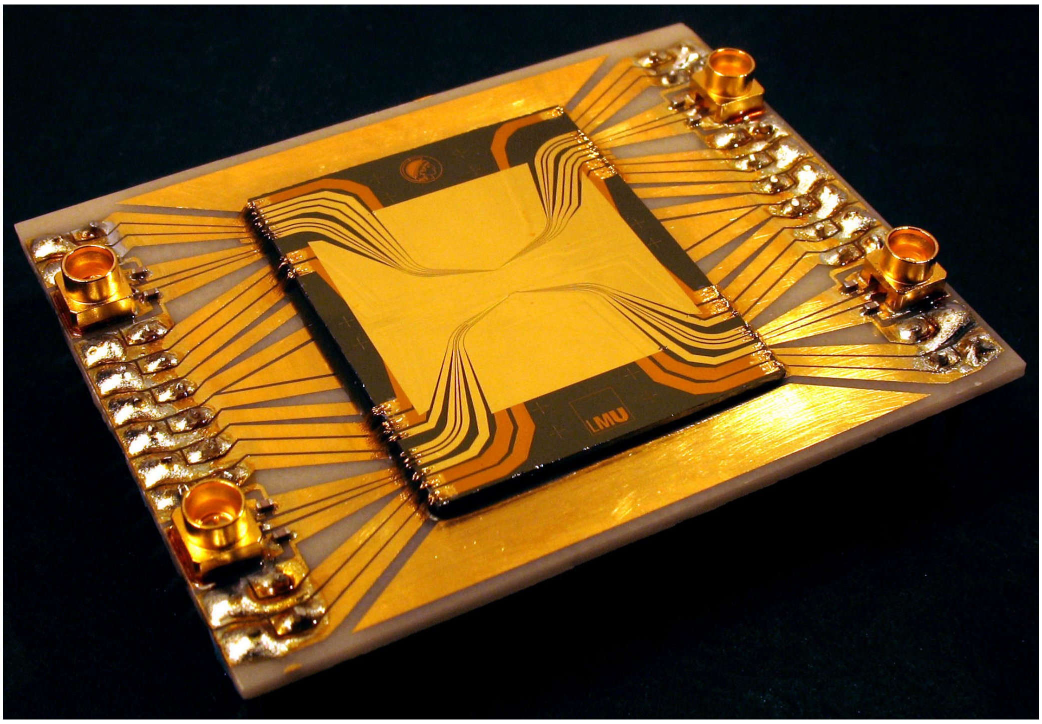

Figure 2.15: Microwave atom chip package. The experiment chip is glued and wire bonded to the base chip. Microwave connectors are soldered onto the front side of the base chip. The DC wires are soldered to pins from a connector on the back side.

2.4 Measurements of the critical current density

To avoid thermal breakdown of the wires, it is important to know the maximum current I_{max} a wire on the chip can support. We determine I_{max} by applying current pulses and recording the voltage drop across the wire, which yields the resistance R. Due to resistive heating, an increase in R is observed as a function of time and applied current. On test substrates, we increase the current until the wires are destroyed, which yields I_{max}. The duty cycle of the measurements is close to a realistic experimental situation, with current pulses of 3 s duration separated by cool-down intervals of 10 s.

Figures 2.16(a+b) show results of such a measurement for a small wire on the upper gold layer. The increase in wire resistance is clearly visible. For this micrometer-sized wire, $I_{\mathrm{max}} = 80$ mA, corresponding to a critical current density of $j_{\mathrm{max}} = 4 \times 10^{10}$ A/m^2. On the upper gold layer, j_{max} is limited by the relatively small heat conductivity of the polyimide. Due to the small total dissipated power, the substrate below the polyimide layer does not heat up significantly, the wire temperature reaches steady state after 200 ms. For a more detailed analysis of such measurements, see [115].

In Fig. 2.16(c+d), a similar measurement is shown for a larger wire on the lower gold layer. For this wire, $I_{\mathrm{max}} = 2.8$ A, corresponding to $j_{\mathrm{max}} = 6 \times 10^{10}$ A/m^2. The wire burns at its smallest constriction when the overall increase in R is still $< 50\%$, which can be explained by the relatively large contribution of the on-chip lead wires to R. This larger wire does not reach steady state during the current pulse, indicating heating of the substrate due to the large dissipated power of 30 W [115]. We have compared measurements on AlN and Si substrates for wires with similar dimensions, but found no significant difference in j_{max}, consistent with the comparable heat conductivities of these substrate materials.

Our measurements were carried out in air, with the substrate placed on the metal chuck of a probe station. Since heat transport from on-chip wires is dominated by conduction to the substrate rather than air convection or radiation, in particular for moderate wire temperatures and substrates with high thermal conductivity, our measurements give a reasonable estimate of j_{max} under vacuum conditions.

We tested the microwave guiding structures on our chip in a similar way, as described in section 5.3.3.

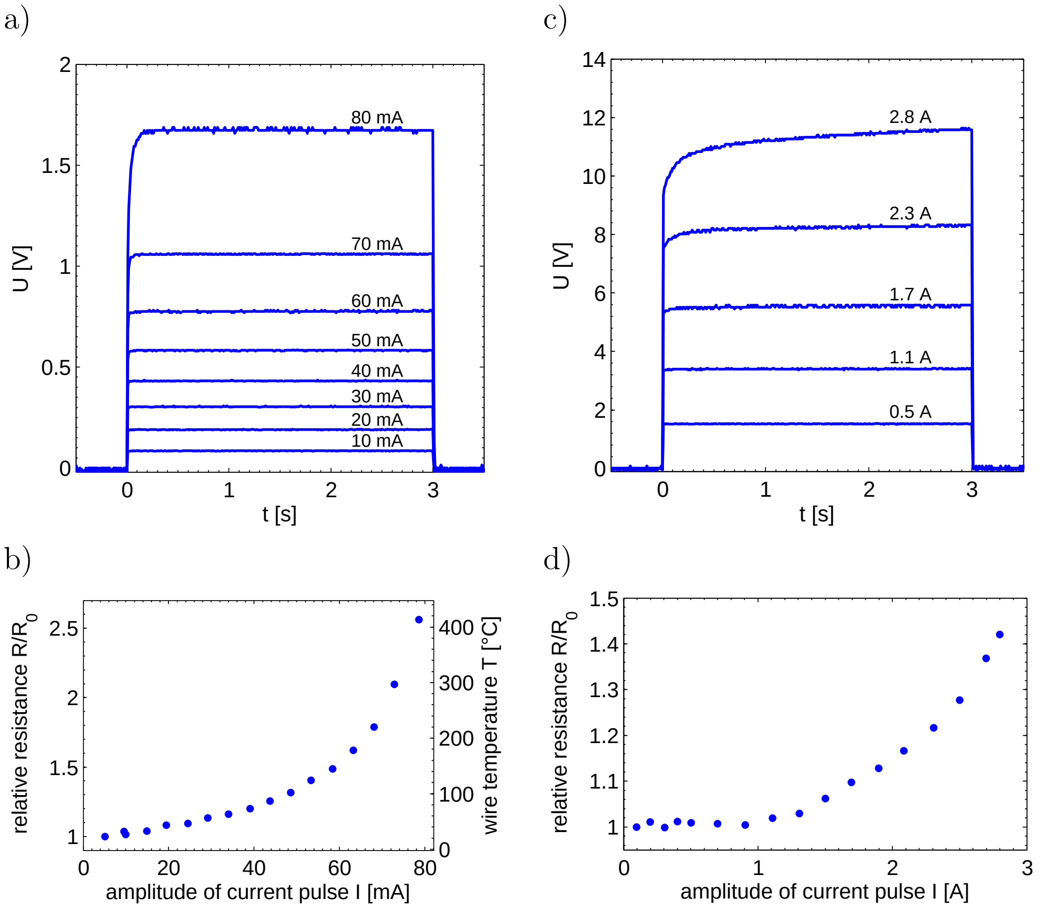

Figure 2.16: Measurements of resistive wire heating. (a) Voltage drop U across a gold wire of length $L = 500$ μm, width $W = 2.0$ μm, and thickness $T = 1.1$ μm on a 6 μm thick layer of polyimide. The amplitudes I of the applied current pulses are indicated. U includes the voltage drop across the lead wires. (b) Increase in relative resistance R/R_0 and inferred wire temperature T as a function of I for the wire in (a). R is determined at the end of the current pulse and corrected for the 2.6 Ω resistance of the lead wires, which we assume to be at constant temperature due to their much larger cross section. $R_0 = 7.4$ Ω is the wire resistance at room temperature. (c) Measurement similar to (a), but for a larger wire on a 725 μm thick Si substrate with 20 nm oxide. The smallest constriction in the wire has $L = 850$ μm, $W = 10$ μm, and $T = 4.5$ μm. The on-chip lead wires have $L = 10$ mm and $W = 40$ μm. The wire temperature does not reach steady state during the current pulse. (d) R/R_0 at the end of the current pulse ($R_0 = 2.6$ Ω). Here, the on-chip lead wires are included due to their small cross section.

Chapter 3

Experimental setup and BEC preparation

The experimental apparatus and a typical sequence for the preparation of a BEC on our chip are the subject of the present chapter. A BEC or a similarly prepared ultracold thermal ensemble with a temperature just above condensation serves as the starting point for the experiments described in subsequent chapters.

Our experimental apparatus consists of the atom chip, an ultrahigh-vacuum chamber of which the chip is an integral part, low-noise current sources connecting to the chip wires, Helmholtz coils for the generation of homogeneous magnetic bias fields, a diode laser system for laser cooling, a CCD camera for imaging of the atoms, radio-frequency electronics for evaporative cooling, and computers for experiment control and data analysis. These components are described in this chapter. The radio-frequency and microwave electronics involved in the coherent manipulation of the atoms' internal state are described in chapter 4. The techniques involved in guiding microwave near-fields on the chip are discussed in chapter 5.

Figure 3.1 shows the main part of our setup. In its present version, it contains the microwave atom chip, fabricated as detailed in chapter 2. The experimental work reported in this thesis also involves other chips in earlier versions of the setup. The experimental conditions and the techniques used for BEC preparation are similar in all cases.

A distinctive feature of our apparatus is the very compact single-chamber vacuum system where the chip substrate itself serves as one wall of a vacuum glass cell. This eliminates the need for bulky vacuum feed throughs for the up to 44 chip wires. Despite the fact that the vacuum seal is provided by epoxy glue and the whole experimental sequence from loading of the magneto-optical trap (MOT) to condensation takes place in the same cell, the pressure is sufficiently low for BEC and we measure magnetic trap lifetimes of several seconds. The detailed description of the glass cell and vacuum assembly is one emphasis of this chapter. A second emphasis is on the absorption imaging setup, which we have optimized to detect small atomic ensembles with very low noise in atom number.

In the following I assume the reader is familiar with standard experimental techniques used in BEC experiments — if not, see [128, 61] and references therein.

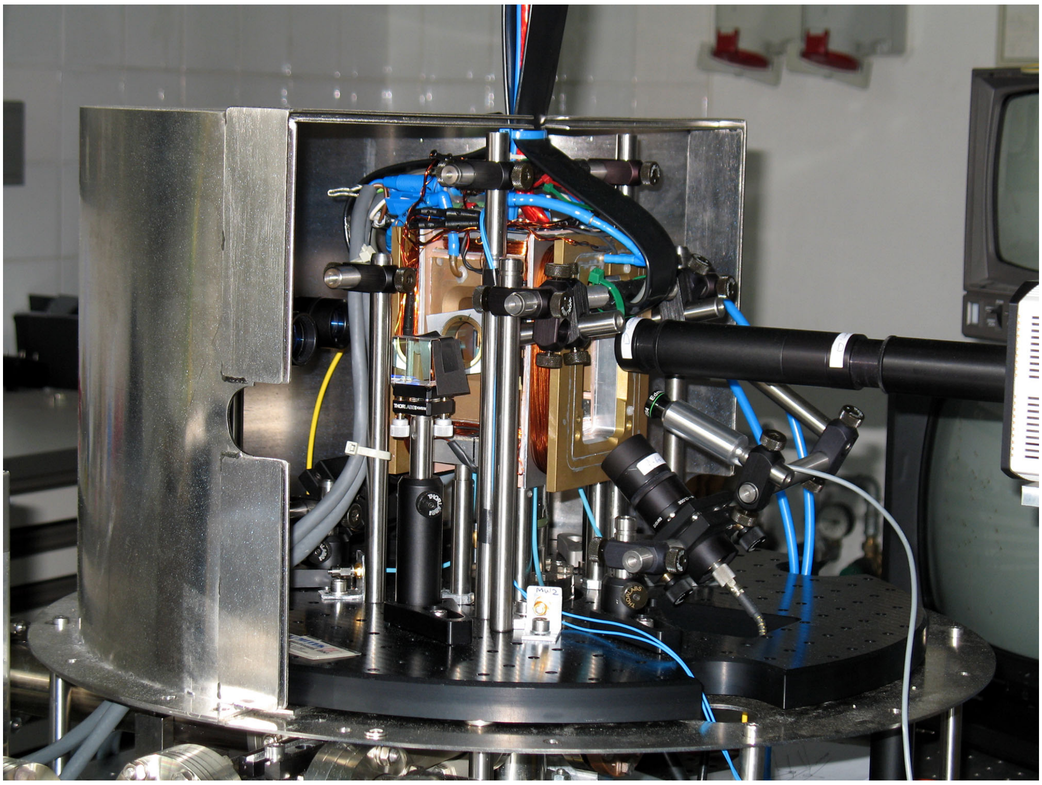

Figure 3.1: Main part of the microwave atom chip setup. Three pairs of Helmholtz coils surround the chip and glass cell assembly (see the close-up in Fig. 3.2). The laser beams for cooling and imaging are fiber coupled. The setup can be enclosed in a magnetic shielding measuring 50 cm in diameter. One half of the shielding is removed in the picture.

3.1 Compact glass cell vacuum system

Experiments with ultracold atoms require an ultrahigh-vacuum chamber to isolate the atoms from the environment. The magnetic trap lifetime is ulti-

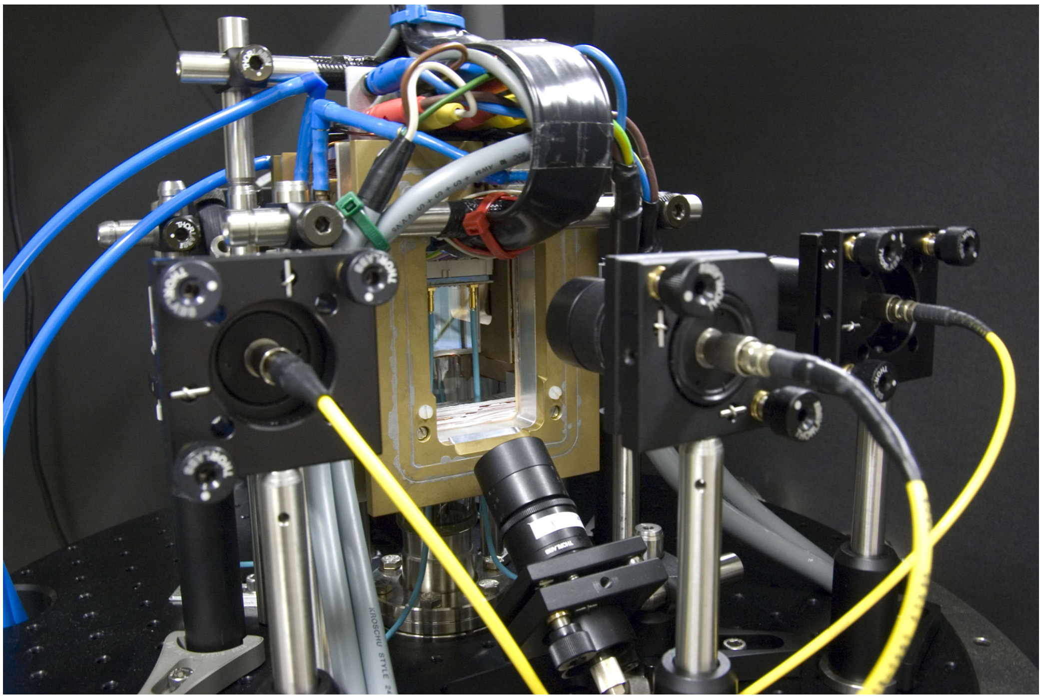

Figure 3.2: Close-up of the setup in Fig. 3.1. Chip and glass cell are visible between the Helmholtz coils.

mately limited by collisions of the trapped atoms with atoms from the residual gas. Already the first atom chip BEC experiments in our group [29, 129] showed that the tight confinement provided by magnetic chip traps reduces the cycle time of a BEC experiment from about one minute in standard non-chip setups to a few seconds in our setup. To achieve trap lifetimes of the same order, a single-chamber vacuum system with a background pressure in the 10^{-10} mbar range is sufficient. Compared with the earlier experiments in our group, we now use an even more compact vacuum system where the chip is directly glued to a glass cell so that the substrate itself serves as one wall of the vacuum chamber, as shown in Fig. 3.3. This technique, which was invented by D. Anderson and J. Reichel [35], is further optimized here. It eliminates the need for electrical feed through and intra-vacuum wiring to the chip. In our current experiment the chip has 44 wires, some of which carry microwave signals, so that compactness and easy access to the chip wires is of great benefit.

3.1.1 Chip and glass cell assembly

The fabrication of the atom chip is described in chapter 2. After the chip has been glued and bonded to the base chip, see Fig. 2.15, it is ready to be connected to the glass cell in which the whole experiment takes place. Figure 3.3 shows chip and glass cell fully assembled. For time-of-flight imaging the chip is oriented upside down so that the atoms fall away from the chip surface due to gravity if the trap is switched off. The whole assembly is glued together with the UHV-compatible epoxy 353ND from Epo-Tek (www.epotek.com). We always outgas the glue prior to application (30 min at $\approx 10^{-2}$ mbar) to remove air bubbles formed during mixing of the two components.

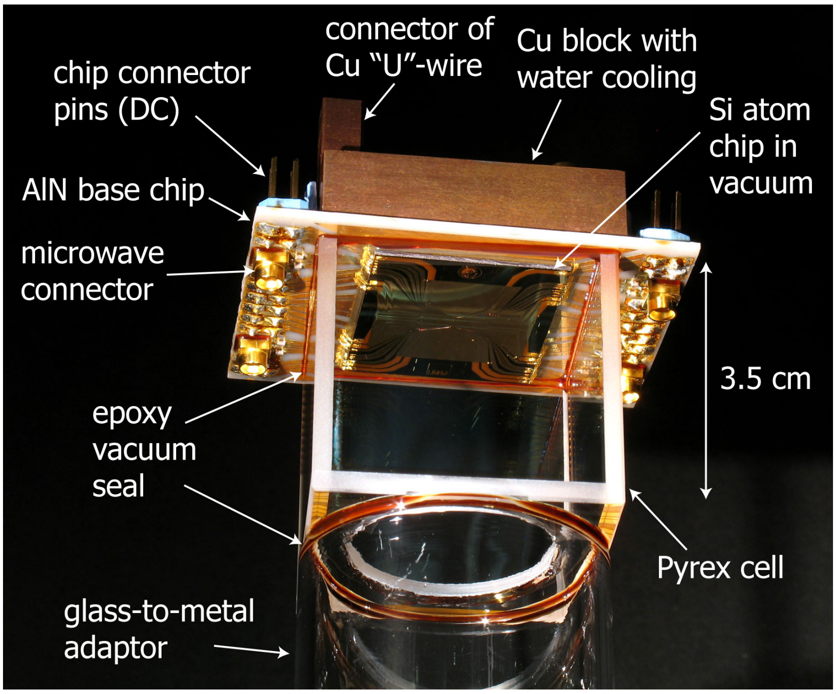

Figure 3.3: Atom chip and glass cell vacuum chamber.

The cubic glass cell (Hellma 704.027-BF, www.hellma-worldwide.de)[1] has an inner edge length of 3.0 cm. It is anti-reflection coated for 780 nm on the outside. We have either used cells made of crown glass or Pyrex. Pyrex has the advantage that its thermal expansion coefficient is smaller and better matched to that of the AlN base chip [23]. The cell is open on one face, this is where the chip will be attached. With a diamond drill we drill out a 23 mm diameter hole in the opposite face which will be attached to a

---

[1] We use a modified version, without the company label printed on the cell.

glass-to-metal adaptor (Caburn DN40CF Pyrex to stainless steel adaptor, www.caburn.co.uk). We polish the edge of the glass end of the adaptor to ensure it is flush with the glass cell face. After thorough cleaning, the two parts are glued together. The epoxy is cured at 150 °C, with temperature ramps of at least 1.5 h duration and ensuring a homogeneous temperature distribution.

In the next step, the chip is glued to the open face of the glass cell. We place the chip on a hot plate, supporting it with a metal block. Epoxy glue is applied to the polished edges of the glass cell, which is then placed on top of the chip in the desired place. We slightly rotate the glass cell with respect to the wire layout to avoid interferences of the laser between the uncoated inner glass cell walls during imaging. The glass cell is pressed against the chip only by the weight of the glass-to-metal adaptor. The amount of glue used in this step is important. A sufficient amount should be used to completely fill the gap between the mating faces. On the other hand, using too much glue should be avoided since excess glue forms a meniscus in the corner between glass and base chip, which can obstruct optical access to the experiment chip for beams parallel to the chip surface. If the experiment chip substrate is very thin, a spacer substrate glued between the experiment and base chips helps to avoid this problem. The curing schedule is critical. We first let the epoxy cure for two days at room temperature, during which it shrinks and turns yellow. The whole assembly is then covered with a metal cylinder and heated with the hot plate. The epoxy is fully cured in this "oven" by ramping within 1.5 h to a chip temperature of 150 °C, staying for 1 h at this temperature, and then ramping back to room temperature within 1.5 h. After this step the epoxy is hard and has a brown color. The glass cell is now ready to be flanged to the vacuum system.

The choice of the right glue and the curing schedule are critical for achieving vacuum pressures sufficient for BEC. According to the manufacturer, the epoxy 353ND shrinks a lot during cure. In earlier experiments this has led to cracks in the glass cell or at the interface between glass cell and chip. We now avoid this problem with the curing schedule described above which lets the epoxy adjust slowly at room temperature. The final cure at high temperature ensures good mechanical and vacuum properties. We have also tried to use a room-temperature curing epoxy instead of 353ND, however, some of the cells glued in this way had reduced vacuum long-term stability. With our new curing recipe, we have up to now fabricated three vacuum cells without any of the abovementioned problems.

In [130], a slow degrading of the vacuum has been reported for cells glued with Epo-Tek 353ND. We do not observe this problem. One of our glass cells glued with 353ND has been operated for more than four years at a pressure of

$< 5 \times 10^{-10}$ mbar. In [130] there is evidence that the reported short vacuum lifetime of about one month is related to a very intense UV flash lamp used to desorb atoms from the glass cell inner walls, which might degrade the epoxy. We use light bulbs for Rb desorption with much less power in the UV (see below), which seem to have no effect on the epoxy vacuum seal.

3.1.2 Vacuum chamber

Chip and glass cell are attached to a stainless steel ultrahigh-vacuum (UHV) chamber made of 35 mm tubing with DN40CF flanges, see Fig. 3.4. During the experiments, the pressure is maintained by a 40 l/s ion pump (Varian VacIon Plus 40 Diode) and a Ti-sublimation pump. The Ti pump is turned on about once every month by applying 35 A for 3 × 1 min to one filament. An ion gauge (Leybold Ionivac IE514 Extractor) reads the background gas pressure. A viewport on the bottom of the chamber provides additional optical access to the chip. Three Rb dispensers (see below) are attached to an electrical feed through.

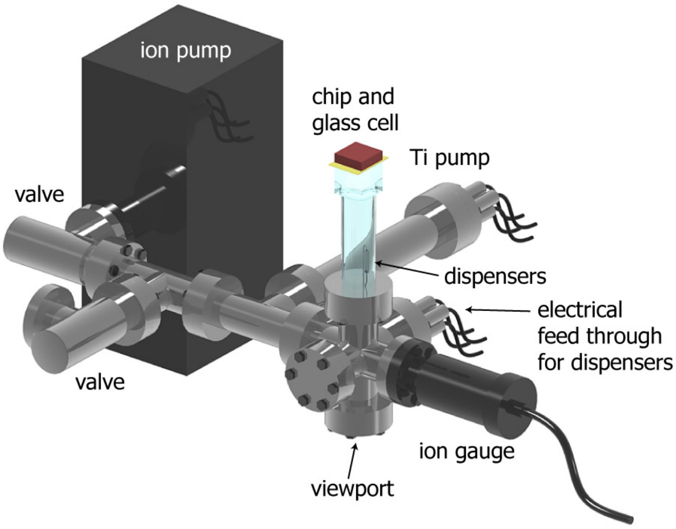

Figure 3.4: Vacuum chamber.

We bake out the vacuum system in two steps. First, the steel chamber is baked for about ten days at 200 °C with a blind flange attached instead of the glass cell. The ion pump is baked with the magnets in place. During initial pump down and bake out, the chamber is pumped by a turbo pump. After a pressure $< 10^{-7}$ mbar has been reached, the ion pump is switched on. During bake out we activate the Rb dispensers by slowly increasing the current to 5.0 A and operating at this value for 5 min. This procedure is repeated several times. A few 30 s long pulses to 6.0 A are applied as well. The Ti filaments are cleaned by applying 35 A for 1 min, repeated several times. During cool down of the chamber (one day), we continuously run 3.0 A through the dispensers to avoid that contaminants accumulate on them. After the system has reached room temperature and we have turned on the Ti-sublimation pump once again, the ion gauge typically reads 3×10^{-10} mbar.

We then flood the chamber with nitrogen and attach the glass cell. With the glass cell in place, the system is pumped down and a quick helium leak check is performed. Then it is baked out again for about ten days. Bake out temperatures in this second step are 110 °C at the chip and glass cell, 125 °C at the flange of the glass-to-metal adaptor, and 150 °C at the steel chamber. We try to maintain a homogeneous temperature distribution over the chip and glass cell and use slow temperature ramps (one day). The temperature at the glass cell is ramped up first and cooled down last. We again operate the dispensers and Ti filaments a few times as described above and leave the dispensers on during cool down. The pressure the ion gauge reads after the system has cooled down is almost identical to that after the first baking step, typically 3×10^{-10} mbar.

For our current experiments a further miniaturization of the steel part of the vacuum system is not necessary and was not attempted. In [35] it is shown that the vacuum system can be significantly miniaturized, and there is now a commercial company selling portable vacuum systems for atom chip experiments (www.coldquanta.com). This is very beneficial for future applications of atom chips e.g. as portable atomic clocks or inertial sensors.

Rb dispensers

As a source of atomic Rb we use three Rb dispensers which are placed inside the glass-to-metal adaptor. They are spot welded to Kapton-coated wires, which are connected to the electrical feed through and also serve as mechanical support for the dispensers. Two dispensers from SAES getters (Rb/NF/3.4/12 FT10+10, www.saesgetters.com) and one dispenser from Alvatec (Alvasource AS-RbIn-5-F, www.alvatec.com) are built into the chamber for redundancy. The SAES dispensers contain Rb chromate mixed with a reducing agent, the Alvatec dispenser contains a RbIn alloy. Both dispenser types release atomic Rb together with additional contaminants (“dirt”) when they are heated to a few hundred degrees Celsius by sending a current through them.[2] Rb is released only above a certain threshold current, whose value varies from one dispenser to the next and also depends on dispenser mounting. It typically lies between 2.5 and 3.5 A for the SAES dispensers. In the experiment, only one dispenser is used at a time, a few hundred mA above its threshold. We have observed in several experiments that the ratio of the Rb to dirt partial pressures increases, i.e. the dispenser improves if it has been operated for several weeks. Note that the ion gauge does not accurately measure the Rb pressure in the glass cell. Rb atoms stick to the walls very well and the Rb pressure can therefore vary substantially within the chamber. The quality of the vacuum near the chip is best determined by magnetic trap lifetime measurements, see below.

Light induced atom desorption

At low atomic densities and distances larger than several tens of micrometers from the chip surface, the lifetime of trapped atoms is limited by collisions with background gas atoms. The background gas consists of Rb atoms, whose partial pressure is a highly nonlinear function of the dispenser current, and other atomic species, whose density shows a weaker dependence on dispenser current. Both a large initial atom number and a long magnetic trap lifetime are needed for successful evaporative cooling to BEC. This implies a compromise between high Rb pressure during MOT loading and low Rb pressure during magnetic trap operation.

In a single chamber vacuum system this compromise is facilitated if the Rb pressure can be quickly modulated in time. One option to achieve this is to modulate the dispenser current [131]. However, it takes several tens of seconds until the dispenser has completely cooled off after a current pulse, which is longer than our experimental cycle of < 15 s. We therefore use light induced atom desorption (LIAD) in some of our experiments, which allows one to modulate the Rb pressure on a timescale of about one second [129, 29, 132]. In this technique, light from a 35 W halogen lamp (Phillips 13165) desorbs Rb from the walls of the vacuum chamber. The pressure is modulated by switching the lamp on and off. The Rb on the chamber walls is continuously replenished by running the Rb dispenser at a moderate constant current. Under typical experimental conditions, see below, the effect of the halogen lamp is to increase the MOT atom number by a factor of 3–5 without decrease in magnetic trap lifetime. This factor strongly depends on the Rb background pressure which is set by the dispenser current. The MOT can

---

[2] We normally use one of the SAES dispensers for the experiment. We have not yet thoroughly investigated the Alvatec dispenser, but first tests indicate that it unfortunately does not work better than the SAES dispensers.

be loaded by LIAD even if the dispenser is turned off. On the other hand, at very high dispenser current, LIAD is no longer effective in increasing the MOT atom number. One drawback of using LIAD is that shot-to-shot atom number fluctuations in the MOT are larger. Finally, we note that we have successfully created BECs both with and without using LIAD.

Ioffe trap lifetime as a function of dispenser current

To characterize the vacuum in the glued glass cell, we measure the lifetime of atoms in a Ioffe trap as a function of the dispenser current. Figure 3.5 shows such a measurement with atoms in a Ioffe Z-trap generated by a wire current of 2 A and a bias field of 10 G. The dispenser used for this measurement is typically operated at a current of 3.0 A, where we load about 1×10^7 atoms into the MOT with the help of LIAD, see section 3.7. Under these conditions, BEC preparation is possible without the need for carefully optimizing atom number in each step of the experimental sequence.

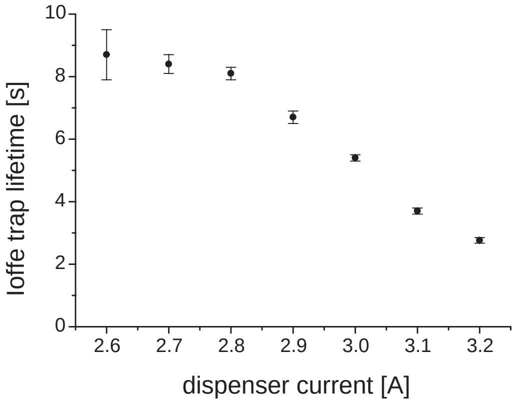

Figure 3.5: Magnetic trap lifetime in the glued glass cell as a function of dispenser current.

3.2 Laser system

Magnetic traps for neutral atoms are not deep enough to capture atoms directly from a room-temperature vapor. Typical microtrap depths for ^{87}Rb atoms correspond to temperatures of the order of 1 mK. Efficient trap loading therefore requires a laser-cooled atomic ensemble with a temperature in the microkelvin range [133, 134]. Chip-based magnetic traps which are sufficiently tight to hold atoms against gravity form at distances $\lesssim 1$ mm from the surface, where optical access from one half space is blocked by the chip. We therefore use a mirror magneto-optical trap (mirror MOT) in the first laser cooling stage, which can be operated sufficiently close to the surface [27, 21]. The atoms are further cooled in optical molasses [135, 136] to a temperature of 10 μK. To increase the loading efficiency, we optically pump all atoms into a weak-field seeking state before we switch on the magnetic trap. At the end of each experiment, the atoms are imaged by a laser beam onto a CCD camera. The details of trap loading and imaging of the atoms are described in more detail below. In this section I discuss the laser setup used for this purpose. Figure 3.6 shows the laser beams entering the glass cell.

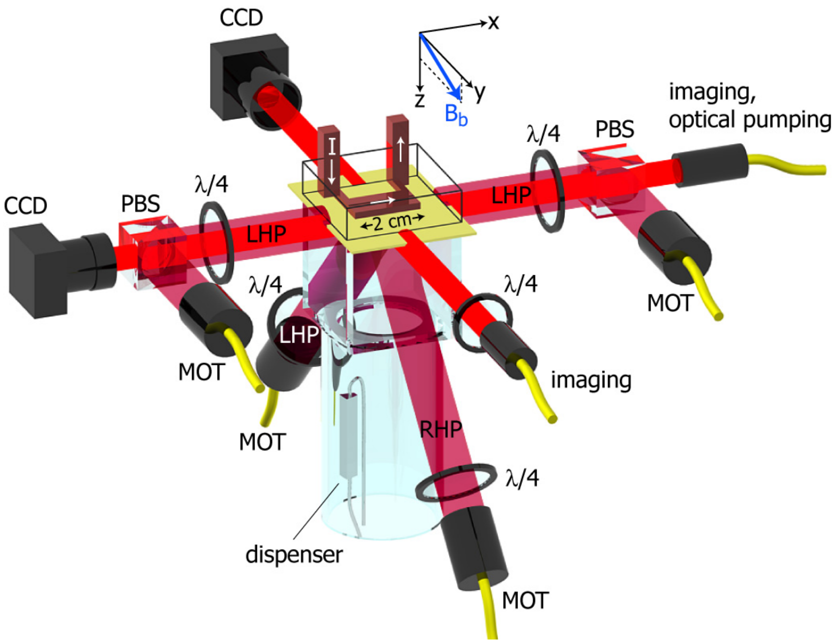

Figure 3.6: Laser beams for cooling, optical pumping, and imaging. All beams are guided to the experiment by optical fibers. Polarizing beam splitters (PBS), quarter wave plates ($\lambda/4$), cameras (CCD), and polarization of the four MOT beams are indicated. RHP (LHP) corresponds to right (left) handed polarization with respect to the beam propagation direction. The current I in the "U"-shaped copper structure behind the chip is used in combination with the homogeneous bias field B_b to generate the magnetic quadrupole field for the first mirror MOT stage. The outline of the water-cooled copper block is shown.

3.2.1 Mirror MOT

In a MOT, radiation pressure forces provided by red detuned laser beams result in viscous damping and cooling of the atomic motion. In addition, an inhomogeneous magnetic field is applied to make the light forces position-dependent and thus provide spatial confinement as well [137, 133]. The MOT can cool and trap atoms directly from a room-temperature vapor [138, 139]. A standard MOT requires six laser beams on three perpendicular axes. This configuration cannot be used to trap atoms close to the chip. A solution which was developed in our group is the "mirror MOT" [27, 21], where two of the laser beams are reflected from the chip surface, as shown in Fig. 3.6. The resulting total light field is similar to that of a six-beam MOT. The magnetic quadrupole field for the MOT can be generated by a "U"-shaped wire on or behind the chip in combination with a homogeneous field, as described in section 1.4.3. With a mirror MOT, the atoms can be trapped at distances < 1 mm from the surface. This enables loading of the magnetic microtraps without the need for magnetic transport by macroscopic coils.

The four mirror MOT cooling beams are circularly polarized and red detuned with respect to the $F = 2 \rightarrow F' = 3$ hyperfine transition of the ^{87}Rb D$_2$ line. Atoms in the MOT can be off-resonantly pumped by the cooling laser via other excited hyperfine states to the $F = 1$ ground state. To pump the atoms back into the cooling cycle, a repumping beam on the $F = 1 \rightarrow F' = 2$ transition is overlapped with the two cooling beams which are reflected from the chip. The same beams used for the MOT are also used (without the magnetic field) for sub-Doppler cooling in optical molasses.

Mirror on the chip surface

The chip surface has to be a highly reflective mirror for the mirror MOT. In some of our experiments, the experiment chip is coated in a replica technique [21] prior to wire bonding to the base chip. Either a homogeneous metal layer or a dielectric transfer coating from O.I.B. Jena (www.oib-jena.de) is used. This provides a very good mirror quality, although the wire structures are not perfectly planarized and their topography is still faintly visible in the reflected light. The disadvantage of this technique is that the additional layer of glue and coating of > 10 μm thickness on top of the chip makes it impossible to create traps with trap-wire distances $\lesssim 10$ μm. Furthermore, the layer would act as a dielectric overlay for the guiding structures on the microwave chip. For our most recent chips we have therefore chosen a layout in which the upper gold wire layer itself serves as the mirror, see chapter 2. In the chip center, the gaps between the wires are ≤ 5 μm wide. However, tapering of the microwave guides necessitates larger gaps in the outer chip regions, cf. Fig. 2.15. We observe a strong distortion of the MOT laser beams reflected from this chip. Nevertheless, the number of atoms trapped in the MOT is sufficiently large for BEC experiments.

Copper block with water cooling and U-wire

To generate the magnetic quadrupole field in the first MOT stage of the experiment, we use a “U”-shaped copper wire structure installed behind the chip, see Fig. 3.6. This structure can carry large currents (at least several tens of amperes). It replaces the bulky anti-Helmholtz coils used in the first MOT stage in our earlier experiments [27, 21]. This reduces the size of the apparatus without compromising MOT performance. Compared with on-chip wires, the large copper structure allows for a MOT with more atoms since it provides a magnetic field which is close to an ideal quadrupole in a larger region of space [140]. The “U”-shaped conductor is integrated into a water cooled copper block, which also serves as a heat sink for the chip. It is attached to the back side of the base chip after vacuum bake out, see Fig. 3.3, using heat-conductive paste and small drops of epoxy.

3.2.2 Diode laser system

Laser cooling, optical pumping, and imaging of the atoms requires laser light on the D_2 line of ^{87}Rb at 780.2 nm. Several beams driving different hyperfine transitions are needed, as shown in Fig. 3.7. This section briefly describes the setup used to generate laser light at these frequencies. A more detailed description can be found in [141].

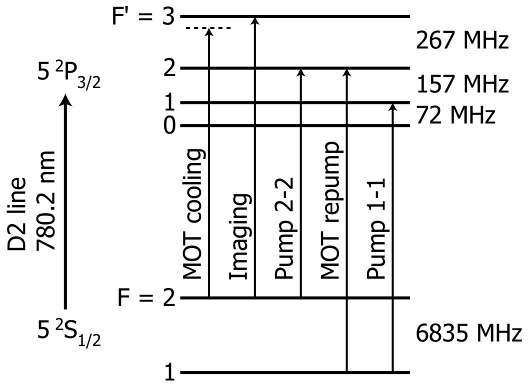

Figure 3.7: Level scheme of the ^{87}Rb D2 line [64] and laser frequencies used in our experiment.

All laser beams are derived from three frequency stabilized diode lasers for which we normally use Sharp laser diodes (GH0781JA2C) with a nominal output power of 120 mW.

The MOT cooling, imaging, and $F = 2 \to F' = 2$ optical pumping beams are derived from two lasers in master-slave configuration. The linewidth of the master laser diode is decreased with an external grating in Littrow configuration [142]. The laser is locked to the $F = 2 \to F' = (2, 3)$ crossover resonance in a Rb vapor obtained by Doppler-free saturation spectroscopy [143]. The error signal is generated in a lock-in technique by radio-frequency modulation of the laser current [144]. It is fed back to the piezo actuator controlling the grating position (integral path) and to the laser current (proportional path). Stabilized in this way, the laser has a linewidth of a few hundred kHz.

Part of the light of the master laser is used for the $F = 2 \to F' = 2$ optical pumping beam (see below). The other part is frequency shifted by a double-pass acousto-optic modulator (AOM) to near the $F = 2 \to F' = 3$ transition. The frequency of this AOM can be adjusted to set the detuning of the cooling and imaging beams from the atomic resonance. The double-pass configuration minimizes the beam deflection due to the change in frequency. The frequency shifted beam is injected into the slave laser diode, thus forcing it to lase at the same frequency. From the slave diode, the cooling and imaging light is derived. The master-slave setup has the advantage that the slave laser does not need to be grating stabilized and thus provides higher output power for the MOT beams. Furthermore, the beam pointing does not change if the AOM frequency is changed.

The third laser provides light for the MOT repumping and $F = 1 \to F' = 1$ optical pumping beams. It is stabilized in the same way as the master laser and locked to the $F = 1 \to F' = (1, 2)$ crossover resonance.

All beams are sent through additional AOMs to set their frequencies and for fast switching before they are guided to the experiment by polarization-maintaining optical fibers. Mechanical shutters in front of the fibers are used to completely block the beams during magnetic trapping.

- The **MOT cooling light** is split into the four beams required for the mirror MOT and each beam is coupled into a separate fiber. After the fibers, the beams are circularly polarized, have an e^{-2} beam diameter of 12 mm, and a power of about 3.4 mW in each horizontal beam and 8.5 mW in each of the two other beams. The frequency detuning $\Delta = \omega - \omega_a$ of the cooling and imaging beams from the $F = 2 \to F' = 3$ resonance at frequency ω_a can be varied from $\Delta = -16\,\Gamma$ to $+7\,\Gamma$, where Γ is the natural linewidth of the D2 line.

- The **MOT repumping** beam is resonant with the $F = 1 \rightarrow F' = 2$ transition. It is coupled into the fibers of the two MOT beams which are reflected from the chip. The power after each fiber is 1.2 mW.

- The **imaging beam** is split up and coupled into two separate fibers for imaging on two independent axes. After the fibers, both beams are circularly polarized and have an intensity of typically $I = 0.1\, I_s$, where I_s is the saturation intensity of the $|F = 2, m_F = 2\rangle \rightarrow |F' = 3, m'_F = 3\rangle$ transition.

- The two beams for **optical pumping** are resonant with the $F = 2 \rightarrow F' = 2$ and $F = 1 \rightarrow F' = 1$ transitions, respectively. They are coupled into one of the imaging beam fibers. After the fiber, the $F = 2 \rightarrow F' = 2$ beam has an intensity of 2 mW/cm^2, the $F = 1 \rightarrow F' = 1$ beam is about two orders of magnitude weaker.

Our laser system uses standard optical components and is already very simple and reliable. We have made no effort to further miniaturize it. Such a miniaturization has been demonstrated in [145], leading to a portable atom chip setup which weighs 150 kg, fits into a volume of 1 m^3, and runs on batteries.

3.3 Magnetic field coils, current sources, and magnetic shielding

Magnetic field coils

The glass cell is surrounded by three pairs of coils which generate homogeneous magnetic bias fields, see Fig. 3.1. The largest coils are for the bias field along y and have 60 windings of copper wire and an inductance of 0.67 mH per coil. The coil pair generates a field of 93 G at a current of 10 A. To reduce thermal drifts, the coils are water cooled from the outside. In favor of a more compact setup the bias coils could be replaced by suitable conductors, placed, e.g., on the base chip. This would allow for faster switching and probably also improve magnetic field stability, since the relative position of the wires is fixed by the substrate. However, the gradients of the wire fields would necessitate different calibrations of the generated bias field at different locations on the chip. For convenience we therefore use external coils as long as the stability and switching requirements are met.

Current sources

The magnetic field coils and the wires on the chip are driven by ultra-stable current sources. We have developed our own bipolar current sources which provide a maximum output current of $I_m = \pm 3$ A into a floating load with RMS current noise $\Delta I/|I_m| = 5 \times 10^{-6}$ in a frequency band of 0.3 Hz – 200 kHz. The current drifts on a time scale of 1 s – 1 h by $1 \times 10^{-5}\,|I_m|$ peak-to-peak. The current through a resistive load of 1 Ω, a typical value for a large chip wire, can be switched with full amplitude in 15 μs (10% - 90% of step size). A second version of the current sources provides a maximum output current of $I_m = \pm 5$ A. It is optimized for inductive loads and switches 5 A through a coil with an inductance of 0.9 mH in 0.6 ms. Details can be found in [141]. Where current stability and switching time are less critical, we use commercial current sources from FuG (www.fug-elektronik.de) and High Finesse (www.highfinesse.com).

Magnetic shielding

In the experiments described in chapter 4 we found that ambient magnetic field noise is one of the factors limiting the coherence time of internal-state superpositions. Furthermore, the atom number and temperature at the end of the RF-induced evaporative cooling process are sensitive to the magnetic field in the trap center [141, 146]. Ambient magnetic field noise leads to atom number fluctuations in the BEC, which prevented the reproducible preparation of BECs with atom numbers significantly below 10^3 in our experiments up to now.

To improve magnetic field stability in future experiments, our most recent apparatus has a removable magnetic shielding, see Fig. 3.1. The shielding is made of a single layer of high permeability material. Without shielding, we measure erratic drifts of the ambient magnetic field on a time scale of 1 min with an amplitude of typically 25 mG peak-to-peak.[3] Inside the shielding, the amplitude of the drift is reduced to 0.3 mG peak-to-peak [141].

3.4 Radio-frequency evaporative cooling

As of now, efforts to reach BEC by laser cooling techniques alone were not successful, and all BEC experiments rely on evaporative cooling in the final cooling stage [146]. Forced evaporative cooling of the atoms is performed by slowly lowering the trap depth. This allows atoms in the high energy tail of

---

[3] The drift is most likely caused by the nearby subway line.

the thermal distribution to escape the trap. The remaining atoms continuously rethermalize via elastic collisions to lower and lower temperatures. A requirement for evaporative cooling is that the collisional re-thermalization time of the atoms in the trap is much shorter than the trap lifetime. Tight microtrap potentials allow for very high atomic densities and thus high collision rates. This speeds up evaporative cooling, and consequently shorter trap lifetimes can be tolerated. This feature enables BEC experiments in the glued glass cell vacuum chamber, where the trap lifetime is of the order of a few seconds.

In a magnetic trap, evaporative cooling can be conveniently performed by driving spin-flip transitions to untrapped states with an oscillating magnetic field at radio frequency. Due to the inhomogeneous static magnetic field in the trap, the spin flips are energy selective. Atoms escape from the trap at the position where the RF is in resonance with the Larmor frequency in the local magnetic field. By sweeping the RF from high to low frequencies, the effective trap depth is lowered.

In our experiment, we apply the RF to a simple 5-turn coil of 3 cm diameter which is placed next to the glass cell. Several RF sweeps generated by different signal generators can be concatenated. Typical frequencies are in the range of $30 - 1$ MHz, sufficient power is provided by a 1 W amplifier.

3.5 Experiment control

The whole experiment is controlled by a computer equipped with several National Instruments digital and analog output cards (two PCI-6733, one PCI-6723, and one PCIe-6259). In total, 20 analog channels with a resolution of 16 bit, 32 analog channels with a resolution of 13 bit, and 48 digital channels are available. A time step size of 50 μs is usually sufficient in the experiment. The experimental sequence is composed and written into memory with a software originally developed by J. Reichel. Two additional computers control image acquisition of the CCD cameras. On these computers, a software written by W. Hänsel was used in the earlier experiments, now we use a MATLAB-based application written by P. Böhi.

3.6 Absorption imaging of small numbers of atoms

In our experiments, all data is taken by resonant absorption imaging [61]. In this technique, the shadow cast by the atoms in a beam of resonant laser light is imaged onto a CCD camera, see Fig. 3.8. The measurements reported in this thesis are performed on ensembles with small atom number $N \sim 10^3 - 10^4$, so that low noise imaging is required. Future experiments will require detection of even smaller ensembles, with a statistical uncertainty in the atom number determination which is smaller than $\sqrt{N}$, so that effects like atom number squeezing are observable. In this section I describe an imaging system which meets this requirement.

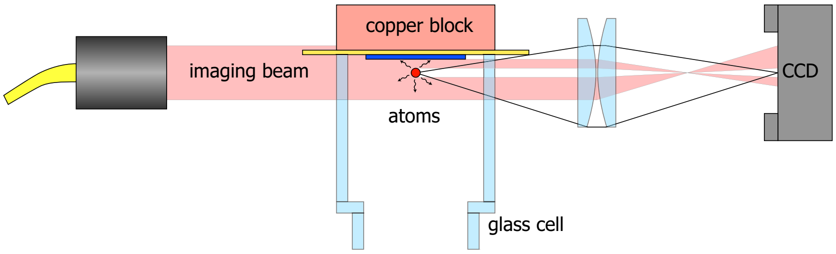

Figure 3.8: Schematic picture of absorption imaging.

Atom-light interaction

The atoms act as a medium of complex refractive index $n_r = \sqrt{1 + n\alpha/\varepsilon_0}$ for the imaging beam, where n is the density distribution and α the polarizability of the atoms. We image with σ^+ light on the cycling transition $|F = 2, m_F = 2\rangle \rightarrow |F' = 3, m'_F = 3\rangle$, which can be described as a two-level system. Assuming $n_r - 1 \ll 1$, the refractive index near resonance can be expressed as [61]

$$n_r = 1 + n \cdot \frac{3\lambda^3}{8\pi^2} \cdot \frac{i - \delta}{1 + \delta^2 + I/I_s}, \tag{3.1}$$

where $\delta = 2(\omega - \omega_a)/\Gamma$ is the detuning in half linewidths, $I_s = \hbar\Gamma\omega_a^3/12\pi c^2$ is the saturation intensity of the transition, and $\lambda = 2\pi c/\omega_a$. The imaginary part of n_r gives rise to absorption of the probe light.[4] The collimated imaging beam with transverse intensity distribution $I_0(x, y)$ is attenuated by the atomic cloud to $I(x, y) = I_0(x, y)\exp[-D(x, y)]$, where

$$D(x, y) = \int \sigma(x, y, z) n(x, y, z) dz \tag{3.2}$$

---

[4] The absorbed light is reemitted approximately isotropically. This emitted light could be used for fluorescence imaging. In the analysis of absorption images, the reemitted light is neglected, since only a small fraction of it is collected by the imaging optics. The phase shift of the light due to the real part of n_r could also be used for imaging, but the maximum achievable signal is lower than for resonant absorption imaging [61].

is the optical density of the atoms and

$$\sigma = \frac{\sigma_0}{1+\delta^2+I/I_s}, \quad \text{with} \quad \sigma_0 = \frac{3\lambda^2}{2\pi}, \tag{3.3}$$

is the scattering cross section, which in general depends on position through I. The largest signal is obtained by imaging on resonance, $\delta = 0$. We usually choose $I \ll I_s$ so that $\sigma \approx \sigma_0$ is a constant and the atomic column density can be determined as

$$\tilde{n}(x,y) \equiv \int n(x,y,z)dz = D(x,y)/\sigma_0. \tag{3.4}$$

The intensity distribution of the light in the plane of the atoms is imaged onto a CCD camera. In each run of the experiment, the camera takes two pictures, one with atoms, F_a, and one without atoms, F_r. Taking two pictures allows one to compensate for inhomogeneities in the intensity distribution of the imaging beam [61]. A third picture F_d taken about once a day without imaging light accounts for stray light and electronic offsets. The optical density is determined pixelwise as

$$D \equiv -\ln[I/I_0] = -\ln[(F_a - F_d)/(F_r - F_d)]. \tag{3.5}$$

From D, the number of atoms located in an area A in the plane of the atoms is calculated by summing over the pixels (i,j) corresponding to that area,

$$N \equiv \int_A \tilde{n}(x,y)dxdy = \frac{A}{\sigma_0} \sum_{(i,j)\in A} D_{ij}. \tag{3.6}$$

Imaging setup

We use the CCD camera Ap1E from Apogee, equipped with a Kodak sensor (KAF-0401E). The CCD has a quantum efficiency $Q_e = 0.35$ at 780 nm, a RMS readout noise of $\Delta N_r = 15\ e^-$/pixel, and an electronic gain of $g = 8\ e^-$/count. The pixel size is 9 μm × 9 μm. Two anti-reflection coated achromatic lenses with 2.5 cm diameter form the image on the CCD. The magnification is 3.5, so that a single pixel corresponds to an area $A_p = (2.6\ \mu\text{m})^2$ in the plane of the atoms. Two lenses provide higher spatial resolution than a single lens since the lenses we use are optimized for infinite conjugate ratio. The first lens is placed at a distance of 12 cm from the atoms. The measured spatial resolution of our imaging system is $x_i = 8\ \mu$m.

The imaging beam is usually oriented parallel to the chip surface. To image atoms at small atom-surface distance, the beam can be tilted by a few degrees towards the surface, so that both the atoms and their mirror image in the chip surface are visible [147]. This allows one to determine the atom-surface distance, which corresponds to half the distance between the two images, see section 4.6.

Figure 3.9 shows an absorption image of a BEC containing 2.51×10^3 atoms after 7 ms of time-of-flight (for BEC preparation, see section 3.7). The image is taken with an imaging pulse of intensity $I = 0.04\, I_s$ and duration $\tau = 200\ \mu$s. The small ensembles we detect in time-of-flight always have $D < 1$.

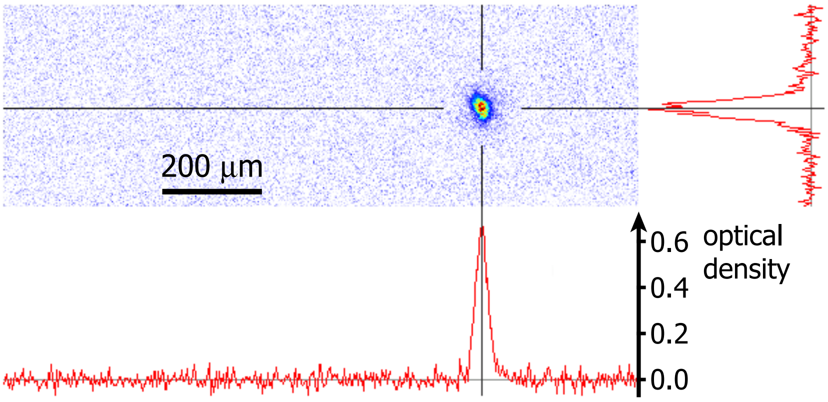

Figure 3.9: Absorption image of a BEC. The noise on the image is dominated by photon shot noise. The cross sections are 3 pixels wide.

Noise in absorption imaging

The predominant source of noise in most absorption imaging setups are interference fringes in the imaging beam with high spatial frequency, caused by diffraction from the chip surface, from dirt on the optics, and by reflections from the various optical surfaces in the beam path. In the presence of mechanical vibrations, these fringes are cancelled out incompletely by the normalization procedure described above, because their position is fluctuating between F_a and F_r. We have put substantial effort into eliminating this source of noise in our experiment. To suppress vibrations, all optical elements are supported by robust mounts, the mechanical shutter and the fan of the camera are disabled. The dark count rate of the CCD is low enough so that it does not have to be cooled below ambient temperature. We minimize the number of reflecting surfaces by taking out all uncoated windows inside the camera.[5] Fringes due to reflections from the glass cell are avoided by tilting the imaging beam with respect to the cell windows. Although there are still some fringes in the imaging beam, probably caused by the lens surfaces, they are stable and do not show up in the optical density.

The remaining noise in Fig. 3.9 is actually dominated by photon shot noise, which is the fundamental limitation of signal to noise in absorption imaging. On average, each pixel is hit by

$$\langle N_p \rangle = I A_p \tau / \hbar\omega = 3.5 \times 10^3 \tag{3.7}$$

photons, creating

$$\langle N_e \rangle = Q_e \cdot \langle N_p \rangle = 1.2 \times 10^3 \tag{3.8}$$

electrons (all numbers given are for the parameters of Fig. 3.9). The RMS noise in the detected number of electrons per pixel is

$$\Delta N_e = \sqrt{(\Delta N_s)^2 + (\Delta N_r)^2 + (\Delta N_o)^2} \approx \Delta N_s = \sqrt{\langle N_e \rangle} = 35, \tag{3.9}$$

where we have assumed that photon shot noise ΔN_s dominates over readout noise ΔN_r and other noise contributions ΔN_o, as is the case for our imaging system. For $D < 1$, the images F_a and F_r show relative fluctuations in the counts per pixel[6] of comparable magnitude, $\Delta F_a / \langle F_a \rangle \approx \Delta F_r / \langle F_r \rangle \approx \Delta N_e / \langle N_e \rangle$. The expected noise in the optical density on a single pixel is thus

$$\Delta D = \sqrt{2} \cdot \Delta N_e / \langle N_e \rangle = \sqrt{2 / \langle N_e \rangle} = 0.04, \tag{3.10}$$

where the factor $\sqrt{2}$ accounts for the uncorrelated shot noise on F_a and F_r. We indeed observe noise with $\Delta D \approx 0.04$ on the camera pixels. The observed ΔD corresponds to noise in the detected atom number per pixel of

$$\Delta N = (A_p / \sigma_0) \Delta D = 1.0. \tag{3.11}$$

If we integrate over k pixels, which corresponds to replacing the area A_p by $A = kA_p$ in Eqs. (3.7–3.11), the noise increases. For photon shot noise limited atom detection, one expects $\Delta N \sim \sqrt{k}$. We observe a somewhat faster increase with k for $k > 10$, indicating residual technical noise. The actual uncertainty in the detected atom number depends on how well the atoms are localized. For the cloud in Fig. 3.9, which is detected in time-of-flight, we have $k = 410$ and a statistical uncertainty in the detected atom

---

[5] To protect the CCD, the window directly in front of it should be replaced with an anti-reflection coated window rather than just taken out.

[6] Note that the amplifier gain g enters the number of counts registered on the pixels as $N_c = N_e / g$, but drops out of the optical density or signal-to-noise, because it amplifies all signals in the same way.

number of $\Delta N = 30$. This uncertainty is already somewhat smaller than the uncertainty of $\sqrt{N} = 50$ which would be required for the detection of atom number squeezing in the BEC of Fig. 3.9.

The noise in atom number can be reduced by detecting the cloud directly after release from the trap, so that it is better localized. However, the expansion of the cloud during to the imaging pulse still has to be taken into account. The area over which the atoms are spread out at the end of the pulse can be estimated to

$$A = x_i^2 + x_0^2 + (v_0\tau)^2 + \frac{\sigma_0 I}{3\hbar\omega} v_r^2 \tau^3, \tag{3.12}$$

where x_i is the spatial resolution of the imaging system, x_0 is the initial size and v_0 the velocity spread of the cloud. The last term takes into account the transverse blurring of the cloud due to the random photon recoils during scattering of imaging light [61, 148]. On average, each photon scattering event changes the atomic velocity by $v_r = h/m\lambda$. Another issue is the displacement of the atoms along the imaging beam, $d = (\sigma_0 I/2\hbar\omega)v_r\tau^2$, which has to be smaller than the depth of focus of the imaging system. Taking these effects into account, the statistical uncertainty in the detected atom number is $\Delta N = 4$ for a small BEC imaged with our setup directly after release from the trap, with $I/I_s = 0.04$ and $\tau = 200\ \mu$s which yields $A = (12\ \mu\text{m})^2$. Systematic errors in atom number determination due to uncertainty in δ or I are estimated to a few percent of the detected N.

A theoretical optimization of signal to noise shows that resonant absorption imaging can barely reach single atom detectivity [148]. Improvements towards this goal are to use a lens which provides higher spatial resolution, a CCD with higher Q_e, and a shorter imaging pulse at $I \simeq I_s$. In this case, a careful calibration of intensity is necessary [149].

3.7 Experimental sequence for BEC

In this section I describe a typical experimental sequence for BEC preparation. The quoted numbers are taken from our first BEC in a glued glass cell. The chip used in this experiment was fabricated by B. Lev [111]. Similar experimental sequences are employed in our other experiments. For a detailed discussion of BEC on an atom chip, see also [129, 29].

3.7.1 Mirror MOT

In the first stage of the experiment, we collect atoms in a mirror MOT from a Rb vapor. A constant Rb background pressure is maintained by one of the SAES dispensers at a continuous current of typically 3.0 A. The ion gauge reads 5.7×10^{-10} mbar while the dispenser is on. The choice of the dispenser current involves a compromise between magnetic trap lifetime and atom number. At this dispenser current, we observe magnetic trap lifetimes of typically 6 s. The experiment involves three MOT stages:

1. The first MOT is optimized to collect as many atoms as possible. We therefore operate it at a relatively large atom-surface distance of 3 mm. The magnetic field gradient is ≈ 10 G/cm in the strongest direction, the detuning of the cooling beams from resonance is $\Delta = -1.9\,\Gamma$. We modulate the Rb pressure by LIAD with a halogen lamp. The light is switched on at the beginning and switched off again 0.8 s before the end of the MOT loading stage. After 8 s of loading in this way, the MOT typically contains 1.0×10^7 atoms.

   The quoted MOT atom number was obtained on a chip with a dielectric mirror coating, the magnetic field gradient of the first MOT was provided by external coils. We achieve similar MOT atom numbers on the microwave atom chip (Fig. 3.3) where the upper gold wire layer serves as the mirror and the "U"-shaped copper structure provides the quadrupole field [141]. If instead a smaller "U"-shaped wire on the chip is used for the first MOT, the atom number is smaller.

2. In the second MOT stage the atoms are quickly moved closer to the chip surface. We switch off the quadrupole field of the first MOT and switch on a quadrupole field generated by a current in a "U"-shaped wire on the base chip in combination with a bias field (cf. Fig. 1.5). The wire is 1 mm wide and the length of the central part of the "U" is 1 cm. Using a chip wire at this stage has the advantage that the MOT position is well defined with respect to subsequent magnetic traps. During magnetic field switching, the laser beams are turned off for 2 ms. After switching, the MOT is ramped within 25 ms to a distance of 0.6 mm from the surface by decreasing the wire current from 7.0 A to 2.4 A at a bias field of 3.1 G. This also compresses the MOT by increasing the field gradient. The MOT steady-state atom number at the new position is much lower than the number of atoms which can be transferred from the first MOT, therefore the duration of this stage and the next should not exceed several tens of ms.

3. In the third MOT stage, the MOT density is increased and the temperature is decreased by increasing Δ by a few Γ for the duration of a few milliseconds.

3.7.2 Optical molasses

At the end of the MOT stage, the laser beams and all magnetic fields are switched off. After the magnetic fields have decayed, we switch the cooling and repumping beams back on for a 4 ms long stage of optical molasses cooling, at lower intensity of the cooling light and a detuning of $\Delta = -12\,\Gamma$. This reduces the temperature of the atoms to 10 μK.

Low molasses temperatures can only be reached if the ambient magnetic fields are properly zeroed. This is achieved by a variant of Hanle spectroscopy. Our technique involves absorption imaging of the atoms with the circularly polarized $F = 2 \rightarrow F' = 2$ optical pumping beam. The repumping light is turned on simultaneously to avoid optical pumping to $F = 1$. We scan the magnetic field components transverse to the pumping beam with a constant longitudinal field applied. The detected atom number has a minimum if the transverse components are zero because of optical pumping of the atoms into a dark state. We then scan the longitudinal field component with a constant transverse field applied. The detected atom number has a maximum at zero longitudinal field because the dark state ceases to exist. After a few iterations of this process, the ambient fields are zeroed to about 20 mG, which corresponds to their temporal drift in our laboratory.

3.7.3 Optical pumping

Before we switch on the magnetic trap we optically pump the atoms into the desired hyperfine sublevel.

- To prepare the atoms in $|F = 2, m_F = 2\rangle$, we switch on the $F = 2 \rightarrow F' = 2$ pumping light and the repumping light simultaneously for 200 μs. During pumping, a magnetic field of 1.5 G is applied, whose direction is chosen such that the pumping beam has σ^+ polarization with respect to the field.

- Alternatively, the atoms can be prepared in $|F = 1, m_F = -1\rangle$ by switching on the $F = 2 \rightarrow F' = 2$ and $F = 1 \rightarrow F' = 1$ pumping beams simultaneously, but not the repumping light. In this case, the magnetic field is oriented such that the beams have σ^- polarization.

The pumping efficiency is close to unity for $|2, 2\rangle$ and somewhat lower for $|1, -1\rangle$, the scattering of photons during pumping increases the temperature of the atoms to 13 μK. At this stage, the cloud contains about 80% of the atoms from the first MOT.

3.7.4 Magnetic traps and evaporative cooling

After optical pumping, the magnetic trapping fields are turned on fast compared to the atomic motion but slow compared to the Larmor precession frequency, so that the atoms remain spin-polarized. We maximize the transfer efficiency by optimizing the position of the last MOT. For small numbers of atoms in $|2,2\rangle$, the transfer efficiency is above 90%, indicating a very high optical pumping efficiency. For larger atom numbers, the transfer efficiency drops, because the size of the laser-cooled atomic cloud exceeds the magnetic trap volume. For the above parameters and atoms in state $|2,2\rangle$, the first magnetic trap contains 5.4×10^6 atoms after a holding time of 200 ms at a distance of 500 μm from the surface. In the experiment described here, the first trap was a quadrupole trap,[7] generated by a current of 3 A in a "U"-shaped wire of 1.6 mm length and a bias field of 8 G. Within 300 ms, about 5×10^6 atoms were transferred from this trap into a Ioffe Z-trap (trap Z1, see Fig. 3.10 and Tab. 3.1), where they had a temperature of 70 μK. In our other experiments, comparable atom numbers were directly loaded into a similar Ioffe Z-trap.

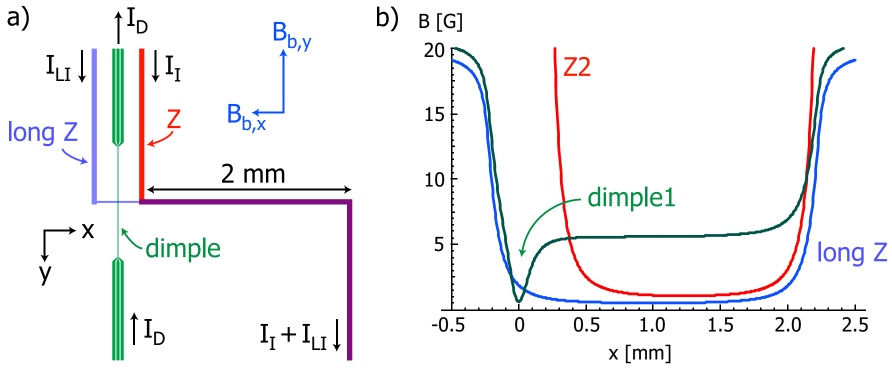

Figure 3.10: (a) Wire layout of the Ioffe traps used for evaporative cooling. The Z-wire is 50 μm wide. The long Z-wire has a section of 20 μm width at the position where the dimple wires cross. The dimple trap is formed by three 3 μm wide parallel wires, each carrying a current $I_D/3$. All wires are in a single gold layer of 4 μm thickness on an AlN substrate. (b) Trapping potentials for some of the traps listed in Tab. 3.1. The magnetic field minimum in the yz-plane is shown as a function of x. In the yz-plane, the trapping potentials are harmonic near the trap center.

---

[7] This has only historical reasons. The chip was originally designed for a different purpose.

Step	Δt	I_I	I_{LI}	I_D	$B_{b,x}$	$B_{b,y}$	d	f_1	f_2	f_3	B_0	ν_{RF}
	[ms]		[A]			[G]	[μm]		[kHz]		[G]	[MHz]
Z1	10	2	0	0	0	10.8	350	0.028	0.40	0.41	1.2	
ramp	250	2	0	0	$\downarrow$	$\downarrow$						
Z2	1500	2	0	0	0.8	55	70	0.017	8.6	8.6	1.1	$30 \rightarrow 8.5$
ramp	150	$\downarrow$	0	0	$\downarrow$	$\downarrow$						
Z3	3	1	0	0	0.4	20	100	0.013	3.2	3.3	0.6	
ramp	50	$\downarrow$	$\downarrow$	0	0.4	20						
long Z	1	0	1	0	0.4	20	100	0.009	3.4	3.4	0.5	
ramp	150	0	1	$\downarrow$	$\downarrow$	20						
dimple1	1000	0	1	0.3	5.5	20	90	0.42	4.1	4.1	0.5	$4 \rightarrow \nu_{\mathrm{stop}}$
ramp	50	0	1	0.3	5.5	$\downarrow$						
dimple2	5	0	1	0.3	5.5	8	170	0.12	0.37	0.42	4.1	

Table 3.1: Sequence of Ioffe traps created with the wires in Fig. 3.10. Duration Δt, trap-wire distance d, trap frequencies f_i, magnetic field in the trap center B_0, and radio frequency for evaporative cooling ν_{RF} shown in addition to wire currents and bias fields. Arrows indicate smooth parameter ramps. All magnetic field ramps are adiabatic with respect to the atomic motion.

Evaporative cooling in a dimple trap

Evaporative cooling to BEC is performed in the sequence of Ioffe traps shown in Fig. 3.10 and Tab. 3.1. The goal of this sequence is to reach the BEC phase transition directly in the dimple trap where subsequent experiments take place. If the BEC was prepared at a different location on the chip (e.g. in the trap Z2) and then transported into the dimple trap, problems with heating and excitation of dipole oscillations would arise. Direct loading of the dimple trap with laser-cooled atoms is not an alternative, because the dimple is created by very small wires and its trapping volume is too small to capture a sufficiently large number of atoms. Our solution is to first capture atoms in a large-volume Z-trap and pre-cool the ensemble in a first evaporative cooling stage until it is cold enough to fit into the dimple. After the transfer, a second evaporative cooling stage cools the atoms in the dimple and thus prepares the BEC at the desired location.

In detail, the sequence proceeds as follows: After the atoms have been captured in trap Z1, the trap is compressed adiabatically to increase the elastic collision rate and thus enable fast evaporative cooling. The initial temperature of the ensemble in the tight trap Z2 is around 450 μK. A first RF sweep for evaporative cooling is applied. At the end of this sweep, 8×10^5 atoms are left, the temperature is 130 μK. The Z-trap is decompressed (Z3), mainly to decrease the current in the Z-wire. Subsequently, the wire current is switched from the Z wire to the long Z wire (long Z). The decrease in wire current is necessary because the long Z wire has a narrow section and cannot carry currents as high as the Z wire. The narrow section of the long Z wire is crossed by wires which can be used to create the dimple trap. After the dimple has been turned on (dimple1), a second RF cooling sweep empties the plateau-like part of the potential and transfers all atoms into the dimple. BEC is reached if the final RF frequency $\nu_{\rm stop}$ of this sweep is lowered to about 70 kHz above the dimple trap bottom.

3.7.5 Time-of-flight and absorption imaging

The dimple is decompressed in order to reduce the trapping frequencies (dimple2) before the atoms are released from the trap by switching off all wire currents. After a few ms of ballistic expansion, the atoms are imaged by absorption imaging in a homogeneous bias field of 8 G. Because of the lower trap frequencies in the final trap, it is easier to switch off the trap fast compared to the inverse of the trapping frequencies. In this way, images taken directly after release reveal the atomic density distribution in the trap. Images taken after a time-of-flight which is long compared to the inverse trapping frequencies reveal the momentum distribution of the atoms.

The ground hyperfine states $F = 1$ and $F = 2$ can be imaged selectively. State $F = 2$ can be imaged directly with the σ^+-polarized $F = 2 \rightarrow F' = 3$ imaging beam. Atoms in the magnetic sublevel $m_F = 2$ scatter photons with maximum Clebsch-Gordan coefficient on the cycling transition to $|F' = 3, m'_F = 3\rangle$. Atoms in other magnetic sublevels are first optically pumped into $m_F = 2$. For convenience we sometimes use a single pulse of imaging light for both optical pumping and imaging. This works if the number of photons scattered by each atom is much larger than one and the magnetic field is not larger than a few Gauss. We usually use an imaging pulse of 200 μs duration with an intensity of $I = 0.1\, I_s$. To detect the state $F = 1$, the atoms are first transferred to $F = 2$ by a short pulse of repumping light and then imaged as described for $F = 2$.

3.7.6 Observation of Bose-Einstein condensation

Figure 3.11 shows absorption images of the BEC phase transition in the glued glass cell vacuum chamber, obtained with atoms in state $|F = 2, m_F = 2\rangle$. BEC reveals itself in the sharp increase in the optical density below T_c, in the bimodal velocity distribution of the partly condensed cloud, and in the anisotropy of the velocity distribution of the BEC in contrast to the isotropic velocity distribution of the thermal cloud [61]. The images are taken after 15 ms of time-of-flight, the temperature is adjusted by the value of ν_{stop}. We observe BEC at a critical temperature of $T_c = 1.5\ \mu$K in an ensemble of 9×10^3 atoms. Temperatures are quoted for the "dimple1"-trap. Using the calculated trapping frequencies from Tab. 3.1, we expect a critical temperature of 1.8 μK from Eq. (1.18), which is valid for a non-interacting gas. If we include corrections due to interactions and finite-size effects [70], we expect $T_c = 1.5\ \mu$K, which is precisely what we observe. The main axes of the elliptic BEC cloud in the absorption image reflect the orientation of the main axes of vibration in the final magnetic trap, which are tilted with respect to gravity.

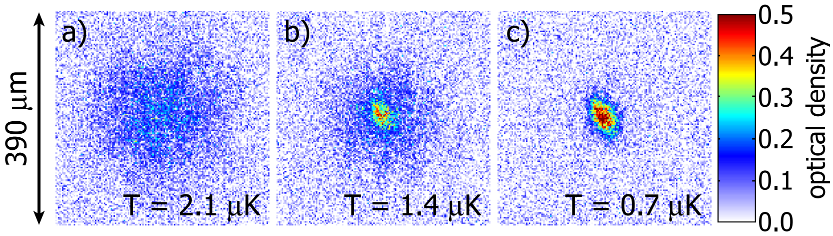

Figure 3.11: Absorption images of the BEC phase transition observed in the glued glass cell vacuum chamber. The difference in ν_{stop} between the pictures is 40 kHz. Left: isotropic cloud of a thermal ensemble at $T > T_c$. Center: ensemble just below the phase transition, $T \lesssim T_c$, showing a bimodal velocity distribution. Right: BEC of 3.5×10^3 atoms without discernible thermal component. The anisotropic expansion of the BEC is visible. The temperature of this "pure" BEC has been extrapolated from an observed linear dependence of T on ν_{stop}. Gravity points downward in the picture.

The presented sequence is taken from our first experiment in which we obtained BEC in a glued glass cell vacuum chamber. Similar wire structures and sequences have been used in the experiments of chapter 4 to prepare the atoms in the trap for coherence measurements close to the surface, and, more recently, on the microwave atom chip to prepare a BEC in a trap near the microwave guiding structures. The main difference in these experiments is that the atoms are magnetically trapped in state $|1, -1\rangle$ instead of $|2, 2\rangle$. For this we use magnetic traps with similar trap frequencies and potential gradients as described here. Because of the smaller magnetic moment of $|1, -1\rangle$, which is only $\mu_B/2$ compared with μ_B for state $|2, 2\rangle$, this requires stronger magnetic field gradients and curvatures, which we achieve with a combination of higher wire currents and bias fields and traps at smaller atom-surface distance.

Chapter 4

Coherence near the surface: an atomic clock on a chip

In this chapter I report on experiments in which ultracold atoms are manipulated coherently on an atom chip. The atoms are prepared in a coherent superposition of two hyperfine ground states which are both magnetically trappable and very robust against magnetic-field induced decoherence. With a thermal ensemble close to quantum degeneracy we perform Ramsey spectroscopy in a magnetic chip trap and study the effect of the chip surface on coherence and trap lifetimes. Coherence and trap lifetimes exceeding 1 s are observed with atoms at distances of $d = 5 - 130\ \mu$m from the microchip surface. For $d < 5\ \mu$m, the atoms are lost in the Casimir-Polder surface potential. The coherence lifetime in the chip trap is independent of d within our measurement accuracy, and agrees well with the results of similar measurements in macroscopic magnetic traps. The long coherence lifetime allows us to demonstrate the first application of an atom chip. In a proof-of-principle experiment, we realize a chip-based atomic clock and measure its frequency stability to $1.7 \times 10^{-11}\ (\tau[\mathrm{s}])^{-1/2}$.

Some of the results reported in this chapter were published in [87].

4.1 Magnetically trappable "qubit" or "clock" states

The ability to create and manipulate superpositions of internal states of the trapped atoms is essential for atom chip applications. Take quantum information processing as an example [34]. In most of the proposed schemes, two internal states $|0\rangle$ and $|1\rangle$ of the atom serve as qubit states. In order to be able to perform a large number of gate operations, long coherence lifetimes of the superposition states $\alpha|0\rangle + \beta|1\rangle$, $|\alpha|^2 + |\beta|^2 = 1$ are required and therefore decoherence processes have to be avoided.[1] As another example, consider an atomic clock, where the transition frequency ν_{10} between the internal states is used as a frequency reference. The coherence lifetime yields an upper limit on the interrogation time. This, in turn, limits the spectral resolution with which ν_{10} can be determined.

Achieving long coherence lifetimes with trapped atoms is complicated by the fact that trapping relies on the sensitivity of atomic energy levels to external fields. Technical, thermal, and quantum-mechanical fluctuations of these fields can thus disturb the energy levels and lead to decoherence. Furthermore, a trap requires non-uniform fields, which leads to spatially dependent energy shifts and thus to inhomogeneous broadening of the transition for trapped ensembles. A further complication in the case of trapped ensembles are collisional losses and energy shifts, which scale with density and are therefore much more severe in traps than in atomic fountains or beams. In addition to these decoherence mechanisms, which are also present in macroscopic traps [84], atoms in chip traps can potentially suffer from a reduction of trap and coherence lifetimes due to interaction with the surface of the chip, as described in section 1.9.

In order to obtain long coherence lifetimes with magnetically trapped atoms near the chip surface, we choose the $|0\rangle \equiv |F = 1, m_F = -1\rangle$ and $|1\rangle \equiv |F = 2, m_F = 1\rangle$ hyperfine levels of the ^{87}Rb ground state for our experiments (Fig. 4.1). This state pair, which has previously been used for precision spectroscopy in macroscopic magnetic traps [84], has unique properties which greatly suppress the effects mentioned above and thus make it particularly well suited for the use as “qubit” or “clock states”.

Both states are magnetically trappable, and the magnetic moments of the two states are approximately equal. As shown in section 1.2.2, the Breit-Rabi formula predicts that at a magnetic field of $B_m = 3.229$ G, both states experience the same first-order Zeeman shift and the remaining magnetic field dependence of the transition frequency ν_{10} is minimized (see also Fig. 4.2 below). In all of our experiments, we therefore adjust the field in the center of the trap to B_m. This greatly reduces spatial inhomogeneities of ν_{10} in the trap, since both states experience the same trapping potential to a good approximation. Furthermore, superpositions of this state pair are particularly robust against decoherence due to magnetic field noise, because, to lowest order, this only leads to common-mode shifts. This suppression

---

[1] Here we use the term “decoherence” for any process that disturbs the relative phase of the states $|0\rangle$ and $|1\rangle$ in the superposition in an experimentally uncontrolled way. For a discussion of the various physical mechanisms which can lead to decoherence in our experiment, see below.

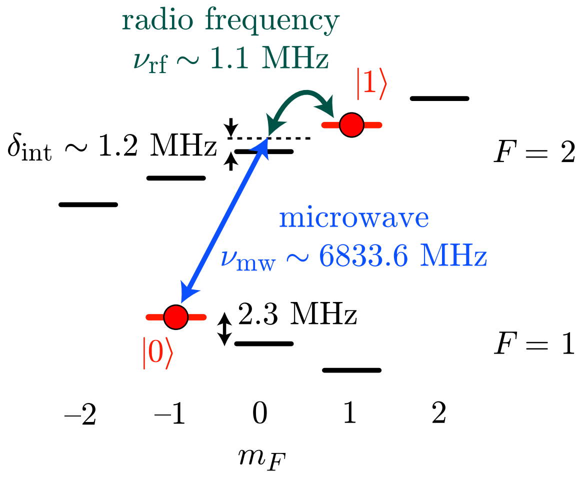

Figure 4.1: Hyperfine states of ^{87}Rb used for the coherence experiments. The approximate microwave and radio frequencies used to drive the two-photon transition between the qubit states $|0\rangle$ and $|1\rangle$ are indicated.

is very important for our experiments, considering that technical magnetic field noise is usually one of the dominant sources of decoherence for magnetic-field sensitive states [150], and thermal magnetic near-field noise is a relevant atom-surface coupling mechanism in the regime of distances studied here (cf. section 1.9). A further advantage in using ^{87}Rb for the experiments is that collisional losses in superpositions of different spin states are greatly reduced compared with other alkali atoms (cf. section 1.8).

4.2 The two-photon transition

Coherent internal-state manipulation is achieved by coupling $|0\rangle$ and $|1\rangle$ through a two-photon microwave-radio frequency transition, as shown in Fig. 4.1. The microwave frequency $\nu_{\mathrm{mw}} = \omega_{\mathrm{mw}}/2\pi$ is typically detuned $\delta_{\mathrm{int}} = \Delta_{\mathrm{int}}/2\pi = 1.2$ MHz above the $|F = 2, m_F = 0\rangle$ intermediate state. The radio frequency $\nu_{\mathrm{rf}} = \omega_{\mathrm{rf}}/2\pi$ can be adjusted to set the detuning

$$\Delta = \omega_{\mathrm{mw}} + \omega_{\mathrm{rf}} - \omega_{10} \tag{4.1}$$

of the two-photon drive from the two-photon resonance at frequency $\nu_{10} = \omega_{10}/2\pi$. If the Rabi frequencies Ω_{mw} and Ω_{rf} of the microwave and radio frequency single-photon transitions satisfy $\Omega_{\mathrm{mw}}^2, \Omega_{\mathrm{rf}}^2 \ll \Delta_{\mathrm{int}}^2$ and the detunings satisfy $|\Delta| \ll |\Delta_{\mathrm{int}}|$, the two states $|0\rangle$ and $|1\rangle$ can be treated as a two-level system which is coupled by an effective two-photon Rabi frequency [151]

$$\Omega_R = \Omega_{\mathrm{mw}}\Omega_{\mathrm{rf}}/2\Delta_{\mathrm{int}}. \tag{4.2}$$

The single-photon Rabi frequencies are given by $\hbar\Omega_{\mathrm{mw}} = \sqrt{\frac{1}{8}}\,\mu_B B_{\mathrm{mw}}$ and $\hbar\Omega_{\mathrm{rf}} = \sqrt{\frac{3}{8}}\,\mu_B B_{\mathrm{rf}}$, where B_{mw} (B_{rf}) is the microwave (radio frequency) field amplitude, and we have assumed linear polarization perpendicular to the static magnetic field in the trap center. For the calculation of hyperfine transition matrix elements, see chapter 5 and appendix A.3.

Microwave and radio-frequency electronics

The microwave is generated by a phase locked dielectric resonator oscillator (PDRO-6378, 6835 ± 5 MHz, Communication Techniques, Inc.). The PDRO phase locks its internal crystal oscillator to the 100th harmonic of an external reference frequency (generated by a Rohde & Schwarz SMG). The phase lock can be operated in a narrow range of output frequencies of 6835 ± 5 MHz. The microwave signal is sent through a switch and then amplified by two amplifiers in series (Kuhne Electronic KU 682 TR-UM, 500 mW, 6835 ± 10 MHz, and KU 682 XH-UM, 15 W, 6835 ± 10 MHz) to a power of 15 W, which is radiated from a sawed-off rectangular waveguide. To protect the high power amplifier from reflections, we use a circulator between the amplifier and the waveguide with a high-power 50 Ω termination at one port. The waveguide is placed outside the glass cell, radiating towards the chip surface. The linear polarization of the microwave is approximately perpendicular to the magnetic field in the trap center.

The radio frequency is generated by a function generator (Stanford Research Systems DS345), sent through a switch, and amplified to 1 W. It is either applied to the same external coil that is used for radio frequency evaporative cooling, or directly to a wire on the chip.

All frequency generators of our experiment are phase locked to an ultrastable 10 MHz quartz oscillator (Oscilloquartz OCXO 8607-BM, for specifications of the frequency stability see Fig. 4.18 below).

Magnetic field dependence of the transition frequency

By performing Ramsey spectroscopy (see below) of the two-photon transition, we measure ν_{10} as a function of the magnetic field in the trap center, B_0, as shown in Fig. 4.2. Measurements of this type allow us to calibrate our magnetic field and the frequency of the quartz reference oscillator, using the frequency dependence which is expected from the Breit-Rabi formula (section 1.2.2), which can be approximated in the vicinity of $B_m = 3.228\,917(3)$ G by [84]

$$\nu_{10} = \nu_{\min} + k\,(B_0 - B_m)^2\,, \tag{4.3}$$

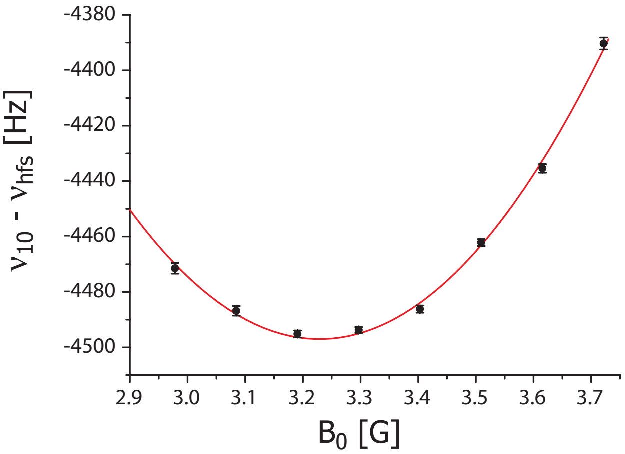

Figure 4.2: Measured magnetic field dependence of the two-photon transition frequency. The frequency ν_{hfs} is the hyperfine splitting for $B_0 = 0$.

with $\nu_{\mathrm{min}} = 6\ 834\ 678\ 113.59(2)$ Hz and $k = 431.359\ 57(9)$ Hz/G^2.

Microwave level shifts

While the two-photon drive is turned on, the two-photon resonance frequency is shifted to ν'_{10}, away from the value ν_{10} it has in the undriven system, typically by a few tens of Hz (see also [151]). The frequency shift scales linearly with the applied microwave power. It arises because the microwave causes AC Zeeman shifts of the hyperfine levels — this is the same physical mechanism that is used to generate the microwave potentials discussed in chapter 5. Various transitions contribute, because several polarization components are present in the microwave field. For the experiments described in the present chapter, the spatial dependence of the AC Zeeman shift is negligible, because microwave field gradients are very weak in the far field of the rectangular waveguide. The radio frequency causes similar level shifts, however, for linear radio frequency polarization, the shifts are identical for $|0\rangle$ and $|1\rangle$ and thus do not lead to a frequency shift of the transition.

The microwave level shift can be measured by comparing the resonance frequency obtained in Rabi spectroscopy with that obtained in Ramsey spectroscopy. A Rabi experiment is sensitive to the level shifts and yields ν'_{10}. A Ramsey experiment is largely insensitive and yields ν_{10}, because the shift arises only during the short $\pi/2$-pulses and the microwave is turned off between the pulses (see below). For our measurements, we have decreased the shift by decreasing the ratio $\Omega_{\mathrm{mw}}/\Omega_{\mathrm{rf}}$, keeping the product $\Omega_{\mathrm{rf}} \cdot \Omega_{\mathrm{mw}} \sim \Omega_R$ constant. In this way, we obtain $\Omega_R/2\pi \gg |\nu'_{10} - \nu_{10}|$ and can thus drive high contrast Rabi oscillations with the two-photon drive tuned near the Ramsey resonance at ν_{10}.

4.3 Phenomenological description of loss and decoherence

For comparison with our experiments, we use a density matrix model for the two-level system $\{|0\rangle, |1\rangle\}$, which includes population loss and decoherence in a phenomenological way [152, 153]. Below we show measurements of the loss and decoherence rates and identify the physical mechanisms behind them.

Density matrix description of a two-level system

A two-level atom can be described by a 2×2 density matrix ρ_{ij}, where ρ_{00} and ρ_{11} are the populations of state $|0\rangle$ and $|1\rangle$, respectively, and $\rho_{01} = \rho_{10}{}^*$ are the coherences (Fig. 4.3). The atom is coherently driven by a classical oscillatory field of frequency ω (in our case $\omega = \omega_{\mathrm{mw}} + \omega_{\mathrm{rf}}$), with resonant Rabi frequency Ω_R and detuning $\Delta = \omega - \omega_{10}$ from resonance (neglecting the microwave level shifts). The dynamics are described in a frame rotating at frequency ω, and because $\Delta, \Omega_R \ll \omega_{10}$, we can make the rotating-wave approximation. In the following, ρ_{ij} are the components of the density matrix in the rotating frame, the components in the stationary frame are $\tilde{\rho}_{ii} = \rho_{ii}$, $\tilde{\rho}_{10} = e^{-i\omega t}\rho_{10}$, and $\tilde{\rho}_{01} = e^{i\omega t}\rho_{01}$. The equations of motion are

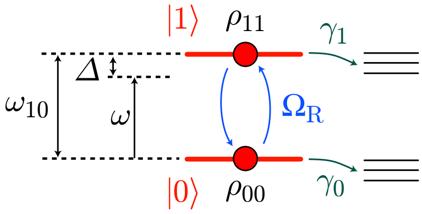

Figure 4.3: Two-level system with coherent driving and population loss (see text).

$$\begin{aligned}
\frac{d}{dt}\rho_{11} &= \frac{i}{2}\left(\Omega_R^*\rho_{10} - \Omega_R\rho_{01}\right) - \gamma_1\rho_{11}, \\
\frac{d}{dt}\rho_{00} &= -\frac{i}{2}\left(\Omega_R^*\rho_{10} - \Omega_R\rho_{01}\right) - \gamma_0\rho_{00}, \quad \text{and} \\
\frac{d}{dt}\rho_{10} &= i\Delta\rho_{10} + \frac{i}{2}\Omega_R\left(\rho_{11} - \rho_{00}\right) - \gamma_c\rho_{10}.
\end{aligned} \tag{4.4}$$

Loss and decoherence are taken into account by introducing phenomenological rate constants, which can be measured in experiments. γ_i is the rate at which the population of state $|i\rangle$ decays, and

$$\gamma_c = (\gamma_0 + \gamma_1)/2 + \gamma_\phi \tag{4.5}$$

is the decay rate of the coherences. Consistency requires that γ_c can never be smaller than the average population loss rate of the two states. The rate γ_ϕ affects only the coherences ("pure dephasing"). In the specific case of our experiment, γ_0 and γ_1 are dominated by trap loss, so that the total population $\rho_{11} + \rho_{22}$ is not conserved. Loss processes which empty one of the levels and populate the other have negligible rates.

Our experiments are performed on ensembles of N atoms simultaneously, and we use ρ_{ij} as a calculational tool to describe ensemble averages.[2] The expectation value of the number of atoms detected in state $|i\rangle$ is $N_i = N\rho_{ii}$. As shown below, trap loss in atomic ensembles includes effects of inelastic collisions. The rates γ_i thus depend on time and on the initial state $\rho_{ij}(t=0)$. On short time scales, we can use the constants $\gamma_i \equiv \gamma_i(t=0)$ to describe loss. Similarly, decoherence may be non-exponential. However, we find that our experiments are well described by assuming a constant γ_ϕ.

Mechanisms of decoherence

Different mechanisms of decoherence can be distinguished [7, 154, 155]. Decoherence in the narrow sense is caused by progressive entanglement of a system with its environment, accompanying collisional loss or spontaneous scattering of stray light in our case. This is to be distinguished from dephasing caused by fluctuating or spatially inhomogeneous classical fields, e.g. ambient magnetic fields. From the practical point of view of a "quantum engineer", dephasing is equally deleterious to coherent manipulation as decoherence by entanglement.

It is useful to distinguish homogeneous from inhomogeneous dephasing. Homogeneous dephasing affects all atoms in the same way and would be present in experiments on single atoms as well. Inhomogeneous dephasing arises only in the ensemble average, if the phases of different atoms in the ensemble evolve at different rates. Because each individual atom maintains phase coherence, inhomogeneous dephasing can be reversed by the spin echo method, in contrast to the (in practice) irreversible homogeneous dephasing.

---

[2] We keep in mind that a single-atom density matrix does not provide a complete description of an ensemble of atoms. It yields correct predictions only for single-atom observables measured in the ensemble average [7].

Coupling between internal and motional dynamics

A possible coupling between the internal state and the motional dynamics of the atoms is neglected in Eqs. (4.4). In a series of experiments, the group of E. A. Cornell has shown that such a coupling arises due to small differences in the confining potentials and collisional effects, both for BECs [156, 157] and ultracold thermal gases at high atomic densities [158, 159].[3] In our coherence measurements, we usually work with thermal ensembles at relatively low mean densities $\langle n \rangle < 3 \times 10^{12}$ cm^{-3} and in traps which are only moderately anisotropic. In this regime, we expect coupling between internal and motional dynamics to be weak [158, 160]. Indeed, we do not observe such a coupling in the absorption images. Because we integrate the atom number over the whole sample, the effect of an unresolved coupling between internal and motional degrees of freedom is included in the measured γ_ϕ.

In the following, I describe several experiments in which we investigate the dynamics of the system just described. Measurements of γ_i and γ_ϕ as a function of atom-surface distance allow us to search for atom-surface coupling mechanisms.

4.4 Chip layout and atom preparation

The experiments reported in this chapter were performed with an earlier version of our setup, which is described in detail in [65, 129, 27, 29]. Figure 4.4 shows the relevant wires and the layer structure of the chip. The experimental parameters and the sequence used for the preparation of the atoms are very similar to the ones described in chapter 3.

We first load a laser-cooled ensemble of atoms in state $|0\rangle$ into a large Ioffe Z-trap at position C1 in Fig. 4.4(a). After a first stage of evaporative cooling, the atoms are transferred into a Ioffe dimple trap at position C2, where a second stage of evaporative cooling prepares an ultracold thermal ensemble with a temperature close to quantum degeneracy. This ensemble is then loaded into a Ioffe-type “measurement trap”, also centered at position C2, in which all subsequent experiments are performed. The measurement trap typically contains a thermal ensemble of $N = 1.5 \times 10^4$ atoms in state $|0\rangle$ at a temperature of 0.6 μK, a factor of three above the critical temperature for BEC. We use a thermal ensemble instead of a BEC for our measurements because the lower density of a thermal ensemble reduces the effect of collisions on trap and coherence lifetimes. Low temperatures are required to reduce

---

[3] Interestingly, in low-density samples, collisions between atoms can also help to maintain coherence across the sample, as shown in [84].

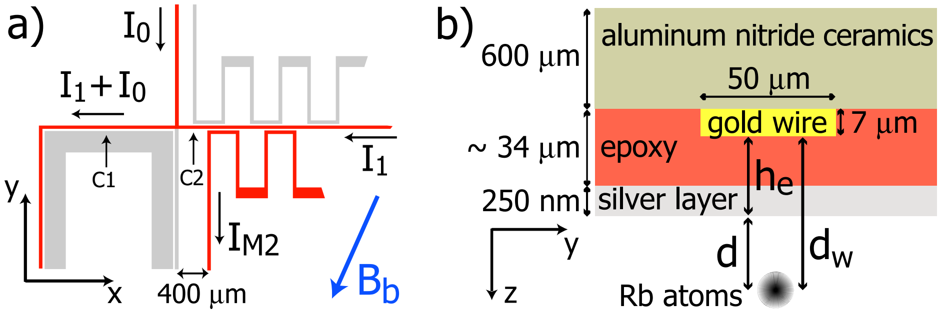

Figure 4.4: (a) Layout of the relevant wires on the chip substrate. C1: position of the initial magnetic trap. C2: position of the "measurement trap" used in the experiments. (b) Layer structure of the substrate. Current is carried by gold wires $h_e \sim 27\ \mu$m below the silver surface. d denotes the atom-surface distance, while d_w refers to the atom-wire distance.

inhomogeneous broadening of the transition due to the residual differential Zeeman effect.

The measurement trap is created by the currents I_0, I_1, and I_{M2} and the bias field $\mathbf{B}_b = (B_{b,x}, B_{b,y}, 0)$ as shown in Fig. 4.4(a). Although the wire geometry is somewhat different, the trapping potential is similar to that of a Ioffe Z-trap. By adjusting all three currents and $B_{b,y}$, the atoms can be placed at distances $d = 0 - 130\ \mu$m from the chip surface (see Fig. 4.4(b)), with relatively small changes in the shape of the magnetic potential. For each experimentally studied distance, the field magnitude B_0 in the trap center was calibrated spectroscopically as shown in Fig. 4.2 and set to $B_0 = B_m$ by adjusting $B_{b,x}$. Typical experimental parameters are $I_0 = 500$ mA, $I_1 = 120$ mA, $I_{M2} = 700$ mA, $B_{b,y} = -5.50$ G, and $B_{b,x} = -2.18$ G, leading to trap frequencies $(f_x, f_y, f_z) = (50, 350, 410)$ Hz at $d = 9\ \mu$m. The atoms are held in the measurement trap while the coherent internal-state manipulation is performed. After the manipulation, the trap is switched off within 150 μs and the atoms are detected after a time of flight of typically 4 ms. Atoms are detected by absorption imaging on the $F = 2 \rightarrow F' = 3$ transition, as explained in chapter 3. This allows direct determination of the number of atoms in state $|1\rangle$, N_1. To alternatively determine the number of atoms in state $|0\rangle$, N_0, we first blow away all atoms in $|1\rangle$ with the resonant probe light. The $|0\rangle$ atoms are then optically pumped to $|F = 2, m_F = +2\rangle$ and imaged as before.

4.5 Rabi oscillations

When we apply the two-photon drive to atoms in the microtrap for a variable time τ, we observe Rabi oscillations, Fig. 4.5, in which the atomic population oscillates coherently between $|0\rangle$ and $|1\rangle$. In this way, qubit rotations would be realized in a quantum computer.

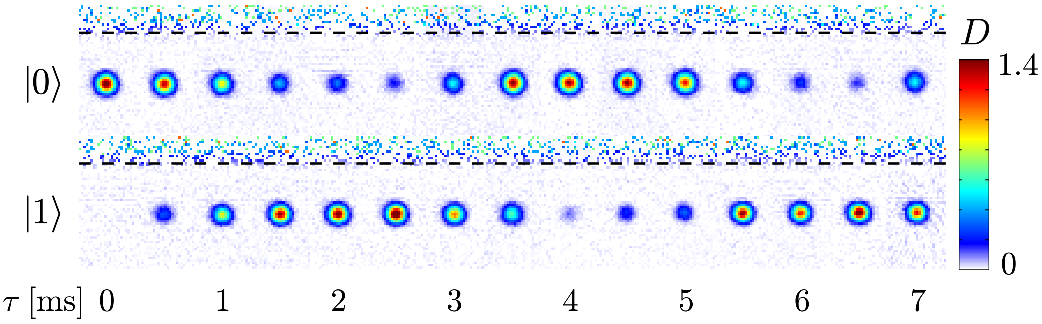

Figure 4.5: Rabi oscillations between $|0\rangle$ and $|1\rangle$ as a function of microwave and radio frequency pulse duration τ. Each absorption image corresponds to a single shot of the experiment in which either $|0\rangle$ or $|1\rangle$ is detected. The dashed line indicates the chip surface.

Figure 4.6 shows the measured $N_i(\tau)/[N_0(\tau) + N_1(\tau)]$ obtained by integrating the density distributions in Fig. 4.5. The observed oscillation of the atomic population is described by [152]

$$\begin{aligned} \frac{N_1(\tau)}{N} &= \frac{\Omega_R^2}{\Omega^2} \sin^2\left[\tfrac{1}{2}\Omega\tau\right], \\ \frac{N_0(\tau)}{N} &= 1 - \frac{N_1(\tau)}{N}, \end{aligned} \tag{4.6}$$

where $\Omega = \sqrt{\Omega_R^2 + \Delta'^2}$. Eqs. (4.6) are obtained from Eqs. (4.4) in the limit of weak damping, $\Omega_R \gg (\gamma_i, \gamma_c)$, and for $|0\rangle$ as the initial state. We fit Eqs. (4.6) to the data, which yields $\Omega_R/2\pi = 226 \pm 4$ Hz and $\Delta'/2\pi = 63 \pm 13$ Hz. The detuning $\Delta' = \omega - \omega'_{10}$ measured in this way includes the microwave level shifts, as discussed in section 4.2. The data for N_0 and N_1 were taken consecutively. Therefore shot-to-shot fluctuations in the initially prepared atom number N show up as noise in Fig. 4.6.

We typically work with two-photon Rabi frequencies in the range of $\Omega_R/2\pi = 0.2 - 0.8$ kHz for $\Delta_{\mathrm{int}}/2\pi = 1.2$ MHz, while the single-photon Rabi frequencies $\Omega_{\mathrm{mw}}/2\pi$ and $\Omega_{\mathrm{rf}}/2\pi$ are of the order of a few tens of kHz. In the experiments described here, Ω_R is limited by the available microwave power. Microwave single-photon Rabi frequencies of a few MHz can be obtained if

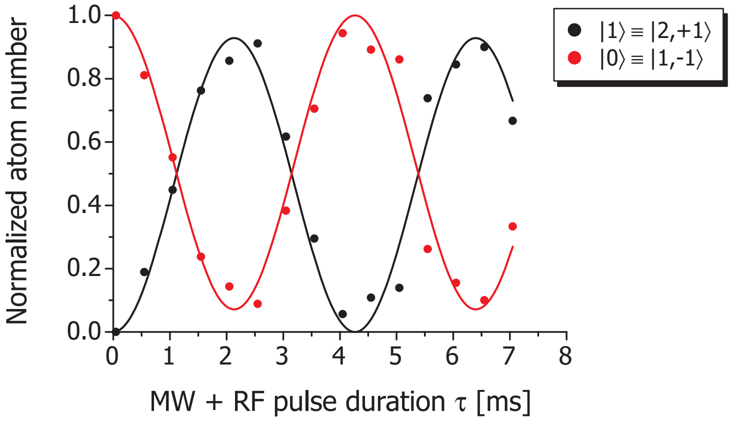

Figure 4.6: Normalized atom numbers $N_i/(N_0 + N_1)$ in state $|i\rangle$ obtained by integrating the absorption images of Fig. 4.5.

the microwave is applied to waveguiding structures on the chip instead of being radiated from outside the vacuum chamber, as explained in chapter 5.

Below we use Rabi oscillations for internal-state manipulation. With the help of a resonant π-pulse ($\Omega_R\tau = \pi$, $\Delta' = 0$), the atoms can be transferred from $|0\rangle$ to $|1\rangle$. The measured transition probability is $> 95\%$. With a $\pi/2$-pulse ($\Omega_R\tau = \pi/2$, $\Delta' = 0$), an equal superposition $\frac{1}{\sqrt{2}}\left(|0\rangle + e^{i\varphi}|1\rangle\right)$ can be prepared, the relative phase φ depends on the phase offset of the two-photon drive. Before we investigate trap and coherence lifetimes of such states near the surface, we describe our calibration of the atom-surface distance.

4.6 Calibration of the trap-surface distance

An investigation of surface effects requires an accurate calibration of the distance d between the chip surface and the center of the trap. The trap-wire distance d_w can be inferred from a simulation of the trapping potential, but $d = d_w - h_e$ depends on the thickness h_e of the epoxy layer above the wires, see Fig. 4.4(b), which was not well controlled during chip fabrication. We therefore use two different methods to directly measure d.

Distance calibration by imaging with a reflected probe beam

In the first technique [147], the imaging beam is tilted by an angle of 2° towards the mirror on the chip surface, so that both a direct and a mirror image of the atoms are simultaneously visible in the absorption image, see Fig. 4.7. The distance between the cloud centers equals $2d$. Due to the finite resolution of the imaging system, this technique is limited to $d > 10\ \mu\text{m}$. We take images such as Fig. 4.7 at several values of d and determine corresponding values of d_w from a simulation of the trapping potentials. This yields $h_e = 25.2 \pm 2.2\ \mu\text{m}$.

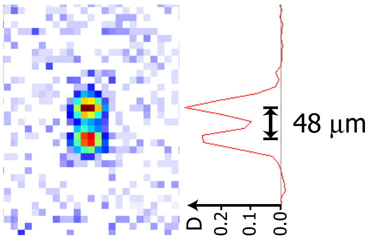

Figure 4.7: Absorption image taken with a tilted imaging beam. Pixel size is $10.6\ \mu\text{m} \times 10.6\ \mu\text{m}$. A fit to the density distribution with two Gaussians (not shown) gives $d = 24 \pm 1\ \mu\text{m}$ for this picture.

Distance calibration from trap loss in the Casimir-Polder potential

In the second technique, the surface is located by measuring the loss of atoms in the attractive Casimir-Polder surface potential, compare section 1.9.2 and [44]. Starting with N atoms (all in state $|0\rangle$) in a trap at $d = d_0$ sufficiently far from the surface, we move the trap to a distance $d < d_0$ by increasing $B_{b,y}$. We hold the atoms there for a time t_h, then move back to the original location, and determine the remaining number of atoms N_r. Figure 4.8(b) shows the remaining atom fraction $\chi = N_r/N$ as a function of d.

We model the observed loss of atoms in the Casimir-Polder surface potential as a sudden truncation of the tail of the Boltzmann energy distribution due to the finite trap depth V_b, see Fig. 4.8(a). The theoretical value for the remaining fraction of atoms is $\chi = 1 - \exp(-V_b/k_B T)$, where V_b is the trap depth at $d = d_w - h_e$. The model contains h_e as the only free parameter. The temperature $T = 200$ nK of the cloud used for this measurement, the atom number $N = 1.48 \times 10^4$, the trap frequencies $(f_x, f_y, f_z) = (37, 279, 332)$ Hz, and the scaling $d_w(B_{b,y})$ are determined independently. The chip surface is modeled as a perfect conductor, V_b is determined using Eq. (1.45) for the surface potential.

Because of the Casimir-Polder potential, the trap disappears at finite d. The corresponding shift in d is $1.1\ \mu\text{m}$ if one compares with a model where the Casimir-Polder potential is neglected. If the optical method to determine h_e described in the previous section was more accurate, we could use this for a measurement of the Casimir-Polder potential, similar to [44]. Here, we

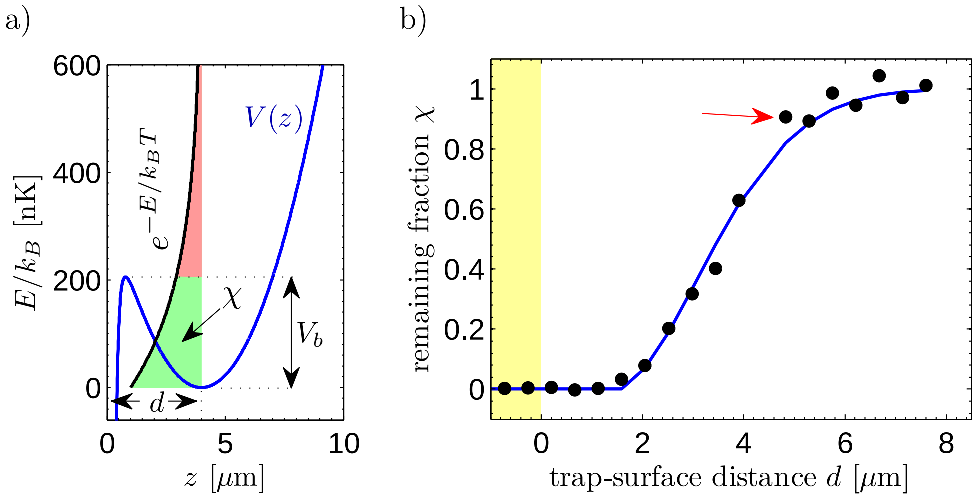

Figure 4.8: Loss of atoms in the Casimir-Polder surface potential. (a) The surface potential decreases the trap depth, atoms in the tail of the Boltzmann distribution are lost. (b) Remaining fraction of atoms χ as a function of d for a hold time $t_h = 10$ ms. Measured data (black dots) in comparison with a fit to our model (blue line, see text). The red arrow indicates the trap with smallest d in which coherence measurements were made.

turn the situation around and use the Casimir-Polder potential to calibrate the trap-surface distance. From a fit of our model to the data, we determine $h_e = 27.1$ μm with a statistical error of ± 0.1 μm, consistent with the value of h_e obtained from the absorption images. Figure 4.8(b) shows the fit and the resulting calibration of d. Including errors in the other model parameters and the trap simulations, we estimate an uncertainty in d of ± 0.8 μm. The arrow in Fig 4.8 corresponds to the trap at $d = 4.9$ μm, the smallest d at which coherence measurements were performed.

A hold time of $t_h = 10$ ms is short enough to avoid systematic errors in the calibration due to other surface-related loss mechanisms, which affect the atoms only on a much longer time scale (see section 4.7 below). We also neglect in our model the collisional rethermalization of the atoms during t_h and the associated additional loss through evaporation [44]. In our case it is reasonable to include only the sudden loss since $t_h < \gamma_{\mathrm{el}}^{-1} = 40$ ms, where γ_{el} is the elastic collision rate in the trap. Note that for significantly longer t_h, we do indeed observe surface evaporation, as expected (see section 4.7).

We also considered the possibility that the surface potential is dominated by ^{87}Rb adsorbates, as discussed in section 1.9.3. More than 10^8 adatoms localized on the chip surface in an area corresponding to the size of the trapped atomic cloud would be required to shift the measured value of h_e by 0.1 μm. This corresponds to 10^4 deposited atom clouds, while we have intentionally deposited only 10^2 clouds in the course of the distance calibration. Even more deposited adatoms would be required if we consider a less localized adatom distribution, which is more realistic because of surface diffusion [107]. This leads us to the conclusion that the surface potential is not dominated by adsorbates, although some caution is in order because the number and distribution of atoms deposited unintentionally on the surface is not known.

With the atom-surface distance calibrated as described, we can search for possible effects of the surface on trap and coherence lifetimes.

4.7 Trap lifetime measurements

To investigate surface-induced loss, we measure trap lifetimes as a function of d. In every trap, we perform one measurement in which all atoms are in state $|0\rangle$, and a separate measurement in which a π-pulse first transfers the atoms to state $|1\rangle$. Because $|0\rangle$ and $|1\rangle$ have very different collisional loss rates, a comparison of the two measurements allows us to determine the initial density of the sample, and to discriminate between surface-induced and collisional losses.

Fig. 4.9(a) shows such measurements in a trap at $d = 130$ μm, far away from the surface. If all atoms are in state $|0\rangle$, we observe an exponential decay of the atom number with a rate $\gamma_0 = (29\text{ s})^{-1}$. The situation is different if the atoms are prepared in $|1\rangle$. A non-exponential decay is observed, a signature of inelastic collisions between the trapped atoms. The initial density $\langle n(t = 0)\rangle = \langle n_0(t = 0)\rangle + \langle n_1(t = 0)\rangle$ was similar in both measurements. The solid lines in Fig. 4.9(a) are a numerical solution to the rate equations (1.33), which include all relevant collisional loss mechanisms. As explained in section 1.8, we use the rate constants for a thermal ensemble, and $\langle n_i^2\rangle = (8/\sqrt{27})\langle n_i\rangle^2$ for a thermal distribution. The slightly lower initial atom number in $|1\rangle$ is due to the finite efficiency of the π-pulse, the residual population in $|0\rangle$ is included in the model. We use the same $\langle n(t = 0)\rangle$ and γ_{bg} for comparison with both measurements and adjust their values to fit the data. This yields $\langle n(t = 0)\rangle = 2.7 \times 10^{12}$ cm^{-3} and $\gamma_{\text{bg}} = (29\text{ s})^{-1}$. Assuming a higher $\langle n(t = 0)\rangle$ would be inconsistent with the measurement for $|1\rangle$. The model confirms that loss due to collisions between the trapped atoms is negligible if all atoms are in state $|0\rangle$. The decay of state $|0\rangle$ can thus be used to study surface effects.

Fig. 4.9(b) shows a similar trap loss measurement at $d = 9$ μm. We

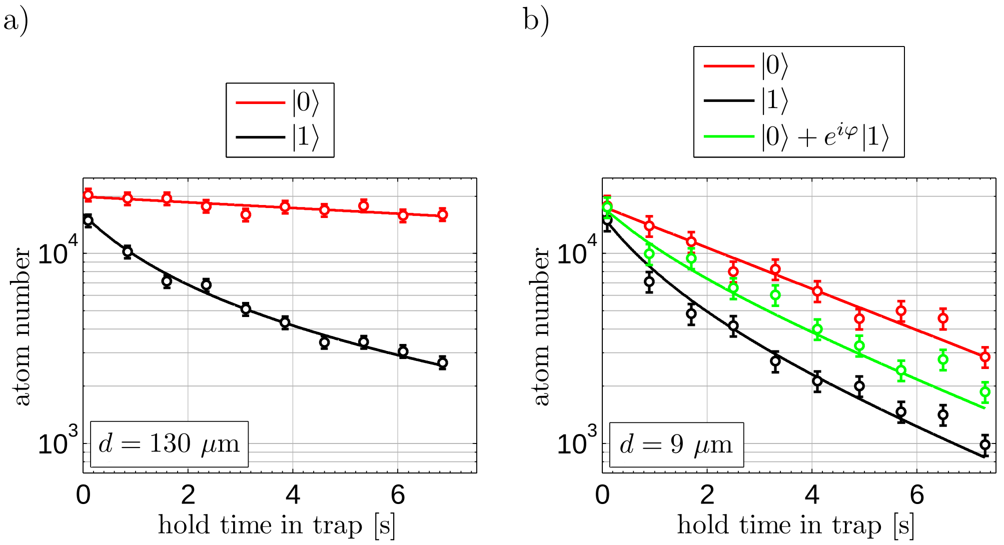

Figure 4.9: Trap loss at different atom-surface distances: (a) $d = 130\ \mu$m, (b) $d = 9\ \mu$m. Measurements are shown for different internal states prepared in the trap and compared to a theoretical model (see text). Temperatures and initial densities are similar in all cases.

observe a much faster decay, with a rate $\gamma_0 = (4.0\ \mathrm{s})^{-1}$ for state $|0\rangle$. The increased loss rate cannot be explained by an increase in γ_{bg}. Although the background pressure in the vacuum chamber shows some variation depending on the dispenser setting, we always have $\gamma_{\mathrm{bg}} < (10\ \mathrm{s})^{-1}$ at large d in this experiment. We account for the faster loss by adding a surface-induced loss rate γ_s to Eqs. (1.33), which is identical for $|0\rangle$ and $|1\rangle$ and independent of density. As before, we compare a solution to Eqs. (1.33) with our measurements, which allows us to determine $\langle n(t = 0)\rangle = 2.6 \times 10^{12}\ \mathrm{cm}^{-3}$, comparable to Fig. 4.9(a), and $\gamma_s = (4.6\ \mathrm{s})^{-1}$. In principle, γ_s could be different for the two states, e.g. because of the different matrix elements involved in spin-flip loss due to thermal magnetic near-field noise. However, the similar decay rate of $|0\rangle$ and $|1\rangle$ observed at long times shows that γ_s is comparable.

In this trap, we have also measured the trap lifetime of the superposition state $\frac{1}{\sqrt{2}}(|0\rangle + e^{i\varphi}|1\rangle)$. The state is created by a $\pi/2$-pulse, φ is irrelevant for the present purpose. After a variable hold time, the total population $N_0 + N_1$ is detected in a phase-insensitive way, i.e. *without* applying a second $\pi/2$-pulse before the absorption image is taken. As expected, the decay rate lies between that of $|0\rangle$ and $|1\rangle$, see Fig. 4.9(b).

In Fig. 4.10 we show how the measured trap lifetime $\tau_0 = \gamma_0^{-1}$ of state $|0\rangle$ varies with d. The decrease for small d is a clear indication of surface

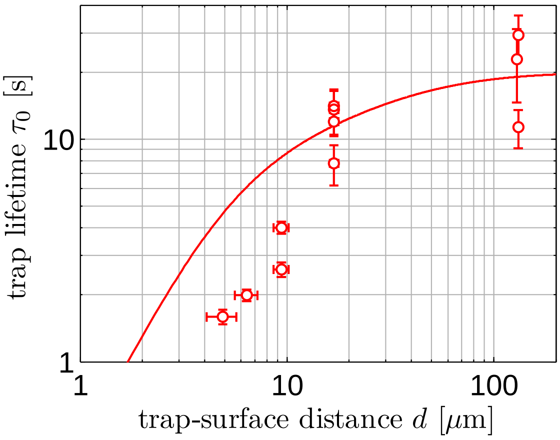

Figure 4.10: Trap lifetime of state $|0\rangle$ as a function of d. Solid line: theoretical curve for spin-flip loss due to magnetic near-field noise and $\tau_{\mathrm{bg}} = 20$ s.

effects. In comparison with the data, we plot the theoretical curve $\tau_0 = [1/\tau_s + 1/\tau_{\mathrm{bg}}]^{-1}$, where τ_s takes into account spin flip loss due to magnetic near-field noise, given by Eq. (1.38) adapted to the layer structure of our chip. The thin silver mirror contributes a larger rate than the gold wires, because it is closer to the atoms (Fig. 4.4). The trap lifetimes we observe at small d are significantly lower than what is expected due to magnetic near-field noise alone. This additional loss is caused by surface evaporation. Because of the Casimir-Polder potential, see Fig. 4.8, the trap depth decreases from 12 μK at $d = 17$ μm to 0.4 μK at $d = 5$ μm, which is comparable to the initial temperature of the atoms. Indeed, for small d we observe that the sample cools while the atoms are lost. Surface evaporation is not state-dependent, which also explains why we observe similar decay rates for $|0\rangle$ and $|1\rangle$ at long times. The loss due to surface evaporation could be reduced by increasing the trap frequency and thus the Casimir-Polder limited trap depth at given d, at the expense of stronger collisional losses in $|1\rangle$.

To parametrize loss in state $|1\rangle$ at short times, we use the measured initial loss rate

$$\gamma_1 \equiv -\frac{1}{N_1}\frac{dN_1}{dt}\bigg|_{t=0} . \tag{4.7}$$

It corresponds to a lifetime $\tau_1 = \gamma_1^{-1}$ which is shown in Fig. 4.11 as a function of $\langle n_1\rangle$, for $\langle n_0\rangle \approx 0$. We find that τ_1 shows a stronger dependence on $\langle n_1\rangle$ than on d. In the coherence measurements discussed below, we use low-density ensembles to avoid strong losses in state $|1\rangle$.

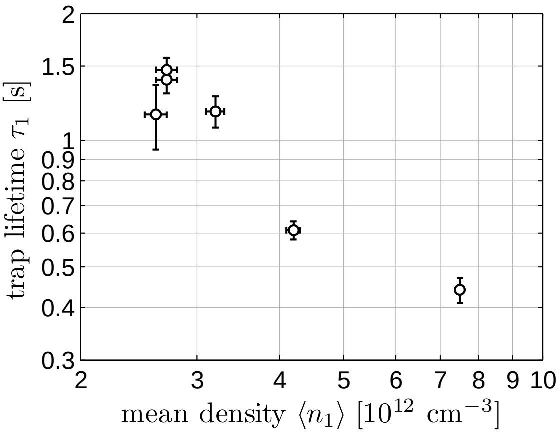

Figure 4.11: Time constant of the measured initial decay of state $|1\rangle$ as a function of $\langle n_1 \rangle$. Data was taken in traps at different d and with $\langle n_0 \rangle \approx 0$.

Conclusion

We do observe increased trap loss close to the surface, but the lifetimes of low-density ensembles are still > 1 s, even at $d = 5$ μm. This is sufficient for most applications of atom chips. The lifetimes close to the thin silver layer on our chip are much longer than what was observed at comparable distance close to thick metal layers [32, 88], where thermal magnetic near-field noise is stronger. This shows that it is advantageous to use chips with metal layers which are as thin as the desired wire currents allow it. Similar results have been obtained by [44].

4.8 Coherence measurements

Ramsey spectroscopy

To measure the coherence lifetime, we perform Ramsey spectroscopy [161] with the pulse sequence shown in Fig. 4.12(a). We start with N atoms in state $|0\rangle$ at $t = 0$. The atoms are held in the measurement trap for a time T_H before a first $\pi/2$-pulse of the two-photon drive transfers every atom into an equal coherent superposition of $|0\rangle$ and $|1\rangle$. The atoms are then allowed to evolve freely for a time $T_R \gg \tau$. During this time, the phase difference between our local oscillator (i.e. the microwave and radio frequency) and the atomic superposition state evolves at a rate Δ. After this time, a second $\pi/2$-pulse is applied and the resulting state is probed. The Ramsey pulse sequence can be thought of as an atom interferometer, with the two pulses corresponding to the beam splitters. The detected state depends on the accumulated relative phase ΔT_R between the local oscillator and the atomic superposition. Time-domain interference fringes are recorded by varying T_R while keeping Δ fixed. Alternatively, frequency-domain interference fringes are recorded by scanning Δ with constant T_R.

Ramsey spectroscopy has the advantage over Rabi measurements that it is most sensitive to the transition frequency during the time interval T_R, during which the two-photon drive is turned off. The signal is thus affected very little by spatial inhomogeneities of Ω_R or by the microwave level shifts which arise only while the two-photon drive is on.

4.8.1 Time-domain Ramsey fringes

Figure 4.12(b) shows time-domain Ramsey fringes. The number of atoms detected in state $|1\rangle$ oscillates at the frequency difference $\Delta/2\pi = 6.4$ Hz, while the interference contrast shows a weak decay with a time constant of 2.8 ± 1.6 s. The measurement of Fig. 4.12 was performed at $d = 9$ μm from the room-temperature chip surface. In [84], similar coherence lifetimes are reported for the same state pair, but with atoms in a macroscopic magnetic trap, far away from any material objects. This suggests that atom-surface interactions do not limit the coherence lifetime in our experiment.

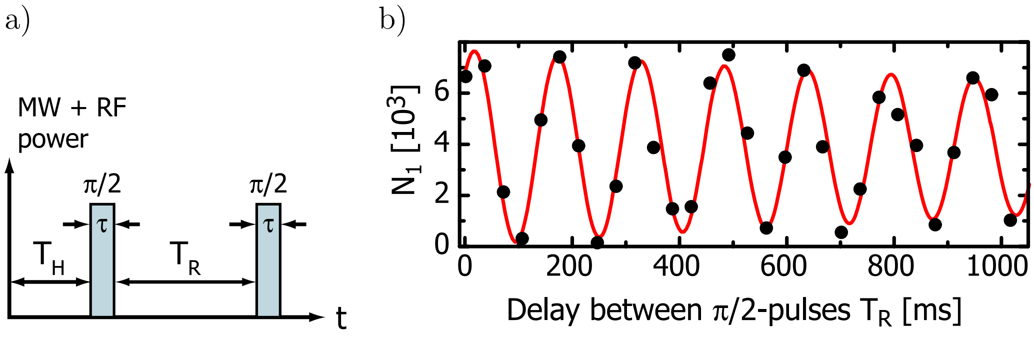

Figure 4.12: Ramsey spectroscopy of the $|0\rangle \leftrightarrow |1\rangle$ transition with atoms held at a distance $d = 9$ μm from the chip surface. (a) Ramsey pulse sequence. (b) Observed interference fringes. An exponentially damped sine fit yields a $1/e$ decay time of the interference contrast of 2.8 ± 1.6 s. Each data point corresponds to a single shot of the experiment.

4.8.2 Analysis of the observed fringes

The Ramsey fringes obtained with our sequence can be described by

$$\frac{N_{1,0}}{N} = \frac{1}{4} e^{-\gamma_0 T_H} \left[\left(e^{-\gamma_0 T_R} + e^{-\gamma_1 T_R} \right) \pm 2 e^{-\gamma_c T_R} \cos(\Delta T_R + \phi_0) \right] , \tag{4.8}$$

where the $+$ ($-$) sign is for N_1 (N_0). This expression is obtained from Eqs. (4.4) by making the approximation that $\Delta \approx 0$ and $\gamma_i \approx \gamma_c \approx 0$ during the short times τ of the $\pi/2$-pulses. This is a good approximation for $\Omega_R \gg (\Delta, \gamma_i, \gamma_c)$. Loss, decoherence, and finite detuning are only considered during the much longer times of free evolution $(T_R, T_H) \gg \tau$, where $\Omega_R = 0$. The phase offset ϕ_0 is included to account for the details of the dynamics during the pulses. It is influenced, among other things, by the detuning caused by the microwave level shifts during the pulses.

To better distinguish the contributions of trap loss γ_i and pure dephasing γ_ϕ to the decoherence rate γ_c, we keep $T_H + T_R$ constant during the Ramsey scan by appropriately adjusting the hold time T_H for each value of T_R. Thus, the overall time the atoms spend close to the surface is independent of T_R. The overall atom number $N_0 + N_1$ at the time of detection then shows a weaker dependence on T_R in the presence of trap loss. The Ramsey fringe signal for N_1 obtained with this sequence is

$$N_1 = A \left[\left(1 + e^{-\gamma_d T_R} \right) + 2 e^{-\gamma_d T_R/2} e^{-\gamma_\phi T_R} \cos(\Delta T_R + \phi_0) \right] , \tag{4.9}$$

where A is a constant. This signal allows an easier determination of γ_ϕ because it is sensitive only to the difference of the trap loss rates $\gamma_d = \gamma_1 - \gamma_0$. For $\gamma_d \approx 0$, the decay of the Ramsey signal directly yields γ_ϕ. The γ_i can be measured independently as described in section 4.7; here, the loss rates for a superposition state are relevant. In Fig. 4.12(b), we have $\gamma_0 = (3.2\text{ s})^{-1}$, $\gamma_1 = (2.6\text{ s})^{-1}$, and $\gamma_\phi = (3.1\text{ s})^{-1}$. This yields a coherence lifetime of $\tau_c = \gamma_c^{-1} = 1.5$ s.

4.8.3 Mechanisms of decoherence

Figure 4.13 shows how coherence is lost in our system at long times. The data is fit with Eq. (4.9). Loss of coherence shows up in different ways:

A spatial variation of ν_{10} results in inhomogeneous dephasing. This leads to the observed decay of the fringe contrast. It is caused by a combination of the residual differential Zeeman shift and the density-dependent collisional shift of ν_{10} across the magnetically trapped atomic ensemble [158, 84]. Consequently, we observe a dependence of γ_ϕ on the temperature T and on the mean density $\langle n \rangle$ of the atoms.

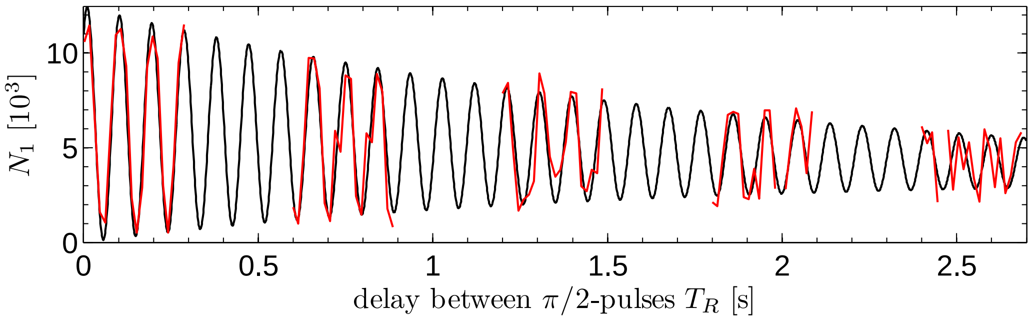

Figure 4.13: Decay of the Ramsey fringes as a function of T_R, for $d = 17$ μm, $\langle n \rangle = 3\times10^{12}$ cm^{-3}, and $T = 0.5$ μK. Each data point (connected by red lines to guide the eye) corresponds to a single shot of the experiment. A fit (black line) with Eq. (4.9) to the data yields $\gamma_d^{-1} = 2.6 \pm 0.7$ s and $\gamma_\phi^{-1} = 2.6 \pm 0.5$ s.

Temporal fluctuations of ν_{10} cause homogeneous dephasing. Because of the way the data in Fig. 4.13 was taken, with one shot of the experiment per data point, this shows up as increasing phase noise on the interference signal as T_R is increased. The frequency of the fluctuations is of importance. Low frequency fluctuations ($\sim 1/T_R$) are most harmful to the coherence time [162]. Faster fluctuations average out on the time scale T_R of a single shot of the experiment. The phase noise observed in our measurements can be attributed to slow ambient magnetic field fluctuations, and to fluctuations of the collisional shift due to shot-to-shot variations in N (see the atomic clock measurement below). Note that the setup in which these experiments were performed was not magnetically shielded. If we had used a magnetic-field sensitive transition, the coherence would have been lost in < 1 ms.

We have also performed measurements with a $\frac{\pi}{2}$-π-$\frac{\pi}{2}$ spin-echo pulse sequence. At very high $\langle n \rangle$, where the contrast in Ramsey-measurements decays on a time scale $\ll 1$ s, we were able to recover the interference with the spin-echo technique. This shows that inhomogeneous dephasing due to collisional shifts is the main decoherence mechanism at high $\langle n \rangle$. In measurements at low $\langle n \rangle$, such as in Fig. 4.13, where the coherence decays on a timescale of seconds, we did not observe significantly longer coherence times with the spin echo technique. This is a further indication that fluctuations of ν_{10} in time are dominant at large T_R.

4.8.4 Frequency-domain Ramsey fringes

Figure 4.14 shows frequency-domain Ramsey fringes for $T_R = 10$ ms. The width of the fringes in frequency space is given by $1/T_R$. For high resolution spectroscopy, narrow fringes and thus long T_R is desired, necessitating long trap and coherence lifetimes. For the atomic clock experiment in section 4.9 below, we use $T_R = 1$ s. The finite width of the envelope in Fig. 4.14 is one of the effects neglected in Eq. (4.8). It arises because the efficiency of the Ramsey pulses decays for $\Delta > \Omega_R$. In the following we concentrate on the fringes in the center of the envelope.

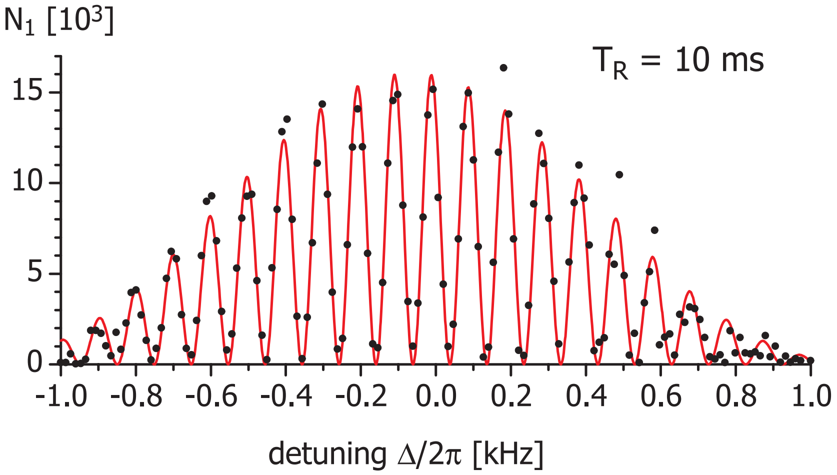

Figure 4.14: Frequency-domain Ramsey fringes in the microtrap.

4.8.5 Coherence lifetime vs. atom-surface distance

To further probe for surface effects, we study decoherence as a function of atom-surface distance d. At each distance, we record frequency-domain Ramsey fringes for several values of T_R and determine the contrast $C(T_R)$ of each fringe set. The fringe contrast $C(T_R) = (N_{\max} - N_{\min})/(N_{\max} + N_{\min})$ is obtained from a sinusoidal fit to the data, $N_{\max}$ ($N_{\min}$) is the maximum (minimum) of the oscillation in N_1. Figure 4.15 shows such measurements for $T_R = 50$ ms and $T_R = 1$ s in the trap at $d = 5$ μm, the smallest atom-surface distance at which coherence measurements were made. High contrast fringes are observed even though the trap lifetimes in this trap are only $\tau_0 = 1.4$ s and $\tau_1 = 1.1$ s, so that the atom number for $T_R = 1$ s is already considerably reduced by surface evaporation. The coherence of the atoms remaining in the trap is not disturbed by this loss.

Figure. 4.16 shows the observed contrast as a function of d. Within experimental error, the contrast does not show a dependence on atom-surface distance in the range of $d = 5 - 130$ μm. For $d < 5$ μm, trap loss due to surface evaporation prohibits coherence measurements with $T_R \sim 1$ s. To

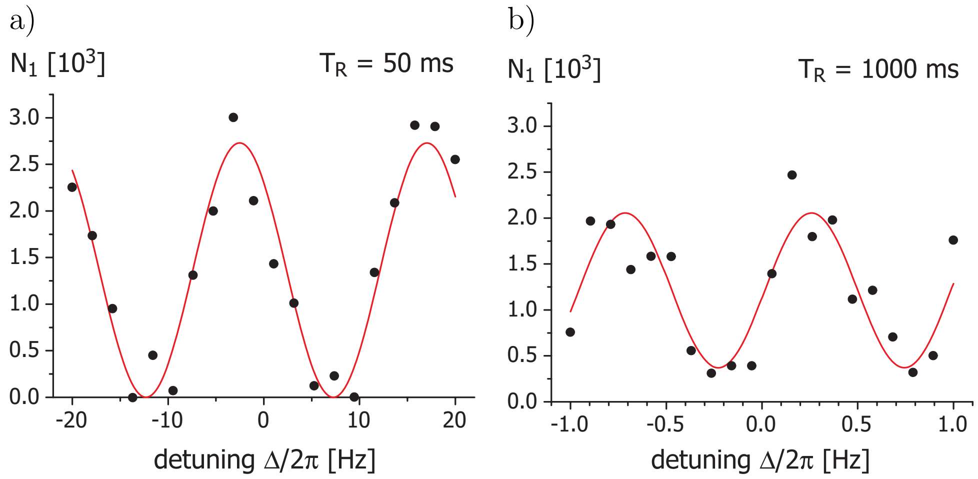

Figure 4.15: Frequency-domain Ramsey fringes in the trap at $d = 5\ \mu$m. (a) For $T_R = 50$ ms the fringe contrast is $C = 100^{+0}_{-10}\%$. (b) For $T_R = 1000$ ms, $C = 69 \pm 11\%$.

avoid systematic errors, we have checked that there is no systematic variation of T and $\langle n \rangle$ as d is varied.

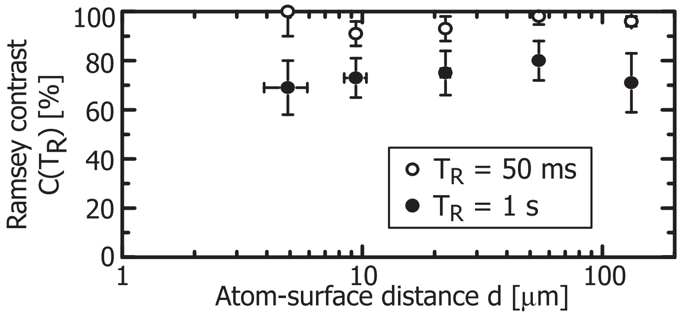

Figure 4.16: Contrast $C(T_R)$ of the Ramsey fringes as a function of atom-surface distance d for two values of T_R. The data points for $d = (5, 9, 22, 54, 132)\ \mu$m were measured with atomic ensembles of temperatures $T = (0.2, 0.6, 0.7, 0.6, 0.3)\ \mu$K and mean densities $\langle n \rangle = (14, 10, 5, 5, 18) \times 10^{11}\ \mathrm{cm}^{-3}$.

Additionally, we have analyzed the signal-to-noise ratio S/N of the interference signals, where S is the peak-to-peak amplitude of the sinusoidal fit to the Ramsey oscillation and N is the standard deviation of the fit residuals over one oscillation period. We typically observe $S/N = 6$ for $T_R = 1$ s, independent of d within experimental error. This indicates that the processes causing amplitude and phase fluctuations of the interference signal do not depend on atom-surface distance on this time scale, suggesting that they are of technical origin. In the quietest mode of operation, $S/N = 30$ can be achieved, see Fig. 4.17 below.

Conclusion

Our measurements show that internal-state coherence on our chip is limited by the same effects that limit internal-state coherence in macroscopic traps. Coherence lifetimes > 1 s can be achieved. Coherence is maintained down to atom-surface distances of a few micrometers where the trap vanishes due to the Casimir-Polder potential and the atoms stick to the surface. Still smaller d could be reached by using tighter traps, as shown in section 1.9, at the expense of increasing density and thus losses in state $|1\rangle$. The long coherence lifetimes are an extremely encouraging result for applications of atom chips. In the next section, I describe the first such application in precision measurement.

4.9 Atomic clock on a chip

One motivation for atom chip research is the perspective of creating miniaturized cold-atom devices. Due to the long coherence lifetime, it is natural to consider utilizing the $|0\rangle \leftrightarrow |1\rangle$ transition in an atomic clock on the chip. We demonstrate the principle of such a clock and measure its frequency stability relative to the quartz reference oscillator. This is a proof-of-principle experiment, and several straightforward improvements are discussed at the end.

4.9.1 Principle of the atomic clock

Figure 4.17(a) shows frequency-domain Ramsey fringes for $T_R = 1$ s. We set the two-photon drive to the slope of the Ramsey resonance and repeat the experiment many times with a cycle period of 23 s. Any temporal drift $\delta\nu$ of ν_{10} with respect to the quartz reference oscillator will change Δ and therefore show up as a variation δN_1 of N_1. Figure 4.17(b) shows such data for 1473 consecutive experiments with identical settings.

4.9.2 Allan variance

From repeated measurements of δN_1 we determine $\delta\nu = \delta N_1/(\pi C T_R N)$ and the relative frequency fluctuations $y = \delta\nu/\nu_{10}$. The stability of an atomic

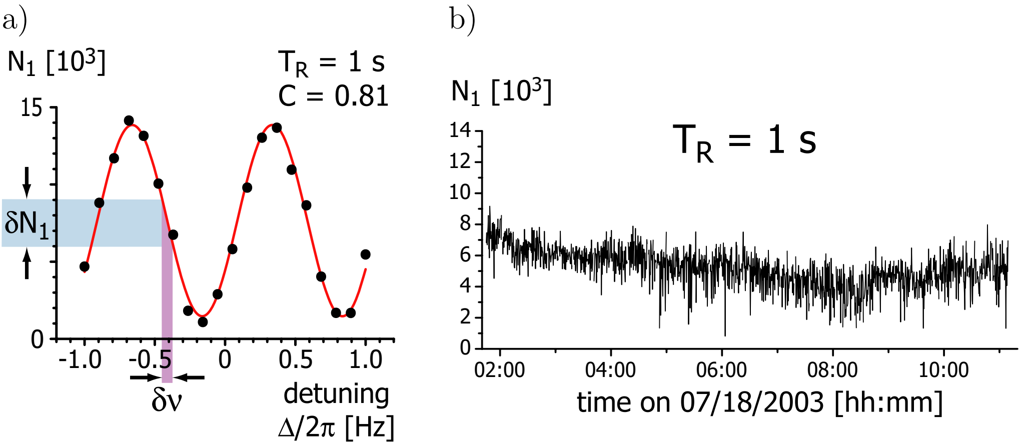

Figure 4.17: Atomic clock in the microtrap. (a) Ramsey resonance for $T_R = 1$ s at $d = 54\ \mu$m from the surface (solid circles). The line is a sinusoidal fit to the data. On the slope of the resonance, frequency fluctuations $\delta\nu$ lead to fluctuations δN_1 in the detected number of atoms. (b) Measurement of the frequency stability. The experiment is set to the slope of the resonance in (a) and N_1 is measured repeatedly.

clock is characterized by the Allan standard deviation [163] of y,

$$\sigma(\tau) = \sqrt{\frac{\sum_{k=1}^{M-1} (\bar{y}_k - \bar{y}_{k-1})^2}{2(M-1)}}, \quad \bar{y}_k = \frac{1}{\tau} \int_{t_k}^{t_k+\tau} y(t)dt, \tag{4.10}$$

where τ is the averaging time and $t_{k+1} = t_k + \tau$. In Fig. 4.18 we plot $\sigma(\tau)$ as a function of τ. For short τ, the Allan deviation decreases as $\sigma(\tau) = 1.7 \times 10^{-11}\ (\tau[\mathrm{s}])^{-1/2}$, corresponding to shot-to-shot fluctuations of $\delta\nu = 24$ mHz RMS. For $\tau > 6 \times 10^2$ s, the long-term drift of the quartz reference leads to a departure from the $\tau^{-1/2}$ line.

By performing measurements in which we alternate the setting of the experiment between a positive and a negative slope of the Ramsey fringe [163], we were able to separate random shot-to-shot fluctuations, most likely attributable to the atoms in the chip trap, from a slow drift in frequency, most likely caused by the quartz. In a practical implementation of our clock, such a signal would be used to lock the quartz frequency to the atomic resonance.

4.9.3 Analysis of the observed stability

We have estimated the shot-to-shot frequency fluctuations and can account for the observed value of $\delta\nu$. It is dominated by ambient magnetic field noise

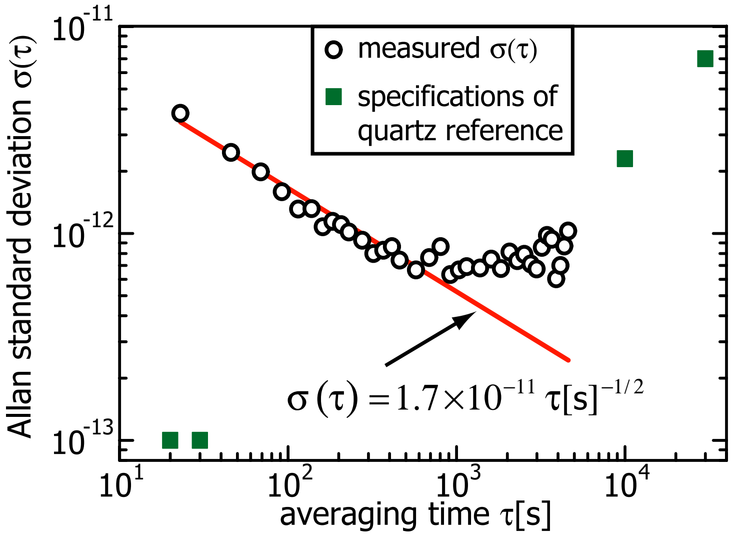

Figure 4.18: Measured Allan standard deviation $\sigma(\tau)$ of the atomic clock in the microtrap compared to the quartz reference oscillator (open circles). The solid line is a fit with $\sigma(\tau) \propto \tau^{-1/2}$ representing the performance of the atomic clock. For $\tau > 6 \times 10^2$ s the drift of the quartz reference becomes apparent. The manufacturers' specification of the quartz stability is shown in solid squares.

of $\delta B = 6$ mG RMS which we observe along the direction of B_0. From Eq. (4.3), we estimate the corresponding RMS frequency fluctuations to

$$\delta\nu_B = \sqrt{2}\, k(\delta B)^2 = 22 \text{ mHz}. \tag{4.11}$$

A second contribution arises from the collisional frequency shift [84], which is fluctuating due to fluctuations in the prepared atom number with $\delta N/N = 0.04$. At $\langle n\rangle = 4 \times 10^{11}$ cm^{-3}, this leads to fluctuations of

$$\delta\nu_c = \frac{2\hbar}{m}(a_{11} - a_{00})\langle n\rangle \frac{\delta N}{N} = -6 \text{ mHz}, \tag{4.12}$$

where a_{ii} are the scattering lengths given in appendix A.1. Furthermore, imperfections of the detection system contribute. In a single shot of the experiment, only N_1 is detected. Any fluctuation of N affects N_1 and will therefore also be interpreted as being due to frequency fluctuations. This contributes apparent fluctuations of

$$\delta\nu_N = \frac{1}{2\pi C T_R}\frac{\delta N}{N} = 7 \text{ mHz}. \tag{4.13}$$

Note that $\delta\nu_N$ and $\delta\nu_c$ are correlated, the relative sign depends on which slope of the Ramsey fringe is used. By detecting N_1 and N_0 (or N) in a single shot, it is possible to correct the data for atom number fluctuations. The fundamental detection limit is $\delta\nu_N = 1/(2\pi C T_R \sqrt{N})$, given by quantum projection noise [163].

4.9.4 Future improvements

We estimate that realistic improvements — magnetic shielding to $\delta B <$ 0.5 mG RMS, operation with $N = 10^5$ atoms at $T = 200$ nK in a shallower trap with $(f_x, f_y, f_z) = (5, 70, 70)$ Hz, projection-noise limited detection, and a 6 s cycle (which is realistic in a chip trap [29]) — will lead to a frequency stability of 2×10^{-13} $(\tau[\mathrm{s}])^{-1/2}$. While this does not reach the stability level of atomic fountain clocks, an atom-chip based clock has the advantage of a simple, compact and portable setup. Such a clock may find applications as a secondary standard with a small, portable "physics package". With a short-term stability approaching 10^{-13} $(\tau[\mathrm{s}])^{-1/2}$, it would outperform the best commercially available portable standards[4] by one order of magnitude.

In addition to stability, the accuracy of an atomic clock is of importance. We have not performed a detailed analysis of the systematics which lead to frequency shifts in our experiment. For a secondary standard, stability is the main concern, since it can be calibrated from time to time against a primary reference.

Motivated by the results reported here, an improved atom chip clock experiment is currently being set up by a team headed by P. Rosenbusch at l'Observatoire de Paris.

4.10 Conclusion

In conclusion, we have performed coherent internal-state manipulation in a magnetic microchip trap, with coherence and trap lifetimes exceeding 1 s at distances down to 5 μm from the chip surface. This paves the way for a variety of atom chip applications, most notably chip-based quantum gates and atomic clocks.

In chapter 6, an atom chip quantum gate is theoretically investigated which makes use of our robust state pair. A key role in this proposal is played by collisions of the qubit atoms in potentials which depend on the internal state. In the next chapter, I describe how the required internal-state selectivity can be added to our magnetic traps by microwave near-fields on the atom chip.

---

[4] The 5071A (www.symmttm.com). P. Rosenbusch, l'Observatoire de Paris, private communication.

Chapter 5

Microwave near-fields on atom chips

Microwave fields with large amplitudes and strong gradients arise in the near-field of microwave guiding structures on a chip. In this chapter, I show how such microwave near-fields can be used to manipulate atoms in chip traps. Via microwave dressing of hyperfine states it is possible to generate potentials for the atoms, in close analogy with the optical potentials used for optical lattices. Microwave potentials allow one to overcome some of the restrictions which apply to static magnetic traps. This makes microwave potentials a useful tool for atom chip experiments, such as the quantum gate proposed in chapter 6.

The chapter begins with the theory of microwave dressed-state potentials. The benefits of using microwave near-fields instead of far-field radiation are highlighted, and the resulting potentials are compared to static magnetic, optical dipole, and radio-frequency potentials. Then, I show how microwave guiding structures can be designed and integrated on a chip. An experimental characterization of such structures follows. An example for the use of microwave near-field potentials which will guide our discussion is sketched in Fig. 5.1. Microwave near-fields can be used to selectively remove the barrier of a static magnetic double well potential for one of the qubit states $|0\rangle$ or $|1\rangle$. Such a potential is required for the quantum gate in chapter 6. It can also be employed for the state-selective manipulation of BECs in atom interferometry, studies of the Josephson effect, and investigations of BEC entanglement (see chapter 8). A simulation of the potential concludes this chapter.

The theory of microwave near-field potentials on atom chips is also covered in our publications [87, 164, 165].

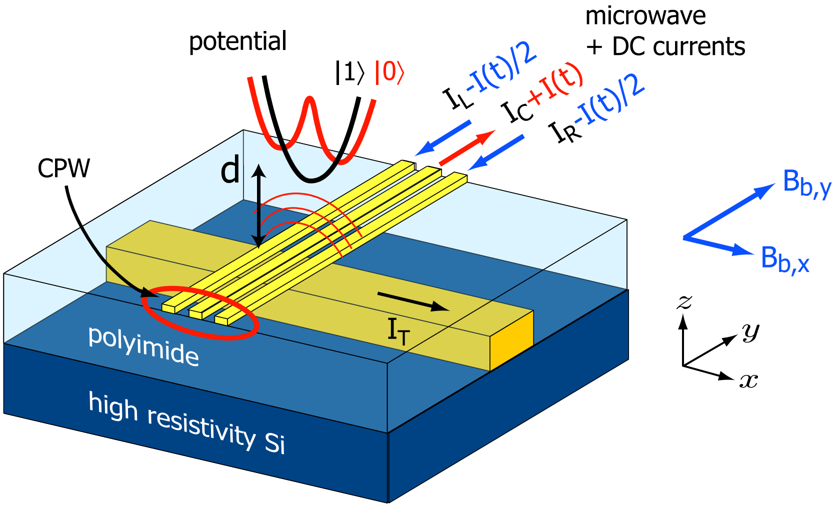

Figure 5.1: State-dependent double well potential created in the near field ($d \approx 10\ \mu\text{m} \ll \lambda_{\text{mw}}$) of a microwave coplanar waveguide (CPW). DC currents (I_T, I_L, I_C, and I_R) and bias fields ($B_{b,x}$ and $B_{b,y}$) provide harmonic confinement in the yz-plane and a static magnetic double well along x. The barrier of the double well can be state-selectively removed by turning on the microwave current $I(t) = \text{Re}\,[I_{\text{mw}} e^{i\omega t}]$ (see also Figs. 5.10 and 5.11).

5.1 Theory of microwave potentials

We consider the hyperfine states $|F, m_F\rangle$ of the ^{87}Rb electronic ground state in a static magnetic field $\mathbf{B}$. The static field leads to a Zeeman shift of the energy levels. In addition, the atom is exposed to a microwave with a frequency $\omega/2\pi$ near the hyperfine splitting of 6.8 GHz. The atom interacts with both the magnetic field and the electric field of the microwave. The microwave magnetic field $\mathbf{B}_{\text{mw}}(t)$ couples the $|F = 1, m_F\rangle$ to the $|F = 2, m_F\rangle$ sublevels via magnetic dipole transitions. This leads to a "dressing" of the states, giving rise to energy shifts that depend on F and m_F, as shown schematically in Fig. 5.2. These energy shifts, which can also be understood as an AC Zeeman effect (the magnetic analog of the AC Stark effect which gives rise to optical dipole potentials), are the main effect of the microwave. In addition, the microwave electric field $\mathbf{E}_{\text{mw}}(t)$ leads to an AC Stark shift, which is identical for all states $|F, m_F\rangle$ and usually much smaller than the effect of the microwave magnetic field.

In the following discussion, $\mathbf{B} \equiv \mathbf{B}(\mathbf{r})$, $\mathbf{B}_{\text{mw}}(t) \equiv \mathbf{B}_{\text{mw}}(\mathbf{r}, t)$, and $\mathbf{E}_{\text{mw}}(t) \equiv \mathbf{E}_{\text{mw}}(\mathbf{r}, t)$ are the fields seen by the atom at a given point $\mathbf{r}$ in space. Our task is to determine the eigenenergies of the atom at $\mathbf{r}$. To calculate the potentials, we will then make use of the adiabatic approximation by assuming that the

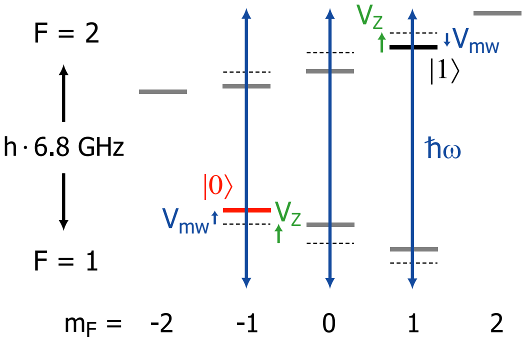

Figure 5.2: Hyperfine levels in a static magnetic and microwave field (shown here for a microwave with π-polarization and frequency ω detuned above resonance). The static field causes a static Zeeman shift V_Z, which is nearly identical for $|0\rangle$ and $|1\rangle$, while the microwave magnetic field causes an AC Zeeman shift V_{mw}, which has opposite sign for $|0\rangle$ and $|1\rangle$.

atom remains in a local energy eigenstate as it moves around (see section 5.1.3 below).

5.1.1 Effect of the microwave magnetic field

In this section we discuss in some detail how the eigenenergies of an atom in the magnetic fields $\mathbf{B}$ and $\mathbf{B}_{\mathrm{mw}}(t)$ can be calculated. This requires a diagonalization of the atomic Hamiltonian in the presence of hyperfine coupling, static Zeeman effect, and microwave coupling. We start from the most general case and subsequently introduce several approximations. We employ the dressed-state picture [166], treating the microwave field quantum-mechanically. Although the microwave fields in our experiments are essentially classical, a quantum description has the advantage that the Hamiltonian can be made time-independent by choosing the Schrödinger representation [151].

The Hamiltonian of the coupled system

$$H = H_A + H_F + H_{AF} \tag{5.1}$$

consists of the Hamiltonian H_A of the atom in the presence of the static field only, the Hamiltonian H_F of the microwave field, and the Hamiltonian H_{AF} of the atom-microwave interaction. The Hamiltonian of the atom

$$H_A = A_{\mathrm{hfs}}\mathbf{I}\cdot\mathbf{J} + \mu_B B\left(g_J J_z + g_I I_z\right) \tag{5.2}$$

is the Breit-Rabi Hamiltonian of Eq. (1.4), with eigenstates $|F, m_F\rangle$ and eigenenergies E_{F,m_F} given by Eq. (1.5). Defined in this way, the $|F, m_F\rangle$

depend on B. We have chosen our quantization axis along the local direction of the static field, so that $\mathbf{B} = B\mathbf{e}_z$. The hyperfine splitting at $B = 0$ is $\hbar\omega_{\mathrm{hfs}} = 2A_{\mathrm{hfs}}$. The Hamiltonian of the quantized microwave field is

$$H_F = \hbar\omega(a^+a + \tfrac{1}{2}), \tag{5.3}$$

where a^+ (a) are the conventionally defined creation (annihilation) operators of the microwave field mode of frequency ω. Eigenstates of H_F are the photon number states $|n\rangle$, with $a^+a|n\rangle = n|n\rangle$. Spontaneous emission is negligible at microwave frequencies and the atom interacts only with the macroscopically occupied mode at frequency ω. We define the microwave detuning $\Delta_0 = \omega - \omega_{\mathrm{hfs}}$ with respect to the resonance at $B = 0$.

The energy eigenstates of the uncoupled system $H_A + H_F$ are the "bare" states $|F, m_F\rangle|n\rangle$, with the corresponding eigenvalues

$$E(F, m_F, n) = E_{F,m_F} + \hbar\omega\left(n + \tfrac{1}{2}\right). \tag{5.4}$$

The $E(F, m_F, n)$ form a "ladder" of energy levels, sketched in Fig. 5.3, with groups of 8 states separated by multiples of $\hbar\omega$. The figure shows $E(F, m_F, n)$ for $\mu_B B \ll \hbar\omega_{\mathrm{hfs}}$, $|\Delta_0| \ll \omega$, and $\Delta_0 > 0$. Note, however, that Eq. (5.4) is completely general.

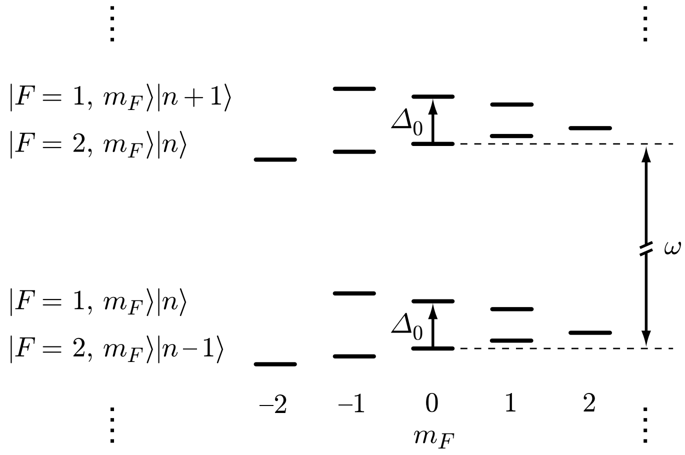

Figure 5.3: "Ladder" of energy levels $E(F, m_F, n)$ of the uncoupled system ($B_{\mathrm{mw}} = 0$), sketched for $\Delta_0 > 0$ and weak static magnetic field.

The interaction Hamiltonian is given by the coupling of the microwave magnetic field to the magnetic moment of the atom,

$$H_{AF} = \mu_B\,(g_J\mathbf{J} + g_I\mathbf{I}) \cdot \hat{\mathbf{B}}_{\mathrm{mw}}. \tag{5.5}$$

In the Schrödinger picture, the quantized field operator is

$$\hat{\mathbf{B}}_{\mathrm{mw}} = \sqrt{\frac{\hbar\omega\mu_0}{2V}}\left(\boldsymbol{\epsilon} a + \boldsymbol{\epsilon}^* a^+\right), \tag{5.6}$$

where $\boldsymbol{\epsilon}$ is a unit polarization vector and V is the quantization volume. Note that $\hat{\mathbf{B}}_{\mathrm{mw}}$ is real but $\boldsymbol{\epsilon}$ may be complex, e.g. to describe circular polarization. A quasi-classical field is described by a coherent state

$$|\alpha\rangle = \exp\left(-\tfrac{1}{2}|\alpha|^2\right)\sum_{n=0}^{\infty}\frac{\alpha^n}{\sqrt{n!}}|n\rangle, \tag{5.7}$$

expressed in terms of photon number states $|n\rangle$. For a mean photon number $\bar{n} = |\alpha|^2 \gg 1$, the uncertainty in photon number is $\Delta n = \sqrt{\bar{n}} \ll \bar{n}$, so that only values of n near $\bar{n}$ contribute significantly to $|\alpha\rangle$. We will make use of this property below. In the Schrödinger picture, the state $|\alpha\rangle$ carries the time dependence via $\alpha(t) = |\alpha|e^{-i\omega t}$ (we include the phase at $t = 0$ in the complex $\boldsymbol{\epsilon}$). Classically, the magnetic field is described by

$$\mathbf{B}_{\mathrm{mw}}(t) = \frac{B_{\mathrm{mw}}}{2}\left(\boldsymbol{\epsilon} e^{-i\omega t} + \boldsymbol{\epsilon}^* e^{i\omega t}\right). \tag{5.8}$$

Correspondence between the two descriptions requires $\langle\alpha(t)|\hat{\mathbf{B}}_{\mathrm{mw}}|\alpha(t)\rangle = \mathbf{B}_{\mathrm{mw}}(t)$. This yields

$$B_{\mathrm{mw}} = 2\sqrt{\bar{n}}\sqrt{\frac{\hbar\omega\mu_0}{2V}}, \tag{5.9}$$

which allows us to eliminate V in favor of the classical field amplitude B_{mw}. We thus obtain

$$H_{AF} = \frac{\mu_B B_{\mathrm{mw}}}{2\sqrt{\bar{n}}}\left\{g_J\left[(\boldsymbol{\epsilon}\cdot\mathbf{J})a + (\boldsymbol{\epsilon}^*\cdot\mathbf{J})a^+\right] + g_I\left[(\boldsymbol{\epsilon}\cdot\mathbf{I})a + (\boldsymbol{\epsilon}^*\cdot\mathbf{I})a^+\right]\right\}. \tag{5.10}$$

The Hamiltonian H_{AF} couples the bare states $|F, m_F\rangle|n\rangle$. Only states which differ in n by ± 1 are coupled by the operators a and a^+. When we take the corresponding matrix elements, see below, we encounter terms of the form $\langle n-1|a|n\rangle = \sqrt{n}$ and $\langle n+1|a^+|n\rangle = \sqrt{n+1}$. Because $n \approx \bar{n} \gg 1$ for the relevant $|n\rangle$ contributing to the coherent state, we can approximate[1] these matrix elements by $\sqrt{\bar{n}}$, which cancels the factor $1/\sqrt{\bar{n}}$ in Eq. (5.10). For our quasi-classical coherent field, the matrix elements of H_{AF} are thus approximately independent of n and $\bar{n}$. The strength of the microwave field enters only through the classical field amplitude B_{mw}.

---

[1] For $B_{\mathrm{mw}} = 1$ G, Eq. (5.9) yields $\bar{n}/V \sim 10^{21}$ m^{-3}.

The energy eigenstates of the coupled system H are the so-called "dressed" states [166], which we denote $|K,n\rangle$, with corresponding energy levels $E(K,n)$. For experimentally relevant parameters (see below), the dressed states fall into groups of 8 energy levels separated by multiples of $\hbar\omega$, similar to the bare states. We label the members of one group by $K = 1\ldots 8$, the different groups are labeled by n. This does not imply that the $|K,n\rangle$ are eigenstates of the photon number; the $|K,n\rangle$ are (in general complicated) superpositions of bare states $|F,m_F\rangle|n\rangle$ with different n.

General solution

The dressed states can be obtained in the most general case by numerical diagonalization of the full Hamiltonian H, Eqs. (5.2), (5.3), and (5.10). This calculation is beyond the scope of the present discussion, but I briefly comment on how I have done it. A convenient set of basis states to set up the calculation is $|m_I,m_J\rangle|n\rangle$, using the eigenstates of I_z and J_z, $|m_I,m_J\rangle \equiv |I=\frac{3}{2},m_I\rangle|J=\frac{1}{2},m_J\rangle$ for the atom. The matrix elements of H_{AF} are more readily evaluated in this basis than in $|F,m_F\rangle$, which depend on B because they are eigenstates of H_A. For the microwave, we use a truncated Fock space, including a few values of n around $\bar{n}$ in order to allow for effects beyond the rotating-wave approximation. The only assumption which we have made up to this point is that the microwave is in a coherent field state. With this approximation, our formalism is equivalent to Floquet theory [167], and the resulting $E(K,n)$ are periodic in n. Since we are not interested in details of the field state, we can take $E(K) = E(K,n=\bar{n}) - E_o$ to describe the energy of the atom, where E_o is an energy offset, including the term $\bar{n}\hbar\omega$. The resulting $E(K)$, which include effects of the nuclear spin and effects beyond the rotating-wave approximation, allow one to study subtle phenomena such as the location of the "sweet spot" in the energy splitting of $|0\rangle$ and $|1\rangle$ (cf. Fig. 1.2), which is shifted away from $B = 3.229$ G by the microwave. For most other purposes, however, it is sufficient to use a simpler solution for the dressed state energies, which is obtained by making the following approximations.

Approximations

Our system is characterized by four energies: the zero-field hyperfine splitting $\hbar\omega_{\mathrm{hfs}}$, the static Zeeman energy $\mu_B B$, the microwave detuning $\hbar\Delta_0$, and the microwave coupling strength $\mu_B B_{\mathrm{mw}}$. Typically, $\hbar\omega_{\mathrm{hfs}}$ is by far the largest energy. The three other energies are widely tunable and may all be of comparable magnitude.

For $\mu_B B \ll \hbar\omega_{\rm hfs}$ and $|\Delta_0| \ll \omega_{\rm hfs}$ (and therefore also $|\Delta_0| \ll \omega$), the bare energy levels fall into sets of 8 nearly degenerate levels, see Fig. 5.3 above. If furthermore $\mu_B B_{\rm mw} \ll \hbar\omega$, which is well satisfied in experiments, the rotating wave approximation can be made. It consists in including only the microwave couplings within a given set of levels, and neglecting the coupling between different sets. We thus restrict our attention to the 8 states

$$\mathcal{S}(n) = \{|F=1, m_F=-1\dots 1\rangle|n+1\rangle, |F=2, m_F=-2\dots 2\rangle|n\rangle\}\,, \tag{5.11}$$

which form a basis of one of the sets.

Furthermore, we treat the static Zeeman effect perturbatively, which is a good approximation for $\mu_B B \ll \hbar\omega_{\rm hfs}$, and neglect the coupling of $\mathbf{I}$ to B, because $|g_I/g_J| \sim 10^{-3}$. In this approximation, one neglects the dependence of $\mathcal{S}(n)$ on B by taking $|F, m_F\rangle$ equal to the eigenstates of H_A at $B=0$, given in appendix A.3. The energies to first order in B are

$$E_{F,m_F} \approx \delta_{F,2}\,\hbar\omega_{\rm hfs} + m_F \frac{g_F}{|g_F|}\hbar\omega_L + \text{const.}, \tag{5.12}$$

where $\delta_{i,j}$ is the Kronecker delta and $\omega_L = \mu_B B/2\hbar$ is the Larmor frequency for $|g_F| = \frac{1}{2}$. With these approximations, we can express the Hamiltonian of the uncoupled system in the basis $\mathcal{S}(n)$ as

$$\begin{aligned} H_A + H_F = &\sum_{m_2} \left(-\tfrac{1}{2}\hbar\Delta_0 + \hbar\omega_L m_2\right) |2,m_2\rangle|n\rangle\langle n|\langle 2,m_2| \\ &+ \sum_{m_1} \left(\tfrac{1}{2}\hbar\Delta_0 - \hbar\omega_L m_1\right) |1,m_1\rangle|n+1\rangle\langle n+1|\langle 1,m_1|. \end{aligned} \tag{5.13}$$

We have dropped constant terms, including the term $n\hbar\omega$, which is a common energy offset for the states in $\mathcal{S}(n)$.

The full expression for H_{AF}, Eq. (5.10), includes couplings of the microwave magnetic field to $\mathbf{J}$ and $\mathbf{I}$. Again, because $|g_I/g_J| \sim 10^{-3}$, the coupling to $\mathbf{I}$ is much weaker and can be neglected to a good approximation. We now take matrix elements of H_{AF} between the states in $\mathcal{S}(n)$, noting that states with identical F do not couple because of the selection rules imposed by a and a^+. We define the Rabi frequencies Ω_{1,m_1}^{2,m_2} by

$$\begin{aligned} \tfrac{1}{2}\hbar\Omega_{1,m_1}^{2,m_2} &\equiv \langle n|\langle 2,m_2|H_{AF}|1,m_1\rangle|n+1\rangle \\ &= \tfrac{1}{2}\mu_B g_J B_{\rm mw}\frac{\langle n|a|n+1\rangle}{\sqrt{\bar{n}}}\langle 2,m_2|\boldsymbol{\epsilon}\cdot\mathbf{J}|1,m_1\rangle \\ &\approx \mu_B B_{\rm mw}\langle 2,m_2|\boldsymbol{\epsilon}\cdot\mathbf{J}|1,m_1\rangle, \end{aligned} \tag{5.14}$$

where we have used $g_J \approx 2$ and $\langle n|a|n+1\rangle \approx \sqrt{\bar{n}}$ for the states $|n\rangle$ contributing to the coherent field state, as discussed above. The angular momentum matrix elements $\langle 2, m_2|\boldsymbol{\epsilon}\cdot\mathbf{J}|1, m_1\rangle$ are calculated in appendix A.3. The coupling Hamiltonian becomes

$$H_{AF} = \sum_{m_1,m_2} \left[\tfrac{1}{2}\hbar\Omega^{2,m_2}_{1,m_1}|2, m_2\rangle|n\rangle\langle n+1|\langle 1, m_1| + \text{c.c.}\right] . \tag{5.15}$$

With these approximations, H does not depend on the set of levels (i.e. the value of n) we have chosen, and we might as well suppress the reference to the field state completely,

$$\begin{aligned} H = &\sum_{m_2} \left(-\tfrac{1}{2}\hbar\Delta_0 + \hbar\omega_L m_2\right) |2, m_2\rangle\langle 2, m_2| \\ &+ \sum_{m_1} \left(\tfrac{1}{2}\hbar\Delta_0 - \hbar\omega_L m_1\right) |1, m_1\rangle\langle 1, m_1| \\ &+ \sum_{m_1,m_2} \left[\tfrac{1}{2}\hbar\Omega^{2,m_2}_{1,m_1}|2, m_2\rangle\langle 1, m_1| + \text{c.c.}\right] . \end{aligned} \tag{5.16}$$

In our simulations of microwave potentials, we usually work at this level of approximation and obtain the dressed states $|K\rangle$ and corresponding energy levels $E(K)$ by numerical diagonalization of the 8×8-matrix for H in Eq. (5.16). Results are shown in Figs. 5.4 and 5.5. Within the figure resolution, the results are indistinguishable from the exact solution obtained using Eqs. (5.2), (5.3), and (5.10).

Dressed-state energies

In Fig. 5.4, the $E(K)$ are shown as a function of Δ_0 for a weak microwave field, $B_{\text{mw}} \ll B$, and all polarization components equally strong. The microwave coupling gives rise to 9 anticrossings, 3 for each microwave polarization. Each anticrossing is associated with one of the Ω^{2,m_2}_{1,m_1}. Since $B_{\text{mw}} \ll B$ and thus $|\Omega^{2,m_2}_{1,m_1}| \ll \omega_L$, the anticrossings are well separated. By varying Δ_0, it is possible to tune into the various anticrossings and selectively shift the energy of the hyperfine states with the microwave. This leads to great flexibility in the design of state-dependent potentials. The states $|K\rangle$ are superpositions of the bare states $|F, m_F\rangle$. The line colors of the levels $E(K)$ in Fig. 5.4 indicate which of the $|F, m_F\rangle$ is the dominant contribution to $|K\rangle$. Far away from the resonances, each $|K\rangle$ is nearly identical to one of the $|F, m_F\rangle$, as labeled in the figure. For the well separated anticrossings of Fig. 5.4, the situation is relatively simple. An anticrossing between the bare

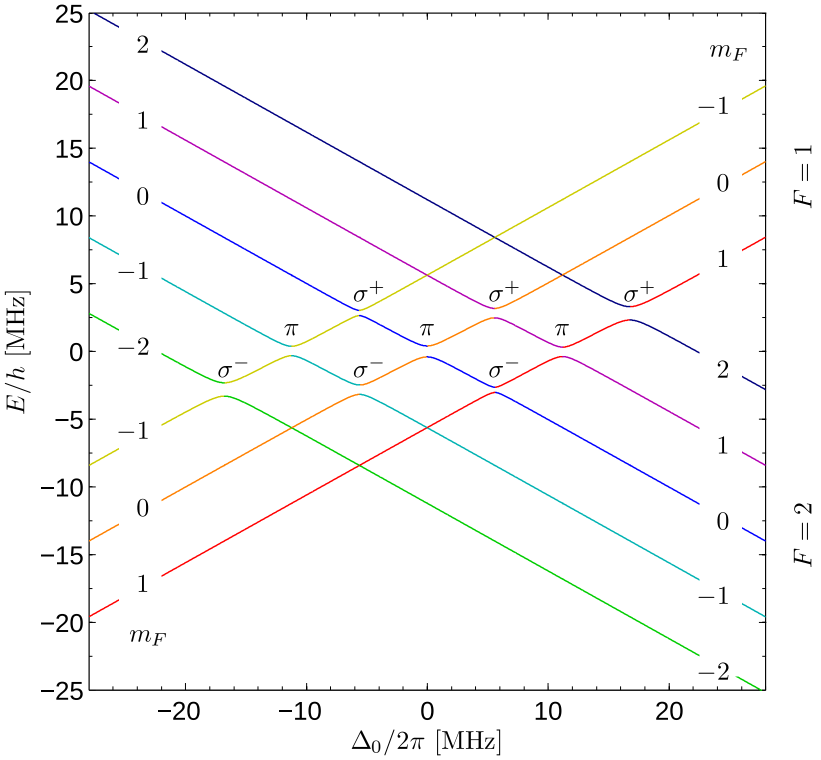

Figure 5.4: Microwave dressed-state energy levels $E(K)$ as a function of Δ_0, for $B = 8$ G, $B_{\text{mw}} = 1$ G, and $\boldsymbol{\epsilon} = \frac{1}{\sqrt{3}}(1, 1, 1)$. The avoided crossings are associated with the indicated microwave polarization components. The line color indicates which bare state is dominant in the dressed state.

states $|1, m_1\rangle$ and $|2, m_2\rangle$ occurs if the detuning

$$\Delta_{1,m_1}^{2,m_2} = \Delta_0 - (m_2 + m_1)\omega_L \tag{5.17}$$

vanishes but the corresponding Ω_{1,m_1}^{2,m_2} is non-vanishing.[2] Near a given resonance, only the two bare states which form the anticrossing contribute significantly to the two dressed states. The energy splitting between the states can then be approximately described with the usual formula for a two-state system [166],

$$E_+ - E_- \approx \hbar\sqrt{|\Omega_{1,m_1}^{2,m_2}|^2 + |\Delta_{1,m_1}^{2,m_2}|^2}, \tag{5.18}$$

---

[2] If both $\Delta_{1,m_1}^{2,m_2} = 0$ and $\Omega_{1,m_1}^{2,m_2} = 0$, the levels cross, as can be seen in Fig. 5.4. For strong B_{mw}, additional anticrossings appear due to higher-order effects.

where + (−) refers to the upper (lower) dressed state. The splitting on resonance is $\hbar|\Omega_{1,m_1}^{2,m_2}|$. The energy shift due to the microwave is

$$V_{\mathrm{mw}}^{\pm} = \pm\frac{\hbar}{2}\left[\sqrt{|\Omega_{1,m_1}^{2,m_2}|^2 + |\Delta_{1,m_1}^{2,m_2}|^2} - |\Delta_{1,m_1}^{2,m_2}|\right]. \tag{5.19}$$

Such a two-state description is also possible for strong B_{mw} if only one microwave polarization component is present, so that each bare state $|1, m_1\rangle$ is only coupled to one bare state $|2, m_2\rangle$. For strong B_{mw} and general microwave polarization, simple analytical formulae for $E(K)$ do not exist and the $|K\rangle$ are complicated superpositions of several bare states $|F, m_F\rangle$.

In Fig. 5.5, the $E(K)$ are shown as a function of B_{mw}, for pure π-polarization of the microwave, as in Fig. 5.2 at the beginning of this chapter. The parameters Δ_0 and B are fixed such that all Δ_{1,m_1}^{2,m_2} have the same sign. In this case, the microwave shifts the levels of $F = 1$ and $F = 2$ in opposite directions, leading to a differential potential for the qubit states $|0\rangle$ and $|1\rangle$. The magnitude of the shift is not identical for $|0\rangle$ and $|1\rangle$, because the relevant Δ_{1,m_1}^{2,m_2} are different. The levels $|F = 2, m_F = \pm 2\rangle$ are not shifted because they do not couple to π-polarization. In the trap simulations below, the main contribution to the differential potential of $|0\rangle$ and $|1\rangle$ is due to π-polarization, but other polarization components contribute as well.

Energy shifts in the regime of large detuning

If the microwave is far detuned from all transitions, $|\Delta_{1,m_1}^{2,m_2}|^2 \gg |\Omega_{1,m_1}^{2,m_2}|^2$ for all m_1 and m_2, the states $|F, m_F\rangle$ are only weakly coupled. The effect of H_{AF} can then be evaluated in time-independent perturbation theory [151]. Each dressed state $|K\rangle$ is approximately equal to one of the bare states $|F, m_F\rangle$, the amplitude of other states in $|K\rangle$ is only of order $\Omega_{1,m_1}^{2,m_2}/2\Delta_{1,m_1}^{2,m_2}$. This is the regime in which optical dipole potentials are usually operated in order to avoid spontaneous emission. For microwaves, spontaneous emission is negligible, but a large detuning has the advantage that the coherence properties of the states $|0\rangle$ and $|1\rangle$ are only weakly modified by the "contamination" with other states which have different magnetic moments.

In this regime, the energy of state $|K\rangle \approx |F, m_F\rangle$ is

$$E(K) \approx E_0^F + V_Z^{F,m_F} + V_{\mathrm{mw}}^{F,m_F}. \tag{5.20}$$

The offset $E_0^F = \pm\frac{1}{2}\hbar\Delta_0$ with + (−) for $F = 1$ ($F = 2$) is spatially homogeneous and does not lead to a potential. The static Zeeman shift is

$$V_Z^{F,m_F} = \mu_B g_F m_F B. \tag{5.21}$$

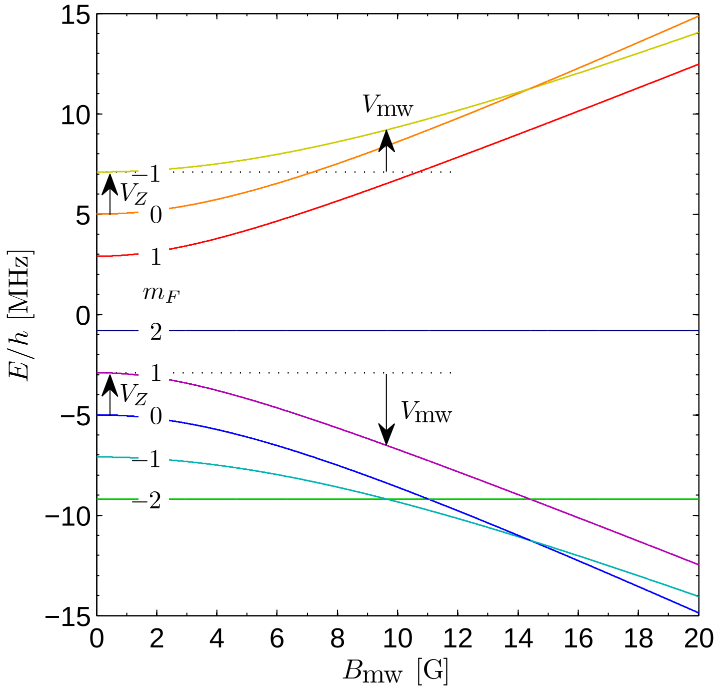

Figure 5.5: Microwave dressed-state energy levels $E(K)$ as a function of $B_{\rm mw}$, for $B = 3$ G, $\Delta_0/2\pi = 10$ MHz, and $\boldsymbol{\epsilon} = (0, 0, 1)$. This is the situation of Fig. 5.2, shown here in the dressed-state picture. Line colors as in Fig. 5.4.

The microwave gives rise to the AC Zeeman shift $V_{\rm mw}^{F,m_F}$. For the sublevels of $F = 1$, it is

$$V_{\rm mw}^{1,m_1} = \frac{\hbar}{4} \sum_{m_2} \frac{|\Omega_{1,m_1}^{2,m_2}|^2}{\Delta_{1,m_1}^{2,m_2}}, \tag{5.22}$$

while for $F = 2$, it is

$$V_{\rm mw}^{2,m_2} = -\frac{\hbar}{4} \sum_{m_1} \frac{|\Omega_{1,m_1}^{2,m_2}|^2}{\Delta_{1,m_1}^{2,m_2}}. \tag{5.23}$$

The AC Zeeman shift of $|F, m_F\rangle$ in the limit or large detuning thus equals the sum of the energy shifts due to the individual transitions connecting to this level.

5.1.2 Effect of the microwave electric field

The microwave electric field

$$\mathbf{E}_{\rm mw}(t) = \frac{E_{\rm mw}}{2} \left(\boldsymbol{\kappa} e^{-i\omega t} + \boldsymbol{\kappa}^* e^{i\omega t} \right) \tag{5.24}$$

also gives rise to energy shifts. It polarizes the atoms, leading to a time-averaged quadratic Stark shift

$$V_{\text{el}} = -\frac{\alpha_0}{4} E_{\text{mw}}^2, \tag{5.25}$$

where α_0 is the static polarizability of the ^{87}Rb ground state. In (5.25), we have averaged over the fast oscillation of the microwave at frequency ω, which is much faster than the atomic motion. Because V_{el} depends only on the field magnitude E_{mw}, the polarization and phase of $\mathbf{E}_{\text{mw}}(t)$ are irrelevant. Equation (5.25) is actually the DC limit of optical dipole potentials [168], for a frequency ω which is far below any transitions which can be driven by $\mathbf{E}_{\text{mw}}(t)$. Since all levels $|F, m_F\rangle$ belong to the electronic ground state, their static polarizabilities are equal, and the energy shift V_{el} is the same for all levels.

The field strengths E_{mw} and B_{mw} are related. For microwave radiation in free space, $E_{\text{mw}} = cB_{\text{mw}}$. Although this relation is not generally valid in the near field (see below), we use it to roughly estimate how V_{el} compares to V_{mw}. For typical microwave field strengths (B_{mw} a few Gauss), we find $V_{\text{el}} \ll V_{\text{mw}}$. Since both V_{el} and V_Z are (nearly) identical for $|0\rangle$ and $|1\rangle$, it is furthermore possible to compensate for V_{el} by a corresponding adjustment in V_Z, if desired.

5.1.3 Adiabatic potentials

The dressed state energies $E(K)$ turn into a state-dependent potential landscape if the fields $\mathbf{B}$ and $\mathbf{B}_{\text{mw}}(t)$ are position dependent. If the motion of the atom is sufficiently slow, its internal state follows adiabatically the spatially varying fields, and the atom always remains in the dressed state $|K\rangle$ in which it was prepared. As a rough guideline, the adiabatic approximation is valid if the trap frequency is much smaller than the frequency splitting between $|K\rangle$ and the closest other dressed state $|K'\rangle$ to which a transition is allowed [169]. Then, motion-induced transitions are exponentially suppressed. The same approximation is also made in static magnetic traps (cf. section 1.2). The adiabatic approximation also applies to modulations in time of the microwave power or detuning, if the modulation is sufficiently slow.

In calculating the adiabatic potentials, one has to be careful because a position dependence of $\mathbf{B}$ implies that our quantization axis is position dependent. To calculate the potentials at $\mathbf{r}$, we choose coordinates in which the quantization axis is along the local direction of $\mathbf{B}(\mathbf{r})$. We then determine the microwave polarization $\boldsymbol{\epsilon}(\mathbf{r})$ in this local coordinate system in order to calculate the matrix elements for $\Omega_{1,m_1}^{2,m_2}(\mathbf{r})$ in Eq. (5.14). All other parameters, such as $B_{\mathrm{mw}}(\mathbf{r})$ or $\Delta^{2,m_2}_{1,m_1}(\mathbf{r})$, are scalar and do not depend on the orientation of the quantization axis. The dressed-state potentials $E(K,\mathbf{r})$ are then obtained by numerical diagonalization of $H(\mathbf{r})$, or, in the limit of large detuning, from Eqs. (5.21), (5.22), and (5.23). This procedure is repeated at every point $\mathbf{r}$. The AC Stark potential $V_{\mathrm{el}}(\mathbf{r})$ is calculated from $E^2_{\mathrm{mw}}(\mathbf{r})$, which does not depend on the orientation of the coordinates. The overall potential for state $|K\rangle$ used in our simulations is thus

$$U_K(\mathbf{r}) = E(K,\mathbf{r}) + V_{\mathrm{el}}(\mathbf{r}) + V_o(\mathbf{r}), \tag{5.26}$$

where $V_o(\mathbf{r})$ indicates additional terms, e.g. due to gravity or the Casimir-Polder surface potential.

5.2 Advantages of using microwave near-fields

A trap for neutral atoms based on microwave potentials has already been realized in the 1990s [170, 171]. This trap employed microwave radiation in the far field of the source. Unlike in the case of optical radiation, which can be tightly focussed due to its short wavelength, the long wavelength of microwave radiation ($\lambda_{\mathrm{mw}} = 4.4$ cm at 6.8 GHz) poses severe limitations on far-field traps: field gradients are very weak, even at very high microwave power, and structuring the potential on the micrometer scale is impossible. In [171], a microwave power of 83 W was resonantly enhanced in a cavity to a circulating power of 0.5 MW. Still, the microwave potential alone was too weak to hold the atoms against gravity. We speculate that because of these difficulties, the technique was abandoned after the initial experiment [171].

On atom chips, there is a natural solution to these problems [87]. The atoms are trapped at distances $d \ll \lambda_{\mathrm{mw}}$ from the chip surface. Thus, they can be manipulated with microwave near fields, generated by microwave signals in on-chip transmission lines [172], as illustrated in Fig. 5.1 above. In the near field of the source currents and voltages, the microwave fields have the same position dependence as the static fields created by equivalent stationary sources [68]. The maximum field gradients depend on the size of the transmission line conductors and on the atom-wire distance d, not on λ_{mw}. Already milliwatts of microwave power result in sufficiently strong gradients, and state-dependent potentials varying on the micrometer scale can be realized.

Consider a waveguide on a chip with a characteristic impedance of $Z_c = 50\ \Omega$ carrying a microwave signal of $P = 10$ mW, corresponding to a microwave current amplitude of $I_{\mathrm{mw}} = \sqrt{2P/Z_c} = 20$ mA on the signal conductor. At a distance of $d = 10\ \mu$m from the conductor, the microwave magnetic field amplitude is of order $B_{\mathrm{mw}} \approx \mu_0 I_{\mathrm{mw}}/(2\pi d) = 4.0$ G, and the gradient is $B'_{\mathrm{mw}} \approx B_{\mathrm{mw}}/d = 4 \times 10^3$ G/cm. The microwave induces a coupling with a Rabi frequency of the order of $\Omega_{\mathrm{mw}}/2\pi \approx \mu_B B_{\mathrm{mw}}/h = 5.6$ MHz. The order of magnitude of microwave potentials is given by $\hbar\Omega_{\mathrm{mw}}$. The high Ω_{mw}, which varies on a micrometer scale, leads to strong potential gradients.

Microwave potentials may arise because of gradients in microwave field strength $B_{\mathrm{mw}}(\mathbf{r})$, because of gradients in detuning caused by $B(\mathbf{r})$, or because of polarization gradients $\boldsymbol{\epsilon}(\mathbf{r})$, i.e. a spatial dependence of the orientation of $\mathbf{B}_{\mathrm{mw}}(\mathbf{r}, t)$ relative to $\mathbf{B}(\mathbf{r})$. This leads to great flexibility in trap design. Even greater flexibility is possible if several microwave frequencies are combined in the same waveguide.

Comparison with static magnetic potentials

Dressed-state potentials are not subject to the same restrictions that limit static magnetic potentials. An interesting feature of the AC Zeeman shift is that the sign of V_{mw}^{F,m_F} can be controlled via the detuning. Therefore, all states $|F, m_F\rangle$ are trappable either in maxima or in minima of B_{mw}, including those which cannot be trapped in static magnetic fields. As explained in the context of Fig. 5.4, a suitable combination of microwave detuning, polarization, and static Zeeman splitting allows one to shift only selected levels. Furthermore, near-resonant state dressing allows one, in certain geometries, to create features in the potentials which are significantly smaller than the distance d of the atoms to the wires [43].

Comparison with optical potentials

The concept of microwave potentials is similar to the optical potentials created by nonresonant laser beams, which have been used with enormous success to generate potentials for the manipulation of ultracold atoms [16]. The main difference is that spontaneous emission is negligible between ground state sublevels, so that (near-)resonant coupling is possible in the case of microwaves. Interference effects, which lead to the periodic potentials of optical lattices, cannot be used to the same extent with microwaves, because they arise only on the centimeter scale of λ_{mw}. Instead, a suitable arrangement of chip wires is necessary to structure the potential in the near-field, similar to the case of static magnetic traps (cf. section 1.5).

Comparison with radio-frequency potentials

Similar to the microwave potentials considered here, which arise from coupling hyperfine states with *different* F, radio-frequency potentials can be created by coupling m_F-sublevels within a single hyperfine state with *fixed* F. Adiabatic radio-frequency potentials have been investigated with great success in recent experiments [173, 46, 43]. Microwave potentials are more flexible than radio-frequency potentials, because the different transitions are split by the Zeeman effect (cf. Fig. 5.4), which allows one to tune into specific transitions and address hyperfine states selectively. With radio frequencies, all m_F sublevels are always simultaneously coupled. Furthermore, for the purpose of creating a differential potential for $|0\rangle$ and $|1\rangle$, microwaves are the natural choice, because the qubit states belong to different hyperfine states, and all microwave polarization components provide a differential shift. With radio-frequencies, a differential potential for these states can only be created with circular polarization.

A significant advantage of radio-frequency potentials is that radio-frequency currents can be readily coupled into the chip wires without technological difficulties. The wavelength is much longer than the size of the atom chip, so that resonances cannot occur, propagation effects are irrelevant, and losses are weak. To couple microwaves into the chip wires, on the other hand, requires properly designed guiding structures, because λ_{mw} is comparable to the atom chip dimensions. Furthermore, suitable chip materials have to be chosen to avoid strong dielectric losses. Microwave design aspects are discussed in the next section.

5.3 Microwave guiding structures

We have designed and fabricated an atom chip with microwave guiding structures. The chip fabrication is described in chapter 2, a picture of the whole chip is shown in Fig. 2.15. In the chip center, there are "experiment regions" with structures of the kind shown in Fig. 5.1. In order to calculate the microwave potentials, we have to determine the microwave field components $\mathbf{B}_{\mathrm{mw}}(\mathbf{r},t)$ and $\mathbf{E}_{\mathrm{mw}}(\mathbf{r},t)$ in the experiment regions by numerical simulations. In addition, we have to design transmission lines which guide the microwaves from the chip connectors into the experiment regions. In this section, I describe these aspects of microwave design and show measurements of microwave transmission line characteristics.

5.3.1 Coplanar waveguides

The microwave transmission lines [172] on our chip are coplanar waveguides (CPW) with finite ground planes [122, 174]. A cross section is shown in Fig. 5.6. There are several advantages of CPWs for our purpose:

- All CPW conductors lie in one plane of metallization so that it is possible to have additional DC wires crossing in a conductor plane below the CPW without short circuiting the waveguide.
- CPWs can be easily tapered from millimeter dimensions at the connectors to micrometer dimensions in the experiment regions, without substantial change in impedance.
- CPWs integrate smoothly with the structures used for magnetostatic traps, which frequently require several parallel wires. DC and radio frequency currents can be superimposed on the microwave signal with suitable bias injection circuits [175].

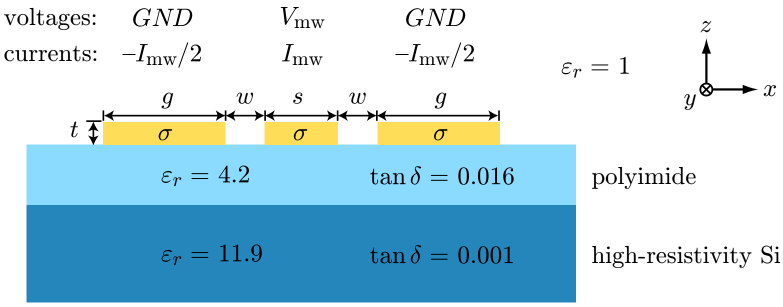

Figure 5.6: Cross section of a CPW with finite ground planes employed on our chip. The dielectric substrate consists of several layers of finite thickness.

Quasi-TEM fields

Because the characteristic transverse size $s + 2w$ of the CPW is much smaller than λ_{mw}, only quasi-TEM modes can propagate [172]. Quasi-TEM waves are similar to pure transverse electromagnetic (TEM) waves, except for small longitudinal field components. These arise because of conductor losses and at the boundary between the dielectrics. Electromagnetic waves traveling on the CPW along y are of the form

$$\mathbf{E}_{\mathrm{mw}}(\mathbf{r}, t) = \mathrm{Re}\left[\mathbf{E}(x, z)\exp(i\omega t - \gamma y)\right], \tag{5.27}$$

$$\mathbf{B}_{\mathrm{mw}}(\mathbf{r}, t) = \mathrm{Re}\left[\mathbf{B}(x, z)\exp(i\omega t - \gamma y)\right], \tag{5.28}$$

where γ is the complex propagation constant. The complex microwave field amplitudes can be decomposed as $\mathbf{E}(x, z) = \mathbf{E}_t(x, z) + \mathbf{e}_y E_y(x, z)$ and $\mathbf{B}(x, z) = \mathbf{B}_t(x, z) + \mathbf{e}_y B_y(x, z)$. For quasi-TEM waves, the transverse field components $\mathbf{E}_t$ and $\mathbf{B}_t$ are much stronger than the longitudinal components $E_y(x, z)$ and $B_y(x, z)$, respectively.

Because a CPW is a three-conductor transmission line, it supports two quasi-TEM modes of propagation. We excite primarily the symmetric (CPW) mode by connecting both outer conductors to ground. The microwave currents and voltages corresponding to this mode are indicated in Fig. 5.6. Here we use phasor notation [172], e.g. the microwave current on the signal conductor is represented by the complex phasor I_{mw}, the corresponding real and time-dependent current is $I(t) = \mathrm{Re}\,[I_{\mathrm{mw}} e^{i\omega t}]$.

Equivalent circuit parameters

A piece of transmission line with uniform cross section can be described by the equivalent circuit in Fig. 5.7 [172]. The inductance L, capacitance C, series resistance R, and shunt conductance G are defined per unit length of the transmission line. From these, the complex characteristic impedance

$$Z_c = \sqrt{\frac{R + i\omega L}{G + i\omega C}} \tag{5.29}$$

and the complex propagation constant

$$\gamma \equiv \alpha + i\beta = \sqrt{(R + i\omega L)(G + i\omega C)} \tag{5.30}$$

can be calculated. α is the attenuation constant, β is the propagation constant, $\lambda_{\mathrm{mw}} = 2\pi/\beta$ is the wavelength of the guided wave, and $v = \omega/\beta$ is the phase velocity. Current I_{mw} and voltage V_{mw} on the line are related by $V_{\mathrm{mw}} = Z_c I_{\mathrm{mw}}$. A complex Z_c introduces a phase shift between I_{mw} and V_{mw}, however, the microwave potentials are independent of this phase.

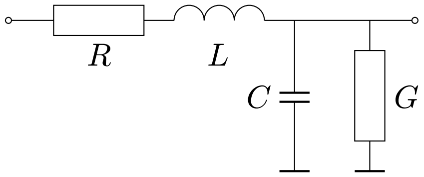

Figure 5.7: Equivalent circuit model of a transmission line.

The equivalent circuit parameters are important for impedance matching and to evaluate losses on the CPW. They are determined by integrals of the fields $\mathbf{E}(x, z)$ and $\mathbf{B}(x, z)$ [172]. To minimize G (dielectric losses), one has to choose a substrate material with a small dielectric loss tangent. We use high-resistivity Si substrates, the two layers of gold wires are separated by a thin layer of polyimide (see chapter 2). For typical parameters, we have

$G \ll \omega C$. The resistance R represents conductor losses. For micrometer-sized CPWs, R may be comparable to ωL, even for the high conductivity σ of gold conductors.

The impedance of an "ideal" CPW (which is lossless, has $t \to 0$, $g \to \infty$ (see Fig. 5.6), and a uniform dielectric filling the half space below the conductors), is a function of the effective dielectric constant $\varepsilon_{\mathrm{eff}} = (1 + \varepsilon_r)/2$ and of the ratio $s/(s+2w)$ only [122]. Thus, Z_c does not change if s and w are scaled by a common factor. This greatly simplifies the design of tapered CPWs, which guide the microwave into the experiment regions. A lossy CPW with finite dimensions shows deviations from this ideal behavior. Analytical formulae for Z_c exist for various parameter regimes [122, 176]. A useful transmission line design tool is TXLINE from AWR (www.appwave.com). In parameter regimes not covered by the design tools, in particular for micrometer-sized CPWs, we employ quasistatic field simulations to determine the transmission line parameters.

5.3.2 Simulation of microwave near-fields

Quasistatic simulations

For quasi-TEM waves on a transmission line with uniform cross-section, the problem of solving the full Maxwell's equations in three dimensions reduces to a two-dimensional quasistatic problem in the transverse plane. The results of this calculation are $\mathbf{E}(x, z)$ and $\mathbf{B}(x, z)$, which can then be used to calculate the microwave potentials and to determine the equivalent circuit parameters of the CPW.

In transmission lines with micrometer-sized wires, conductor losses play an important role [176]. The finite conductivity σ not only leads to attenuation, it also changes the electromagnetic field distribution in and around the wires via a more or less pronounced skin effect. The skin depth is $\delta = \sqrt{2/\omega\mu_0\sigma} = 0.9\ \mu\mathrm{m}$ for gold conductors at $\omega/2\pi = 6.8$ GHz. If the wire dimensions are comparable to δ, the skin effect is not fully developed, and standard calculations of transmission line parameters are inaccurate, because they often assume that the interior of the conductors is field-free. In this regime it is possible to obtain accurate fields and transmission line parameters by an electrostatic and a magneto-quasistatic simulation, which takes the skin effect properly into account [176, 177, 178]. The magneto-quasistatic simulation yields $\mathbf{B}_t$ and E_y as a function of I_{mw}, so that L and R can be calculated. It is assumed that $B_y = 0$. The electrostatic simulation determines $\mathbf{E}_t$ from V_{mw}, so that C and G can be calculated. The two simulations are then related by imposing the condition $V_{\mathrm{mw}} = Z_c I_{\mathrm{mw}}$. The result of such a calculation is shown in Fig. 6.4 in chapter 6. It shows that the magnetic field is not fully screened from the inside of the conductors, i.e. the skin effect is not fully developed. Furthermore, $\mathbf{B}_t$ and $\mathbf{E}_t$ have different spatial dependence near the conductors, see Fig. 6.4(a). For sufficiently large distance, the TEM result $\mathbf{E}_t = -v\,\mathbf{e}_y \times \mathbf{B}_t$ is recovered approximately, see Fig. 6.4(b).

These two-dimensional simulations apply to CPWs with a uniform cross section only. To analyze the effect of the transverse wire on the lower gold layer, we perform three-dimensional simulations of the microwave fields.

Full wave simulations

We use the software packages Sonnet and AWR Microwave Office for the simulation of three-dimensional, mostly planar conductor layouts. In addition, F. Perretti and G. Csaba from the group of Prof. Lugli at TU Munich have performed a 3D full wave simulation of one of our CPW structures, using the software package HFSS from Ansoft Corporation. The layout of this test structure is shown in Fig. 5.8(a). The two layers of gold wires are separated by a 4 μm thick layer of polyimide. The substrate material is high-resistivity Si. The CPW is on the upper gold layer, it is tapered from a size of about 1 mm at the chip edge to a size of a few micrometers in the chip center, where it crosses a 50 μm wide DC wire on the lower gold layer. The impedance of the CPW changes from $|Z_c| = 50\ \Omega$ at the edge to $|Z_c| = 80\ \Omega$ in the center. Figure 5.8(b) shows the fabricated structure in the chip center, where the CPW crosses the DC wire. The simulated magnetic and electric fields in a cross section of the CPW above the DC wire are shown in Fig. 5.8(c). We find that the distortion of the microwave fields caused by the wire on the lower layer is small if the CPW size $s + 2w$ is not much larger than the thickness of the polyimide layer. The fields obtained from quasi-static and full wave simulations agree well in this case. The fields are used to calculate scattering parameters for the structure, which we have compared with measurements.

5.3.3 S-parameter measurements

In our experiment, the atoms can be used as a scanning probe to map out the microwave field distribution in the near-field of micrometer-sized CPWs. However, we are not able to directly measure the field distribution before we attach the chip to the vacuum chamber. To confirm that the microwave guiding structures work, we measure the scattering parameters (S-parameters) [172] with a network analyzer connected to a microwave probe station, and compare with the simulation. Microwave transmission from port i to port j

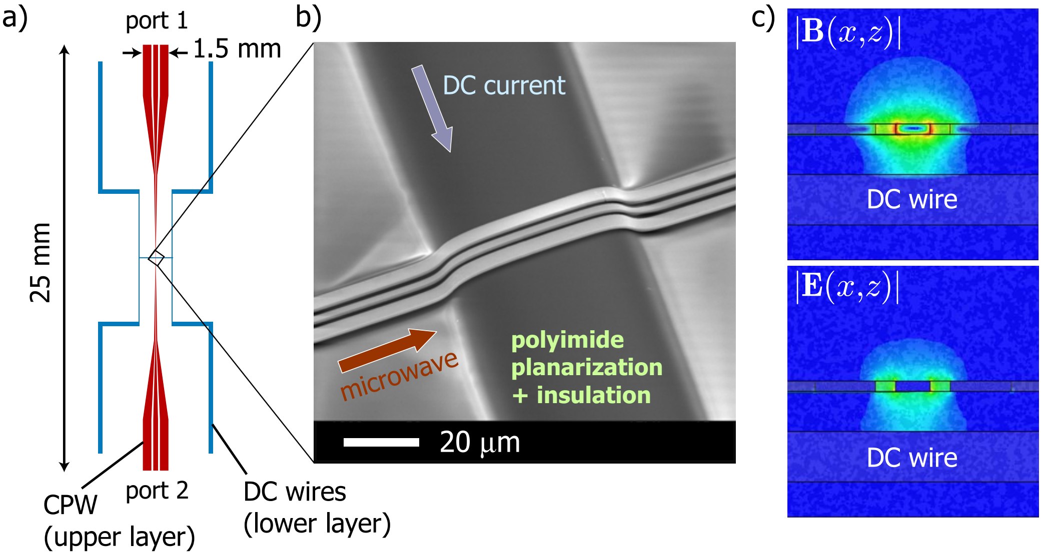

Figure 5.8: Tapered CPW crossing a DC wire on the lower gold layer. (a) Layout of the structure. (b) Center region of the fabricated structure. (c) Simulated microwave magnetic and electric fields in a cross-section of the CPW in the chip center.

is characterized by a complex S-parameter $S_{ji} = V_j^-/V_i^+$, where V_j^- is the voltage wave scattered out of port j if V_i^+ is incident at port i. In Fig. 5.9, a comparison of the measured and simulated S-parameters is shown for the structure of Fig. 5.8, at a system impedance of 50 Ω. Because of symmetry, $S_{12} = S_{21}$ and $S_{11} = S_{22}$. In view of the micrometer dimensions and the extreme tapering of the CPW, the magnitude of the measured transmission coefficient $|S_{12}|$ is fairly high. This shows that the microwave signal is effectively guided by the structure. The simulation underestimates transmission loss. The magnitude of the reflection coefficient $|S_{11}|$, on the other hand, agrees remarkably well with measurement. A resonance is visible in $|S_{11}|$ near 7 GHz, where λ_{mw} matches the length of the whole structure. Note that the corresponding relative modulation of $|S_{12}|$ is small, as expected if reflections at the ports and at the crossing wire are weak.

Similar characteristics are measured for the structures on the chip in Fig. 2.15. Because the CPW tapers work well, the microwave field strength in the experiment region is limited by the maximum current the small CPW wires can sustain, and not by the available microwave power at the input port. We have performed measurements of the microwave current at which the signal wire of the small CPW fails, and compared the result with the DC current tests described in section 2.4. A microwave pulse was launched into

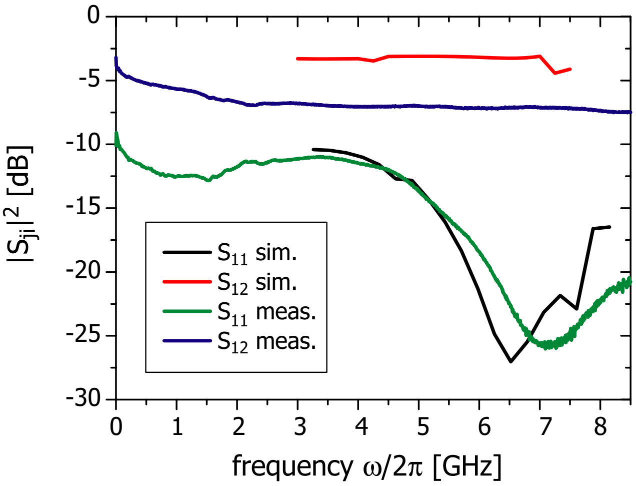

Figure 5.9: Comparison of measured and simulated S-parameters for the structure in Fig. 5.8.

the CPW from one port and the power transmitted to the other port was measured. Because resonances are weak, and making use of symmetry, the microwave power in the chip center and the corresponding RMS current can be inferred. The maximum RMS current the micrometer-sized signal conductor could support was comparable to the maximum DC current we measured for this conductor. This confirms that conductor losses are the dominant dissipation effect in micrometer-sized CPWs, and that the skin effect is not fully developed, so that there is only a small difference between microwave and DC current distributions inside the signal conductor. Dielectric losses in the substrate are only relevant for larger structures. On a test chip, we increased the injected microwave power until the CPW failed. We observed that the signal conductor was destroyed right in the chip center where the conductor cross-section is smallest. This shows that the microwave signal is indeed successfully guided to where it will be needed for the atom manipulation.

5.4 A state-dependent double well potential

The structure shown in Fig. 5.1 at the beginning of this chapter can be used to generate a state-dependent double well potential for the qubit states $|0\rangle$ and $|1\rangle$. The potential arises from a combination of static magnetic and microwave near-field potentials as illustrated in Fig. 5.10.

Figure 5.11 shows a simulation of the potential. The CPW dimensions are $s = g = 2.5$ μm, $w = 2.0$ μm, and $t = 1.0$ μm, the cross section of the trans-

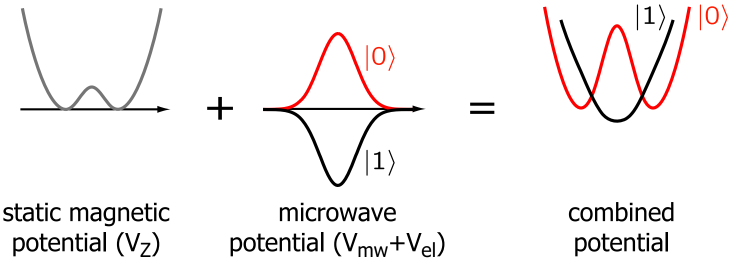

Figure 5.10: The barrier of a static magnetic double well can be selectively removed for state $|1\rangle$ with microwave near-field potentials. V_Z is identical for $|0\rangle$ and $|1\rangle$, while V_{mw} has opposite sign, as in Fig. 5.5.

verse wire is 11 μm × 5 μm, and the gold layers are spaced by 6 μm of polyimide. These dimensions correspond to a structure which we have fabricated on the microwave atom chip for experiments with BECs. The simulation is based on numerical diagonalization of the Hamiltonian in Eq. (5.16), using microwave fields calculated in the quasistatic approximation. We operate the trap in the conceptually simplest regime by choosing a large microwave detuning and making use of the gradients in $B_{\mathrm{mw}}(\mathbf{r})$ in the near-field of the CPW. The trap parameters are $(I_T, I_L, I_C, I_R) = (100, -2, 1.2, -2)$ mA, $\mathbf{B}_b = (3.4, 11, 0)$ G, $I_{\mathrm{mw}} = 30$ mA, and $\Delta_0/2\pi = 20$ MHz (cf. Fig. 5.1). For these parameters, the microwave coupling is weak, $\mu_B B_{\mathrm{mw}}/\hbar\Delta_0 = 0.1$ in the trap center, and we can identify each dressed state $|K\rangle$ with one of the $|F, m_F\rangle$. The potentials U_1 (U_0) for state $|1\rangle$ ($|0\rangle$) include the effect of the static magnetic field, the microwave magnetic and electric fields, gravity, and the surface potential, see Eq. (5.26). The minimum of U_0 is at $d = 8.1$ μm from the CPW surface, the trap frequencies are $(f_x, f_y, f_z) = (0.80, 3.13, 3.20)$ kHz. The minimum of U_1 is at $d = 7.7$ μm, and $(f_x, f_y, f_z) = (0.73, 3.22, 3.00)$ kHz. The static field in the trap center is $B = 2.9$ G, pointing along x. In the figure we have set $U_i = 0$ in the potential minimum of each state.

By modulating I_{mw} and I_C, it is possible to state-selectively split and recombine small BECs in this potential. The chemical potential $\mu_{c,i}$ of a BEC of $N = 500$ atoms in state $|i\rangle$ is indicated. It is calculated using Eq. (1.25); for the calculation of $\mu_{c,0}$ it is assumed that all atoms are in one potential well.

In the next chapter, I discuss an application of microwave near-fields in quantum information processing with single atoms, where atom-atom entanglement is generated via state-dependent collisions in a potential similar to that in Fig. 5.11.

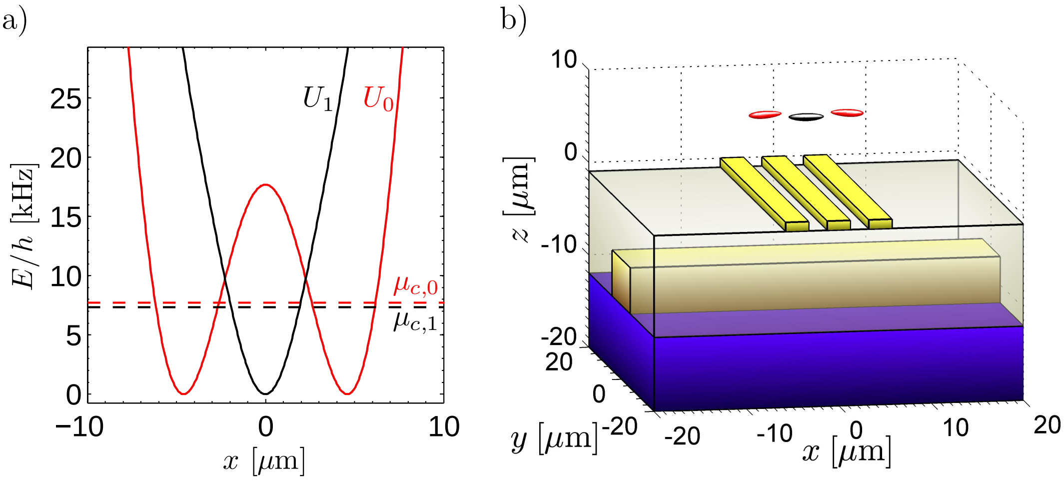

Figure 5.11: State-dependent double well potential. (a) Potential $U_i(x)$ for atoms in state $|i\rangle$. The potential in the yz-plane is harmonic. The chemical potential $\mu_{c,i}$ of a BEC of 500 atoms in state $|i\rangle$ is indicated, see text. (b) Chip layout and isopotential surfaces $U_i(\mathbf{r}) = \mu_{c,i}$.

Chapter 6

Proposal for a robust quantum gate on an atom chip

A two-qubit collisional phase gate on an atom chip is proposed, and its performance is theoretically analyzed. The gate is based on earlier phase gate schemes, but uses the qubit state pair $\{|0\rangle, |1\rangle\}$ whose robustness against decoherence is experimentally demonstrated in chapter 4. Microwave near-fields (see chapter 5) play a key role in our implementation as a means to realize the state-dependent potentials required for conditional dynamics. Quantum control algorithms are used to optimize gate performance. We employ an atom chip wire layout that can be built with current fabrication processes, and extensively discuss the impact of technical noise and imperfections that characterize an actual atom chip. We find an overall infidelity compatible with requirements for fault-tolerant quantum computation.

This chapter, which was published in [165], is the result of a collaboration with A. Negretti and M. Cirone from the group of T. Calarco.

6.1 Quantum information processing on atom chips

The physical implementation of scalable quantum computing unquestionably poses huge challenges. Many proposals exist, most of which in principle satisfy all requirements for scalability [8]. One might be tempted to claim that their realization is simply a matter of technological improvement. Yet, we can fairly say that to date nobody knows how to build a scalable quantum computer. Understanding and overcoming each of the sources of imperfection, specific to a given physical scenario, becomes thus crucial on the way to a possible actual implementation.

Atom chips [23, 22] combine many important features of a scalable architecture for quantum information processing (QIP) [8]: The long coherence lifetimes of qubits based on hyperfine states of neutral atoms [87], accurate control of the coherent evolution of the atoms in tailored micropotentials [42, 46], scalability of the technology through microfabrication [111, 115], which allows the integration of many qubits in parallel on the same device while maintaining individual addressability, and the exciting perspective of interfacing quantum optical qubits with solid-state systems for QIP located on the chip surface [179] (see also chapter 7). However, the experimental demonstration of a fundamental two-qubit quantum gate on an atom chip is an important milestone which still has to be reached.

A first proposal for a quantum phase gate based on collisional interactions between atoms on a chip was put forward in [34]. While it demonstrates the working principle of such a gate, there are problems which could prevent a successful experimental realization: 1) The qubit is encoded in two states with a magnetic-field sensitive energy difference, such that it is hard to maintain the qubit coherence over a long time in a noisy experimental environment. 2) The fidelity is strongly reduced by wave packet distortion due to undesired collisions in some of the qubit basis states. 3) An idealized situation with accurately harmonic potentials for the atoms was considered [34], which is hard to realize experimentally, and deviations from harmonicity spoil the gate performance [180]. 4) Furthermore, transverse excitations of the atoms were not considered in detail. For a successful experimental implementation, however, a scheme is needed which allows for high fidelity gate operations under realistic conditions. A gate infidelity (error rate) below a certain threshold is needed in order to allow for a fault-tolerant implementation of quantum computing. Depending on error models and recovery schemes, estimates of such threshold vary from a few 10^{-3} for active error correcting codes [181] up to well above 10% for error detection schemes [182].

Here we present a substantially improved version of the phase gate of [34] for the robust qubit states $|0\rangle$ and $|1\rangle$ investigated in chapter 4, and give a detailed prescription for its implementation. The decoherence rates of the qubits due to magnetic-field noise are suppressed by a factor of 10^{-3} compared to [34]. In our proposal, a key role is played by microwave near-field potentials, which allow to create the required state-selective potentials for a successful gate operation with the states considered here (cf. chapter 5). Using microwave potentials, the same robust qubit states can be used for information processing and storage. At the same time, the microwave potentials avoid the unwanted collisions limiting the fidelity in the original proposal, by appropriately displacing the potential minima for qubit states $|0\rangle$ and $|1\rangle$. We simulate the gate dynamics in a potential created by a realistic atom chip, which we specify in detail, and which can be fabricated with today's technology. Furthermore, we consider many sources of infidelity in detail, such as loss and decoherence effects due to the proximity of the chip surface, and we find a total infidelity of the order of a few 10^{-3}.

6.2 Principle of the gate operation

To complete the toolbox for quantum information processing on atom chips [164], a fundamental two-qubit quantum gate is needed. Each qubit is represented by an atom in a superposition of the qubit states $|0\rangle$ and $|1\rangle$. Our goal is to realize a phase gate, with the truth table

$$\begin{aligned} |00\rangle &\rightarrow |00\rangle, \\ |01\rangle &\rightarrow |01\rangle, \\ |10\rangle &\rightarrow |10\rangle, \\ |11\rangle &\rightarrow e^{i\phi_g}|11\rangle, \end{aligned} \tag{6.1}$$

for the four two-qubit basis states. ϕ_g is the gate phase, which is to be adjusted to $\phi_g = \pi$. As proposed in [34], the phase gate can be implemented by modulating the trapping potential state-selectively, such that the two atoms interact and pick up a collisional phase shift ϕ_g if and only if both are in internal state $|1\rangle$. In the following, we briefly sketch the working principle of the gate, highlighting the differences between the present approach and [34].

In Figure 6.1, the principle of the gate operation is shown. The atoms are placed in a state-dependent potential

$$U_i(\mathbf{r}, t) = u_c(\mathbf{r}) + \lambda(t) \cdot u_i(\mathbf{r}), \tag{6.2}$$

which can be split into a common part $u_c(\mathbf{r})$ and a state-dependent part $u_i(\mathbf{r})$, where $i = \{0, 1\}$ denotes the states $|0\rangle$ and $|1\rangle$ and $\mathbf{r} = (x, y, z)$. The common part of the potential is time-independent, while the state-dependent part is modulated with a function $\lambda(t)$, $0 \leq \lambda(t) \leq 1$, during the gate operation. At times $t < 0$, when the gate is in its initial state, we have $\lambda(t) = 0$ and the atoms are subject to $u_c(\mathbf{r})$ only, see Fig. 6.1(a). The potential $u_c(\mathbf{r})$ provides a tight confinement in the transverse dimensions y and z, such that the dynamics of the atoms is effectively one-dimensional. In the longitudinal dimension x, $u_c(\mathbf{r})$ is a double well with a sufficiently high barrier to prevent tunneling between the wells. Each of the qubit atoms is prepared in the motional ground state of one potential well. The gate operates during the time $0 \leq t \leq \tau_g$, where τ_g is the gate time. During this time, $\lambda(t) \neq 0$, and the potential is state-dependent as sketched in Fig. 6.1(b). The effect of $u_i(\mathbf{r})$ is twofold: $u_1(\mathbf{r})$ removes the barrier of the double well for state $|1\rangle$, leaving only a single, approximately (but not exactly) harmonic potential well in which atoms in state $|1\rangle$ start to oscillate. $u_0(\mathbf{r})$ shifts the minima of the double well for state $|0\rangle$ further apart in the x-direction. The effect of $u_i(\mathbf{r})$ on the tight transverse confinement is very small. In this way, the truth table (6.1) is implemented: In state $|11\rangle$, both atoms will oscillate and collide each time they pass the center of the trap, which leads to the desired collisional phase shift of the state $|11\rangle$. In states $|00\rangle$, $|01\rangle$, and $|10\rangle$, the atoms do not collide, since atoms in state $|0\rangle$ are shifted out of the way of the oscillating state $|1\rangle$. When the desired phase shift ϕ_g is accumulated after an integer number of oscillations N of the state $|1\rangle$, the gate operation is terminated by returning to $\lambda(t) = 0$ for $t > \tau_g$, recapturing each atom in one of the potential wells of $u_c(\mathbf{r})$ (see again Fig. 6.1(a)).

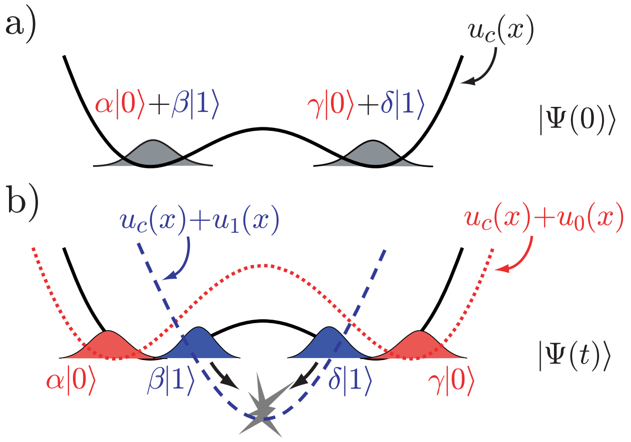

Figure 6.1: State-selective potential, atomic wave functions, and principle of the gate operation. (a) The state-independent potential $u_c(x)$ along x for $t < 0$ and $t > \tau_g$, before and after the gate operation, when $\lambda(t) = 0$. The initial state wave function of the two atoms in this potential is shown. (b) The state-dependent potential $u_c(x) + u_i(x)$ (here $\lambda(t) = 1$) for $0 \leq t \leq \tau_g$, during the gate operation. The atomic wave functions after half an oscillation period are shown. The state-independent part $u_c(x)$ is shown for comparison.

The gate operation described here is different from the original proposal in [34]. There, only the potential for state $|1\rangle$ is switched during the gate operation. This leads to unwanted collisions of atoms in state $|01\rangle$, which are a major source of infidelity and would require an additional transverse shift in the potential minimum [34]. Using microwave potentials, we are able to create a state-dependent potential in which the state $|0\rangle$ is shifted out of the way of the oscillating state $|1\rangle$ in the longitudinal dimension. This is essential to avoid the unwanted collisions and to achieve high fidelity gate performance. A second difference is that we choose a smooth modulating function $\lambda(t)$ for the state-selective part of the potential instead of instantaneous switching as in [34]. Roughly speaking, $\lambda(t)$ is ramped from $\lambda(t) = 0$ to $\lambda(t) = 1$ during the first half of each oscillation, while it is ramped back to $\lambda(t) = 0$ with the inverse temporal profile during the second half. This smooth ramping allows for much better control over the gate dynamics than instantaneous switching of the potential. This is necessary to avoid strong excitations of the atoms in $|0\rangle$ during the shift of the potential well. It also decreases the oscillation amplitude of state $|1\rangle$, thereby further suppressing collisions in the states $|01\rangle$ and $|10\rangle$. The exact time dependence of the function $\lambda(t)$ is determined by an optimal control algorithm which optimizes the fidelity of the quantum gate, as discussed in section 6.5.

6.3 Chip layout and potentials

The state-dependent potential (6.2) which is needed for the gate operation can be realized by a combination of static magnetic and microwave fields on the atom chip, as described in chapter 5. The use of microwaves to create the state-selective potential is essential for our proposal, since a combination of static magnetic and electric fields, as considered in [34, 51], does not provide state-selective potentials for our robust qubit state pair, whose magnetic moments and electrostatic polarizabilities are equal. Optical potentials created by focussed laser beams with a frequency close to the D_1 or D_2 transition of ^{87}Rb are impractical as well: if the detuning of the laser from the atomic resonance is much larger than the hyperfine splitting of the ^{87}Rb ground state, the resulting optical potentials are again nearly identical for the states $|0\rangle$ and $|1\rangle$. If, on the other hand, a detuning comparable to the hyperfine splitting is used, a differential optical potential could be created, but problems with decoherence due to spontaneous scattering of photons would arise.

The common potential in Eq. (6.2) is generated by the static Zeeman effect, which is identical for $|0\rangle$ and $|1\rangle$ (see Fig. 6.2):

$$u_c(\mathbf{r}) = V_Z^{2,+1}(\mathbf{r}) = V_Z^{1,-1}(\mathbf{r}) = \frac{\mu_B}{2} B(\mathbf{r}). \tag{6.3}$$

The state-dependent part of the potential in Eq. (6.2) is generated by the microwave. The trap is operated in the limit of large detuning $|\Delta_{1,m_1}^{2,m_2}|^2 \gg |\Omega_{1,m_1}^{2,m_2}|^2$, which allows for long coherence lifetimes of the qubit states in the

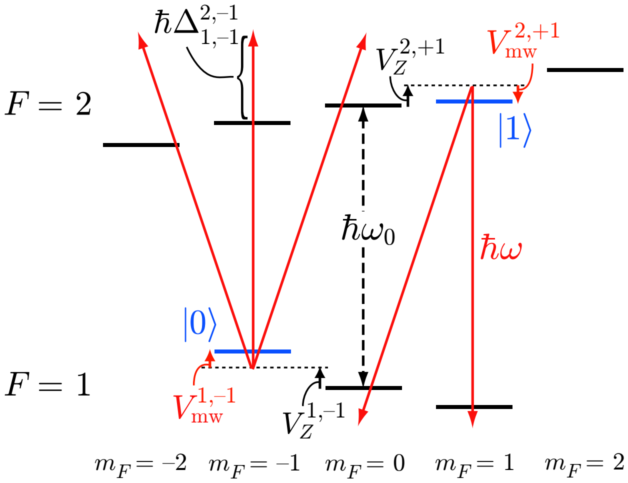

Figure 6.2: Energy-level diagram of the hyperfine structure of the ^{87}Rb ground state in a combined static magnetic and microwave field. V_Z^{F,m_F} indicates the energy shift due to the static Zeeman effect, which is (nearly) identical for $|0\rangle$ and $|1\rangle$. Due to the magnetic field of the microwave, the level $|F, m_F\rangle$ is shifted in energy by V_{mw}^{F,m_F}. This shift has opposite sign for $|0\rangle$ and $|1\rangle$, as indicated in the figure (the shift of the other levels is not shown). The microwave transitions contributing to the shift of $|0\rangle$ and $|1\rangle$ are shown for $\Delta^{2,m_2}_{1,m_1} > 0$ (blue detuning).

microwave potential (see section 6.6). The potential $u_0(\mathbf{r})$ is given by

$$\begin{aligned} u_0(\mathbf{r}) &= V_{\mathrm{el}}(\mathbf{r}) + V_{\mathrm{mw}}^{1,-1}(\mathbf{r}) \\ &= -\frac{\alpha_0}{4} E_{\mathrm{mw}}^2(\mathbf{r}) + \frac{\hbar}{4} \sum_{m_2=-2}^{0} \frac{|\Omega^{2,m_2}_{1,-1}(\mathbf{r})|^2}{\Delta^{2,m_2}_{1,-1}(\mathbf{r})}, \end{aligned} \tag{6.4}$$

while the potential $u_1(\mathbf{r})$ is

$$\begin{aligned} u_1(\mathbf{r}) &= V_{\mathrm{el}}(\mathbf{r}) + V_{\mathrm{mw}}^{2,+1}(\mathbf{r}) \\ &= -\frac{\alpha_0}{4} E_{\mathrm{mw}}^2(\mathbf{r}) - \frac{\hbar}{4} \sum_{m_1=0}^{+1} \frac{|\Omega^{2,+1}_{1,m_1}(\mathbf{r})|^2}{\Delta^{2,+1}_{1,m_1}(\mathbf{r})}. \end{aligned} \tag{6.5}$$

As desired, a differential potential for $|0\rangle$ and $|1\rangle$ can be generated via V_{mw}. In Fig. 6.2, the relevant transitions contributing to the potentials for $|0\rangle$ and $|1\rangle$ are shown for a general microwave field with all polarization components present. From Fig. 6.2 it is evident that the microwave potentials for the two states will not have exactly the same position dependence (in addition to the difference in sign), since only two polarization components contribute to the potential for $|1\rangle$, while all three components contribute to the potential for $|0\rangle$. Furthermore, by reversing the sign of the detuning Δ_{1,m_1}^{2,m_2} for all levels, the overall sign of the microwave potentials and therefore the role of the states during the gate operation can be interchanged, i.e. either $|0\rangle$ or $|1\rangle$ can be chosen as the oscillating state. We choose $\Delta_{1,m_1}^{2,m_2} > 0$, resulting in $|1\rangle$ as the oscillating state, since the potential for $|1\rangle$ is closer to harmonic in our actual trap design.

Chip layout

We propose to use a microwave atom chip with a wire layout as shown in Fig. 6.3. A double well potential with a state-dependent barrier can be generated with this structure, as explained in chapter 5. The structures considered here are smaller than those in section 5.4 to achieve tighter confinement and thus faster gate dynamics.

Static magnetic trap

For the phase gate with three oscillations ($N = 3$, see section 6.5), an initial static trap with DC currents $I_T = 348.440$ mA, $I_C = -0.813$ mA, and $I_L = I_R = 1.204$ mA is used (see Fig. 6.3). The components of the homogeneous bias field $\mathbf{B}_b = (B_{b,x}, B_{b,y}, B_{b,z})$ are $B_{b,x} = -4.464$ G, $B_{b,y} = 103.717$ G, and $B_{b,z} = 0.000$ G. For assumptions about the stability and accuracy of the currents and magnetic fields, see section 6.6. For the parameters given above, $u_c(\mathbf{r})$ is a Ioffe-type double well potential [23] along an axis x' in the xy-plane, which is tilted by a small angle $\theta = 0.02$ with respect to x. The distance of the double well from the wire surface is $d = 1.80$ μm. The magnetic field in the trap center is $|\mathbf{B}_0| = 3.230$ G, which maximizes the coherence time in the absence of microwave coupling, see chapter 4. $\mathbf{B}_0$ is directed approximately along $-x$. The distance between the minima of the double well is $d_x = 1.32$ μm. In the transverse dimensions, the trap provides a tight harmonic confinement with almost identical trap frequencies $\omega_y/2\pi = \omega_z/2\pi = \omega_\perp/2\pi = 77.46$ kHz. For the simulation, we determine $\omega_\perp(x)$ as a function of the longitudinal coordinate x, although the relative variation along x is only $\leq 1\times10^{-3}$. The axial trap frequency of the potential wells is $\omega_x/2\pi = 4.432$ kHz. All traps considered in our gate simulation satisfy $\omega_x \ll \omega_\perp$.

Microwave fields

We determine the microwave fields with a quasi-static simulation, as described in section 5.3.2. The results of this simulation are shown in Fig. 6.4.

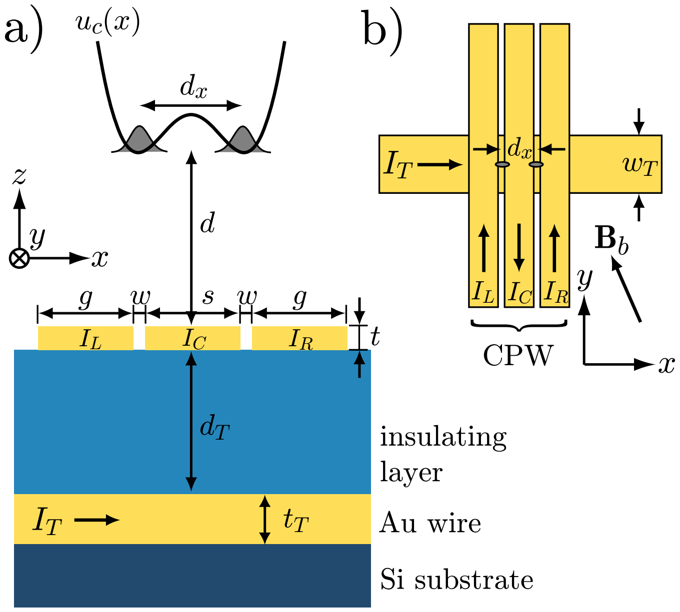

Figure 6.3: Chip layout for the microwave collisional phase gate. (a) Cut through substrate. (b) Top view of wire layout. Wire parameters: $s = g = 0.8\ \mu\mathrm{m}$, $w = 0.1\ \mu\mathrm{m}$, $t = 0.2\ \mu\mathrm{m}$, $d_T = 4.2\ \mu\mathrm{m}$, $w_T = 1.5\ \mu\mathrm{m}$, $t_T = 1.0\ \mu\mathrm{m}$. The lower wire (current I_T) is fabricated into a groove which was etched into the substrate, and covered by an insulating layer. The DC currents I_T, I_C, I_L, and I_R and the orientation of the magnetic bias field $\mathbf{B}_b$ used to create the state-independent potential $u_c(\mathbf{r})$ are shown. The atomic wave functions in this potential are indicated. The three upper wires form a microwave coplanar waveguide (CPW), compare Fig. 6.4.

From the fields, we determine the characteristic impedance of the CPW, $Z_c = 130\ \Omega \cdot e^{-i \cdot 0.24\,\pi}$. The microwave propagation constant $\beta_{\mathrm{mw}} = 2\pi/\lambda_{\mathrm{mw}}$ and the attenuation constant α_{mw} are of comparable magnitude, $\beta_{\mathrm{mw}} \sim \alpha_{\mathrm{mw}} \sim 1 \times 10^3\ \mathrm{m}^{-1}$ at 6.8 GHz. However, on the micrometer scale on which the atomic dynamics takes place, microwave damping and propagation effects are negligible. The influence of the lower wire on the microwave propagation characteristics of the CPW is negligible, since $d_T \gg (s + 2w)$. To estimate the effect of the lower wire, we have included a homogeneous gold layer in the plane of the lower wire in our two-dimensional simulation. This leads to a small relative change in $|Z_c|$ of 1×10^{-2}.

In the simulation of the gate dynamics and in Fig. 6.4, the microwave

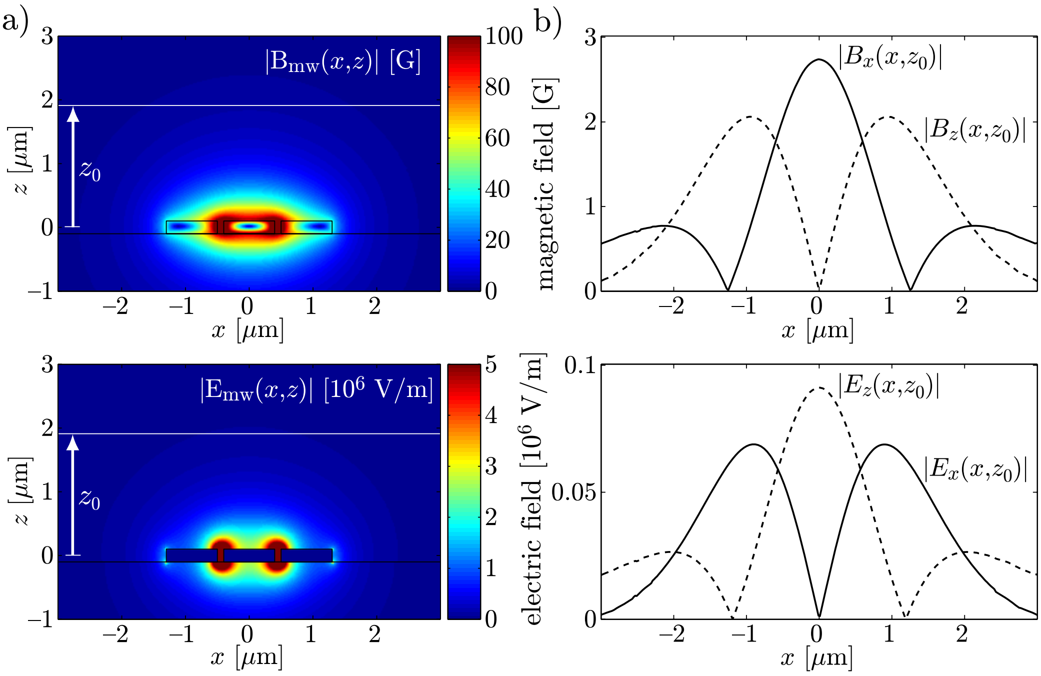

Figure 6.4: Transverse (xz-plane) magnetic and electric fields of the microwave on the coplanar waveguide. The fields were obtained by a quasi-static simulation including conductor-loss effects. The longitudinal (y-direction) electric field, which is several orders of magnitude smaller than the transverse electric field, is not shown in the plots. (a) Magnitude of the fields for $\lambda = 1$ shown in a cross section of the CPW. (b) Transverse microwave field components as a function of x at a distance $d = 1.80$ μm from the wire surface, corresponding to the line $z = z_0 = 1.90$ μm in (a), which indicates the z-position of the static trap minimum. For the size of the conductors, see Fig. 6.3.

voltage and current amplitudes on the CPW are

$$|V_{\mathrm{mw}}| = \sqrt{\lambda(t)} \cdot 1.9895 \text{ V} \tag{6.6}$$

$$|I_{\mathrm{mw}}| = \frac{|V_{\mathrm{mw}}|}{|Z_c|} = \sqrt{\lambda(t)} \cdot 15.343 \text{ mA} \tag{6.7}$$

Here, $\lambda(t)$ is the modulating function of the microwave potential during the gate operation, which will be optimized by optimal control techniques as described in section 6.5. The detuning of the microwave from the transition $|F = 1, m_F = 0\rangle \to |F = 2, m_F = 0\rangle$ is $\Delta_0 = 2\pi \cdot 29.4$ MHz. For these parameters, the ratio between the electric and the magnetic microwave potential is $V_{\mathrm{el}} \sim 0.2\, V_{\mathrm{mw}}$, i.e. the state-selective magnetic part of the microwave potential is dominating. This is important since V_{el} reduces the barrier of the double well also for state $|0\rangle$. It is possible to avoid this unwanted effect of V_{el} by a small adjustment of the magnetostatic potential during the gate operation. To compensate V_{el}, we modulate

$$B_{b,x}(t) = (-4.464 + \lambda_0(t) \cdot 0.036)\ \mathrm{G} \tag{6.8}$$

$$I_C(t) = (-0.813 - \lambda_0(t) \cdot 0.039)\ \mathrm{mA}, \tag{6.9}$$

where $\lambda_0(t) \simeq \lambda(t)$. The function $\lambda_0(t)$ consists of simple linear ramps, as explained below (section 6.5.1).

If the microwave is turned on to full power ($\lambda = 1$ and $\lambda_0 = 1$), the barrier of the static double well trap is removed for state $|1\rangle$, leaving a single potential well of longitudinal trap frequency $\omega_{|1\rangle}/2\pi = 5.448$ kHz, as shown in Fig. 6.1. For state $|0\rangle$, the two potential wells are shifted apart and the trap frequency in each of the wells changes to $\omega_{|0\rangle}/2\pi = 4.775$ kHz. The transverse confinement of the static trap is unchanged, both d and $\omega_\perp$ change by less than 10^{-3}. Although we include the full position dependence of $u_i(\mathrm{r})$ in the simulation, it would be sufficient to consider the state-selective potential $u_i(x, y_0, z_0)$ at the transverse position of the static trap minimum (y_0, z_0).

Chip fabrication

The fabrication of the chip relies on electron beam lithography, which provides sub-micron resolution, in combination with lift-off metallization techniques and anisotropic etching of the Si substrate. The lower gold wire is fabricated as follows: prior to the metal deposition, a groove is etched into a high-resistivity Si substrate by anisotropic reactive ion etching, using lithographically patterned photoresist as etch mask. The gold wire is subsequently fabricated into this groove using the same photoresist for lift-off. The remaining groove is filled and the wire is insulated by depositing a dielectric layer, such as SiO_2 or polyimide. Since the lower wire is contained in the groove, this insulating layer can be very thin and still provide good planarization of the surface. In this way, good thermal contact of the wires to the substrate is guaranteed. On top of the insulating layer, the CPW is fabricated using standard electron-beam lithography and lift-off.

6.4 Simulation of the gate operation

The gate operation is simulated numerically by solving a time-dependent Schrödinger equation of the two-particle dynamics along the direction of the double well x' (in the following, we write x instead of x' to simplify notation).

We assume that the atoms remain in the transverse ground state of the trap throughout the gate operation; this assumption is justified in section 6.5.2 and section 6.6. The initial state of the two atomic qubits in an arbitrary superposition of internal states $|ij\rangle$ is

$$|\Psi(t=0)\rangle = \left(\sum_{i,j\in\{0,1\}} \alpha_{ij}|ij\rangle \right) \otimes |\psi(x_1,x_2,t=0)\rangle, \tag{6.10}$$

where $|\psi(x_1,x_2,t=0)\rangle$ describes the initial motional state of the two atoms, which is independent of the internal state, with one atom in each well of the potential $u_c(x)$ (see Fig. 6.1(a)). During the gate operation, the internal and motional states of the atoms are entangled due to the dynamics in the state-selective potential:

$$|\Psi(t)\rangle = \sum_{i,j\in\{0,1\}} \alpha_{ij}|ij\rangle \otimes |\psi_{ij}(x_1,x_2,t)\rangle. \tag{6.11}$$

The dynamics of $|\psi_{ij}(x_1,x_2,t)\rangle$ (see Fig. 6.1(b)) is governed by the time-dependent Hamiltonian

$$\mathcal{H}_{ij}(t) = T_{x_1} + T_{x_2} + U_i(x_1,t) + U_j(x_2,t) + V_{\text{int}}^{ij}(|x_2-x_1|,t), \tag{6.12}$$

where T_{x_i} denotes the kinetic energy operators and

$$V_{\text{int}}^{ij}(|x_2-x_1|,t) = \frac{2\hbar\omega_\perp(x_1,t)a_s^{ij}}{1-1.46a_s^{ij}/a_\perp(x_1,t)}\delta(|x_2-x_1|) \tag{6.13}$$

is the effective one-dimensional interaction potential between the atoms [183], $a_s^{ij} \simeq 5.4$ nm is the s-wave scattering length for collisions of ^{87}Rb atoms in state $|ij\rangle$, and $a_\perp(x_1,t) = \sqrt{2\hbar/m\omega_\perp(x_1,t)}$ is the size of the ground state in the transverse direction. The transverse trap frequency $\omega_\perp(x_1,t)$ can be used as a control parameter to optimize the dynamics and is therefore time-dependent. The numerical simulation of the dynamics is performed using a Fast Fourier Transform method.

The entanglement between the motional and internal states of the atoms is crucial for establishing the collisional phase shift in state $|11\rangle$. However, at the end of the gate operation, the motional and internal states have to factorize again, so that the truth table (6.1) is implemented. Any residual entanglement between the motional and internal states leads to a reduction of the gate fidelity. To avoid this, the wave function of the atoms has to show a revival at $t=\tau_g$ and regain its initial form, apart from the phase factor in state $|11\rangle$. To quantify this, we define the overlaps

$$O_{ij}(t) = \langle\psi_{ij}(x_1,x_2,t)|\psi(x_1,x_2,0)\rangle, \tag{6.14}$$

from which the overlap fidelities

$$F_{ij}(t) = |O_{ij}(t)|^2 \tag{6.15}$$

are calculated. The evolution of the gate phase is given by [34, 184]

$$\phi_g(t) = \phi_{11}(t) + \phi_{00}(t) - \phi_{01}(t) - \phi_{10}(t), \tag{6.16}$$

where we have defined the collisional phases

$$\phi_{ij}(t) = \arg\left[\langle\psi_{ij}(x_1, x_2, t)|\psi^0_{ij}(x_1, x_2, t)\rangle\right]. \tag{6.17}$$

Here, $|\psi^0_{ij}(x_1, x_2, t)\rangle$ is the motional state evolved from $|\psi(x_1, x_2, 0)\rangle$ in the absence of collisions [34]. $\phi_{ij}(t)$ is well defined even for times t where $O_{ij}(t) \simeq 0$. Optimal gate performance corresponds to $F_{ij}(\tau_g) = 1, \forall_{i,j}$, i.e. a complete revival of the wave function, and a gate phase $\phi_g(\tau_g) = \pi$. In a realistic non-harmonic potential, however, the revival of the atomic wave function will be incomplete, and the collisions between the atoms will lead to an additional distortion of the wave function. Both effects will lead to a reduction of the gate fidelity, and have to be avoided as much as possible by an optimization of the gate dynamics.

6.5 Optimization of the gate

We apply optimal control techniques [185, 186] to optimize the gate performance. This is performed in two steps. First, the dynamics without atom-atom interactions is optimized using $\lambda(t)$ as control parameter. In this way, we optimize the revival of the wave function in the non-harmonic potential. In a second step, the dynamics in the presence of interactions is optimized further using $\omega_\perp(t)$ as control parameter. This reduces wave packet distortion due to collisions. The two steps are discussed in the following subsections for a gate with $N = 3$ oscillations.

6.5.1 Optimal control of $\lambda(t)$

In the first stage of optimization, $\lambda(t)$ is used as control parameter. Experimentally, this corresponds to controlling the microwave power. We start with a trial function $\lambda_0(t)$ which consists of linear ramps, as shown in Fig. 6.5(a). This choice represents a compromise between a sudden removal of the barrier for state $|1\rangle$ and an adiabatic shift of the potential wells for state $|0\rangle$. We optimize τ_g and the slope of the linear ramps of $\lambda_0(t)$ by hand to achieve an initial gate fidelity > 0.95. Starting with $\lambda(t) = \lambda_0(t)$, the function $\lambda(t)$ is then adjusted by an optimal control algorithm, which neglects atom-atom interactions in order to provide faster convergence. This corresponds to setting $a_s = 0$ in (6.13). In the absence of interactions, it is sufficient to optimize the single-particle overlaps $O_i = |\langle \psi_i(x, \tau_g)|\psi(x, 0)\rangle|$, which are optimized simultaneously for $i \in \{0, 1\}$ by the algorithm using the Krotov method [187]. After the optimization has converged, the resulting optimized $\lambda(t)$ is used in a simulation of the two-particle dynamics with interactions ($a_s \neq 0$), in order to determine the two-particle overlap fidelities $F_{ij}(\tau_g)$. The strength of the interaction (6.13) was adjusted by setting the transverse trap frequency $\omega_\perp$ to a value constant in time such that the gate phase is $\phi_g \simeq \pi$. The result of this first stage of optimal control is the microwave power modulation function $\lambda(t)$ shown in Fig. 6.5(a), which deviates from $\lambda_0(t)$ by small modulations, and the fidelities shown in the left part of Table 6.1.

The trial function $\lambda_0(t)$ is also used to modulate the magnetostatic potential in order to compensate the effect of the microwave electric field, as explained in section 6.3. We choose $\lambda_0(t)$ instead of $\lambda(t)$ for this modulation in order to keep the number of experimental parameters which are subject to optimal control as small as possible.

Our simulation shows that collisional interactions between the atoms are negligible in basis states other than $|11\rangle$, with $\phi_{00}(\tau_g) = 0$ and $\phi_{01}(\tau_g) = \phi_{10}(\tau_g) \sim 10^{-3}\,\phi_{11}(\tau_g)$. In Fig. 6.5(d), the phase evolution during the gate operation is shown. The main effect of the interaction is to provide the phase shift in state $|11\rangle$, corresponding to the steps in $\phi_g(t)$ each time a collision in this state takes place. An undesired effect of the collision is to decrease the fidelity $F_{11}(\tau_g)$ compared to the non-interacting case due to wave packet distortion during the collision. We have performed the optimization of the gate for different numbers of oscillations N. For each value of N, a different value of $\omega_\perp$ was chosen to adjust the gate phase to $\phi_g \simeq \pi$. For smaller N, the gate phase has to be acquired in a smaller number of oscillations, therefore the interactions need to be stronger and the phase shift per collision is larger. Correspondingly, the collisional distortion of the wave function is also larger, and F_{11} is smaller. This general tendency can be seen in the left part of Table 6.1 by comparing the values of F_{11} for different N. The best gate performance was achieved for $N = 5$, with $F_{11} = 0.991$ and a gate time of $\tau_g = 1.838$ ms.

6.5.2 Optimal control of $\omega_\perp(t)$

After optimization of $\lambda(t)$, the fidelity of the gate is limited by collisional distortion of the wave function in state $|11\rangle$. To overcome this limitation, we have implemented a second stage of optimization, in which the interaction

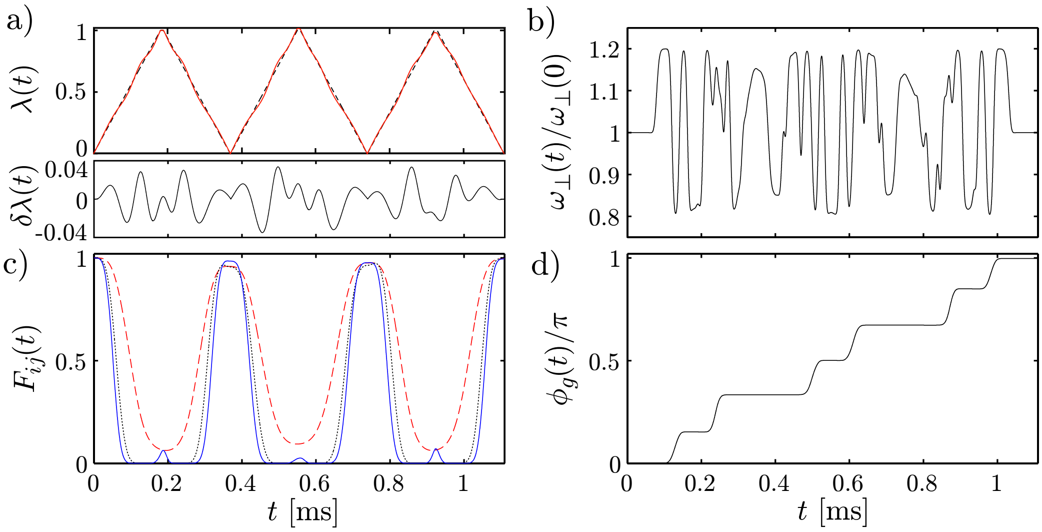

Figure 6.5: Dynamics during the gate operation, shown for $N = 3$ oscillations, the gate time is $\tau_g = 1.110$ ms. Both $\lambda(t)$ and $\omega_\perp(t)$ are used as control parameters. (a) Optimal control of the microwave power. Upper plot: Initial trial function $\lambda_0(t)$ (dashed) and optimized control parameter $\lambda(t)$ (solid line). Each triangular ramp of $\lambda(t)$ corresponds to a full oscillation of state $|1\rangle$. Lower plot: the difference $\delta\lambda(t) = \lambda(t) - \lambda_0(t)$ shows small modulations. (b) Optimal control of the effective one-dimensional interaction strength via modulation of the transverse trap frequency $\omega_\perp(t)$. (c) Evolution of the overlap fidelities during the gate operation: $F_{00}(t)$ (dashed), $F_{01}(t) = F_{10}(t)$ (dotted), $F_{11}(t)$ (solid line). (d) Evolution of the gate phase $\phi_g(t)$. The phase shift steps are due to the six collisions in state $|11\rangle$.

potential (6.13) is controlled during the gate operation with the transverse trap frequency $\omega_\perp(t)$ as control parameter. Experimentally, this corresponds to controlling the bias field component $B_{b,y}(t)$ and the DC current $I_T(t)$ proportional to the desired modulation of $\omega_\perp(t)$. Since the collisions in internal states other than $|11\rangle$ are negligible, this optimization affects only state $|11\rangle$. We optimize the overlap fidelity $F_{11}(\tau_g)$ and the phase $\phi_{11}(\tau_g)$ simultaneously, using again the Krotov method. For the microwave power we use the optimized $\lambda(t)$ determined in the previous section.

Care has to be taken that the modulation of $\omega_\perp(t)$ does not create excitations of the transverse state of the atoms. Since it is not possible to put constraints on the time derivative of the control parameter in the Krotov method of optimization, we have chosen the following strategy to avoid

		Optimal control of $\lambda(t)$						O. c. of $\lambda(t)$ and $\omega_\perp(t)$			
N	τ_g [ms]	O_0	O_1	F_{00}	F_{01}	F_{11}	ϕ_g/π	F_{00}	F_{01}	F_{11}	ϕ_g/π
2	0.696	0.996	0.996	0.993	0.993	0.960	0.996	0.993	0.993	0.987	0.998
3	1.110	0.998	0.997	0.996	0.996	0.986	0.999	0.996	0.996	0.995	0.997
4	1.389	0.996	0.995	0.991	0.991	0.991	0.991				
5	1.838	0.999	0.997	0.997	0.997	0.991	0.995				
6	2.219	0.996	0.998	0.992	0.993	0.985	0.993				

Table 6.1: Optimized gate performance for different numbers of oscillations N and correspondingly different gate times τ_g. All two-particle fidelities F_{ij}, single-particle overlaps O_i, and the gate phase ϕ_g are evaluated at $t = \tau_g$. Either only $\lambda(t)$ (left part of the table) or both $\lambda(t)$ and $\omega_\perp(t)$ (right part of the table) were chosen as control parameters. The optimization of $\omega_\perp(t)$ was performed only for $N \leq 3$, which is particularly interesting due to the short gate times $\tau_g \leq 10^{-3}\,\tau_t$.

transverse excitations. We parameterize the transverse trap frequency

$$\omega_\perp(t) = \omega_\perp(0)[A \tanh \alpha(t) + 1], \tag{6.18}$$

with $\alpha(t)$ being the dimensionless optimal control parameter, and $\omega_\perp(0)$ is determined for a given N as in the previous section. In this way, the optimization is constrained to a maximum modulation amplitude set by A. After the optimization on $\alpha(t)$ has converged, we remove high-frequency components from the resulting modulation of $\omega_\perp(t)$ by filtering with a cutoff frequency ω_c. We choose $\omega_c < 2\,\omega_\perp(0)$ in order to avoid parametric excitation of the transverse degrees of freedom. By performing the gate simulation again with the filtered modulation $\omega_\perp(t)$, we determine the overlap fidelities and the gate phase. We have seen that the filtering does not significantly decrease the fidelity if $\omega_c \gg \omega_x$. This shows that the high frequency components with $\omega > \omega_c$ were artifacts of the optimization algorithm without physical significance. The modulation of $\omega_\perp(t)$ after filtering is shown in Fig. 6.5(b). For this modulation, $A = 0.2$ and $\omega_c = 0.8\,\omega_\perp(0)$. To quantify the transverse excitation probability $p_\perp^m(t)$ during the gate operation, we simulate the transverse dynamics using a harmonic oscillator model, where the frequency is modulated according to the filtered $\omega_\perp(t)$. This simulation yields $p_\perp^m(t) < 7 \times 10^{-4}$, therefore transverse excitations due to the modulation of $\omega_\perp(t)$ do not limit the gate performance.

Fig. 6.5 is the main result of our simulation. It shows the gate dynamics for $N = 3$ after optimization of both $\lambda(t)$ and $\omega_\perp(t)$. Corresponding numbers for the overlap fidelities F_{ij} and the gate phase ϕ_g are shown in the right part of Table 6.1. The improvement compared to optimal control of $\lambda(t)$ alone (left part of Table 6.1) is an increase of F_{11} from $F_{11} = 0.986$ to $F_{11} = 0.995$, which is now comparable to the overlap fidelities in the other states. The gate time is $\tau_g = 1.110$ ms.

6.5.3 Gate fidelity

In order to provide an estimate of the overall gate performance, we use the definition given in [34] for the gate fidelity:

$$F = \min_\chi \left\{ \mathrm{Tr}_{\mathrm{ext}} \left[\langle \tilde{\chi} | \mathcal{U}\, \mathcal{S} \left(|\chi\rangle\langle\chi| \otimes \rho_0 \right) \mathcal{S}^\dagger \mathcal{U}^\dagger |\tilde{\chi}\rangle \right] \right\} . \tag{6.19}$$

Here, $|\chi\rangle$ is an arbitrary internal state of both atoms, and $|\tilde{\chi}\rangle$ is the state resulting from $|\chi\rangle$ using the actual transformation. $\mathcal{U}$ and $\mathcal{S}$ are the operators for time evolution and symmetrization under particle interchange, respectively. The density matrix ρ_0 is the initial two-particle motional state. According to this definition, the gate fidelity is

$$F = 0.997 \quad \text{for} \quad N = 3,\, \tau_g = 1.110 \text{ ms} \tag{6.20}$$

after optimization of both $\lambda(t)$ and $\omega_\perp(t)$. Even after the optimization, wave packet distortion still contributes the largest error reducing the fidelity. The error sources discussed in the next section lead to an additional error of the order of 1×10^{-3}, mainly due to the finite trap lifetime, which is limited by surface effects. If we include this error in the calculation of the fidelity, we get $F = 0.996$. By comparison, with trap and coherence lifetimes $\tau_t \sim \tau_c \sim 10^3\, \tau_g$, the maximum achievable fidelity of the gate with $N = 3$ would be $F = 0.999$, if wave packet distortion due to interaction dynamics could be reduced to negligible values.

6.6 Error sources

In this section, we discuss several effects which could possibly limit the fidelity of the phase gate proposed here, and justify the assumptions made in the description of the gate dynamics.

Finite temperature

The result for the fidelity (6.20) is obtained for zero temperature ($T = 0$) of the atoms. This corresponds to an initial motional state with one atom in the ground state $|n_1 = 0\rangle$ of the left potential well and the other atom in the ground state $|n_2 = 0\rangle$ of the right potential well of $u_c(\mathbf{r})$. To study the effect of finite temperature T on the gate performance, we start with an initial density operator for the motional degrees of freedom

$$\rho_0 = \sum_{n_1,n_2=0}^{\infty} P_{n_1,n_2}(T)|n_1\rangle\langle n_1| \otimes |n_2\rangle\langle n_2|, \tag{6.21}$$

where $P_{n_1,n_2}(T)$ is the probability for the occupation of the motional state $|n_1\rangle$ for atom 1 and $|n_2\rangle$ for atom 2 in the initial double well trap. The probabilities $P_{n_1,n_2}(T)$ are calculated assuming a thermal distribution corresponding to a temperature T in the canonical ensemble. We have evaluated the fidelity $F = F(T)$ of our gate with $N = 3$ as a function of T, see Fig. 6.6. The results show that high fidelity gate operations are only possible if the two atoms can be prepared in the motional ground state of the trap, with very low occupation probability of excited states. We assume that $k_B T/\hbar\omega_x \leq 0.1$ can be reached, corresponding to a temperature $T \leq 20$ nK in the initial double well trap. In this case, the fidelity is not reduced significantly due to the finite temperature.

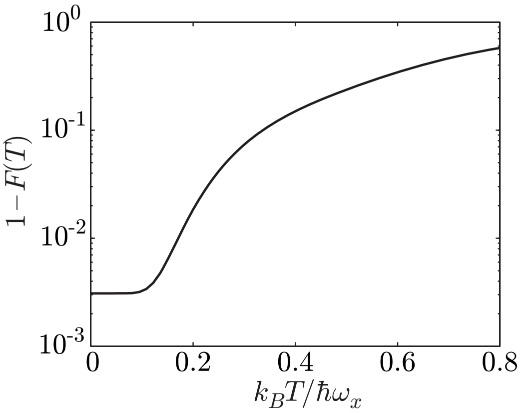

Figure 6.6: Gate infidelity $1 - F(T)$ as a function of temperature for the gate with $N = 3$.

Condition for quasi-1D dynamics

To ensure one-dimensional dynamics of the atoms in the experiment and to justify the one-dimensional simulation of the gate presented above, transverse excitations due to the collisions in state $|11\rangle$ have to be avoided. This mechanism could limit the fidelity even if transverse excitations due to the modulation of the transverse trap frequency $\omega_\perp(t)$ are suppressed (cf. section 6.5.2).

We calculate the probability $p_\perp^c(t)$ of transverse excitations due to collisions using a simple model. We consider two interacting atoms in a three-dimensional anisotropic harmonic oscillator potential, with $\omega_x \ll \omega_y = \omega_z \equiv \omega_\perp$. Exact solutions for this model are known [188]. The atoms are initially in the transverse ground state of the trap, but separated in two harmonic potential wells with separation d_x along the x direction, similar to the initial state of our phase gate. At time $t = 0$, the initial double well is switched off and the atoms evolve in the single anisotropic harmonic oscillator potential. The dynamics is obtained by expanding the initial three-dimensional two-atom state on the interacting basis given in [188]. For each evolution time t, we compute the reduced density matrix of the transverse motion by tracing out the axial degrees of freedom. In this way we compute the probability $p_\perp^c(t)$ as a function of time. We have performed this calculation for different d_x, corresponding to different kinetic energies E_{kin} of one atom at the time of the collision. In Fig. 6.7 we show $p_\perp^c(\tau_g)$ for $N = 3$ as a function of $2\,E_{\mathrm{kin}}/\hbar\omega_\perp$. We find that transverse excitations are energetically suppressed

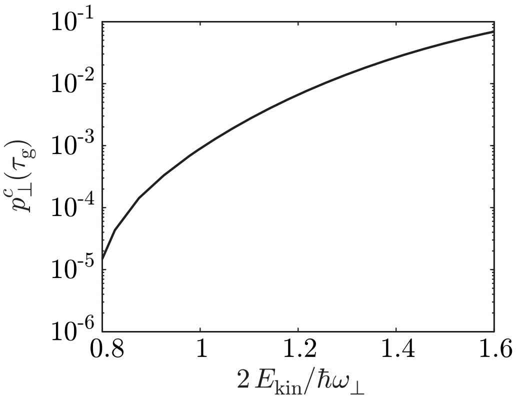

Figure 6.7: Transverse excitation probability $p_\perp^c(\tau_g)$ due to collisions of the atoms for $N = 3$. $p_\perp^c(\tau_g)$ is shown as a function of the kinetic energy E_{kin} of one atom in state $|1\rangle$ at the time of the collision.

if

$$2\,E_{\mathrm{kin}} < \hbar\omega_\perp, \tag{6.22}$$

For all trapping geometries used in our simulation of the phase gate, $2\,E_{\mathrm{kin}}/\hbar\omega_\perp \leq 0.7$, and the transverse excitation probability is suppressed to negligible values.

Microwave coupling and qubit dephasing

In contrast to optical dipole transitions, spontaneous emission is negligible for microwave transitions between ground state sublevels. Therefore microwaves can also be used to create adiabatic potentials with the microwave frequency tuned to resonance with a particular hyperfine transition. However, resonant coupling results in strong mixing of the hyperfine levels connected by the microwave. This is undesirable for our qubit state pair, since it would destroy the excellent coherence properties of the qubit by admixtures of other states with different magnetic moments. For this reason, we concentrate on the limit of large microwave detuning. The large detuning also ensures that the modulation of the microwave power during the gate operation is adiabatic with respect to the internal-state dynamics of the atoms.

For the trap parameters considered here,

$$\max \frac{\Omega_R^2}{\Delta^2} \leq 10^{-2}, \tag{6.23}$$

where we have set $\Omega_R \equiv \Omega_{1,m_1}^{2,m_2}$ and $\Delta \equiv \Delta_{1,m_1}^{2,m_2}$ to shorten notation in this section. In the absence of the microwave coupling, the differential magnetic moment $\delta\mu = \partial E_{|1\rangle}/\partial B - \partial E_{|0\rangle}/\partial B$ of the qubit states $|1\rangle$ and $|0\rangle$ can be calculated from the Breit-Rabi formula Eq. (1.5). For magnetic fields $B_0 < 6$ G, we get $|\delta\mu| < 2 \times 10^{-3}\,\mu_B$, with $\delta\mu = 0$, i.e. a vanishing first-order differential Zeeman shift, for $B_0 = 3.229$ G [84], as in the center of our static trap. In the presence of the microwave coupling, $\delta\mu$ changes due to the admixture of other magnetic sublevels, whose magnetic moments differ by multiples of $\mu_B/2$ from the magnetic moment of the qubit states. For $\Omega_R^2 \ll \Delta^2$, the order of magnitude of this change can be estimated to

$$\delta\mu \simeq \frac{\Omega_R^2}{4\Delta^2}\mu_B \leq 2.5 \times 10^{-3}\mu_B, \tag{6.24}$$

where we have used (6.23).

The differential magnetic moment determines the coherence time τ_c of the qubit in the presence of longitudinal magnetic field fluctuations (pure dephasing of the qubit). The frequency spectrum of the fluctuations plays an important role in this context: Low frequency fluctuations of the magnetic field are most harmful to the coherence time [162], since they do not average out on the time scale τ_g of a single gate operation. In contrast to magnetic near-field noise arising from the chip surface (see section 6.6), which has a flat spectrum in the relevant frequency range [31], technical magnetic field noise typically increases towards low frequencies and dominates in the frequency range $0 < \omega < 10/\tau_g$ considered here.

The atom chip is surrounded by magnetic shielding, so that the residual fluctuations of the magnetic field are limited by the stability of the current sources used for the wires and bias magnetic field coils. We assume that fluctuations in the frequency range $0 < \omega < 10/\tau_g$ can be reduced to an r.m.s. amplitude of $\delta B \leq 0.01$ mG, consistent with the stability of the current sources in our experiments. Under this assumption, we expect a coherence time of the order of

$$\tau_c \sim \frac{\hbar}{\delta\mu\,\delta B} \sim 5 \text{ s}, \tag{6.25}$$

where we have used (6.24). Comparing this value of τ_c with the trap and coherence lifetimes due to surface effects calculated in section 6.6, we find that pure dephasing of the qubit does not limit the fidelity of the gate.

Trap loss and decoherence due to the chip surface

A fundamental source of trap loss, heating, spin- and motional decoherence on atom chips is magnetic near-field noise originating from thermal currents in the chip wires, see section 1.9. For our state pair, pure spin dephasing arising from longitudinal magnetic near-field noise is negligible. The dominating surface effect is trap loss due to spin-flips induced by transverse magnetic field noise. For the chip layout shown in Fig. 6.3 and a distance $d = 1.80$ μm from the chip surface, we estimate an average spin-flip rate of $\gamma_s = 0.9$ s^{-1}, taking the finite thickness and width of the wires [189] and the different matrix elements for spin flips of state $|0\rangle$ and $|1\rangle$ into account. This corresponds to a trap lifetime of

$$\tau_t = \gamma_s^{-1} = 1.1 \text{ s}. \tag{6.26}$$

Compared with surface effects, loss rates due to collisions with background gas atoms are negligible. The rates for heating and motional decoherence due to magnetic near-field noise are comparable to γ_s, see section 1.9, so that we expect an overall coherence lifetime $\tau_c \sim \tau_t$. For $N = 3$, the gate operation time is $\tau_g = 1.110$ ms. The mentioned surface effects introduce an error of $1 - \exp(-\gamma_s\tau_g) = 1 \times 10^{-3}$ in the gate operation. This error is smaller than the error due to wave packet distortion, and therefore does not significantly decrease the gate fidelity (6.20). The error could be further reduced by reducing the wire thickness or using a trap at a slightly higher atom-surface distance.

Two-photon transitions

Another potential source of infidelities are two-photon transitions induced by the microwave. These can arise if more than one polarization component of the microwave is present, as it is in general the case in microwave near-fields. For $\Omega_{Ri}^2 \ll \Delta^2$, the two-photon coupling is characterized by an effective Rabi frequency $\Omega_{\mathrm{2ph}} = \Omega_{R1}\Omega_{R2}/(2\Delta)$, where Ω_{Ri}, $i \in \{1, 2\}$, are the single-photon Rabi frequencies of the transitions involved [151]. The detuning from two-photon resonance $\Delta_{\mathrm{2ph}} = \mu_B B_0/(2\hbar)$ is given by the Zeeman splitting due to the static magnetic field B_0 in the trap center. For our trap parameters

$$\max \frac{\Omega_{\mathrm{2ph}}^2}{\Delta_{\mathrm{2ph}}^2} \leq 2 \times 10^{-3}, \tag{6.27}$$

and two-photon transitions are suppressed by the large two-photon detuning.

Technical limitations

In our simulation, we assume total (microwave + DC) current densities $j_{\mathrm{tot}} \leq 1 \times 10^{11}$ Am^{-2} in the wires forming the coplanar strip line. The DC current density in the lower wire is $j_{\mathrm{tot}} = 2 \times 10^{11}$ Am^{-2}. Comparable current densities have been realized experimentally in [115] on Si substrates with a 20 nm $\mathrm{SiO_2}$ insulating layer.

We have checked that the potentials used in our simulation are robust against current and magnetic field fluctuations. We assume a relative stability on the level of 10^{-5} for the static currents and fields. With available current sources and magnetic shielding, such a stability can be reached in experiments. The accuracy of the currents (magnetic fields) specified in section 6.3 is assumed to be better than 1 μA (1 mG).

In order to study the robustness of the gate against noise on the time-dependent control parameters, we have simulated the gate with white noise on $\lambda(t)$ and $\omega_\perp(t)$. The gate fidelity is reduced by $\sim 10^{-4}$ for relative r.m.s. noise amplitudes $n_a < 10^{-3}$ on the control parameters. For these values of n_a, the small modulations of the experimental parameters used for optimal control are well above the noise level, see Fig. 6.5.

6.7 Conclusion

In conclusion, we have made a realistic proposal for a collisional phase gate using microwave potentials on an atom chip. The gate is implemented for a robust qubit state pair with experimentally demonstrated coherence and trap lifetimes $\tau_c \sim \tau_t \sim 1$ s at micrometer distance from the chip. We have simulated and optimized the gate dynamics for a chip layout which we specify in detail and which can be fabricated with today's technology. We found a gate fidelity of $F = 0.996$ at a gate operation time of $\tau_g = 1.1$ ms, taking many error sources into account. With a total infidelity of the order of a few 10^{-3}, our gate meets the requirements for fault-tolerant quantum computation [181, 182]. The gate fidelity of the present proposal is limited by wave packet distortion due to collisions and the dynamics of the atoms in a non-harmonic potential. We believe that these effects can be reduced by further optimization of the potential and better control of the gate dynamics, at the expense of introducing more control parameters. The ultimate limit to the fidelity will then be given by $\exp(-\tau_g/\tau_t) \sim 0.999$ for the chip layout discussed here.

The major experimental challenge in the realization of the gate proposed here is the deterministic preparation of single neutral atoms in the motional ground state of chip traps with very low occupation probability of excited states. Proposals for single atom preparation have been put forward in [190, 77]. An important prerequisite for single atom preparation is a single atom detector on the atom chip. Such detectors have recently been realized, using either macroscopic optical cavities surrounding the chip [57], or miniaturized optical fiber cavities integrated on the chip [55, 164, 56].

Chapter 7

BEC coupled to a nanomechanical resonator: a proposal

In this chapter, the coupling of Bose-Einstein condensed atoms to the mechanical oscillations of a nanoscale cantilever with a magnetic tip is theoretically investigated. This is an experimentally viable hybrid quantum system which allows one to explore the interface of quantum optics and condensed matter physics. An experiment is proposed where easily detectable atomic spin-flips are induced by the cantilever motion. This can be used to probe thermal oscillations of the cantilever with the atoms. At low cantilever temperatures, as realized in recent experiments, the backaction of the atoms onto the cantilever is significant and the system represents a mechanical analog of cavity quantum electrodynamics. With high but realistic cantilever quality factors, the strong coupling regime can be reached, either with single atoms or collectively with Bose-Einstein condensates.

This chapter was published in [191]. Experimental work towards a realization of the system proposed here is carried out in collaboration with the group of Prof. Kotthaus at LMU Munich.

7.1 Quantum optics meets condensed matter

Quantum optics and condensed matter physics presently show a strong convergence. On the one hand, quantum optical systems, most notably neutral atoms in optical lattices, have been used to experimentally investigate concepts of condensed matter physics such as Bloch oscillations and Fermi surfaces [16]. On the other hand, micro- and nanostructured condensed matter systems enter a regime described by concepts of quantum optics, as exemplified by circuit cavity quantum electrodynamics [192], laser-cooling of mechanical resonators [193, 194, 195, 196, 197, 198], and measurement backaction effects in cryogenic mechanical resonators [199]. A new exciting possibility beyond this successful conceptual interaction is to *physically couple* a quantum optical system to a condensed matter system. Such a hybrid quantum system can be used to study fundamental questions of decoherence at the transition between quantum and classical physics and has possible applications in precision measurement [200] and quantum information processing [201].

Atom chips are ideally suited for the implementation of hybrid quantum systems. Neutral atoms can be positioned with nanometer precision [42] and trapped at distances below 1 μm from the chip surface [44]. Coherent control of internal states (see chapter 4) and motional states [43] of atoms in chip traps is a reality. Atom-surface interactions are sufficiently understood (see chapter 1) so that undesired effects can be mitigated by choice of materials and fabrication techniques. This is an advantage over systems such as ions or polar molecules on a chip, which have recently been considered in this context [201, 202]. A first milestone in this new field of atom chip research is to realize a controlled interaction between atoms and a nanodevice on the chip surface.

As an example of such an interaction, we investigate magnetic coupling between the spin of atoms in a BEC and a single vibrational mode of a nanomechanical resonator [203] on an atom chip. We find that the BEC can be used as a sensitive quantum probe which allows one to detect the thermal motion of the resonator at room temperature. At lower resonator temperatures, the backaction of the atoms onto the resonator is significant and the coupled system realizes a mechanical analog of cavity quantum electrodynamics (cQED) in the strong coupling regime. We specify in detail a realistic setup for the experiment, which can be performed with available atom chip technology, and thus allows one to explore this fascinating field already today.

7.2 Coupling mechanism

The physical situation is illustrated in Fig. 7.1(a). ^{87}Rb atoms are trapped in a magnetic microtrap at a distance y_0 above a cantilever resonator, which is nanofabricated on the atom chip surface. The cantilever tip carries a single-domain ferromagnet which creates a magnetic field with a strong gradient G_m. The magnet transduces out-of-plane mechanical oscillations $a(t) =$

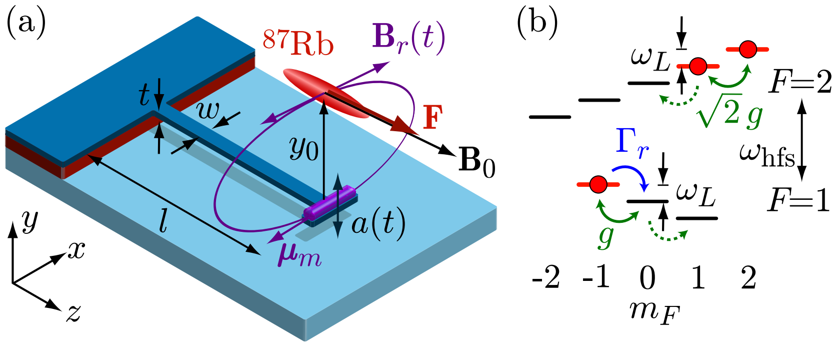

Figure 7.1: BEC-resonator coupling mechanism. (a) Atom chip with a BEC of ^{87}Rb atoms (red: BEC wave function) at a distance y_0 from a nanomechanical resonator. The free-standing structure (dark blue) is supported at one end to form a cantilever-type resonator that performs out-of-plane mechanical oscillations $a(t)$. The single-domain ferromagnet (purple) on the resonator tip creates a magnetic field with oscillatory component $\mathbf{B}_r(t)$ which couples to the atomic spin $\mathbf{F}$. (b) Hyperfine structure of ^{87}Rb in the magnetic field $\mathbf{B}_0$. Hyperfine levels $|F, m_F\rangle$ are coupled (blue or green arrows, depending on experiment) if the Larmor frequency ω_L is tuned to the oscillation frequency of the resonator. Magnetically trappable states indicated in red.

$a\cos(\omega_r t + \varphi)$ of the cantilever tip of amplitude $a \ll y_0$ into an oscillatory magnetic field $\mathbf{B}_r(t) = G_m a(t)\mathbf{e}_x$ in the center of the microtrap. The orientation of the magnet is chosen such that $\mathbf{B}_r$ is perpendicular to the static magnetic field $\mathbf{B}_0 = B_0\mathbf{e}_z$ in the trap center. The atomic spin $\mathbf{F}$ interacts with $\mathbf{B}_r(t)$ via the Zeeman Hamiltonian

$$H_Z = -\boldsymbol{\mu} \cdot \mathbf{B}_r(t) = \mu_B g_F F_x G_m a(t), \tag{7.1}$$

where $\boldsymbol{\mu} = -\mu_B g_F \mathbf{F}$ is the operator of the magnetic moment. In this way, the ferromagnet establishes a coupling between the spin and the resonator mechanical motion.

The ground state hyperfine spin levels $|F, m_F\rangle$ of ^{87}Rb are shown in Fig. 7.1(b). The energy splitting between adjacent m_F-levels is given by the Larmor frequency $\omega_L = \mu_B |g_F| B_0/\hbar$. Note that ω_L is widely tunable by adjusting B_0. This allows one to control the detuning $\delta = \omega_r - \omega_L$ between a given resonator mode of frequency ω_r and the atomic resonance in the trap center. Quickly changing δ switches the coupling on and off. Near resonance ($\delta \approx 0$), the coupling leads to spin flips.

In a magnetic trap, only weak-field seeking states are trapped, as indicated in Fig. 7.1(b). This can be exploited in a simple way to detect the spin flips induced by the coupling: atoms initially trapped in state $|1,-1\rangle$ are coupled by the nanoresonator to $|1,0\rangle$, where they are quickly lost from the trap. This is analogous to a cw atom laser experiment [204], with the mechanical resonator inducing the radio-frequency magnetic field for output coupling. The rate Γ_r at which atoms are coupled out of the BEC is a sensitive probe revealing the temporal dynamics of the resonator motion.

To derive Γ_r, we follow the theory of [205], which includes effects of interatomic interactions, but neglects gravity. This is justified here due to the high trap frequencies. The trapped BEC in $|1,-1\rangle$ is assumed to be in the Thomas-Fermi (TF) regime (see section 1.7). It is coupled with Rabi frequency $\Omega_R = \mu_B G_m a/\sqrt{8}\hbar$ to $|1,0\rangle$, where a continuum of untrapped motional states is available to the atoms. The energy width of this continuum is given by the BEC chemical potential μ_c. For typical parameters (see below), $\hbar\Omega_R \ll \mu_c$, and only a fraction $\simeq \hbar\Omega_R/\mu_c$ of the BEC atoms is resonantly coupled. In this limit [205],

$$\Gamma_r = \frac{15\pi}{8}\frac{\hbar\Omega_R^2}{\mu_c}\left(r_c - r_c^3\right), \tag{7.2}$$

where $r_c = \sqrt{\hbar\delta/\mu_c}$. Output coupling takes place on a thin ellipsoidal shell of resonance with main axes $r_i = r_c R_i$, where R_i are the TF radii of the BEC.

7.3 Chip layout

Figure 7.2(a) shows an implementation which we envisage in collaboration with the Kotthaus group at CeNS, LMU Munich [206]. The atom chip is fabricated by several steps of e-beam lithography on a Si-on-insulator wafer in combination with lift-off metallization and selective etching of the oxide to create free-standing Si structures. Atoms are trapped in a Ioffe-type trap created by currents in the chip wires [24]. Our numerical simulation of the trapping potential (Fig. 7.2(b)) includes the magnetic fields of the wires, the Co magnets, the homogeneous field $\mathbf{B}_b$, gravity, and the Casimir-Polder surface potential Eq. (1.45). Trap frequencies are adjustable in the kHz-range, the aspect ratio is $\omega_z/\omega_{x,y} \approx 0.1$. The trap loss rate $\gamma = \gamma_{3\mathrm{b}} + \gamma_s + \gamma_{\mathrm{bg}}$ in the absence of the coupling to the resonator is dominated by three-body collisions, with a rate $\gamma_{3\mathrm{b}} = 2.2 \times 10^{-12}\ \mathrm{s}^{7/5} \times \omega_{\mathrm{ho}}^{12/5} N^{4/5}$ for state $|1,-1\rangle$ in the TF-regime, see Eq. (1.32), where $\omega_{\mathrm{ho}} = (\omega_x\omega_y\omega_z)^{1/3}$. Background gas collisions (γ_{bg}) and atom-surface interactions (γ_s) contribute much smaller rates, $\gamma_s + \gamma_{\mathrm{bg}} \ll \gamma_{3\mathrm{b}}$.

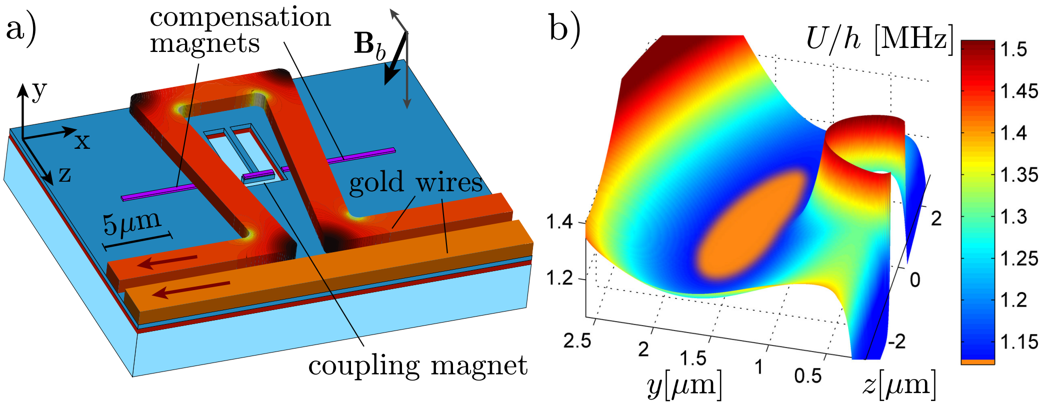

Figure 7.2: (a) Atom chip layout. The trapping potential is created by gold wires (width 2 μm, current 4.4 mA) and a homogeneous field $\mathbf{B}_b = (-0.1, -4.2, -1.6)$ G. The wire color indicates the current density obtained from a finite elements simulation. The Co coupling magnet on the tip of the Si cantilever is located directly below the center of the atom trap. Compensation magnets on each side of the tip reduce distortion of the trapping potential due to the static field of the coupling magnet. (b) Trapping potential in the yz-plane intersecting the resonator. Trap minimum at $(y_0, z_0) = (1.5, 0.0)$ μm, trap frequencies $\omega_{x,y,z}/2\pi = (8.9, 9.7, 1.2)$ kHz for $|1, -1\rangle$. The static field of the magnets causes a repulsive potential around $y = z = 0$. The attractive Casimir-Polder surface potential is visible for $y \to 0$. The orange area in the trap center shows the extension of the BEC.

The ferromagnet is a single magnetic domain whose magnetic moment $\boldsymbol{\mu}_m$ is spontaneously oriented along its long axis due to the shape anisotropy. For Co nanobars, a switching field > 500 G [207] ensures that the magnetization of the bar is nearly unaffected by the fields applied for magnetic trapping, which are < 100 G. Approximating the bar by a magnetic dipole, we have $G_m = 3\mu_0|\boldsymbol{\mu}_m|/4\pi y_0^4$. By changing y_0 and the magnet dimensions, G_m can be adjusted. Equation (7.1) suggests that the strength of the atom-nanoresonator coupling can be maximized by increasing G_m as much as possible. However, the atoms experience a force in this field gradient, and an excessively large G_m would strongly distort the trapping potential. To mitigate distortion, two compensation magnets are placed next to the coupling magnet with identical direction of magnetization. This reduces the static field gradient at the location of the atoms, while the oscillatory field $\mathbf{B}_r(t)$ remains unaffected as the compensation magnets do not oscillate.

Nanomechanical resonators have a complex spectrum of vibrational modes. Due to their high quality factors $Q = 10^3 - 10^5$ [203, 199], the modes are well resolved. The BEC is coupled to the fundamental out-of-plane flexural oscillation at frequency $\omega_r/2\pi \approx 0.16\sqrt{E/\varrho(1+c)}\,(t/l^2)$. Here, $t \leq w \ll l$ are the dimensions, E is Young's modulus, and ϱ is the mass density of the cantilever, while $c = m/0.24\varrho lwt$ accounts for the additional mass m of the magnet and the Si paddle at the cantilever tip. The force acting on the coupling magnet in the magnetic field of the compensation magnets leads to an additional shift of ω_r which is determined numerically and included in the numbers given below.[1] We model the cantilever tip as a harmonic oscillator of frequency ω_r with an effective mass $m_{\text{eff}} \approx 0.24\varrho lwt + m$, obtained by integrating over the mode function.

7.4 Thermal motion of the cantilever

In contrast to the BEC, which is a prime example of quantum-mechanical coherence, dissipation and thermal effects play an important role in the cantilever dynamics. In thermal equilibrium with its environment at temperature T, the cantilever performs oscillations at frequency ω_r with random amplitude a and phase φ [208]. Both a and φ change on a timescale κ^{-1}, where $\kappa = \omega_r/2Q$ is the damping rate. For a high-Q cantilever, however, this timescale is longer than the time scale Γ_r^{-1} of coupling to the BEC, as we will show below. This allows one to use the BEC as a probe to directly monitor the thermal fluctuations. In a single shot of such an experiment, the cantilever performs simple harmonic motion with constant a and φ. The BEC in $|1,-1\rangle$ is coupled to the cantilever for a time $\tau \ll \kappa^{-1}$ and the remaining number of atoms $N(a,\tau) = N\exp[-\Gamma_r(a)\,\tau]$ is measured. Repeating the experiment, one observes fluctuations of $N(a,\tau)$ due to the fluctuations of a. Figure 7.3 shows a simulated histogram of $N(a,\tau)/N$. Since $\Gamma_r \propto a^2 \propto n$, the histogram reflects the exponential distribution of phonon numbers n in the thermal state of the resonator, with $\langle\Gamma_r\rangle$ given by the mean phonon number $n_{\text{th}} = [\exp(\hbar\omega_r/k_BT)-1]^{-1}$.

As a realistic example, we take a Si cantilever with $(l,w,t) = (7.0, 0.2, 0.1)$ μm, $m_{\text{eff}} = 3\times10^{-16}$ kg, and $\omega_r/2\pi = 1.12$ MHz. It carries a Co magnet of dimensions $(l_m, w_m, t_m) = (1.3, 0.2, 0.08)$ μm; the two compensation magnets have the same cross section and 5 μm length, the gap between magnets is $d = 200$ nm. Trap parameters optimizing $\langle\Gamma_r\rangle/\gamma$ for a BEC of $N = 10^3$ atoms are given in Fig. (7.2). For given ω_{ho}, we adjust G_m to the maximum value allowed by trap distortion.[2] The mean coupling rate for $r_c = 1/\sqrt{3}$ is

---

[1] We have estimated that cantilever damping due to this interaction as well as due to eddy currents induced in the gold wires is negligible in our geometry.

[2] In calculating G_m, we use the formula of [209].

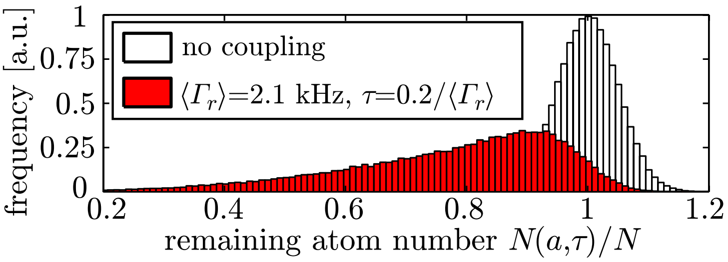

Figure 7.3: Coupling of the BEC to a thermally driven cantilever at $T = 300$ K. Simulated histogram of the fraction of atoms remaining in the trap after a time τ, including background loss. For comparison, the atom number distribution without coupling is shown. We have assumed 5% fluctuations in atom number due to technical noise.

$\langle\Gamma_r\rangle = 2.1$ kHz. Background losses are much smaller, $\gamma = 0.01\,\langle\Gamma_r\rangle$. Taking a moderate $Q = 5 \times 10^3$ and $\tau = 0.2/\langle\Gamma_r\rangle$, we have $\kappa\tau = 0.07$. This shows that coupling the BEC to the thermal motion of the resonator is easily achieved with parameters which are based on fabrication results at CeNS.

7.5 A mechanical cavity QED system

At room temperature, the thermal equilibrium state of the resonator has an average phonon number $n_{\text{th}} \gg N$, and the coupling does not significantly perturb the state of the resonator. By cooling a resonator in a dilution refrigerator, phonon numbers as low as $n_{\text{th}} = 25$ have been observed [199]. Recently, laser cooling of mechanical oscillations was demonstrated [193, 194, 195, 196, 197, 198], which opens the exciting perspective of preparing a single mode of the resonator with very low n_{th} or even reaching the quantum mechanical ground state ($n_{\text{th}} \ll 1$) without a cryostat. At low mode temperatures, $n_{\text{th}} \sim N$ and the backaction of the BEC onto the resonator cannot be neglected. Every atom changing its state changes the number of phonons in the resonator mode by one. In this regime, it is possible to use the BEC as an actuator for the mechanical oscillations. The two systems exchange energy coherently, increasing or decreasing the number of phonons depending on the initial state of the BEC.

In analogy with cQED, we derive a fully quantum-mechanical theory for the dynamics of the coupled system. We now consider a transition between two trapped atomic states $|0\rangle \leftrightarrow |1\rangle$. In a magnetic trap, $|0\rangle \equiv |2,1\rangle$ and $|1\rangle \equiv |2,2\rangle$ can be used (see Fig. 7.1(b)). However, the different trap frequencies lead to entanglement between internal and motional atomic degrees of freedom. Here, we discuss the simpler situation of an optical or electrodynamic microtrap [52], which provides identical trapping potentials for all hyperfine states. In such a trap, all atoms in the BEC couple simultaneously to the resonator. Since collisional losses are lower in $F = 1$, we choose $|0\rangle \equiv |1, 0\rangle$ and $|1\rangle \equiv |1, -1\rangle$. The transition $|0\rangle \leftrightarrow |1\rangle$ can be decoupled from other m_F-levels by making use of the quadratic Zeeman effect or by using microwaves to induce m_F-dependent energy shifts, see chapter 5.

A BEC of N two-level atoms with level spacing $\hbar\omega_L$ can be described by a collective spin $S = N/2$ with Hamiltonian $H_{\mathrm{BEC}} = \hbar\omega_L S_z$ and eigenstates $|S, m_S\rangle$, $|m_S| \leq S$ [210]. The Hamiltonian of the quantized resonator is $H_r = \hbar\omega_r a^+ a$, where a (a^+) is the annihilation (creation) operator for phonons in the fundamental mechanical mode. The coupling Hamiltonian is obtained by replacing $\sqrt{2}\, g_F F_x \rightarrow S_x$ and $a(t) \rightarrow a_{\mathrm{qm}}(a^+ + a)$ in Eq. (7.1), where $a_{\mathrm{qm}} = \sqrt{\hbar/2m_{\mathrm{eff}}\omega_r}$ is the r.m.s. amplitude of the quantum mechanical zero-point motion. For the coupled system, $H = H_r + H_{\mathrm{BEC}} + H_Z$. With $S^{\pm} = S_x \pm iS_y$ and applying the rotating-wave approximation, we obtain the Tavis-Cummings Hamiltonian [210],

$$H = \hbar\omega_r a^+ a + \hbar\omega_L S_z + \hbar g(S^+ a + S^- a^+), \tag{7.3}$$

where $g = \mu_B G_m a_{\mathrm{qm}}/\sqrt{8}\hbar$ is the single-atom single-phonon coupling constant. In cQED, Eq. (7.3) usually describes the coupling of atoms to the electromagnetic field of a single mode of an optical or microwave cavity [210]. Here, it describes the coupling to the phonon field of a mode of mechanical oscillations. In this sense, this is a mechanical cQED system.

We now investigate whether the strong coupling regime of cQED [211] can be reached, where coherent dynamics occurs at a faster rate than dissipative dynamics. For a single atom ($N = 1$), this requires $g > (\kappa, \gamma)$. We maximize $g/(\kappa + \gamma)$ by optimizing resonator, magnet, and trap parameters. We take a Si cantilever with $(l, w, t) = (8.0, 0.3, 0.05)$ μm and assume $Q = 10^5$ as in recent experiments at low T [199]. It carries a Co magnet with $(l_m, w_m, t_m) = (250, 50, 80)$ nm and $d = 40$ nm, resulting in $\omega_r/2\pi = 2.8$ MHz. For $N = 1$ there is not collisional loss; therefore, higher ω_{ho} is possible. In a trap with $\omega_{\mathrm{ho}}/2\pi = 250$ kHz and $y_0 = 250$ nm, realistic on atom chips [212], we obtain strong coupling with $(g, \kappa, \gamma) = 2\pi \times (62, 14, 0.3)$ Hz. A related quantity is the cooperativity parameter, $C = g^2/2\kappa\gamma$. For $C > 1$, mechanical analogs of optical bistability and squeezing can be observed. We obtain $C = 430$. To prepare the resonator with $n_{\mathrm{th}} < 1$, $T < 0.1$ mK is required. Such low temperatures could perhaps be achieved by laser cooling.

For N atoms identically coupled to the resonator, the coupling is collectively enhanced. Coherent dynamics now occurs if the weaker condition

$g\sqrt{N} > (\kappa, \gamma)$ is met [211]. This is still true for a resonator in a thermal state as long as $n_{\text{th}} \ll N$, putting less stringent limits on T. For resonator dimensions as above, $(l_m, w_m, t_m) = (2.0, 0.06, 0.12)$ μm, and $d = 100$ nm we obtain $\omega_r/2\pi = 1.1$ MHz. Maximizing $g\sqrt{N}/(\kappa + \gamma)$ for a BEC with $N = 10^4$ atoms, we find a trap with $\omega_{\text{ho}}/2\pi = 2.9$ kHz and $y_0 = 2.0$ μm. At $T = 50$ mK (typical in a dilution refrigerator), $n_{\text{th}} \approx 980 \ll N$. Collective strong coupling is reached with $(g\sqrt{N}, \kappa, \gamma) = 2\pi \times (21, 5, 10)$ Hz and the N-atom cooperativity is $CN = 4$.

In a quantum Monte Carlo simulation, we couple a BEC in state $|S = N/2, m_S = N/2\rangle$ (i.e. all atoms in state $|1\rangle$) to a resonator with $n_{\text{th}} \ll N$. The coupling drives the resonator out of thermal equilibrium into a state with a mean phonon number $\langle n\rangle \gg n_{\text{th}}$. Conversely, if the BEC is prepared in state $|S = N/2, m_S = -N/2\rangle$ (all atoms in state $|0\rangle$), excitations are initially transferred from the resonator to the BEC, creating a state with $\langle n\rangle \ll n_{\text{th}}$. The time scale for both processes is $\pi/2g\sqrt{N}$. Depending on the initial conditions, the BEC can therefore be used to drive or cool the resonator mode. In a similar way, Rydberg atoms have been used to either reduce or increase the number of photons inside a microwave cavity in a controlled way [213].

7.6 Conclusion

We have shown that a BEC on an atom chip can be used as a sensitive probe, as a coolant, and as a coherent actuator for a nanomechanical resonator. The coupling could be used to transfer nonclassical states of the BEC to the mechanical system. Due to the dissipative coupling of the resonator to its environment, interesting questions of decoherence arise and can be studied with this system. Instead of coupling different spin levels, it is also possible to couple the resonator to the motional degrees of freedom of either a BEC or a single atom, similar to the coupling mechanism proposed for a nanoscale ion trap in [201]. In a recent experiment, a spin resonance transition in a thermal atomic vapor was excited by an externally driven mechanical resonator with a magnetic tip [200]. Compared to this experiment, our system requires a much smaller resonator and much better control over the atoms. This is crucial for observing backaction effects of the atoms onto the resonator. In collaboration with the Kotthaus group, we are currently working towards an experimental realization of our system. Figure 7.4 shows a first chip prototype which we have fabricated according to the design in Fig. 7.2.

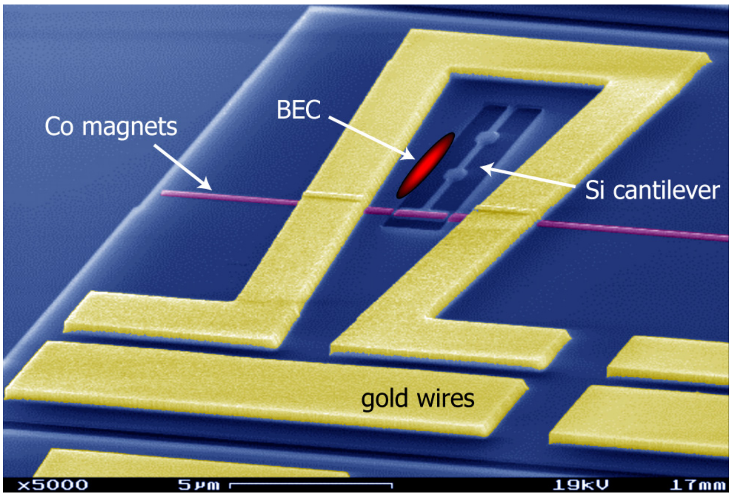

Figure 7.4: SEM image of a prototype of the BEC-nanoresonator chip. Color highlights the chip components, position of BEC is sketched. Chip fabricated by S. Camerer in collaboration with D. König in the cleanroom facilities of the Kotthaus group at CeNS, LMU Munich.

Chapter 8

Outlook

The experiments reported in this thesis show that atoms can be manipulated coherently on an atom chip, despite the close proximity of the atoms to the room-temperature chip surface. This is crucial for the use of atom chips in quantum engineering and enables new experiments at the boundary between quantum optics and condensed matter physics.

The proposals for an atom chip quantum gate and a Bose-Einstein condensate coupled to a nanomechanical resonator described in chapters 6 and 7 of this thesis, respectively, represent a detailed outlook on two specific experiments. Further ideas are briefly outlined in the following.

Further applications of microwave near-fields

The microwave near-fields investigated in chapter 5 are a useful new tool for atom chip experiments. Recently, we have succeeded in performing internal-state manipulation of atoms with the help of the waveguides on our new chip. We observed Rabi-frequencies of ~ 1 MHz at only ~ 10 mW of microwave power, and strong microwave field gradients as a function of distance from the waveguide.

Chip-based atomic clocks will benefit from the large Rabi frequencies, tailored field configurations, and temporal stability of microwave near-fields, as well as the small size of the field-generating structures. Microwave near-field potentials could be utilized to trap atoms in internal states which cannot be trapped with static magnetic fields [170, 171]. State-dependent potentials can be employed for trapped-atom interferometry with internal-state labeling of the interferometer paths. The advantage is that the interferometer signal can be read out by state-selective detection without the need for spatially resolving the interference fringes [214, 4, 215]. Many more potential geometries are conceivable beyond the double well considered in chapters 5 and 6. Furthermore, an extension to multiple microwave frequencies seems promising and is technically straightforward.

Josephson effect and BEC entanglement

A BEC in a double well potential has been used in experiments on the Josephson effect and related phenomena [216, 217]. With a two-state BEC in a state-dependent potential, not only the “external-state” but also the “internal-state” variant of the Josephson effect is accessible [218, 69]. This allows for greater flexibility in tuning the system parameters “tunneling coupling” (adjustable via the two-photon Rabi frequency) and “on-site interaction” (adjustable via the potential for each state separately). In a number of theoretical papers it has been proposed that such a system could be used to create entangled number states of small BECs [219, 220, 76, 221]. Enhanced tunability might facilitate the generation of entangled number states, in particular if optimal control techniques are used to optimize the time dependence of the parameters. Moreover, it would be interesting to study whether BECs can be entangled via internal-state selective collisions, similar to the entanglement between single atoms created during the operation of the quantum gate proposed in chapter 6. For such experiments, the reproducible preparation of BECs with a few tens to a few hundreds of atoms is important.

Miniaturized cold-atom devices: portable atomic clocks and interferometers

Another perspective is the creation of miniaturized cold atom devices. The atomic clock on a chip which we have realized in a proof-of-principle experiment indicates that the first “real-world” applications of atom chips may lie in precision measurement. As mentioned in chapter 4, an improved version of the atomic clock is currently being set up in Paris. This clock uses the microwave near-field technology developed in this thesis, and the chip was fabricated with our fabrication process. The clock could outperform today’s best commercial atomic clocks by a factor of 10, while being much smaller than the atomic fountain primary standards. This combination of features opens a clear perspective for applications as a secondary standard and in satellite navigation.[1] In addition to atom chip clocks, portable inertial sensors are conceivable, based on the spatial splitting of BECs on an atom chip, as demonstrated in [45, 46, 60]. Further miniaturization of the atom chip experimental apparatus is currently pursued in the context of

---

[1] P. Rosenbusch, l’Observatoire de Paris, private communication.

a BEC experiment for a space mission [145], and a first commercial company has been founded which sells miniaturized atom chip vacuum systems (www.coldquanta.com).

Coupling of atoms to solid-state systems on the chip

Hybrid quantum systems composed of neutral atoms, ions, or polar molecules which are coupled to solid-state systems have recently attracted great theoretical interest [179, 201, 202, 191]. This is partly motivated by quantum information processing, where hybrid approaches promise to combine the long coherence times of isolated particles with the fast dynamics characteristic of solid-state implementations. Experiments with neutral atoms will benefit from the exquisite control over the atoms and the interface to solid state systems provided by atom chips.

For the coupling of ultracold atoms to nanomechanical systems, several alternatives to the Si resonator investigated in chapter 7 come to mind. Carbon nanotubes or graphene sheets [222, 223, 224, 225] are interesting because of their small effective mass, but at present clamping losses limit the attainable quality factors to $Q \sim 10^3$. GaN nanowires could be an alternative, where $Q = 6 \times 10^4$ has been observed near room temperature [226]. Different coupling mechanisms, e.g. via the surface potential, deserve further investigation. Carbon nanotubes have also been considered as current-carrying wires on an atom chip [227].

Atoms could also be coupled to superconducting systems[2] such as Josephson junction circuits [229, 230, 231, 19] or coplanar microwave cavities [192, 20]. In these solid-state systems, quantum behavior such as Rabi oscillations and entanglement has been demonstrated. The coupling could be magnetic, or the atoms could be excited to Rydberg states, whose large electric dipole moments would provide strong coupling [179, 232].

BECs on an atom chip can be used as a "scanning probe tip" for measurements of small electric and magnetic fields as well as surface forces [44, 233]. The BEC is different from probe tips used in atomic force microscopy (AFM) in that all degrees of freedom of the BEC are controlled on the quantum level. Similar to an AFM tip, which can be used for detection *and* manipulation, a sufficiently strong coupling could be used to manipulate the quantum state of the condensed matter system with the atoms. This would be an interesting approach to investigate whether the peculiar features of quantum mechanics such as coherent superpositions of quantum states, quantum interference, and entanglement can be preserved as the systems become more macroscopic.

---

[2] See [228] for an early experiment on atom detection with a SQUID.

Appendix A

Useful data and formulae

A.1 Fundamental constants and important ^{87}Rb data

Planck's constant	h $\hbar = h/2\pi$	$6.626\ 068\ 76(52) \times 10^{-34}$ J s $1.054\ 571\ 596(82) \times 10^{-34}$ J s
Bohr magneton	μ_B	$9.274\ 008\ 99(37) \times 10^{-24}$ J/T $h \cdot 1.399\ 624\ 624(56)$ MHz/G
Speed of light	c	$2.997\ 924\ 58 \times 10^{8}$ m/s (exact)
Permeability of vacuum	μ_0	$4\pi \times 10^{-7}$ N/A^2 (exact)
Permittivity of vacuum	$\varepsilon_0 = (\mu_0 c^2)^{-1}$	$8.854\ 187\ 817\ldots \times 10^{-12}$ F/m
Bohr radius	a_0	$0.529\ 177\ 208\ 3(19) \times 10^{-10}$ m

Table A.1: Selected fundamental constants, taken from [64] if no other source is specified.

General properties

Atomic mass	m	$1.443\ 160\ 60(11) \times 10^{-25}$ kg
Nuclear spin	I	$3/2$
Relative natural abundance		27.83(2)%

D_2 transition ($5^2S_{1/2} \leftrightarrow 5^2P_{3/2}$) optical properties

Wavelength (vacuum)	λ	780.241 209 686(13) nm
Natural line width	Γ	$2\pi \cdot 6.065(9)$ MHz
Saturation intensity $\lvert F=2, m_F=\pm 2\rangle \leftrightarrow \lvert F'=3, m_F{}'=\pm 3\rangle$ cycling transition ($\sigma^{\pm}$-polarized light)	I_s	1.669(2) mW/cm^2

$5^2S_{1/2}$ ground state properties

Hyperfine structure constant	A_{hfs}	$h \cdot 3.417\ 341\ 305\ 452\ 15(5)$ GHz
Zero-field hyperfine splitting	E_{hfs} $= 2A_{\mathrm{hfs}}$	$h \cdot 6.834\ 682\ 610\ 904\ 29(9)$ GHz
Electron spin g-factor	g_J	2.002 331 13(20)
Nuclear spin g-factor	g_I	$-0.000\ 995\ 141\ 4(10)$
Static polarizability	α_0	$h \cdot 0.0794(16)$ Hz/(V/cm)^2
S-wave scattering lengths		values from [80]
$\lvert 1,-1\rangle - \lvert 1,-1\rangle$	a_{00}	$100.40\,a_0 = 5.3129$ nm
$\lvert 2,1\rangle - \lvert 1,-1\rangle$	a_{10}	$97.66\,a_0 = 5.1679$ nm
$\lvert 2,1\rangle - \lvert 2,1\rangle$	a_{11}	$95.00\,a_0 = 5.0272$ nm

Table A.2: Selected properties of ^{87}Rb, taken from [64] if no other source is specified.

A.2 Magnetic field of a rectangular wire of finite length

The magnetic field of a straight rectangular wire extending over $x_0 \leq x \leq x_1$, $y_0 \leq y \leq y_1$, $z_0 \leq z \leq z_1$ and carrying a homogeneous current density $\mathbf{j} = j\mathbf{e}_x$ can be obtained by integration of the Biot-Savart law [68]

$$\mathbf{B}(\mathbf{r}) = \frac{\mu_0}{4\pi} \int_{x_0}^{x_1} dx' \int_{y_0}^{y_1} dy' \int_{z_0}^{z_1} dz' \, \frac{\mathbf{j} \times (\mathbf{r} - \mathbf{r}')}{|\mathbf{r} - \mathbf{r}'|^3}. \tag{A.1}$$

With the definitions

$$\begin{aligned} f(x, y, z) \equiv{} & z \arctan \left[\frac{xy}{z\sqrt{x^2 + y^2 + z^2}} \right] \\ & - x \ln \left[y + \sqrt{x^2 + y^2 + z^2} \right] - y \ln \left[x + \sqrt{x^2 + y^2 + z^2} \right], \end{aligned} \tag{A.2}$$

and $\tilde{x}_k = x - x_k$, $\tilde{y}_l = y - y_l$, $\tilde{z}_m = z - z_m$, we obtain

$$B_x = 0, \tag{A.3}$$

$$B_y = -\frac{\mu_0 j}{4\pi} \sum_{k,l,m=0}^{1} (-1)^{k+l+m} f(\tilde{x}_k, \tilde{y}_l, \tilde{z}_m), \tag{A.4}$$

$$B_z = \frac{\mu_0 j}{4\pi} \sum_{k,l,m=0}^{1} (-1)^{k+l+m} f(\tilde{x}_k, \tilde{z}_m, \tilde{y}_l). \tag{A.5}$$

Note that $\nabla \cdot \mathbf{B} \neq 0$ since for a single isolated wire of finite length, $\nabla \cdot \mathbf{j} \neq 0$ at the wire ends, thus violating the continuity equation. A real wire carrying a stationary current is always connected to leads and a current source, which ensure that the continuity equation is valid and thus $\nabla \cdot \mathbf{B} = 0$. For practical calculations, the wire ends have to be sufficiently far away from the region of interest where the field is calculated.

A.3 Angular momentum matrix elements

The strength of magnetic dipole transitions between hyperfine states

$$|F, m_F\rangle \equiv |J, I, F, m_F\rangle \tag{A.6}$$

is related to the corresponding angular momentum matrix elements. The total angular momentum is $\mathbf{F} = \mathbf{J} + \mathbf{I}$, where $\mathbf{J}$ is the electron angular momentum and $\mathbf{I}$ is the nuclear spin. Within the ground state hyperfine manifold of ^{87}Rb, $J = 1/2$ and $I = 3/2$ have fixed values, which can be combined to $F = 1$ and $F = 2$. In terms of the cartesian components of $\mathbf{F} = (F_x, F_y, F_z)$, we define $F_\pm \equiv F_x \pm iF_y$. Similar definitions are used for $I_\pm$ and $J_\pm$.

In this appendix, $|F, m_F\rangle$ refers to the eigenstates of the operators $\mathbf{F}^2$ and F_z. Note that in the main text of this thesis, we let $|F, m_F\rangle$ refer more generally to the eigenstates of the full Breit-Rabi Hamiltonian, Eq. (1.4), which are a function of the external magnetic field B. Both definitions are equivalent for $B \to 0$. The difference is neglected if the Zeeman effect is treated perturbatively.

The matrix elements $\langle F', m_F{}'|F_q|F, m_F\rangle$, $(q = +, -, z)$ between states with $F' = F$ are

$$\begin{aligned} \langle F, m_F{}'|F_z|F, m_F\rangle &= m_F\, \delta_{m_F{}', m_F} \\ \langle F, m_F{}'|F_\pm|F, m_F\rangle &= \sqrt{(F \mp m_F)(F \pm m_F + 1)}\, \delta_{m_F{}', m_F \pm 1}. \end{aligned} \tag{A.7}$$

Matrix elements of $\mathbf{F}$ between states with $F' \neq F$ vanish,

$$\langle F' \neq F, m_F{}'|F_q|F, m_F\rangle = 0. \tag{A.8}$$

Using $F_q = I_q + J_q$, we find

$$\langle F', m_F{}'|I_q|F, m_F\rangle = -\langle F', m_F{}'|J_q|F, m_F\rangle \quad \text{for} \quad F' \neq F. \tag{A.9}$$

The matrix elements of I_q and J_q are most easily calculated by decomposing the states $|F, m_F\rangle$ into states $|I, m_I\rangle|J, m_J\rangle$ using the appropriate Clebsch-Gordan coefficients $\langle I m_I J m_J|F m_F\rangle$. Using the sign convention of [234] for the Clebsch-Gordan coefficients, we obtain for the states:

$$
\begin{aligned}
|F, m_F\rangle &= \sum_{m_I=-I}^{+I} \sum_{m_J=-J}^{+J} |I, m_I\rangle |J, m_J\rangle \langle I m_I J m_J | F m_F\rangle \qquad \text{(A.10)}\\
|2,2\rangle &= |\tfrac{3}{2},\tfrac{3}{2}\rangle|\tfrac{1}{2},\tfrac{1}{2}\rangle\\
|2,1\rangle &= \sqrt{\tfrac{1}{4}}\,|\tfrac{3}{2},\tfrac{3}{2}\rangle|\tfrac{1}{2},-\tfrac{1}{2}\rangle + \sqrt{\tfrac{3}{4}}\,|\tfrac{3}{2},\tfrac{1}{2}\rangle|\tfrac{1}{2},\tfrac{1}{2}\rangle\\
|2,0\rangle &= \sqrt{\tfrac{1}{2}}\,|\tfrac{3}{2},\tfrac{1}{2}\rangle|\tfrac{1}{2},-\tfrac{1}{2}\rangle + \sqrt{\tfrac{1}{2}}\,|\tfrac{3}{2},-\tfrac{1}{2}\rangle|\tfrac{1}{2},\tfrac{1}{2}\rangle\\
|2,-1\rangle &= \sqrt{\tfrac{3}{4}}\,|\tfrac{3}{2},-\tfrac{1}{2}\rangle|\tfrac{1}{2},-\tfrac{1}{2}\rangle + \sqrt{\tfrac{1}{4}}\,|\tfrac{3}{2},-\tfrac{3}{2}\rangle|\tfrac{1}{2},\tfrac{1}{2}\rangle\\
|2,-2\rangle &= |\tfrac{3}{2},-\tfrac{3}{2}\rangle|\tfrac{1}{2},-\tfrac{1}{2}\rangle\\
|1,1\rangle &= \sqrt{\tfrac{3}{4}}\,|\tfrac{3}{2},\tfrac{3}{2}\rangle|\tfrac{1}{2},-\tfrac{1}{2}\rangle - \sqrt{\tfrac{1}{4}}\,|\tfrac{3}{2},\tfrac{1}{2}\rangle|\tfrac{1}{2},\tfrac{1}{2}\rangle\\
|1,0\rangle &= \sqrt{\tfrac{1}{2}}\,|\tfrac{3}{2},\tfrac{1}{2}\rangle|\tfrac{1}{2},-\tfrac{1}{2}\rangle - \sqrt{\tfrac{1}{2}}\,|\tfrac{3}{2},-\tfrac{1}{2}\rangle|\tfrac{1}{2},\tfrac{1}{2}\rangle\\
|1,-1\rangle &= \sqrt{\tfrac{1}{4}}\,|\tfrac{3}{2},-\tfrac{1}{2}\rangle|\tfrac{1}{2},-\tfrac{1}{2}\rangle - \sqrt{\tfrac{3}{4}}\,|\tfrac{3}{2},-\tfrac{3}{2}\rangle|\tfrac{1}{2},\tfrac{1}{2}\rangle
\end{aligned}
$$

The matrix elements $\langle F', m_F{}'|J_q|F, m_F\rangle$ (and similarly $\langle F', m_F{}'|I_q|F, m_F\rangle$) can now be easily evaluated, using the formulae for $\langle J, m_J{}'|J_q|J, m_J\rangle$ and $\langle I, m_I{}'|I_q|I, m_I\rangle$, which are formally identical to Eq. (A.7).

In the calculation of the microwave potentials (chapter 5), we encounter the matrix elements

$$\langle 2, m_2|\boldsymbol{\epsilon}\cdot\mathbf{J}|1, m_1\rangle \equiv \langle F'=2, m_F{}'=m_2|\boldsymbol{\epsilon}\cdot\mathbf{J}|F=1, m_F=m_1\rangle, \qquad \text{(A.11)}$$

where $\boldsymbol{\epsilon}=(\epsilon_x,\epsilon_y,\epsilon_z)$ is a unit polarization vector, whose components may be complex. Using $J_x=\frac{1}{2}(J_+ + J_-)$ and $J_y=-\frac{i}{2}(J_+ - J_-)$, we express $\boldsymbol{\epsilon}\cdot\mathbf{J}$ as

$$\boldsymbol{\epsilon}\cdot\mathbf{J} = \epsilon_x J_x + \epsilon_y J_y + \epsilon_z J_z = \tfrac{1}{2}(\epsilon_x - i\epsilon_y)J_+ + \tfrac{1}{2}(\epsilon_x + i\epsilon_y)J_- + \epsilon_z J_z. \qquad \text{(A.12)}$$

The matrix elements $\langle 2, m_2|J_q|1, m_1\rangle$, $(q=+,-,z)$ can be calculated as described above. The result is (listing only the non-vanishing elements):

$$
\begin{aligned}
\langle 2,2|J_+|1,1\rangle &= \sqrt{\tfrac{3}{4}}\\
\langle 2,1|J_+|1,0\rangle &= \sqrt{\tfrac{3}{8}} \qquad \text{(A.13)}\\
\langle 2,0|J_+|1,-1\rangle &= \sqrt{\tfrac{1}{8}}
\end{aligned}
$$

$$\begin{aligned} \langle 2,0|J_-|1,1\rangle &= -\sqrt{\tfrac{1}{8}} \\ \langle 2,-1|J_-|1,0\rangle &= -\sqrt{\tfrac{3}{8}} \\ \langle 2,-2|J_-|1,-1\rangle &= -\sqrt{\tfrac{3}{4}} \end{aligned} \tag{A.14}$$

$$\begin{aligned} \langle 2,1|J_z|1,1\rangle &= -\sqrt{\tfrac{3}{16}} \\ \langle 2,0|J_z|1,0\rangle &= -\sqrt{\tfrac{1}{4}} \\ \langle 2,-1|J_z|1,-1\rangle &= -\sqrt{\tfrac{3}{16}} \end{aligned} \tag{A.15}$$

Appendix B

Cigar-shaped vs. pancake-shaped dimple traps

In some experiments it is desirable to have nearly isotropic or pancake-shaped traps. Examples are tunneling experiments and experiments with two-dimensional or rotating quantum gases. The magnetic microtraps demonstrated up to now are in the cigar-shaped regime. Here I revisit the dimple trap (Fig. 1.4) in detail in order to investigate whether it is possible to tune the trap aspect ratio similar to the ideal Ioffe trap of Eq. (1.10).

In the limit of infinitely thin wires and with the wire intersection placed at the origin, the magnetic field components in Fig. 1.4 are

$$\begin{aligned} B_x &= -A_1 + \frac{\mu_0 I_1}{2\pi} \cdot \frac{z}{x^2+z^2}, \\ B_y &= A_0 - \frac{\mu_0 I_0}{2\pi} \cdot \frac{z}{y^2+z^2}, \quad \text{and} \\ B_z &= \frac{\mu_0 I_0}{2\pi} \cdot \frac{y}{y^2+z^2} - \frac{\mu_0 I_1}{2\pi} \cdot \frac{x}{x^2+z^2}. \end{aligned} \tag{B.1}$$

We have defined $A_0 \equiv B_{b,y}$ and $A_1 \equiv -B_{b,x}$ so that one of the valid Ioffe-type dimple trap configurations corresponds to all parameters I_0, I_1, A_0, and A_1 being positive. The trap minimum must be a stationary point of the field modulus $B(\mathbf{r}) = \sqrt{B_x^2 + B_y^2 + B_z^2}$. We find a stationary point at $x = 0$, $y = 0$, and $z = z_m$, with

$$z_m = \frac{\mu_0}{2\pi} \cdot \frac{I^2}{A_0 I_0 + A_1 I_1} \quad \text{and} \quad B_m = \frac{|A_1 I_0 - A_0 I_1|}{|I|}, \tag{B.2}$$

where $B_m \equiv B(x = 0, y = 0, z = z_m)$ is the field modulus in the trap center and $I^2 \equiv I_0^2 + I_1^2$. Expanding $B(\mathbf{r})$ to second order in the displacements from the trap center, we obtain

$$B(\mathbf{r}) \approx B_m + \frac{k}{4}\,(1-q)\,x^2 - \frac{kp}{2}xy + \frac{k}{4}\,(1+q)\,y^2 + \frac{k}{2}(z-z_m)^2, \qquad \text{(B.3)}$$

where we have defined

$$\begin{aligned} k &\equiv \frac{\mu_0^2 I^2}{4\pi^2 z_m^4 B_m}, \\ p &\equiv \frac{2I_0 I_1}{I^2}, \quad \text{and} \\ q &\equiv \frac{I_0^2}{I^2} - \frac{I_1^2}{I^2} - \frac{4I_0 I_1}{I^2} \cdot \frac{A_1 I_0 - A_0 I_1}{A_0 I_0 + A_1 I_1}. \end{aligned} \qquad \text{(B.4)}$$

Indeed, the first-order terms vanish in Eq. (B.3), but the main axes of vibration in the xy-plane do not coincide with the coordinate axes. We therefore rotate the coordinate system around the z-axis by an angle

$$\theta = \frac{1}{2}\arctan\left(\frac{p}{q}\right) \qquad \text{(B.5)}$$

in order to eliminate the mixed term. This yields

$$\begin{aligned} B(\mathbf{r}) = B_m &+ \frac{k}{4}\left(1 - \sqrt{p^2+q^2}\right)\tilde{x}^2 \\ &+ \frac{k}{4}\left(1 + \sqrt{p^2+q^2}\right)\tilde{y}^2 + \frac{k}{2}(z-z_m)^2 \end{aligned} \qquad \text{(B.6)}$$

in the rotated coordinates $\tilde{x} = x\cos\theta + y\sin\theta$, $\tilde{y} = -x\sin\theta + y\cos\theta$. The trap frequencies are

$$\begin{aligned} \omega_{\tilde{x}} &= \left[\frac{\mu}{m}\cdot\frac{k}{2}\left(1 - \sqrt{p^2+q^2}\right)\right]^{1/2}, \\ \omega_{\tilde{y}} &= \left[\frac{\mu}{m}\cdot\frac{k}{2}\left(1 + \sqrt{p^2+q^2}\right)\right]^{1/2}, \quad \text{and} \\ \omega_z &= \left[\frac{\mu}{m}\cdot k\right]^{1/2}. \end{aligned} \qquad \text{(B.7)}$$

The stationary point corresponds to a Ioffe-type trap minimum if all trap frequencies are real and $B_m > 0$. This implies $p^2 + q^2 < 1$, which leads to the condition $|I_1/I_0| < \min\left(|A_1/A_0|, |A_0/A_1|\right)$ for the currents. We have chosen $|I_1/I_0| < 1$ by convention, an analogous solution exists for $|I_0/I_1| < 1$ with the role of the two wires interchanged.

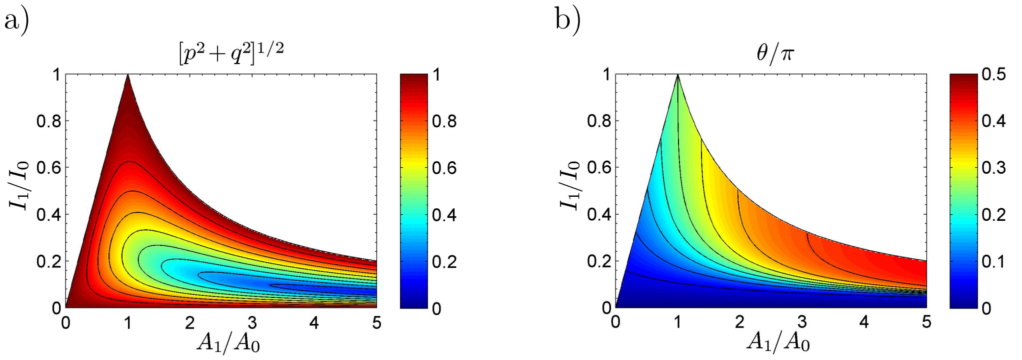

Figure B.1: Parameter space of the dimple trap. (a) The value of $\sqrt{p^2+q^2}$ in the parameter space spanned by I_1/I_0 and A_1/A_0. In the white area no trap forms since $\sqrt{p^2+q^2} > 1$ (see text). Contours spaced by 0.1. (b) The angle θ by which the $\tilde{x}$-axis of vibration is rotated in the xy-plane. Contours spaced by 0.05.

According to Eqs. (B.7), the trap frequencies satisfy $\omega_{\tilde{x}}^2 + \omega_{\tilde{y}}^2 = \omega_z^2$. Unlike in the case of the ideal Ioffe trap, Eq. (1.10), it is therefore not possible to create a completely isotropic dimple trap. The shape of the trap is determined by $\sqrt{p^2+q^2} = (\omega_{\tilde{y}}^2 - \omega_{\tilde{x}}^2)/\omega_z^2$, see Eq. (B.7). In Fig. B.1, we plot $\sqrt{p^2+q^2}$ and θ as a function of the current and magnetic field ratios I_1/I_0 and A_1/A_0. For $\sqrt{p^2+q^2} \longrightarrow 1$ the trap is cigar-shaped, see Fig. B.2(a), with $\omega_{\tilde{x}} \ll \omega_{\tilde{y}} \approx \omega_z$. For $\sqrt{p^2+q^2} \longrightarrow 0$, which corresponds to $|A_1/A_0| \gg 1$ and $I_1 \approx I_0 A_0/3A_1$, a slightly pancake-shaped trap is formed, as shown in Fig. B.2(b), with $\omega_{\tilde{x}} \approx \omega_{\tilde{y}} \approx \omega_z/\sqrt{2}$. In such a trap, $B_m \approx A_1$ is large and the trap frequencies are relatively low.

This shows that the trap aspect ratio of a dimple trap can be tuned from (extremely) cigar-shaped to slightly pancake-shaped. In the intermediate region, the trap frequencies are different along all three axes. Compared with the ideal Ioffe trap, Eq. (1.10), the tuning range is reduced. This is due to the additional unnecessary field components and gradients introduced by the wires. Simulations show that the effects of finite wire width improve the situation. The transverse confinement becomes closer to an ideal quadrupole field if the width of the wire carrying the current I_0 is comparable to the trap-surface distance. This enables aspect ratios further into the pancake-shaped regime, furthermore it is possible to orient the tightly confining direction parallel to the chip surface. Pancake-shaped traps can also be realized by reflecting a laser beam from the chip surface to create a one-dimensional optical lattice.

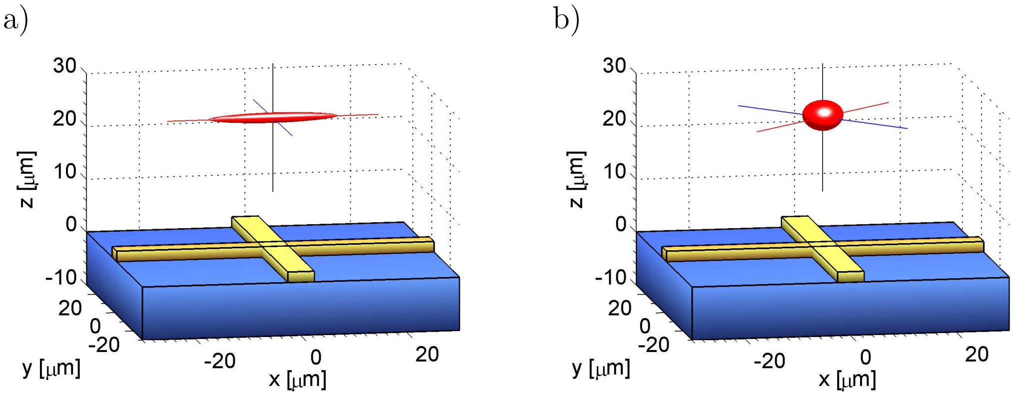

Figure B.2: Dimple traps with different trap aspect ratios at $z_m = 25\ \mu$m. (a) Cigar-shaped trap with $I_0 = 0.2$ A, $I_1/I_0 = 0.01$, $A_0 = 16$ G, and $A_1/A_0 = 0.4$. The simulation yields $(\omega_{\tilde{x}}, \omega_{\tilde{y}}, \omega_z)/2\pi = (0.29, 3.27, 3.28)$ kHz, taking finite wire size and gravity into account. The red isopotential surface corresponds to the chemical potential of a BEC of 10^5 atoms in the Thomas-Fermi limit. The main axes of vibration are indicated. (b) $I_0 = 0.2$ A, $I_1/I_0 = 0.023$, $A_0 = 12.2$ G, and $A_1/A_0 = 15$. A slightly pancake-shaped trap is formed with $(\omega_{\tilde{x}}, \omega_{\tilde{y}}, \omega_z)/2\pi = (0.43, 0.45, 0.58)$ kHz.

Appendix C

Chip fabrication recipe

In the following I describe in detail the recipe used to fabricate the microwave atom chip. The fabrication steps appear in the exact order in which they were carried out in the clean room. At the end, a list of microfabrication company web pages is given. For a general discussion and results of the fabrication process, see chapter 2.

C.1 Chemicals, processes, and equipment

Recipes of frequently used chemicals and processes

Ac. Acetone, VLSI selectipur.

Aqua regia Mix water, hydrochloric acid, and nitric acid in this order and in volume ratio (water):(32% HCl):(65% HNO_3) = 1:3:1. Stir once and wait before use until solution turns yellow. Use fresh aqua regia each time.

Blow dry with nitrogen gun.

IPA Isopropanol, VLSI selectipur.

Plasma cleaner Oxygen plasma cleaner parameters are (duration, RF power, O_2 pressure).

Piranha A:B Piranha etch: mix sulphuric acid and hydrogen peroxide in an open beaker in this order and in volume ratio (96% H_2SO_4):(33% H_2O_2) = A:B. Stir once and wait 1 min before use. For high concentration of hydrogen peroxide (e.g. A:B = 4:1), the solution heats up and comes to a boil. CAUTION! *Never* increase hydrogen peroxide concentration beyond A:B = 3:1 and *never* bring piranha in contact with organic solvents, this would result in an explosion. Piranha etch can be used for about 10 min after mixing (until cooled off). Use fresh piranha etch each time.

USB Place beaker in ultrasound cleaner and clean with given (duration, power, temperature).

Water All water used is deionized water.

Clean room equipment

AFM Atomic force microscope (Digital Instruments Dimension 3000 AFM).

Ellipsometer (Plasmos).

Evaporator Metal deposition system with ultra-high vacuum chamber and electron-beam evaporation (BesTec).

Hot plate for temperatures up to 200 °C with temperature stability of ±1 °C.

Mask aligner (Karl Suss MJB3) for optical lithography with UV light (Hg i-line at 365 nm and h-line at 405 nm).

Optical microscope equipped for dark field microscopy.

GERO oven for baking of chips at temperatures up to 400 °C in nitrogen atmosphere.

Plasma cleaner for oxygen plasma (RF Applications Lab-Ash 100).

RTP oven for rapid temperature processing up to 1100 °C in oxygen and nitrogen atmospheres (A.S.T. elektronik SHS 10).

SEM Scanning electron microscope (LEO 982 Digital Scanning Microscope).

Spin coater (Convac 1001S).

Ultrasound cleaner (Bandelin Sonorex Super).

C.2 Microwave atom chip

Substrate preparation

Wafer used: high resistivity silicon (Topsil, float-zone Si, (100) orientation, resistivity $\rho > 10^4\ \Omega\,\mathrm{cm}$), 100 mm diameter wafer, thickness 525 μm, polished on one side, native oxide.

1. Cleave substrate
   (a) Cleave chip substrate to square shape (35 mm × 35 mm) with diamond scorer.

   (b) Wipe off surface, clean in Ac. USB (5 min, 100%, 55 °C), rinse in IPA, blow dry.

2. Oxidize Si substrate

   Heat substrate in RTP oven in oxygen atmosphere to form a 20 nm thick insulating SiO_2 layer.
   Temperature ramp:

   (a) ramp from room temperature to 400 °C in ≈ 5 min, gas flow 8 slm N_2,
   (b) keep at 400 °C for 4 min, switch to 5 slm O_2,
   (c) ramp from 400 °C to 1100 °C in 10 min, 5 slm O_2,
   (d) keep at 1100 °C for 6 min, 4 slm O_2,
   (e) ramp down to 400 °C in 5 min, 4 slm O_2,
   (f) switch to 10 slm N_2, let cool to room temperature.

   Oxide thickness may be determined with the ellipsometer.

3. Bevel edges of substrate

   (a) Spin on photoresist (e.g. micro resist ma-P 1240) for protection (5 s at 800 rpm, then 40 s at 1500 rpm), soft bake 8 min at 104 °C on hot plate.
   (b) Bevel edges of substrate on wet diamond whetstone. Rinse substrate with water.

4. Clean substrate

   (a) Clean in Ac. USB (5 min, 100%, 55 °C), rinse in IPA, blow dry.
   (b) Clean in piranha (4:1) for 5 min, *rinse well with water!* Do not let dry.
   (c) Clean in Ac. USB (3 min, 100%, 55 °C), rinse in IPA, blow dry.

Lower gold layer

1. Deposit gold seed layer

   (a) Clean chip in oxygen plasma (5 min, 60 W, 2.0 torr).
   (b) Mount chip in UHV evaporation chamber without delay.
   (c) Heat Ti with e-beam, shutter closed in front of chip. Wait until pressure in chamber drops by about one order of magnitude due to Ti gettering (typical pressure 5×10^{-9} mbar after 3 min).
   (d) Open shutter and deposit 20 Å thick Ti adhesion layer at 0.5 Å/s. Close shutter and continue with next step without delay.

   (e) Heat Au with e-beam, shutter closed in front of chip. Wait until Au melts completely (approx. 3 min).
   (f) Open shutter and deposit 50 nm thick Au seed layer at 1 Å/s.

2. Spin on photoresist

   (a) Heat chip on hot plate, > 5 min at 102 °C. Place on spin-coater without delay, blow off surface.
   (b) Dispense photoresist (micro resist ma-P 1240) onto chip until surface is completely covered, avoid (or remove) air bubbles.
   (c) Spin 5 s at 800 rpm, then 40 s at 1500 rpm, resulting film thickness: 6.5 μm.
   (d) Soft bake resist on hot plate, 5 min at 102 °C.

3. Resist exposure and development
   Note: wait a few minutes between soft bake, exposure, and development.

   (a) Use mask aligner to press chip against photomask (Cr mask from Delta Mask), supporting the chip with a rubber ring below its center. Depending on design, Newton's rings may be visible in mask aligner microscope if chip is in flush contact with mask.
   (b) Expose for 120 s. Exposure time may need adjustment from time to time. Slight overexposure might be desirable.
   (c) Develop resist for 150 s in developer (micro resist ma-D 336:water = 3:7), agitate chip while developing. Development time and developer concentration may need adjustment from time to time. Slight overdeveloping might be desirable.
   (d) Stop development in beaker with water, rinse thoroughly with running water, blow dry.
   (e) Inspect structure under microscope. If not fully developed, rinse with water, then continue developing. May be repeated several times.
   (f) Rinse photomask with Ac. and IPA, blow dry.

4. Electroplating

   (a) Heat electroplating solution (Metakem ammonium gold sulfite solution, 1 liter with 15 g of gold) in water bath to $57 \pm 1\,^\circ$C.
   (b) Wipe off photoresist with Ac. and IPA in chip corners to form contact pads for electroplating.
   (c) Remove residual photoresist in developed areas by plasma cleaning (5 min, 50 W, 2.0 torr).

   (d) Mount chip on chip holder without delay. Connect contact pads. Rinse with water.
   (e) Connect chip and anode to power supply, with 1 kΩ resistor in series. Switch on power supply first (output voltage set to 0 V) and then submerge chip in electroplating solution. Make sure no uncontrolled voltage changes occur (e.g. during switching).
   (f) Set output voltage to 8.0 V. Due to the 1 kΩ series resistor, the plating current should be 8 mA. This corresponds to a current density of ≈ 3 mA/cm^2 in our chip design.
   (g) Electroplate gold in 40 min to a thickness of 6 μm. While plating, stir solution with stirring magnet at 100 rpm, in addition agitate chip with motor (set to 3 V) and from time to time by hand.
   (h) Rinse chip thoroughly with running water, blow dry. Do not let solution dry on chip.
   (i) Rinse equipment with water and filter electroplating solution with paper filter.

5. Remove photoresist and etch seed layer
   (a) Remove resist in Ac. USB (5 min, 10%, 55 °C), rinse in IPA, blow dry.
   (b) Remove residual resist in narrow gaps between wires: Submerge chip for 1 min in piranha (4:1), rinse with water, blow dry.
   (c) Etch gold seed layer and Ti adhesion layer: Immerse and agitate chip in aqua regia for typically 40 s (about twice the time needed to remove Au and Ti), rinse with water, blow dry.
   (d) Inspect lower gold layer and determine approximate thickness under microscope.

Polyimide insulation

1. First polyimide layer
   (a) Let polyimide bottle warm up to room temperature.
   (b) Clean chip in Ac., rinse in IPA, blow dry.
   (c) Clean chip in oxygen plasma (5 min, 60 W, 2.0 torr).
   (d) Prepare adhesion promoter (one drop of HD MicroSystems VM651 in 10 ml water corresponds to the recommended dilution of 1:1000).
   (e) Spin on adhesion promoter 5 s at 800 rpm, then 30 s at 3000 rpm.
   (f) Soft bake 1 min at 120 °C on hot plate.

- (g) Dispense polyimide (HD MicroSystems PI2562) on chip until surface is completely covered, using plastic pipette with thick opening. Avoid (or remove) air bubbles.
- (h) Spin on polyimide 5 s at 500 rpm, then 40 s at 2200 rpm, resulting film thickness: 2.0 μm.
- (i) Soft bake on hot plate: ramp in 30 min from 100 °C to 200 °C, then keep 30 min at 200 °C.
- (j) Hard bake polyimide in GERO oven, N_2 flow 200 l/h.
  Temperature ramp:
  - i. keep 0.3 h at 200 °C,
  - ii. ramp with 150 °C/h to 350 °C,
  - iii. bake 2 h at 350 °C,
  - iv. ramp with −400 °C/h to 200 °C,
  - v. let cool to room temperature.
- (k) Planarization results may be determined with AFM.

2. Second and third polyimide layer
   Note: no adhesion promoter required.
   - (a) Clean chip in Ac., rinse in IPA, blow dry.
   - (b) Heat chip on hot plate, 5 min at 120 °C.
   - (c) Dispense and spin on polyimide as for first layer.
   - (d) Soft bake on hot plate: ramp in 20 min from 120 °C to 180 °C.
   - (e) Hard bake polyimide in GERO oven, parameters as for first layer.

Upper gold layer

1. Spin on photoresist
   - (a) Clean chip in Ac., rinse in IPA, blow dry.
   - (b) Clean chip in oxygen plasma (2 min, 50 W, 2.0 torr).
   - (c) Heat chip on hot plate, 3 min at 110 °C. Place on spin-coater without delay, blow off surface.
   - (d) Dispense photoresist (Clariant AZ 5214 E) onto chip until surface is completely covered, avoid (or remove) air bubbles.
   - (e) Spin 3 s at 800 rpm, then 30 s at 3000 rpm, resulting film thickness: 1.6 μm.
   - (f) Soft bake resist on hot plate, 1 min at 110 °C.

2. Resist exposure, image reversal, and development

   Note: wait a few minutes between steps.

   (a) Use mask aligner to press chip against photomask, supporting the chip with a rubber ring below its center. Make sure mask is properly aligned with lower gold layer.
   (b) Expose for 3.5 s. Avoid overexposure.
   (c) Image reversal bake on hot plate, 120 s at $120 \pm 1\,^{\circ}$C.
   (d) Flood UV exposure of chip without mask, 40 s.
   (e) Develop resist for 17 s in developer (AZ 351 B:water = 1:4), agitate chip while developing. Development time may need adjustment from time to time.
   (f) Stop development in beaker with water, rinse thoroughly with running water, blow dry.
   (g) Inspect structure under microscope. A strong undercut can be seen as a bright outline of the resist edges. However, for very small structures, resist mechanical stability requires that development be stopped before bright outline is visible.
   (h) If resist structure needs further development, rinse with water, then continue developing for a few seconds. May be repeated several times.
   (i) Remove residual resist in developed areas by gentle plasma cleaning (10 s, 40 W, 2.0 torr).
   (j) Post bake resist on hot plate, 50 s at $120\,^{\circ}$C.
   (k) Rinse photomask with Ac. and IPA, blow dry.

3. Evaporate gold

   (a) Mount chip in UHV evaporation chamber without delay.
   (b) Heat Ti with e-beam, shutter closed in front of chip. Wait until pressure in chamber drops by about one order of magnitude due to Ti gettering (typical pressure 5×10^{-9} mbar after 3 min).
   (c) Open shutter and deposit 30 Å thick Ti adhesion layer at 0.5 Å/s. Close shutter and continue with next step without delay.
   (d) Heat Au with e-beam, shutter closed in front of chip. Wait until Au melts completely (approx. 3 min).
   (e) Open shutter and deposit 1000 nm thick Au layer at ≤ 1.0 Å/s.

4. Lift-off

   (a) Place chip in beaker with hot Ac. Agitate chip from time to time.

   (b) Wait until resist structure comes off (may take 30 min). Lift-off may be forced with USB (5 min, 10%, 55 °C).
   (c) Remove chip from Ac. only after lift-off is fully completed, rinse with IPA, blow dry.

Chip dicing

1. Spin on photoresist (e.g. micro resist ma-P 1240) for protection (5 s at 800 rpm, then 40 s at 1500 rpm), soft bake 5 min at 100 °C on hot plate.
2. Cut chip to size with diamond blade at 20000 rpm.
3. Clean chip in Ac. USB (5 min, 10%, 55 °C), rinse with IPA, blow dry.

C.3 Base chip

Wafer used: aluminum nitride (Anceram AlN 180, thermal conductivity 180 W/(m K)), 100 mm × 100 mm square wafer, thickness 800 μm, polished on one side (Ra $<$ 40 nm).

The fabrication process for this chip is similar to the lower layer of the experiment chip. The main difference are the lithography parameters. To fabricate thicker gold wires, a 8 μm thick layer of photoresist (ma-P 1240) is used. A printed overhead transparency mask is used for lithography. Because of defects in the mask, the thicker resist layer, and resist edge beads, the exposure time is increased to 9 min and the development time is 8 min. The wires are electroplated to a thickness of 12 μm. This slight "overplating" is uncritical for the larger structures (≥ 90 μm) on the base chip.

C.4 Microfabrication company web pages

A.L.L. Lasertechnik	www.all-laser.de
Anceram	www.anceram.com
Clariant Photoresist	www.microchemicals.com
Delta Mask	www.deltamask.nl
Epo-Tek	www.epotek.com
HD MicroSystems	www.hdmicrosystems.com
Indium Corporation	www.indium.com
Metakem	www.metakem.com
MicroChemicals	www.microchemicals.com
micro resist technology	www.microresist.com
Topsil	www.topsil.com

Bibliography

[1] C. J. Davisson and L. H. Germer, *The scattering of electrons by a single crystal of nickel*, Nature **119**, 558 (1927).

[2] S. J. Freedman and J. F. Clauser, *Experimental test of local hidden-variable theories*, Phys. Rev. Lett. **28**, 938 (1972).

[3] A. Aspect, J. Dalibard, and G. Roger, *Experimental Test of Bell's Inequalities Using Time-Varying Analyzers*, Phys. Rev. Lett. **49**, 1804 (1982).

[4] P. R. Berman, editor, *Atom Interferometry*, Academic Press, San Diego, 1997.

[5] M. Arndt, O. Nairz, J. Vos-Andreae, C. Keller, G. van der Zouw, and A. Zeilinger, *Wave-particle duality of C_{60} molecules*, Nature **401**, 680 (1999).

[6] L. Hackermüller, S. Uttenthaler, K. Hornberger, E. Reiger, B. Brezger, A. Zeilinger, and M. Arndt, *Wave Nature of Biomolecules and Fluorofullerenes*, Phys. Rev. Lett. **91**, 090408 (2003).

[7] M. Schlosshauer, editor, *Decoherence and the quantum-to-classical transition*, Springer, Berlin, 2007.

[8] D. DiVincenzo, *The Physical Implementation of Quantum Computation*, Fortschr. Phys. **48**, 771 (2000).

[9] M. A. Nielsen and I. L. Chuang, *Quantum Computation and Quantum Information*, Cambridge University Press, Cambridge, 2000.

[10] J. A. Dunningham, *Using quantum theory to improve measurement precision*, Contemp. Phys. **47**, 257 (2006).

[11] A. M. Childs, J. Preskill, and J. Renes, *Quantum information and precision measurement*, J. Mod. Opt. **47**, 155 (2000).

[12] S. Lloyd, *Universal Quantum Simulators*, Science **273**, 1073 (1996).

[13] E. Jané, G. Vidal, W. Dür, P. Zoller, and J. I. Cirac, *Simulation of quantum dynamics with quantum optical systems*, Quant. Inf. and Comp. **3**, 15 (2003).

[14] A. J. Leggett, *Testing the limits of quantum mechanics: motivation, state of play, prospects*, J. Phys. CM **14**, 415 (2002).

[15] F. Marquardt, B. Abel, and J. von Delft, *Measuring the size of a Schrödinger cat state*, preprint arXiv:quant-ph/0609007 (2006).

[16] I. Bloch, *Ultracold quantum gases in optical lattices*, Nat. Phys. **1**, 23 (2005).

[17] D. Leibfried, E. Knill, S. Seidelin, J. Britton, R. B. Blakestad, J. Chiaverini, D. B. Hume, W. M. Itano, J. D. Jost, C. Langer, R. Ozeri, R. Reichle, and D. J. Wineland, *Creation of a six-atom 'Schrödinger cat' state*, Nature **438**, 639 (2005).

[18] H. Häffner, W. Hänsel, C. F. Roos, J. Benhelm, D. C. al kar, M. Chwalla, T. Körber, U. D. Rapol, M. Riebe, P. O. Schmidt, C. Becher, O. Gühne, W. Dür, and R. Blatt, *Scalable multiparticle entanglement of trapped ions*, Nature **438**, 643 (2005).

[19] M. Steffen, M. Ansmann, R. C. Bialczak, N. Katz, E. Lucero, R. McDermott, M. Neeley, E. M. Weig, A. N. Cleland, and J. M. Martinis, *Measurement of the Entanglement of Two Superconducting Qubits via State Tomography*, Science **313**, 1423 (2006).

[20] J. Majer, J. M. Chow, J. M. Gambetta, J. Koch, B. R. Johnson, J. A. Schreier, L. Frunzio, D. I. Schuster, A. A. Houck, A. Wallraff, A. Blais, M. H. Devoret, S. M. Girvin, and R. J. Schoelkopf, *Coupling superconducting qubits via a cavity bus*, Nature **449**, 443 (2007).

[21] J. Reichel, W. Hänsel, P. Hommelhoff, and T. W. Hänsch, *Applications of integrated magnetic microtraps*, Appl. Phys. B **72**, 81 (2001).

[22] R. Folman, P. Krüger, J. Schmiedmayer, J. Denschlag, and C. Henkel, *Microscopic Atom Optics: From Wires to an Atom Chip*, Adv. At. Mol. Opt. Phys. **48**, 263 (2002).

[23] J. Reichel, *Microchip traps and Bose-Einstein condensation*, Appl. Phys. B **74**, 469 (2002).

[24] J. Fortágh and C. Zimmermann, *Magnetic microtraps for ultracold atoms*, Rev. Mod. Phys. **79**, 235 (2007).

[25] M. H. Anderson, J. R. Ensher, M. R. Matthews, C. E. Wieman, and E. A. Cornell, *Observation of Bose-Einstein Condensation in a Dilute Atomic Vapor*, Science **269**, 198 (1995).

[26] K. B. Davis, M.-O. Mewes, M. R. Andrews, N. J. van Druten, D. S. Durfee, D. M. Kurn, and W. Ketterle, *Bose-Einstein Condensation in a Gas of Sodium Atoms*, Phys. Rev. Lett. **75**, 3969 (1995).

[27] J. Reichel, W. Hänsel, and T. W. Hänsch, *Atomic Micromanipulation with Magnetic Surface Traps*, Phys. Rev. Lett. **83**, 3398 (1999).

[28] H. Ott, J. Fortágh, G. Schlotterbeck, A. Grossmann, and C. Zimmermann, *Bose-Einstein Condensation in a Surface Microtrap*, Phys. Rev. Lett. **87**, 230401 (2001).

[29] W. Hänsel, P. Hommelhoff, T. W. Hänsch, and J. Reichel, *Bose-Einstein condensation on a microelectronic chip*, Nature **413**, 498 (2001).

[30] C. Henkel, S. Pötting, and M. Wilkens, *Loss and heating of particles in small and noisy traps*, Appl. Phys. B **69**, 379 (1999).

[31] C. Henkel, P. Krüger, R. Folman, and J. Schmiedmayer, *Fundamental limits for coherent manipulation on atom chips*, Appl. Phys. B **76**, 173 (2003).

[32] M. P. A. Jones, C. J. Vale, D. Sahagun, B. V. Hall, and E. A. Hinds, *Spin coupling between cold atoms and the thermal fluctuations of a metal surface*, Phys. Rev. Lett. **91**, 080401 (2003).

[33] J. Fortágh, H. Ott, S. Kraft, A. Günther, and C. Zimmermann, *Surface effects in magnetic microtraps*, Phys. Rev. A **66**, 041604 (2002).

[34] T. Calarco, E. A. Hinds, D. Jaksch, J. Schmiedmayer, J. I. Cirac, and P. Zoller, *Quantum gates with neutral atoms: Controlling collisional interactions in time-dependent traps*, Phys. Rev. A **61**, 022304 (2000).

[35] S. Du, M. B. Squires, Y. Imai, L. Czaia, R. A. Saravanan, V. Bright, J. Reichel, T. W. Hänsch, and D. Z. Anderson, *Atom-chip Bose-Einstein condensation in a portable vacuum cell*, Phys. Rev. A **70**, 053606 (2004).

[36] J. D. Weinstein and K. G. Libbrecht, *Microscopic magnetic traps for neutral atoms*, Phys. Rev. A **52**, 4004 (1995).

[37] J. Fortágh, A. Grossmann, C. Zimmermann, and T. W. Hänsch, *Miniaturized Wire Trap for Neutral Atoms*, Phys. Rev. Lett. **81**, 5310 (1998).

[38] V. Vuletic, T. Fischer, M. Praeger, T. W. Hänsch, and C. Zimmermann, *Microscopic Magnetic Quadrupole Trap for Neutral Atoms with Extreme Adiabatic Compression*, Phys. Rev. Lett. **80**, 1634 (1998).

[39] J. Denschlag, D. Cassettari, and J. Schmiedmayer, *Guiding Neutral Atoms with a Wire*, Phys. Rev. Lett. **82**, 2014 (1999).

[40] S. Aubin, S. Myrskog, M. H. T. Extavour, L. J. Leblanc, D. McKay, A. Stummer, and J. H. Thywissen, *Rapid sympathetic cooling to Fermi degeneracy on a chip*, Nat. Phys. **2**, 384 (2006).

[41] W. Hänsel, J. Reichel, P. Hommelhoff, and T. W. Hänsch, *Magnetic Conveyor Belt for Transporting and Merging Trapped Atom Clouds*, Phys. Rev. Lett. **86**, 608 (2001).

[42] P. Hommelhoff, W. Hänsel, T. Steinmetz, T. W. Hänsch, and J. Reichel, *Transporting, splitting and merging of atomic ensembles in a chip trap*, New J. Phys. **7**, 3 (2005).

[43] S. Hofferberth, I. Lesanovsky, B. Fischer, J. Verdu, and J. Schmiedmayer, *Radiofrequency-dressed-state potentials for neutral atoms*, Nat. Phys. **2**, 710 (2006).

[44] Y. Lin, I. Teper, C. Chin, and V. Vuletić, *Impact of the Casimir-Polder Potential and Johnson Noise on Bose-Einstein Condensate Stability Near Surfaces*, Phys. Rev. Lett. **92**, 050404 (2004).

[45] Y.-J. Wang, D. Z. Anderson, V. M. Bright, E. A. Cornell, Q. Diot, T. Kishimoto, M. Prentiss, R. A. Saravanan, S. R. Segal, and S. Wu, *Atom Michelson Interferometer on a Chip Using a Bose-Einstein Condensate*, Phys. Rev. Lett. **94**, 090405 (2005).

[46] T. Schumm, S. Hofferberth, L. M. Andersson, S. Wildermuth, S. Groth, I. Bar-Joseph, J. Schmiedmayer, and P. Krüger, *Matter-wave interferometry in a double well on an atom chip*, Nat. Phys. **1**, 57 (2005).

[47] C. D. J. Sinclair, E. A. Curtis, I. Llorente Garcia, J. A. Retter, B. V. Hall, S. Eriksson, B. E. Sauer, and E. A. Hinds, *Bose-Einstein condensation on a permanent-magnet atom chip*, Phys. Rev. A **72**, 031603 (2005).

[48] B. V. Hall, S. Whitlock, F. Scharnberg, P. Hannaford, and A. Sidorov, *A permanent magnetic film atom chip for BoseEinstein condensation*, J. Phys. B: At. Mol. Opt. Phys. **39**, 27 (2006).

[49] T. Fernholz, R. Gerritsma, S. Whitlock, I. Barb, and R. J. C. Spreeuw, *A self-biased permanent magnet atom chip for Bose-Einstein condensation*, preprint arXiv:0705.2569 [cond-mat.other] (2007).

[50] R. Gerritsma, S. Whitlock, T. Fernholz, H. Schlatter, J. A. Luigjes, J.-U. Thiele, J. B. Goedkoop, and R. J. C. Spreeuw, *A lattice of microtraps for ultracold atoms based on patterned magnetic films*, preprint arXiv:0706.1170 [physics.atom-ph] (2007).

[51] P. Krüger, X. Luo, M. W. Klein, K. Brugger, A. Haase, S.Wildermuth, S. Groth, I. Bar-Joseph, R. Folman, and J. Schmiedmayer, *Trapping and Manipulating Neutral Atoms with Electrostatic Fields*, Phys. Rev. Lett. **91**, 233201 (2003).

[52] T. Kishimoto, H. Hachisu, J. Fujiki, K. Nagato, M. Yasuda, and H. Katori, *Electrodynamic Trapping of Spinless Neutral Atoms with an Atom Chip*, Phys. Rev. Lett. **96**, 123001 (2006).

[53] T. Nirrengarten, A. Qarry, C. Roux, A. Emmert, G. Nogues, M. Brune, J.-M. Raimond, and S. Haroche, *Realization of a Superconducting Atom Chip*, Phys. Rev. Lett. **97**, 200405 (2006).

[54] T. Mukai, C. Hufnagel, A. Kasper, T. Meno, A. Tsukada, K. Semba, and F. Shimizu, *Persistent Supercurrent Atom Chip*, Phys. Rev. Lett. **98**, 260407 (2007).

[55] T. Steinmetz, Y. Colombe, D. Hunger, T. W. Hänsch, A. Balocchi, R. J. Warburton, and J. Reichel, *Stable fiber-based Fabry-Pérot cavity*, Appl. Phys. Lett. **89**, 111110 (2006).

[56] Y. Colombe, T. Steinmetz, G. Dubois, F. Linke, D. Hunger, and J. Reichel, *Strong atom-field coupling for Bose-Einstein condensates in an optical cavity on a chip*, Nature **450**, 272 (2007).

[57] I. Teper, Y.-J. Lin, and V. Vuletić, *Resonator-Aided Single-Atom Detection on a Microfabricated Chip*, Phys. Rev. Lett. **97**, 023002 (2006).

[58] M. Trupke, J. Goldwin, B. Darquié, G. Dutier, S. Eriksson, J. Ashmore, and E. A. Hinds, *Atom Detection and Photon Production in a Scalable, Open, Optical Microcavity*, Phys. Rev. Lett. **99**, 063601 (2007).

[59] S. Hofferberth, I. Lesanovsky, B. Fischer, T. Schumm, and J. Schmiedmayer, *Non-equilibrium coherence dynamics in one-dimensional Bose gases*, Nature **449**, 324 (2007).

[60] G.-B. Jo, Y. Shin, S. Will, T. A. Pasquini, M. Saba, W. Ketterle, D. E. Pritchard, M. Vengalattore, and M. Prentiss, *Long Phase Coherence Time and Number Squeezing of Two Bose-Einstein Condensates on an Atom Chip*, Phys. Rev. Lett. **98**, 030407 (2007).

[61] W. Ketterle, D. S. Durfee, and D. M. Stamper-Kurn, *Making, probing and understanding Bose-Einstein condensates*, in *Bose-Einstein condensation in atomic gases, Proceedings of the International School of Physics "Enrico Fermi", Course CXL*, edited by M. Inguscio, S. Stringari, and C. E. Wieman, pages 67–176, Amsterdam, 1999, IOS Press.

[62] W. H. Wing, *On neutral particle trapping in quasistatic electromagnetic fields*, Prog. Quant. Electr. **8**, 181 (1984).

[63] G. Breit and I. I. Rabi, *Measurement of Nuclear Spin*, Phys. Rev. **38**, 2082 (1931).

[64] D. A. Steck, *Rubidium 87 D Line Data*, http://steck.us/alkalidata/ , version 1.6 (2003).

[65] W. Hänsel, *Magnetische Mikrofallen für Rubidiumatome*, PhD thesis, Ludwig-Maximilians-Universität München and Max-Planck-Institut für Quantenoptik, 2001, published as MPQ report 263.

[66] K. L. Moore, T. P. Purdy, K. W. Murch, K. R. Brown, K. Dani, S. Gupta, and D. M. Stamper-Kurn, *Bose-Einstein condensation in a mm-scale Ioffe-Pritchard trap*, Appl. Phys. B **82**, 533 (2006).

[67] S. Gov, S. Shtrikman, and H. Thomas, *Magnetic trapping of neutral particles: Classical and quantum-mechanical study of a Ioffe-Pritchard type trap*, J. Appl. Phys. **87**, 3989 (2000).

[68] J. D. Jackson, *Classical Electrodynamics*, Wiley, New York, 3rd edition, 1999.

[69] A. J. Leggett, *Bose-Einstein condensation in the alkali gases: Some fundamental concepts*, Rev. Mod. Phys. **73**, 307 (2001).

[70] A. J. Dalfovo, S. Giorgini, L. P. Pitaevskii, and S. Stringari, *Theory of Bose-Einstein condensation in trapped gases*, Rev. Mod. Phys. **71**, 463 (1999).

[71] C. J. Pethick and H. Smith, *Bose-Einstein Condensation in Dilute Gases*, Cambridge University Press, Cambridge, 2002.

[72] A. M. Mateo and V. Delgado, *Extension of the Thomas-Fermi approximation for trapped Bose-Einstein condensates with an arbitrary number of atoms*, Phys. Rev. A **74**, 065602 (2006).

[73] W. Ketterle and N. J. van Druten, *Bose-Einstein condensation of a finite number of particles trapped in one or three dimensions*, Phys. Rev. A **54**, 656 (1996).

[74] M. Greiner, O. Mandel, T. Esslinger, T. W. Hänsch, and I. Bloch, *Quantum phase transition from a superfluid to a Mott insulator in a gas of ultracold atoms*, Nature **39**, 415 (2002).

[75] J. Reichel and J. H. Thywissen, *Using magnetic chip traps to study Tonks-Girardeau quantum gases*, J. Phys. IV France **116**, 265 (2004).

[76] K. W. Mahmud, H. Perry, and W. P. Reinhardt, *Phase engineering of controlled entangled number states in a single component Bose-Einstein condensate in a double well*, J. Phys. B: At. Mol. Opt. Phys. **36**, 265 (2003).

[77] B. Mohring, M. Bienert, F. Haug, G. Morigi, W. P. Schleich, and M. G. Raizen, *Extracting atoms on demand with lasers*, Phys. Rev. A **71**, 053601 (2005).

[78] E. A. Burt, R. W. Ghrist, C. J. Myatt, M. J. Holland, E. A. Cornell, and C. E. Wieman, *Coherence, Correlations, and Collisions: What One Learns about Bose-Einstein Condensates from Their Decay*, Phys. Rev. Lett. **79**, 337 (1997).

[79] P. S. Julienne, F. H. Mies, E. Tiesinga, and C. J. Williams, *Collisional Stability of Double Bose Condensates*, Phys. Rev. Lett. **78**, 1880 (1997).

[80] K. M. Mertes, J. W. Merrill, R. Carretero-González, D. J. Frantzeskakis, P. G. Kevrekidis, and D. S. Hall, *Nonequilibrium Dynamics and Superfluid Ring Excitations in Binary Bose-Einstein Condensates*, Phys. Rev. Lett. **99**, 190402 (2007).

[81] M. R. Matthews, D. S. Hall, D. S. Jin, J. R. Ensher, C. E. Wieman, E. A. Cornell, F. Dalfovo, C. Minniti, and S. Stringari, *Dynamical Response of a Bose-Einstein Condensate to a Discontinuous Change in Internal State*, Phys. Rev. Lett. **81**, 243 (1998).

[82] E. Tiesinga, B. J. Verhaar, and H. T. C. Stoof, *Threshold and resonance phenomena in ultracold ground-state collisions*, Phys. Rev. A **47**, 4114 (1993).

[83] J. Söding, D. Guéry-Odelin, P. Desbiolles, F. Chevy, H. Inamori, and J. Dalibard, *Three-body decay of a rubidium BoseEinstein condensate*, Appl. Phys. B **69**, 257 (1999).

[84] D. M. Harber, H. J. Lewandowski, J. M. McGuirk, and E. A. Cornell, *Effect of cold collisions on spin coherence and resonance shifts in a magnetically trapped ultracold gas*, Phys. Rev. A **66**, 053616 (2002).

[85] C. Henkel, *The Physics of Atom-Surface Interactions*, preprint arXiv:physics/0405084 (2004).

[86] C. Henkel, *Exploring surface interactions with atom chips*, preprint arXiv:quant-ph/0512043 (2005).

[87] P. Treutlein, P. Hommelhoff, T. Steinmetz, T. W. Hänsch, and J. Reichel, *Coherence In Microchip Traps*, Phys. Rev. Lett. **92**, 203005 (2004).

[88] D. M. Harber, J. M. McGuirk, J. M. Obrecht, and E. A. Cornell, *Thermally Induced Losses in Ultra-Cold Atoms Magnetically Trapped Near Room-Temperature Surfaces*, J. Low Temp. Phys. **133**, 229 (2003).

[89] C. Henkel, *Magnetostatic field noise near metallic surfaces*, Eur. Phys. J. D **35**, 59 (2005).

[90] V. Dikovsky, Y. Japha, C. Henkel, and R. Folman, *Reduction of magnetic noise in atom chips by material optimization*, Eur. Phys. J. D **35**, 87 (2005).

[91] S. Scheel, P. K. Rekdal, P. L. Knight, and E. A. Hinds, *Atomic spin decoherence near conducting and superconducting films*, Phys. Rev. A **72**, 042901 (2005).

[92] B.-S. K. Skagerstam, U. Hohenester, A. Eiguren, and P. K. Rekdal, *Spin Decoherence in Superconducting Atom Chips*, Phys. Rev. Lett. **97**, 070401 (2006).

[93] R. Fermani, S. Scheel, and P. L. Knight, *Spatial decoherence near metallic surfaces*, Phys. Rev. A **73**, 032902 (2006).

[94] M. E. Gehm, K. M. O'Hara, T. A. Savard, and J. E. Thomas, *Dynamics of noise-induced heating in atom traps*, Phys. Rev. A **58**, 3914 (1998).

[95] A. Aspect and J. Dalibard, *Measurement of the atom-wall interaction: from London to Casimir-Polder*, in *Poincaré Seminar 2002*, pages 93–103, Birkhäuser Verlag, Basel, 2003.

[96] M. Antezza, L. P. Pitaevskii, and S. Stringari, *Effect of the Casimir-Polder force on the collective oscillations of a trapped Bose-Einstein condensate*, Phys. Rev. A **70**, 053619 (2004).

[97] J. M. Obrecht, R. J. Wild, M. Antezza, L. P. Pitaevskii, S. Stringari, and E. A. Cornell, *Measurement of the Temperature Dependence of the Casimir-Polder Force*, Phys. Rev. Lett. **98**, 063201 (2007).

[98] D. M. Harber, J. M. Obrecht, J. M. McGuirk, and E. A. Cornell, *Measurement of the Casimir-Polder force through center-of-mass oscillations of a Bose-Einstein condensate*, Phys. Rev. A **72**, 033610 (2005).

[99] T. A. Pasquini, Y. Shin, M. Saba, A. Schirotzek, D. E. Pritchard, and W. Ketterle, *Quantum Reflection from a Solid Surface at Normal Incidence*, Phys. Rev. Lett. **93**, 223201 (2004).

[100] H. B. G. Casimir and D. Polder, *The Influence of Retardation on the London-van der Waals Forces*, Phys. Rev. **73**, 360 (1948).

[101] Z.-C. Yan, A. Dalgarno, and J. F. Babb, *Long-range interactions of lithium atoms*, Phys. Rev. A **55**, 2882 (1997).

[102] T. A. Pasquini, M. Saba, G.-B. Jo, Y. Shin, W. Ketterle, D. E. Pritchard, T. A. Savas, and N. Mulders, *Low Velocity Quantum Reflection of Bose-Einstein Condensates*, Phys. Rev. Lett. **97**, 093201 (2006).

[103] M. Bordag, U. Mohideen, and V. M. Mostepanenko, *New developments in the Casimir effect*, Phys. Rep. **353**, 1 (2001).

[104] K. A. Milton, *The Casimir effect: recent controversies and progress*, J. Phys. A **37**, R209 (2004).

[105] D. Meschede, W. Jhe, and E. A. Hinds, *Radiative properties of atoms near a conducting plane: An old problem in a new light*, Phys. Rev. A **41**, 1587 (1990).

[106] J. M. McGuirk, D. M. Harber, J. M. Obrecht, and E. A. Cornell, *Alkali-metal adsorbate polarization on conducting and insulating surfaces probed with Bose-Einstein condensates*, Phys. Rev. A **69**, 062905 (2004).

[107] J. M. Obrecht, R. J. Wild, and E. A. Cornell, *Measuring electric fields from surface contaminants with neutral atoms*, Phys. Rev. A **75**, 062903 (2007).

[108] J.-B. Trebbia, C. L. Garrido Alzar, R. Cornelussen, C. I. Westbrook, and I. Bouchoule, *Roughness Suppression via Rapid Current Modulation on an Atom Chip*, Phys. Rev. Lett. **98**, 263201 (2007).

[109] J. Schmiedmayer, R. Folman, and T. Calarco, *Quantum information processing with neutral atoms on an atom chip*, J. Mod. Opt. **47**, 1375 (2002).

[110] M. J. Madou, *Fundamentals of Microfabrication: The Science of Miniaturization*, CRC Press, New York, 2nd edition, 2002.

[111] B. Lev, *Fabrication of micro-magnetic traps for cold neutral atoms*, Quant. Inf. Comput. **3**, 450 (2003).

[112] R. Long, T. Rom, W. Hänsel, T. W. Hänsch, and J. Reichel, *Long distance magnetic conveyor for precise positioning of ultracold atoms*, Eur. Phys. J. D **35**, 125 (2005).

[113] M. Drndić, K. S. Johnson, J. H. Thywissen, M. Prentiss, and R. M. Westervelt, *Micro-electromagnets for atom manipulation*, Appl. Phys. Lett. **72**, 2906 (1998).

[114] J. Fortágh, H. Ott, G. Schlotterbeck, C. Zimmermann, B. Herzog, and A. Wharam, *Microelectromagnets for trapping and manipulating ultracold atomic quantum gases*, Appl. Phys. Lett. **81**, 1146 (2002).

[115] S. Groth, P. Krüger, S. Wildermuth, R. Folman, T. Fernholz, J. Schmiedmayer, D. Mahalu, and I. Bar-Joseph, *Atom chips: Fabrication and thermal properties*, Appl. Phys. Lett. **85**, 2980 (2004).

[116] E. Koukharenko, Z. Moktadir, M. Kraft, M. Abdelsalam, D. Bagnall, C. Valeb, M. Jones, and E. Hinds, *Microfabrication of gold wires for atom guides*, Sens. Act. A **115**, 600 (2004).

[117] J. Estève, C. Aussibal, T. Schumm, C. Figl, D. Mailly, I. Bouchoule, C. I. Westbrook, and A. Aspect, *Role of wire imperfections in micromagnetic traps for atoms*, Phys. Rev. A **70**, 043629 (2004).

[118] A. Günther, M. Kemmler, S. Kraft, C. J. Vale, C. Zimmermann, and J. Fortágh, *Combined chips for atom optics*, Phys. Rev. A **71**, 063619 (2005).

[119] L. D. Pietra, S. Aigner, C. vom Hagen, S. Groth, I. Bar-Joseph, H. J. Lezec, and J. Schmiedmayer, *Designing potentials by sculpturing wires*, Phys. Rev. A **75**, 063604 (2007).

[120] K. R. Williams, G. Kishan, and M. Wasilik, *Etch Rates for Micromachining Processing—Part II*, J. Microelectromech. Syst. **12**, 761 (2003).

[121] B. Mussler and D. Brunner, *Aluminiumnitridkeramik*, in *Technische keramische Werkstoffe (DKG), 66. Ergänzung, Kap. 4.3.4.0*, edited by J. Kriegesmann, pages 1–33, Verlagsgruppe Deutscher Wirtschaftsdienst, 2001.

[122] R. M. Simons, *Coplanar Waveguide Circuits, Components, and Systems*, Wiley & Sons, New York, 2001.

[123] Cornell Nanofabrication Facility, *Microlithography Manual*, 2004.

[124] MicroChemicals GmbH, *Lithografie*, 2006.

[125] W. Ruythooren, K. Attenborough, S. Beerten, P. Merken, J. Fransaer, E. Beyne, C. Van Hoof, J. De Boeck, and J. P. Celis, *Electrodeposition for the synthesis of microsystems*, J. Micromech. Microeng. **10**, 101 (2000).

[126] M. Schlesinger and M. Paunovic, editors, *Modern Electroplating*, Wiley & Sons, New York, 4th edition, 2000.

[127] S. R. Wilson and C. J. Tracy, editors, *Handbook of Multilevel Metallization for Integrated Circuits: Materials, Technology, and Applications*, Noyes Publications, Westwood, New Jersey, U.S.A., 1993.

[128] H. J. Lewandowski, D. M. Harber, D. L. Whitaker, and E. A. Cornell, *Simplified System for Creating a BoseEinstein Condensate*, J. Low Temp. Phys. **132**, 309 (2003).

[129] P. Hommelhoff, *Bose-Einstein-Kondensate in Mikrochip-Fallen*, PhD thesis, Ludwig-Maximilians-Universität München and Max-Planck-Institut für Quantenoptik, 2002, published as MPQ report 280.

[130] S. Du, *Atom-chip Bose-Einstein condensation in a portable vacuum cell*, PhD thesis, University of Colorado, Boulder, 2005.

[131] J. Fortágh, A. Grossmann, T. W. Hänsch, and C. Zimmermann, *Fast loading of a magneto-optical trap from a pulsed thermal source*, J. Appl. Phys. **84**, 6499 (1998).

[132] B. P. Anderson and M. A. Kasevich, *Loading a vapor-cell magneto-optic trap using light-induced atom desorption*, Phys. Rev. A **63**, 023404 (2001).

[133] C. S. Adams and E. Riis, *Laser cooling and trapping of neutral atoms*, Prog. Quant. Electr. **21**, 1 (1997).

[134] H. J. Metcalf and P. van der Straten, *Laser Cooling and Trapping*, Springer, Berlin, 1999.

[135] T. W. Hänsch and A. L. Schawlow, *Cooling of gases by laser radiation*, Opt. Commun. **13**, 68 (1975).

[136] S. Chu, L. Hollberg, J. E. Bjorkholm, A. Cable, and A. Ashkin, *Three-Dimensional Viscous Confinement and Cooling of Atoms by Resonance Radiation Pressure*, Phys. Rev. Lett. **55**, 48 (1985).

[137] E. L. Raab, M. Prentiss, A. Cable, S. Chu, and D. E. Pritchard, *Trapping of Neutral Sodium Atoms with Radiation Pressure*, Phys. Rev. Lett. **59**, 2631 (1987).

[138] C. Monroe, W. Swann, H. Robinson, and C. Wieman, *Very Cold Trapped Atoms in a Vapor Cell*, Phys. Rev. Lett. **65**, 1571 (1990).

[139] K. E. Gibble, S. Kasapi, and S. Chu, *Improved magneto-optic trapping in a vapor cell*, Opt. Lett. **17**, 526 (1992).

[140] S. Wildermuth, P. Krüger, C. Becker, M. Brajdic, S. Haupt, A. Kasper, R. Folman, and J. Schmiedmayer, *Optimized magneto-optical trap for experiments with ultracold atoms near surfaces*, Phys. Rev. A **69**, 030901 (2004).

[141] J. Hoffrogge, *Mikrowellen-Nahfelder auf Atomchips*, Master's thesis, Ludwig-Maximilians-Universität München, 2007.

[142] L. Ricci, M. Weidemüller, T. Esslinger, A. Hemmerich, C. Zimmermann, V. Vuletic, W. König, and T. W. Hänsch, *A compact grating-stabilized diode laser system for atomic physics*, Opt. Comm. **117**, 541 (1995).

[143] T. W. Hänsch, M. D. Levenson, and A. L. Schawlow, *Complete Hyperfine Structure of a Molecular Iodine Line*, Phys. Rev. Lett. **26**, 946 (1972).

[144] X. Zhu and D. T. Cassidy, *Modulation spectroscopy with a semiconductor diode laser by injection-current modulation*, J. Opt. Soc. Am. B **14**, 1945 (1997).

[145] A. Vogel, M. Schmidt, K. Sengstock, K. Bongs, W. Lewoczko, T. Schuldt, A. Peters, T. van Zoest, W. Ertmer, E. Rasel, T. Steinmetz, J. Reichel, T. Könemann, W. Brinkmann, W. Göklü, C. Lämmerzahl, H. J. Dittus, G. Nandi, W. P. Schleich, and R. Walser, *Bose-Einstein condensates in microgravity*, Appl. Phys. B **84**, 663 (2006).

[146] W. Ketterle and N. J. van Druten, *Evaporative cooling of atoms*, Adv. At. Mol. Opt. Phys. **37**, 181 (1996).

[147] S. Schneider, A. Kasper, C. vom Hagen, M. Bartenstein, B. Engeser, T. Schumm, I. Bar-Joseph, R. Folman, L. Feenstra, and J. Schmiedmayer, *Bose-Einstein condensation in a simple microtrap*, Phys. Rev. A **67**, 023612 (2003).

[148] T. Liennard, *Développement D'un Système D'imagerie Très Faible Bruit*, Rapport de stage M2, Laboratoire Kastler Brossel, ENS Paris (2006).

[149] J. Merrill, *Characterization of Inelastic Losses from Bose-Einstein Condensates in the* $|2,1\rangle$ *State of* ^{87}Rb, Master's thesis, Amherst College, 2007.

[150] F. Schmidt-Kaler, S. Gulde, M. Riebe, T. Deuschle, A. Kreuter, G. Lancaster, C. Becher, J. Eschner, H. Häffner, and R. Blatt, *The coherence of qubits based on single Ca*$^+$ *ions*, J. Phys. B: At. Mol. Opt. Phys. **36**, 623 (2003).

[151] T. Gentile, B. Hughey, D. Kleppner, and T. Ducas, *Experimental study of one- and two-photon Rabi oscillations*, Phys. Rev. A **40**, 5103 (1989).

[152] M. O. Scully and M. S. Zubairy, *Quantum Optics*, Cambridge University Press, Cambridge, U.K., 1997.

[153] P. Meystre and M. Sargent, *Elements of Quantum Optics*, Springer, Berlin, 1990.

[154] F. Marquardt, *An introduction to the basics of dephasing*, available at www.theorie.physik.uni-muenchen.de/∼florian (2001).

[155] K. Hornberger, *Introduction to the theory of decoherence*, available at www.klaus-hornberger.de (2005).

[156] D. S. Hall, M. R. Matthews, J. R. Ensher, C. E. Wieman, and E. A. Cornell, *Dynamics of Component Separation in a Binary Mixture of Bose-Einstein Condensates*, Phys. Rev. Lett. **81**, 1539 (1998).

[157] D. S. Hall, M. R. Matthews, C. E. Wieman, and E. A. Cornell, *Measurements of Relative Phase in Two-Component Bose-Einstein Condensates*, Phys. Rev. Lett. **81**, 1543 (1998).

[158] H. J. Lewandowski, D. M. Harber, D. L. Whitaker, and E. A. Cornell, *Observation of Anomalous Spin-State Segregation in a Trapped Ultracold Vapor*, Phys. Rev. Lett. **88**, 070403 (2002).

[159] J. M. McGuirk, H. J. Lewandowski, D. M. Harber, T. Nikuni, J. E. Williams, and E. A. Cornell, *Spatial Resolution of Spin Waves in an Ultracold Gas*, Phys. Rev. Lett. **89**, 090402 (2002).

[160] J. E. Williams, T. Nikuni, and C. W. Clark, *Longitudinal Spin Waves in a Dilute Bose Gas*, Phys. Rev. Lett. **88**, 230405 (2002).

[161] N. F. Ramsey, *Molecular Beams*, Clarendon Press, Oxford, 1956.

[162] A. Stern, Y. Aharonov, and J. Imry, *Phase uncertainty and loss of interference: A general picture*, Phys. Rev. A **41**, 3436 (1990).

[163] G. Santarelli, P. Laurent, P. Lemonde, A. Clairon, A. G. Mann, S. Chang, A. N. Luiten, and C. Salomon, *Quantum Projection Noise in an Atomic Fountain: A High Stability Cesium Frequency Standard*, Phys. Rev. Lett. **82**, 4619 (1999).

[164] P. Treutlein, T. Steinmetz, Y. Colombe, B. Lev, P. Hommelhoff, J. Reichel, M. Greiner, O. Mandel, A. Widera, T. Rom, I. Bloch, and T. W. Hänsch, *Quantum information processing in optical lattices and magnetic microtraps*, Fortschr. Phys. **54**, 702 (2006).

[165] P. Treutlein, T. W. Hänsch, J. Reichel, A. Negretti, M. A. Cirone, and T. Calarco, *Microwave potentials and optimal control for robust quantum gates on an atom chip*, Phys. Rev. A **74**, 022312 (2006).

[166] C. Cohen-Tannoudji, J. Dupont-Roc, and G. Grynberg, *Atom-Photon Interactions*, Wiley-VCH, Berlin, 1998.

[167] J. H. Shirley, *Solution of the Schrödinger Equation with a Hamiltonian Periodic in Time*, Phys. Rev. **138**, B 979 (1965).

[168] H. Engler, T. Weber, M. Mudrich, R. Grimm, and M. Weidemüller, *Very long storage times and evaporative cooling of cesium atoms in a quasielectrostatic dipole trap*, Phys. Rev. A **62**, 031402 (2000).

[169] A. Messiah, *Quantum Mechanics*, volume 2, Dover, Mineola, N.Y., 2000.

[170] C. C. Agosta, I. F. Silvera, H. T. C. Stoof, and B. J. Verhaar, *Trapping of Neutral Atoms with Resonant Microwave Radiation*, Phys. Rev. Lett. **62**, 2361 (1989).

[171] R. J. C. Spreeuw, C. Gerz, L. S. Goldner, W. D. Phillips, S. L. Rolston, C. I. Westbrook, M. W. Reynolds, and I. F. Silvera, *Demonstration of Neutral Atom Trapping with Microwaves*, Phys. Rev. Lett. **72**, 3162 (1994).

[172] R. E. Collin, *Foundations for Microwave Engineering*, John Wiley & Sons, Hoboken, 2nd edition, 2001.

[173] Y. Colombe, E. Knyazchyan, O. Morizot, B. Mercier, V. Lorent, and H. Perrin, *Ultracold atoms confined in rf-induced two-dimensional trapping potentials*, Europhys. Lett. **67**, 593 (2004).

[174] G. E. Ponchak, L. P. B. Katehi, and E. M. Tentzeris, *Finite Ground Coplanar (FGC) Waveguide: It's Characteristics and Advantages For Use In RF and Wireless Communication Circuits*, in *3rd International Wireless Communications Conference (WCC '98) Digest, San Diego, CA, Nov. 13, 1998*, pages 75–83, 1998.

[175] P. A. Rizzi, *Microwave Engineering Passive Circuits*, Prentice Hall, Englewood Cliffs, New Jersey, 1988.

[176] W. Heinrich, *Quasi-TEM description of MMIC coplanar lines including conductor-loss effects*, IEEE Trans. Microwave Theory Tech. **41**, 45 (1993).

[177] M. Kunze and W. Heinrich, *Efficient FD formulation for lossy waveguide analysis based on quasi-static field characteristics*, IEEE Microwave and Guided Wave Letters **9**, 499 (1999).

[178] M. Kunze, *Effiziente FD-Berechnung verlustbehafteter planarer Strukturen unter Berücksichtigung quasi-statischer Lösungen*, PhD thesis, Technische Universität Berlin, 2003.

[179] A. S. Sørensen, C. H. van der Wal, L. I. Childress, and M. D. Lukin, *Capacitive Coupling of Atomic Systems to Mesoscopic Conductors*, Phys. Rev. Lett. **92**, 063601 (2004).

[180] A. Negretti, T. Calarco, M. A. Cirone, and A. Recati, *Performance of quantum phase gates with cold trapped atoms*, Eur. Phys. J. D **32**, 119 (2005).

[181] A. Steane, *Overhead and noise threshold of fault-tolerant quantum error correction*, Phys. Rev. A **68**, 42322 (2003).

[182] E. Knill, *Scalable quantum computing in the presence of large detected-error rates*, Phys. Rev. A **71**, 42322 (2005).

[183] M. Olshanii, *Atomic Scattering in the Presence of an External Confinement and a Gas of Impenetrable Bosons*, Phys. Rev. Lett. **81**, 938 (1998).

[184] T. Calarco, J. I. Cirac, and P. Zoller, *Entangling ions in arrays of microscopic traps*, Phys. Rev. A **63**, 062304 (2001).

[185] S. E. Sklarz and D. J. Tannor, *Loading a Bose-Einstein condensate onto an optical lattice: An application of optimal control theory to the nonlinear Schrödinger equation*, Phys. Rev. A **66**, 053619 (2002).

[186] T. Calarco, U. Dorner, P. S. Julienne, C. J. Williams, and P. Zoller, *Quantum computations with atoms in optical lattices: Marker qubits and molecular interactions*, Phys. Rev. A **70**, 012306 (2004).

[187] V. F. Krotov, *Global Methods in Optimal Control Theory*, in *Monographs and Textbooks in Pure and Applied Mathematics, Vol. **195***, Marcel Dekker Inc., New York, 1996.

[188] Z. Idziaszek and T. Calarco, *Two atoms in an anisotropic harmonic trap*, Phys. Rev. A **71**, 050701 (2005).

[189] B. Zhang, C. Henkel, E. Haller, S. Wildermuth, S. Hofferberth, P. Krüger, and J. Schmiedmayer, *Relevance of sub-surface chip layers for the lifetime of magnetically trapped atoms*, Eur. Phys. J. D **35**, 97 (2005).

[190] R. B. Diener, B. Wu, M. G. Raizen, and Q. Niu, *Quantum Tweezer for Atoms*, Phys. Rev. Lett. **89**, 070401 (2002).

[191] P. Treutlein, D. Hunger, S. Camerer, T. W. Hänsch, and J. Reichel, *Bose-Einstein Condensate Coupled to a Nanomechanical Resonator on an Atom Chip*, Phys. Rev. Lett. **99**, 140403 (2007).

[192] A. Wallraff, D. I. Schuster, A. Blais, L. Frunzio, R.-S. Huang, J. Majer, S. Kumar, S. M. Girvin, and R. J. Schoelkopf, *Strong coupling of a single photon to a superconducting qubit using circuit quantum electrodynamics*, Nature **431**, 162 (2004).

[193] C. Höhberger Metzger and K. Karrai, *Cavity cooling of a microlever*, Nature **432**, 1002 (2004).

[194] O. Arcizet, P.-F. Cohadon, T. Briant, M. Pinard, and A. Heidmann, *Radiation-pressure cooling and optomechanical instability of a micromirror*, Nature **444**, 71 (2006).

[195] S. Gigan, H. R. Böhm, M. Paternostro, F. Blaser, G. Langer, J. B. Hertzberg, K. Schwab, D. Bäuerle, M. Aspelmeyer, and A. Zeilinger, *Self-cooling of a micro-mirror by radiation pressure*, Nature **444**, 67 (2006).

[196] D. Kleckner and D. Bouwmeester, *Sub-kelvin optical cooling of a micromechanical resonator*, Nature **444**, 75 (2006).

[197] A. Schliesser, P. Del'Haye, N. Nooshi, K. J. Vahala, and T. J. Kippenberg, *Radiation Pressure Cooling of a Micromechanical Oscillator Using Dynamical Backaction*, Phys. Rev. Lett. **97**, 243905 (2006).

[198] I. Favero, C. Metzger, S. Camerer, D. König, H. Lorenz, J. P. Kotthaus, and K. Karrai, *Optical cooling of a micromirror of wavelength size*, Appl. Phys. Lett. **90**, 104101 (2007).

[199] A. Naik, O. Buu, M. D. LaHaye, A. D. Armour, A. A. Clerk, M. P. Blencowe, and K. C. Schwab, *Cooling a nanomechanical resonator with quantum back-action*, Nature **443**, 193 (2006).

[200] Y.-J. Wang, M. Eardley, S. Knappe, J. Moreland, L. Hollberg, and J. Kitching, *Magnetic Resonance in an Atomic Vapor Excited by a Mechanical Resonator*, Phys. Rev. Lett. **97**, 227602 (2006).

[201] L. Tian and P. Zoller, *Coupled Ion-Nanomechanical Systems*, Phys. Rev. Lett. **93**, 266403 (2004).

[202] A. André, D. DeMille, J. M. Doyle, M. D. Lukin, S. E. Maxwell, P. Rabl, R. J. Schoelkopf, and P. Zoller, *A coherent all-electrical interface between polar molecules andmesoscopic superconducting resonators*, Nat. Phys. **2**, 636 (2006).

[203] K. L. Ekinci and M. L. Roukes, *Nanoelectromechanical systems*, Rev. Sci. Instrum. **76**, 061101 (2005).

[204] I. Bloch, T. W. Hänsch, and T. Esslinger, *Atom Laser with a cw Output Coupler*, Phys. Rev. Lett. **82**, 3008 (1999).

[205] H. Steck, M. Naraschewski, and H. Wallis, *Output of a Pulsed Atom Laser*, Phys. Rev. Lett. **80**, 1 (1998).

[206] D. V. Scheible, C. Weiss, J. P. Kotthaus, and R. H. Blick, *Periodic Field Emission from an Isolated Nanoscale Electron Island*, Phys. Rev. Lett. **93**, 186801 (2004).

[207] L. Kong and S. Y. Chou, *Effects of bar length on switching field of nanoscale nickel and cobalt bars fabricated using lithography*, J. Appl. Phys. **80**, 5205 (1996).

[208] T. Briant, P. F. Cohadon, M. Pinard, and A. Heidmann, *Optical phase-space reconstruction of mirror motion at the attometer level*, Eur. Phys. J. D **22**, 131 (2003).

[209] R. Engel-Herbert and T. Hesjedal, *Calculation of the magnetic stray field of a uniaxial magnetic domain*, J. Appl. Phys. **97**, 074504 (2005).

[210] B. W. Shore and P. L. Knight, *The Jaynes-Cummings model*, J. Mod. Opt. **40**, 1195 (1993).

[211] H. J. Kimble, *Structure and dynamics in cavity quantum electrodynamics*, in *Cavity Quantum Electrodynamics*, edited by P. Berman, pages 203–266, Academic Press, San Diego, U.S.A., 1994.

[212] H. Katori and T. Akatsuka, *Electric Manipulation of Spinless Neutral Atoms on a Surface*, Jpn. J. Appl. Phys. **43**, 358 (2004).

[213] S. Gleyzes, S. Kuhr, C. Guerlin, J. Bernu, S. Deléglise, U. B. Hoff, M. Brune, J.-M. Raimond, and S. Haroche, *Quantum jumps of light recording the birth and death of a photon in a cavity*, Nature **446**, 297 (2007).

[214] C. J. Bordé, *Atomic interferometry with internal state labelling*, Phys. Lett. A **140**, 10 (1989).

[215] A. D. Cronin, J. Schmiedmayer, and D. E. Pritchard, *Atom Interferometers*, preprint arXiv:0712.3703 [quant-ph] (2007).

[216] M. Albiez, R. Gati, J. Fölling, S. Hunsmann, M. Cristiani, and M. K. Oberthaler, *Direct Observation of Tunneling and Nonlinear Self-Trapping in a Single Bosonic Josephson Junction*, Phys. Rev. Lett. **95**, 010402 (2005).

[217] R. Gati and M. K. Oberthaler, *A bosonic Josephson junction*, J. Phys. B: At. Mol. Opt. Phys. **40**, 61 (2007).

[218] J. Williams, R. Walser, J. Cooper, E. Cornell, and M. Holland, *Nonlinear Josephson-type oscillations of a driven, two-component Bose-Einstein condensate*, Phys. Rev. A **59**, 31 (1999).

[219] D. A. R. Dalvit, J. Dziarmaga, and W. H. Zurek, *Decoherence in Bose-Einstein condensates: Towards bigger and better Schrödinger cats*, Phys. Rev. A **62**, 013607 (2000).

[220] A. Micheli, D. Jaksch, J. I. Cirac, and P. Zoller, *Many-particle entanglement in two-component Bose-Einstein condensates*, Phys. Rev. A **67**, 013607 (2003).

[221] I. E. Mazets, G. Kurizki, M. K. Oberthaler, and J. Schmiedmayer, *Schrödinger-cat state creation by a measurement*, preprint arXiv:0710.3578 [quant-ph] (2007).

[222] P. Poncharal, Z. L. Wang, D. Ugarte, and W. A. de Heer, *Electrostatic Deflections and Electromechanical Resonances of Carbon Nanotubes*, Science **283**, 1513 (1999).

[223] B. Babić, J. Furer, S. Sahoo, S. Farhangfar, and C. Schönenberger, *Intrinsic Thermal Vibrations of Suspended Doubly Clamped Single-Wall Carbon Nanotubes*, Nano Lett. **3**, 1577 (2003).

[224] V. Sazonova, Y. Yaish, H. Üstünel, D. Roundy, T. A. Arias, and P. L. McEuen, *A tunable carbon nanotube electromechanical oscillator*, Nature **431**, 284 (2004).

[225] J. S. Bunch, A. M. van der Zande, S. S. Verbridge, I. W. Frank, D. M. Tanenbaum, J. M. Parpia, H. G. Craighead, and P. L. McEuen, *Electromechanical Resonators from Graphene Sheets*, Science **315**, 490 (2007).

[226] S. M. Tanner, J. M. Gray, C. T. Rogers, K. A. Bertness, and N. A. Sanford, *High-Q GaN nanowire resonators and oscillators*, Appl. Phys. Lett. **91**, 203117 (2007).

[227] V. Peano, M. Thorwart, A. Kasper, and R. Egger, *Nanoscale atomic waveguides with suspended carbon nanotubes*, Appl. Phys. B **81**, 1075 (2005).

[228] J. T. M. Walraven and I. F. Silvera, *Measurement of the static magnetization of spin-polarized atomic hydrogen with a SQUID magnetometer*, Physica **107B**, 517 (1981).

[229] Y. Nakamura, Y. A. Pashkin, and J. S. Tsai, *Coherent control of macroscopic quantum states in a single-Cooper-pair box*, Nature **398**, 786 (1999).

[230] D. Vion, A. Aassime, A. Cottet, P. Joyez, H. Pothier, C. Urbina, D. Esteve, and M. H. Devoret, *Manipulating the Quantum State of an Electrical Circuit*, Science **296**, 886 (2002).

[231] I. Chiorescu, Y. Nakamura, C. J. P. M. Harmans, and J. E. Mooij, *Coherent Quantum Dynamics of a Superconducting Flux Qubit*, Science **299**, 1869 (2003).

[232] D. Petrosyan and M. Fleischhauer, *Quantum information processing with single photons and atomic ensembles in microwave coplanar waveguide resonators*, preprint arXiv:0802.2154 [quant-ph] (2008).

[233] S. Wildermuth, S. Hofferberth, I. Lesanovsky, E. Haller, L. M. Andersson, S. Groth, I. Bar-Joseph, P. Krüger, and J. Schmiedmayer, *Microscopic magnetic-field imaging*, Nature **435**, 440 (2005).

[234] M. E. Rose, *Elementary Theory of Angular Momentum*, Wiley, New York, 1957.

Danksagung

Mein herzlicher Dank gilt allen, die zum Gelingen dieser Arbeit beigetragen haben.

Besonders bedanken möchte ich mich bei Prof. Theodor W. Hänsch für die Aufnahme in seine Arbeitsgruppe, die inspirierende Atmosphäre und das mir entgegengebrachte Vertrauen. Die Diskussionen mit ihm waren eine große Bereicherung — besonders beeindrucken mich sein Eintreten für Forschung aus Neugier und seine Ideen für einfache, aber raffinierte Experimente.

Prof. Jakob Reichel möchte ich ganz besonders danken für die Betreuung dieser Arbeit, zunächst in München und dann von Paris aus, sowie für die zahlreichen intensiven Diskussionen, die wir in den vergangenen Jahren geführt haben. In physikalischen Dingen und auch darüber hinaus habe ich viel von ihm gelernt. Den freundschaftlichen Gesprächen und seiner großzügigen Art verdanke ich ebenso viel.

Mit Tilo Steinmetz und Yves Colombe verbinden mich nicht nur der wissenschaftliche Austausch über unsere Experimente und die gemeinsame Zeit in der Schellingstraße, sondern auch diverse freundschaftliche Aktivitäten in München, Paris, Oberbayern und anderswo. Dafür möchte ich ihnen ganz herzlich danken und freue mich schon auf eine Fortführung.

Peter Hommelhoff danke ich für die Einführung in die Geheimnisse des Experiments und die gemeinsam durchgeführten Messungen zu Beginn meiner Arbeit, die sehr viel Spaß gemacht haben.

In den vergangenen zwei Jahren haben David Hunger, Stephan Camerer, Pascal Böhi, Max Riedel und Johannes Hoffrogge zwei ausgesprochen schöne neue Experimente aufgebaut — mit denen wir hoffentlich noch viele spannende Messungen mit Atomen, Mikrowellen und Nanoresonatoren machen werden. Dass darüber auch der Spaß sowie die musikalische und sportliche Betätigung nicht zu kurz kommen, steht ganz in der Tradition der Mikrofallengruppe.

Michael Ingrisch danke ich für die Hilfe bei der nicht immer ganz einfachen Entwicklung des Chip-Fabrikationsprozesses. Rémi Delhuille, Romain Long, Akifumi Takamizawa sowie allen weiteren derzeitigen und ehemaligen

Mitgliedern der Arbeitsgruppen Hänsch und Weinfurter danke ich für inspirierende Diskussionen, das unkomplizierte Aushelfen, wenn im Labor mal wieder ein Teil gefehlt hat, und zahlreiche schöne Erlebnisse z.B. auf Schloss Ringberg.

Daniel König und Prof. Jörg Kotthaus danke ich für die gute Zusammenarbeit am BEC-Nanoresonator-Experiment. Insbesondere ist die Großzügigkeit von Prof. Kotthaus hervorzuheben, der es uns ermöglicht, unsere Chips im Reinraum seiner Arbeitsgruppe zu fabrizieren. Heribert Lorenz, Stefan Schöffberger, Alexander Paul und Philipp Altpeter sei für die Unterstützung bei der Arbeit im Reinraum gedankt.

Antonio Negretti, Markus Cirone und Tommaso Calarco danke ich für die erfolgreiche Zusammenarbeit am theoretischen Vorschlag für das Atomchip-Quantengatter sowie die freundlichen Einladungen nach Trento.

Benjamin Lev danke ich für die Fabrikation des Atominterferometer-Chips sowie für viele anregende Diskussionen während seiner Besuche in München.

Federico Peretti und György Csaba aus der Gruppe von Prof. Lugli an der TU München danke ich für die Simulation eines unserer Mikrowellenleiter. Ebenso sei Franz-Josef Schmückle vom Ferdinand-Braun-Institut für Höchstfrequenztechnik in Berlin für Mikrowellensimulationen gedankt.

Der neuen Arbeitsgruppe von Jakob Reichel in Paris sei für vielfältige Zusammenarbeit gedankt, besonders Tobias Schneider für die Arbeit am Projekt „BEC in Mehrfachmuldenpotentialen“ sowie Friedemann Reinhardt für die Zusammenarbeit bei den Mikrowellensimulationen.

Anton Scheich und Nicole Schmidt danke ich für den Entwurf und den Aufbau diverser elektronischer Geräte, ohne die wir unsere Experimente nicht durchführen könnten. Den Mitarbeitern in den Werkstätten des MPQ und der LMU danke ich gleichermaßen für die präzise Anfertigung vieler mechanischer Teile. Gabriele Gschwendtner und der leider vor kurzem verstorbenen Rosemarie Lechner danke ich für die Unterstützung in administrativen und organisatorischen Fragen.

Ein besonderer Dank geht an Hildegard Luttenbacher, für viele nette Gespräche über die Münchner Musik- und Theaterszene und natürlich den hervorragenden Kuchen!

Ein ganz spezieller Dank geht an Elke Schlote, meine Eltern, Geschwister und Freunde. Sie haben ganz wesentlich dazu beigetragen, dass die Zeit meiner Doktorarbeit — ebenso wie auch die Zeit davor — so großartig war!